

PORTUGALIAE PHYSICA

VOLUME 12
FASCÍCULO 1-2
1981

SOCIEDADE PORTUGUESA DE FÍSICA

PORTUGALIAE PHYSICA

Fundada em 1943 por A. Cyrillo Soares, M. Telles Antunes, A. Marques da Silva e M. Valadares

Director

J. M. Araújo (Faculdade de Ciências, Universidade do Porto)

Comissão Redactorial

J. M. Araújo (Faculdade de Ciências, Universidade do Porto)

J. Gomes Ferreira (Faculdade de Ciências, Universidade de Lisboa)

F. Bragança Gil (Faculdade de Ciências, Universidade de Lisboa)

M. F. Laranjeira (Faculdade de Ciências e Tecnologia, Universidade Nova de Lisboa)

F. D. S. Marques (Universidade do Minho)

A. Farinha Martins (Centro de Física da Matéria Condensada, Lisboa)

R. Vilela Mendes (Centro de Física da Matéria Condensada, Lisboa)

A. M. C. Moutinho (Centro de Física Molecular, Lisboa)

J. Pinto Peixoto (Faculdade de Ciências, Universidade de Lisboa)

A. Policarpo (Faculdade de Ciências e Tecnologia, Universidade de Coimbra)

J. da Providência (Faculdade de Ciências e Tecnologia, Universidade de Coimbra)

F. Carvalho Rodrigues (Laboratório de Física e Engenharia Nucleares, Sacavém).

F. D. Santos (Faculdade de Ciências, Universidade de Lisboa)

E. Ducla Soares (Faculdade de Ciências, Universidade de Lisboa)

O. D. D. Soares (Faculdade de Ciências, Universidade do Porto)

J. B. Sousa (Faculdade de Ciências, Universidade do Porto)

A. T. Rocha Trindade (Instituto Superior Técnico, Lisboa)

L. Alte da Veiga (Faculdade de Ciências e Tecnologia, Universidade de Coimbra)

ISSN 0048 - 4903

PORTUGALIAE PHYSICA

117

VOLUME 12
FASCÍCULO 1-2
1981



TIME DEPENDENT GENERATOR COORDINATE METHOD AND THE N-N INTERACTION *

L. P. BRITO and C. A. SOUSA

Departamento de Física, Universidade de Coimbra
3000 Coimbra, Portugal

(Received 3 February 1981)

ABSTRACT — An attempt is made to describe the nucleon — nucleon interaction in a non — relativistic situation. Explicit expressions are obtained using a non — perturbative method appropriate to the wave packet which describes moving particles.

1 — INTRODUCTION. GENERAL CONSIDERATIONS

The question of the nature of the force between two nucleons has occupied a central place in physics.

Although Yukawa's theory, explaining the nuclear interaction as a result of the exchange of mesons between nucleons, dates back to 1935, the most important calculations of the nucleon-nucleon interaction in terms of π meson exchange was first carried out about 1950.

In this paper we wish to investigate the interaction energy between two nucleons, in a state of relative motion, from a non-perturbative viewpoint.

We consider the system nucleon — meson cloud in a very simplified version, that is, we restrict our discussion to scalar mesons exchanged between scalar nucleons.

(*) Work supported by Instituto Nacional de Investigação Científica, Lisbon.

In this way the Hamiltonian may be written:

$$H = \sum_{\mathbf{p}} (p^2/2m) C_{\mathbf{p}}^+ C_{\mathbf{p}} + \sum_{\mathbf{k}} \omega_{\mathbf{k}} A_{\mathbf{k}}^+ A_{\mathbf{k}} \quad (1)$$

$$+ G \sum_{\mathbf{p}, \mathbf{k}} (2 \omega_{\mathbf{k}} V)^{-1/2} [A_{\mathbf{k}}^+ C_{\mathbf{p}}^+ C_{\mathbf{p}+\mathbf{k}} + C_{\mathbf{p}+\mathbf{k}}^+ C_{\mathbf{p}} A_{\mathbf{k}}]$$

where $C_{\mathbf{p}}^+$ ($C_{\mathbf{p}}$) creates (annihilates) a nucleon with momentum \mathbf{p} and $A_{\mathbf{k}}^+$ ($A_{\mathbf{k}}$) creates (annihilates) a meson with momentum \mathbf{k} .

In equation (1), m denotes the nucleon mass and $\omega_{\mathbf{k}} = (k^2 + \mu^2)^{1/2}$, where μ is the meson mass. G is the coupling constant between nucleons and mesons and V refers to the normalization volume.

The operators $C_{\mathbf{p}}^+$ ($C_{\mathbf{p}}$) and $A_{\mathbf{k}}^+$ ($A_{\mathbf{k}}$) obey the usual commutation relations for fermions and bosons, respectively.

First, we consider the problem of one nucleon state and we calculate the expression of the energy of this system. After the interpretation of these results we follow the same procedure for a system of two interacting nucleons.

2 — ONE NUCLEON STATES

We construct the wave function for the system, as usually [1] [2], using the variational method, proceeding in analogy with the Hartree-Fock theory. To do this, we first consider the state $|\zeta\rangle$ such that

$$A_{\mathbf{k}} |\zeta\rangle = \zeta_{\mathbf{k}} |\zeta\rangle \quad (2)$$

$$C_{\mathbf{p}} |\zeta\rangle = 0 \quad (3)$$

where $\zeta_{\mathbf{k}}$ is a parameter. $|\zeta\rangle$ is a coherent state given by

$$|\zeta\rangle = \mathcal{N} \exp \left(\sum_{\mathbf{k}} \zeta_{\mathbf{k}} A_{\mathbf{k}}^+ \right) |0\rangle \quad (4)$$

where \mathcal{N} is a normalization constant and $|0\rangle$ is the absolute vacuum,

$$A_{\mathbf{k}} |0\rangle = C_{\mathbf{p}} |0\rangle = 0 \quad (5)$$

A one-nucleon state may be obtained by the following construction

$$|\psi, \zeta\rangle = \sum_{\mathbf{p}} \psi_{\mathbf{p}} C_{\mathbf{p}}^+ |\zeta\rangle \quad (6)$$

The ket $|\psi, \zeta\rangle$ is normalized to unity provided the amplitudes $\psi_{\mathbf{p}}$ satisfy the relation

$$\sum_{\mathbf{p}} \psi_{\mathbf{p}}^* \psi_{\mathbf{p}} = 1 \quad (7)$$

The quantities $\psi_{\mathbf{p}}$ and $\zeta_{\mathbf{k}}$ are variational parameters obtained by minimization of the expectation value

$$\langle \psi, \zeta | \mathbf{H} | \psi, \zeta \rangle / \langle \psi, \zeta | \psi, \zeta \rangle \quad (8)$$

We introduce the following simplifying assumption for $\psi_{\mathbf{p}}$

$$\psi_{\mathbf{p}} = [(4\pi\lambda)^{3/2} / V]^{1/2} \exp(-1/2 \lambda p^2) \quad (9)$$

where λ is a parameter.

If we consider now the system placed on a point of space with positional vector \mathbf{r} , the function given by eq. (6) may be written

$$|\psi, \zeta\rangle = \sum_{\mathbf{p}} \psi_{\mathbf{p}} e^{-i\mathbf{p}\cdot\mathbf{r}} C_{\mathbf{p}}^+ \exp\left(\sum_{\mathbf{k}} \zeta_{\mathbf{k}} e^{-i\mathbf{k}\cdot\mathbf{r}} A_{\mathbf{k}}^+\right) |0\rangle \quad (10)$$

The ket $|\psi, \zeta\rangle$, with the structure given by eq. (10), represents a static description of the system nucleon-meson [3]. The introduction of the velocity in that wave function may be done by writing

$$|\psi, \zeta\rangle = \sum_{\mathbf{p}} \psi(\mathbf{p} - \mathbf{p}_0) e^{-i\mathbf{p}\cdot\mathbf{r}} C_{\mathbf{p}}^+ \exp\left(\sum_{\mathbf{k}} \zeta_{\mathbf{k}} e^{-i\mathbf{k}\cdot\mathbf{r}} A_{\mathbf{k}}^+\right) |0\rangle \quad (11)$$

where \mathbf{p}_0 is a new variational parameter.

In order to obtain the expression of the parameter $\zeta_{\mathbf{k}}$ the minimization of eq. (8) should be performed by constraining the momentum operator \mathbf{P} which may be written

$$\mathbf{P} = \sum_{\mathbf{p}} \mathbf{p} C_{\mathbf{p}}^+ C_{\mathbf{p}} + \sum_{\mathbf{k}} \mathbf{k} A_{\mathbf{k}}^+ A_{\mathbf{k}} \quad (12)$$

The expectation value of $(H - \mathbf{b} \cdot \mathbf{P})$ where \mathbf{b} is a Lagrange multiplier, leads to

$$\begin{aligned} \langle \psi, \zeta | (H - \mathbf{b} \cdot \mathbf{P}) | \psi, \zeta \rangle &= (1/2 m) (p_0^2 + 3/(2 \lambda)) + \\ &\sum_{\mathbf{k}} \omega_{\mathbf{k}} \zeta_{\mathbf{k}}^* \zeta_{\mathbf{k}} + G \sum_{\mathbf{k}} (2 \omega_{\mathbf{k}} V)^{-1/2} (\zeta_{\mathbf{k}}^* + \zeta_{\mathbf{k}}) \\ &\exp(-1/4 \lambda k^2) - \mathbf{b} \cdot \mathbf{p}_0 - \mathbf{b} \cdot \sum_{\mathbf{k}} \mathbf{k} \zeta_{\mathbf{k}}^* \zeta_{\mathbf{k}} \end{aligned} \quad (13)$$

To obtain eq. (13) we have used the relations

$$\begin{aligned} \sum_{\mathbf{p}} \psi_{\mathbf{p}}^* \psi_{\mathbf{p}} &= 1 \\ \sum_{\mathbf{p}} \psi_{\mathbf{p}}^* p^2 \psi_{\mathbf{p}} &= p_0^2 + 3/(2 \lambda) \\ \sum_{\mathbf{p}} \psi_{\mathbf{p}+\mathbf{k}} \psi_{\mathbf{p}} &= \exp(-1/4 \lambda k^2) \end{aligned}$$

Variation of eq. (13) with respect to $\zeta_{\mathbf{k}}$ yields

$$\zeta_{\mathbf{k}} = -G (2 \omega_{\mathbf{k}} V)^{-1/2} (\omega_{\mathbf{k}} - \mathbf{b} \cdot \mathbf{k})^{-1} \exp(-1/4 \lambda k^2) \quad (14)$$

Further variation with respect to \mathbf{p}_0 yields $\mathbf{p}_0 = \mathbf{b} m$ which suggests that one can identify the quantity \mathbf{b} as the velocity of the system.

The energy expectation value of the nucleon-meson system is then

$$\begin{aligned} \mathcal{H}_1 &= \langle \psi, \zeta | H | \psi, \zeta \rangle / \langle \psi, \zeta | \psi, \zeta \rangle = 3/(4 m \lambda) + (m/2) \mathbf{b} \cdot \mathbf{b} \\ &- G \sum_{\mathbf{k}} [1/(2 \omega_{\mathbf{k}}^2) - (\mathbf{b} \cdot \mathbf{k})^2 / (2 \omega_{\mathbf{k}}^4)] \exp(-1/2 \lambda k^2) \\ &\approx 3/(4 m \lambda) - G^2 / (4 \pi \sqrt{2 \pi \lambda}) + 1/2 \mathbf{b} \cdot \mathbf{b} [m + G^2 / (6 \pi \sqrt{2 \pi \lambda})] \end{aligned} \quad (15)$$

where we have used the expansion of the expression of $\zeta_{\mathbf{k}}$ (eq. 14) up to second order in powers of \mathbf{b} and performed the summation over \mathbf{k} .

Comparing this expression with the expectation value of the momentum operator which is

$$\langle \psi, \zeta | \mathbf{P} | \psi, \zeta \rangle = \mathbf{b} [m + G^2 / (6 \pi \sqrt{2 \pi \lambda})] \quad (16)$$

we may notice that:

- i) the interpretation already given for the parameter \mathbf{b} is confirmed;
- ii) it is possible to define the nucleon mass as

$$\mathcal{M} = m + G^2 / (6 \pi \sqrt{2 \pi \lambda}) \quad (17)$$

When we write the Lagangian of this system

$$\mathcal{L} = \dot{\mathbf{r}} \cdot \mathbf{b} [m + G^2 / (6 \pi \sqrt{2 \pi \lambda})] - \mathcal{H}_1 \quad (18)$$

we can also define the momentum canonically conjugate to \mathbf{r} as

$$\mathbf{p} = \mathcal{M} \mathbf{b} \quad (19)$$

3 — TWO NUCLEON STATES: THE NUCLEAR INTERACTION

In analogy with the procedure followed in the previous section to construct the one-nucleon states, we may now write the wave function to describe two nucleons with opposite velocities \mathbf{b} and $-\mathbf{b}$ and localized at points a distance $|\mathbf{r}|$ apart

$$\begin{aligned} \psi_{1,2}(\mathbf{r}, \mathbf{b}) = \sum_{\mathbf{p}, \mathbf{p}'} \psi(\mathbf{p} - \mathbf{b} m) e^{-i \mathbf{p} \cdot \mathbf{r} / 2} C_{\mathbf{p}}^+ \exp\left(\sum_{\mathbf{k}} \zeta_{\mathbf{k}, \mathbf{b}} e^{-i \mathbf{k} \cdot \mathbf{r} / 2} A_{\mathbf{k}}^+\right) \\ \psi(\mathbf{p}' + \mathbf{b} m) e^{i \mathbf{p}' \cdot \mathbf{r} / 2} C_{\mathbf{p}'}^+ \exp\left(\sum_{\mathbf{k}'} \zeta_{\mathbf{k}', \mathbf{b}} e^{i \mathbf{k}' \cdot \mathbf{r} / 2} A_{\mathbf{k}'}^+\right) |0\rangle \end{aligned} \quad (20)$$

With the Hamiltonian written in eq. (1) and eq. (20) we can write

$$\begin{aligned} \mathcal{H}_{12} = \langle \psi_{1,2}(\mathbf{r}, \mathbf{b}) | \mathbf{H} | \psi_{1,2}(\mathbf{r}, \mathbf{b}) \rangle / \langle \psi_{1,2}(\mathbf{r}, \mathbf{b}) | \psi_{1,2}(\mathbf{r}, \mathbf{b}) \rangle \\ = [3 / (2 m \lambda) + b^2 m] + \sum_{\mathbf{k}} \omega [\zeta_{\mathbf{k}, \mathbf{b}}^2 + \zeta_{\mathbf{k}, -\mathbf{b}}^2 + \\ \zeta_{\mathbf{k}, \mathbf{b}} \zeta_{\mathbf{k}, -\mathbf{b}} (e^{i \mathbf{k} \cdot \mathbf{r}} + e^{-i \mathbf{k} \cdot \mathbf{r}})] \end{aligned} \quad (21)$$

and, after performing the calculations, we find

$$\begin{aligned} \mathcal{H}_{12} = & 2 [3 / (4 m \lambda) - G^2 / (4 \pi \sqrt{2 \pi \lambda})] + (\mathbf{b} \cdot \mathbf{b}) \\ & [m + G^2 / (6 \pi \sqrt{2 \pi \lambda})] - (G^2 / 4 \pi) [1 + 1/2 \mathbf{b} \cdot \mathbf{b} \quad (22) \\ & - (\mu / 2 r) (\mathbf{b} \cdot \mathbf{r})^2 - (1/2 r^2) (\mathbf{b} \cdot \mathbf{r})^2] (e^{-\mu r} / r) \end{aligned}$$

We may notice, by comparison of this equation with eq. (15), that the first part of the previous expression is twice the nucleon energy. So, one can write for the interaction energy between the two nucleons

$$\begin{aligned} \mathcal{V}_{\text{int}} = & - (G^2 / 4 \pi) [1 + 1/2 \mathbf{b} \cdot \mathbf{b} - (\mu / 2 r) (\mathbf{b} \cdot \mathbf{r})^2 \\ & - (1/2 r^2) (\mathbf{b} \cdot \mathbf{r})^2] (e^{-\mu r} / r) \quad (23) \end{aligned}$$

For systems described by the Schrödinger equation the Lagrangian is

$$\mathcal{L} = \langle \psi | i d/dt - H | \psi \rangle \quad (24)$$

When we perform the calculation we obtain

$$\langle \psi | \partial / \partial \vec{\mathbf{r}} | \psi \rangle = - i \mathbf{b} [m + G^2 / (6 \pi \sqrt{2 \pi \lambda})] \quad (25)$$

and, therefore, we can write

$$\mathcal{L} = \dot{\mathbf{r}} \cdot \mathbf{b} [m + G^2 / (6 \pi \sqrt{2 \pi \lambda})] - \mathcal{H}_{12} \quad (26)$$

where \mathbf{r} represents the relative coordinate of the two particles and $\mathcal{H}_{1,2}$ is given by eq. (21).

From $\partial \mathcal{L} / \partial \vec{\mathbf{b}} = 0$ we conclude that

$$\begin{aligned} \dot{\mathbf{r}} = & 2 \mathbf{b} - (G^2 / 4 \pi) [m + G^2 / (6 \pi \sqrt{2 \pi \lambda})]^{-1} [\mathbf{b} - (\mathbf{b} \cdot \mathbf{r}) (\mathbf{r} / r^2) \\ & - (\mathbf{b} \cdot \mathbf{r}) (\mu \mathbf{r} / r)] (e^{-\mu r} / r) \quad (27) \end{aligned}$$

Inspection of eq. (24) and (26) allows us to conclude that:

- i) the relation between \mathbf{r} and \mathbf{b} is now given by eq. (27), so the relative velocity is equal to $2\mathbf{b}$ when $|\mathbf{r}| \rightarrow \infty$, as it should be;
- ii) the momentum canonically conjugate to the relative distance between the two nucleons, \mathbf{r} , is

$$\mathbf{p} = [m + G^2 / (6\pi\sqrt{2\pi\lambda})] \mathbf{b}$$

in agreement with the expression of the reduced mass for the relative motion of two identical interacting particles, which is half of the mass \mathcal{M} given by eq. (17).

4 — CONCLUSIONS

The study of interacting nucleon systems by means of the exchange of scalar mesons was performed considering systems with one and two nucleons.

In the first case we obtain an expression for the energy of the system when the parametrization introduced is clearly defined.

The expression obtained for systems with two nucleons reduces to the Yukawa interaction for zero relative velocity and introduces new factors which depend on the relative velocity of the nucleons in the other cases.

The authors are greatly indebted to Prof. J. da Providência for his guidance of this work.

REFERENCES

- [1] J. DA PROVIDÊNCIA, *Nucl. Phys.*, **B57** (1973), 536.
- [2] J. DA PROVIDÊNCIA, M. C. RUIVO, C. A. SOUSA, *Annals of Physics*, **91** (1975), 366.
- [3] E. M. HENLEY and W. THIRRING, *Elementary Quantum Field Theory* (McGraw-Hill, New York, 1962).



FUNDAMENTAL PROPERTIES OF LIQUID ARGON, KRYPTON AND XENON AS RADIATION DETECTOR MEDIA

TADAYOSHI DOKE

Science and Engineering Research Laboratory, Waseda University, Kikuicho-17, Shinjuku-ku,
Tokyo, Japan

(Received 23 June 1981)

ABSTRACT — The fundamental properties of liquid argon, krypton and xenon required from a point of view of radiation detector media, such as W-values, Fano factors, electron drift velocities, etc., have been measured during the past decade. These results are summarized and the author's considerations for its physical understanding are presented. Also, the possibilities of application of these liquids to nuclear radiation detectors are discussed.

1 — INTRODUCTION

Since Alvarez suggested the possibility of the use of liquefied rare gases, such as liquid argon or liquid xenon, as detector media of counters to be used in experiments of elementary particle physics [1], some trials for developing liquid argon or liquid xenon detectors were undertaken [2-9]. In the middle of the 1970's, liquid argon was successfully used as detector medium of calorimeters for high energy gamma-rays or electrons [10-15]. After a few years, a proposal of a «liquid argon time projection chamber» (LATPC), which is a new type three dimensional position sensitive detector with large sensitive volume and is used for neutrino detection, has been made by high energy physicists [16] and at present, the fundamental experiments for LATPC are in progress [17, 18].

Since the end of the 1960's, we began the studies on the fundamental properties of liquid rare gases [19-26] required for applications as radiation detector media, independently of Alva-

rez's suggestion, and recently have developed some new type liquid xenon detectors [27-30].

On the basis of the results obtained so far [19-30], in this article the fundamental properties of liquid rare gases as detector media are summarized and considerations are made regarding the physical understanding of their properties and the possibilities of application of these liquids to nuclear radiation detectors.

2 — IONIZATION

In the design of a liquid rare gas detector which is operated in the ionization mode it is necessary to know the mean number of ion pairs produced in the liquid by the ionizing radiation and its fluctuation around the mean value. The former can easily be estimated by knowing the W -value in the liquid, defined as the average energy required to produce an ion pair and the latter by knowing its Fano factor, which expresses the degree of fluctuation of the ionization.

Here, we will discuss the W -values and the Fano-factors of liquid argon, liquid krypton and liquid xenon recently measured or estimated by us and briefly describe the reasons why W -values in liquid rare gases are near the values in the gaseous state, rather than those in semiconductors, although Fano-factors are close to the values in semiconductors rather than those in the gaseous state.

2.1 — W -values in liquid argon, krypton and xenon

For measurement of the W -value in liquid rare gases, the steady current method by irradiation with X-rays or alpha-rays has often been used by several investigators until recently [19, 20, 31-34]. However, this method is not suitable for precise measurement of W -values, because in X-ray irradiation, it is difficult to accurately determine the absorbed energy in the liquid medium and in alpha-particle irradiation, it is also difficult to completely collect the charge produced by alpha-particles. To overcome these difficulties of the measurement technique, we tried to use the electron pulse method and energetic conversion

electrons as ionizing radiation, for measurement of W-values in liquid rare gases [21, 22]. This method has the two following advantages: 1) the energy of individual pulses is known without any uncertainty, 2) the saturation of ionization pulses can easily be achieved because the specific ionization of energetic electrons is considerably low compared with that of alpha-particles. The W-values in liquid argon and liquid xenon obtained by this method are shown in Table 1, as well as those previously obtained by the steady current method [20]. From this table, it is clear that the accuracy of the determination of W-values by this method is remarkably improved, but the W-values obtained by both methods are in good agreement within the experimental errors.

TABLE 1 — The W values in the gas and liquid phases of argon, krypton and xenon. The number in parenthesis shows the ratio, W_{gas}/I or W_{liq}/E_g .

Liquid	I (eV)	W_{gas} (eV) (W_{gas}/I)	E_g (eV)	Experimental W_{liq} (eV)		Calculated W_{liq} (eV) (W_{liq}/E_g)
				Steady current method	Electron pulse method (W_{liq}/E_g)	
Ar	15.76	26.4 (1.68)	14.3	23.7 ± 0.7	23.6 ± 0.3 (1.65)	24.4 (1.70)
Kr	14.00	24.1 (1.72)	11.7	20.5 ± 1.5		20.2 (1.72)
Xe	12.13	21.9 (1.81)	9.28	16.4 ± 1.4	15.6 ± 0.3 (1.68)	15.7 (1.69)

It is a well known fact that the ratios of W-values to ionization potentials in rare gases are nearly 1.7 and this was semi-quantitatively explained by Platzman on the basis of the result calculated for helium gas [35]. The existence of the electron band structure in solid rare gases, such as solid argon or solid xenon, has been already confirmed, but in the liquid state is confirmed only for liquid xenon. Let us assume that the same electron band structure as that in solid rare gases also exists in the liquid state. In this case, it is considered that the band gap energy E_g in the liquid state corresponds to the ionization poten-

tial I in the gaseous state. From such a view-point, in liquid rare gases, the ratio W/E_g of the W-value to the band gap energy will be used in place of the ratio W/I in the gaseous state. As seen from Table 1, however, the values of W/E_g in liquid rare gases are almost equal to the values of W/I in the gas state and differ from those in semiconductors such as silicon or germanium (~ 3). This fact can be explained from the phenomenological theory given by Shockley [36] and developed by Klein [37].

Namely, Shockley proposed the following relation for the balance of the energy dissipated in semiconductors in order to phenomenologically understand the ionization mechanism [35],

$$W = E_t^+ + E_t^- + E_i + r E_r, \quad (1)$$

where E_t^+ and E_t^- are the mean energies of a subionization hole and electron respectively which are finally transferred to the lattice, E_i is the energy absorbed in production of an electron-hole pair, and rE_r is the energy transferred to the lattice while a free electron or a free hole, with energies higher than E_i , crosses the mean distance for electron-ion pair production. Assuming that the widths of the conduction band and the valence band are wider than the band gap and E_i is equal to E_g , Shockley derived the following formula for the W-value in a semiconductor (*):

$$\begin{aligned} W &= 2 E_t + E_g + r E_r \\ &= 2 \times 0.6 E_g + E_g + r E_r \\ &= 2.2 E_g + r E_r \end{aligned} \quad (1')$$

After that, Klein obtained the following improved formula assuming that $E_i = 3 E_g/2$,

$$W = (14/5) E_g + r E_r \quad (1'')$$

A good agreement between both values of dW/dE_g from the above formulas and the experimental results is obtained. By

(*) $0.6 E_g$ is obtained assuming that electrons or holes, with energies lower than E_i , distribute proportionally to their level density which is proportional to the square root of the kinetic energy.

fitting the formula (1'') to the experimental results, rE_r was estimated to be between 0.5 and 1.0 eV.

Now, let us apply such considerations to liquid rare gases, assuming that they have the same electron band structures as in solid state. In solid rare gases such as solid argon and xenon, there exists conduction band but no valence band. Therefore, E_f^+ should be neglected. Since E_g is larger than ten times rE_r , we can also neglect the last terms in the formulas (1), (1') and (1''). Thus, we can obtain the following relation between the W -value and E_g in liquid rare gases,

$$W = 1.6 E_g \quad (\text{from Shockley's formula})$$

$$W = 1.9 E_g \quad (\text{from Klein's formula}).$$

These ratios (1.9 or 1.6) roughly agree with the experimental values of 1.65 for liquid argon [21] and 1.68 for liquid xenon [22]. More accurate estimation of W -values in liquid rare gases on the basis of the solid model will be made in the next section.

By admixing a small amount of a gas whose ionization potential is lower than the first excited state of the main gas, enhanced ionization is often observed in rare gases. Such a phenomenon is called Jesse effect. From the analogy with the Jesse effect in rare gases, it is expected that the same effect will occur in liquid rare gases. For example, the apparent ionization potential of a xenon atom doped in solid argon is 10.5 eV [38], which is lower than the energy of excitons in solid argon (≥ 12.0 eV) [38]. This clearly shows that enhanced ionization is expected in xenon doped liquid argon. Actually, we observed such an enhanced ionization in the experiment of xenon doped liquid argon [24]. Figure 1 shows the variation of the ionization yield as a function of the doped xenon concentration. The enhanced ionization is also expected when some molecular gases are doped into liquid rare gases, but the mixing of molecular gases often leads to reduction of the pulse height of electron induced signals [23], because of the loss of electrons due to electron attachment to the molecular gases. Therefore, the observable enhancement of ionization may be limited to the case of mixing between rare gases.

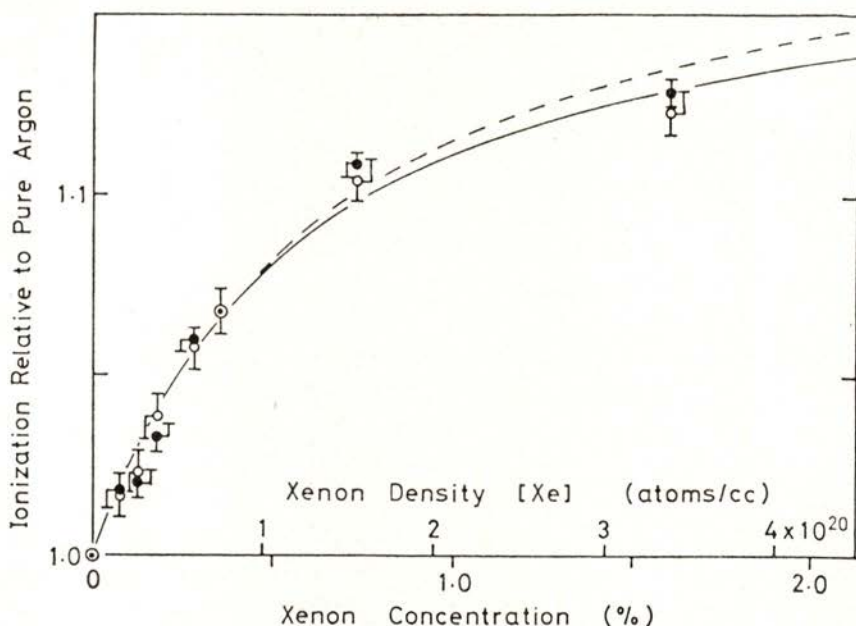


Fig. 1—Relative ionization yield as a function of the Xe concentration, for the ionization measured at 17 kV/cm(o) and for the saturation value estimated from the 1/I versus 1/E plot(•), where I is the ionization yield and E is the electric field.

2.2 — Estimate of W-values on the basis of the solid model

In this section, we describe more accurate estimations of W-values in liquid rare gases on the basis of the solid model. Namely, it is possible to accurately estimate the W-value in liquid rare gases, if its band structure and its oscillator strength are given. At present, we know the band structures in solid state obtained by theoretical calculation [39] and the oscillator strengths in solid state derived from the photo absorption spectra of these solid [40]. Assuming that these data are also applicable to liquid state, we try to estimate each term in the following energy balance equation previously applied to gases by Platzman [35]

$$W_1 / E_g = (E_i / E_g) + (E_{ex} / E_g) (N_{ex} / N_i) + (\epsilon / E_g), \quad (2)$$

where W_1 is the W-value in liquid rare gas, N_{ex} is the number of excited atoms at an average expenditure E_{ex} , N_i is the number of ions produced at an average energy expenditure E_i and ε is the average kinetic energy of subionization electrons. Here, E_i is estimated as a mean value of the gap energy in the electron momentum space. The ratios E_{ex}/E_g and N_{ex}/N_i are also estimated with the optical approximation using the oscillator strength spectra of solid rare gases. In these estimations, it is assumed that all the excitations which lie in the continuum above E_g dissociate to electron-hole pairs immediately. The estimation of the energy ε is made under the assumptions that the subionization electrons have energy less than E_i and distribute proportionally to the state density dn/dE for the energy levels. The results obtained in this way are shown in the last column of Table 1. The optical approximation used in this calculation is not valid for collisions due to low energy secondary electrons, which are a main part of collisions in the slowing down process of the primary particle. As seen from the table, nevertheless, the agreement between the estimated values and the experimental ones is very good.

From extrapolation of the enhanced ionization in xenon doped liquid argon to high concentration of xenon, the value of N_{ex}/N_i can be also estimated under the assumption that the excitons with energy higher than the ionization potential of the doped xenon atom contribute to the enhanced ionization. Then the estimated value of N_{ex}/N_i was 0.19 ± 0.02 [24], which is in good agreement with that (0.21) used in the estimation of the W-value. This fact shows that the assumptions made in the estimation of W-values are reasonable. In the next section, therefore, we will try to estimate the Fano-factors in liquid rare gases by the use of the results obtained for the W-values.

2.3 — *Fano-factors in liquid rare gases*

The fundamental formula for the fluctuation of the number of ions produced by an ionizing particle when all its energy is absorbed in a stopping material was given by Fano [41]. For

convenience of calculation, the Fano's formula is transformed as follows [42, 43]:

$$\begin{aligned}
 F &= F_1 + F_2 + F_3 \\
 &= (N_{\text{ex}}/N_i) [1 + (N_{\text{ex}}/N_i)] (W_{\text{ex}}^2/W^2) + [(\varepsilon_i - W_i)^2/W^2] \\
 &\quad + (N_{\text{ex}}/N_i) [(\varepsilon_{\text{ex}} - W_{\text{ex}})^2/W^2] \quad (3)
 \end{aligned}$$

where $W_{\text{ex}} = E_{\text{ex}}$, $W_i = E_i + \varepsilon$, and ε_i or ε_{ex} are the energy absorbed per ionization collision or per excitation collision in a large number of collisions in the slowing down process of an ionizing particle in matter, respectively. In this formula, the first term F_1 is due to redistributions of the numbers of excited and ionized atoms, the second term F_2 and the third term F_3 are due to the energy loss fluctuations in ionization and excitation, respectively. In the calculation of Fano-factors, the values of N_{ex}/N_i and ε at the end of the ionization process should be used, because the fluctuation of the number of ion pairs produced by the ionizing particle is then determined and is not affected by the process of the excitation collisions after that. The values of N_{ex}/N_i , E_i , E_{ex} and ε at the end of the ionization process for liquid argon, krypton and xenon, obtained by the method described in the previous section, are given in Table 2. Table 3 shows the Fano-factors in liquid rare gases calculated from formula (3) by using these values and they are clearly small compared to those in the gaseous state. This is mainly attributed to the small values of N_{ex}/N_i in liquid state. From the view-point of detector application, in particular, it should be noted that the Fano-factors in liquid krypton and liquid xenon are comparable to those in semiconductors such as silicon and germanium.

TABLE 2—Quantities appearing in the energy balance equation for liquid argon, krypton and xenon.

Liquid	E_i (eV)	E_{ex} (eV)	N_{ex}/N_i	ε (eV)
Ar	15.4	12.7	0.21	6.3
Kr	13.0	10.3	0.10	6.13
Xe	10.5	8.4	0.06	4.65

TABLE 3 — F_1 , F_2 , F_3 and F (Fano-factor) in liquid argon, krypton and xenon for the solid model.

Liquid	F_1	F_2	F_3	F
Ar	0.076	0.027	0.004	0.107
Kr	0.032	0.024	0.001	0.057
Xe	0.019	0.021	0.0006	0.041

We can also estimate the Fano-factor in xenon doped liquid argon by using the formula for gas mixtures, derived by Alkhazov et al. [42]. The result is given by the following formula,

$$F_m = 0.107 - 0.067 \sigma,$$

where σ is the probability of deexcitation followed by an additional ionization. Considering the practical use as detector medium, therefore, we estimate the Fano-factor for xenon doped (1.6 %) liquid argon, whose ionization relative to that in pure liquid argon is 1.13 ($\sigma \sim 0.68$),

$$F_m = 0.064.$$

2.4 — *Energy resolution in liquid rare gas chambers*

Let us estimate the energy resolutions when these liquid rare gases are used as detector media in an ionization pulse chamber. In order to get the energy resolution of the chamber, first, the electronic noise level in the pulse amplification system must be given. We assume $N_{n\text{ eq}} = 65e$ as the r.m.s. value of the noise equivalent charge in the electronic system, which can easily be achieved by using FETs (commercially available) kept at low temperature. If the W -value and the Fano factor for the detector media are known, the ultimate energy resolution ΔE_T , which is

expressed by full width at half maximum (fwhm), is calculated from the following formula

$$\Delta E_T = (\Delta E_n^2 + \Delta E_j^2)^{1/2}$$

where $\Delta E_n = 2,36 W$ (eV) $N_{n \text{ eq}} \times 10^{-3}$ keV, and $\Delta E_j = 2,36 \times \sqrt{E_\gamma}$ (MeV) FW (eV) keV and E_γ is the energy of ionizing radiation. The ultimate energy resolutions in liquid argon, liquid krypton and liquid xenon were calculated for $E_\gamma = 1$ MeV, using the above formula. The results are shown in Table 4 [25]. From this table, it is clear that the ultimate energy resolutions for these liquid chambers are from 3 keV to 5 keV. In the conventional Ge(Li) detector with large volume, the actual energy resolution (fwhm) for gamma-rays of 1 MeV is about 1.5 keV. Therefore, the fwhm obtained in the liquid xenon ionization chamber is expected to be near that of the Ge(Li) detector. This encourages the development of a liquid xenon gamma-ray spectrometer.

TABLE 4 — Ultimate energy resolutions (fwhm) in liquid rare gas ionization chambers.

Liquid	ΔE_n	ΔE_j (keV) for $E_\gamma = 1\text{MeV}$	ΔE_T (keV) for $E_\gamma = 1\text{MeV}$
Ar	3.57	3.77	5.19
Kr	2.99	2.49	3.89
Xe	2.36	1.88	3.02

In order to check the theoretical estimation as mentioned above, we tried to measure the energy resolution for 0.569 MeV gamma-rays emitted from ^{207}Bi source using a small size liquid xenon gridded ionization chamber [22]. Figure 2 shows the relative energy resolution expressed by fwhm versus the electric field strength as well as the electronic noise level, corresponding to 17 keV, which is not so good. This curve is in fairly good agreement with that recently obtained by using a large volume liquid xenon chamber [29] and that of a Russian group using

a small size chamber [44]. From this figure, it is clear that the energy resolution (about 6% fwhm) is about twice the electronic noise level even for the electric field of 17 kV/cm, although the fwhm value still decreases with increase of the electric field.

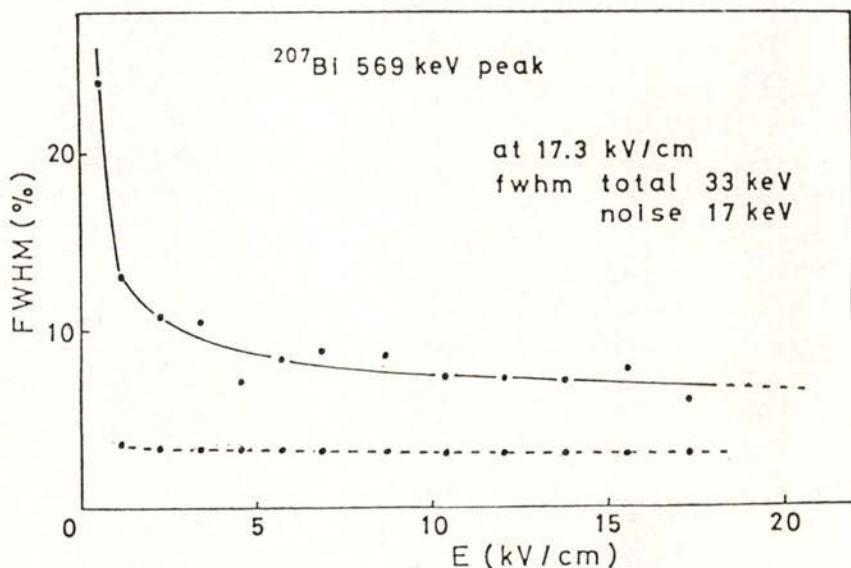


Fig. 2 — Variation of the energy resolution (fwhm) for gamma-rays of 569 keV with the electric field. Dashed line shows the level of electronic noise.

Such a large value of fwhm can not be attributed to attachment of electrons to electro-negative impurities in the liquid, because it had been experimentally shown that the pulse height of the ionization signals scarcely depends on the drift distance of electrons. Contributions to the energy resolution other than the electronic noise, such as the positive ion effect caused by the shielding inefficiency of the grid and the rise time effect of the ionization pulse, are considerably smaller than that of the electronic noise. Also, it may be difficult to explain such a large discrepancy between the theoretical estimation and the experimental results by the non-saturation effect of the collected charge for the applied electric field, because the difference between the collected charge at 17 kV/cm and its saturated value

obtained by Onsager's theory is estimated to be only 3% [22]. However, it is necessary to check whether the energy resolution is improved in much higher electric field or not, because at present the applicability of Onsager's theory to the ionization due to fast electrons in liquid rare gases is not sufficiently tested.

2.5 — *Electron multiplication in liquid and solid rare gases*

Several years ago, we tried to observe the occurrence of electron multiplication in liquid argon, and xenon doped or organic molecule doped liquid argon, by using a simple cylindrical counter with a center wire of about 5 μm in diameter, but could not find it before electrical breaking occurs. To confirm the electron multiplication in solid argon or solid xenon as observed by Pisarev's group [45], furthermore, we also tried to test it using a parallel plate solid argon filament chamber [46]. In this test, a maximum multiplication factor of about ten was observed for a tungsten filament wire of 5 μm in diameter. With increase of the anode voltage, however, the rise time of the output pulses became long and its decay time rapidly increased. At last, the pulses became unobservable because of pile-up. At present, these phenomena are interpreted assuming that the electron multiplication in solid argon occurs in a thin layer of gaseous argon near the wire surface and the slow component of the pulse is caused by space charge effect of electrons trapped in the imperfections of the interface between gas and solid. After these efforts, it was concluded that the electron multiplication to be useful in nuclear radiation detectors occurs only in liquid xenon as has already been confirmed by Derenzo et al [47].

The typical curves of charge gain versus applied voltage for a liquid xenon cylindrical counter with a center wire 5 μm in diameter, obtained with internal conversion electrons from ^{207}Bi and collimated ^{137}Cs gamma rays, are shown in Fig 3 [48]. Here, the unit gain is equal to the saturated pulse height which is obtained in a small gridded ionization chamber filled with liquid xenon. The maximum gain obtained so far is about 200.

According to our experiences, the resolution of liquid xenon proportional counters becomes poor with the increase of the applied voltage. This degradation of resolution seems due to

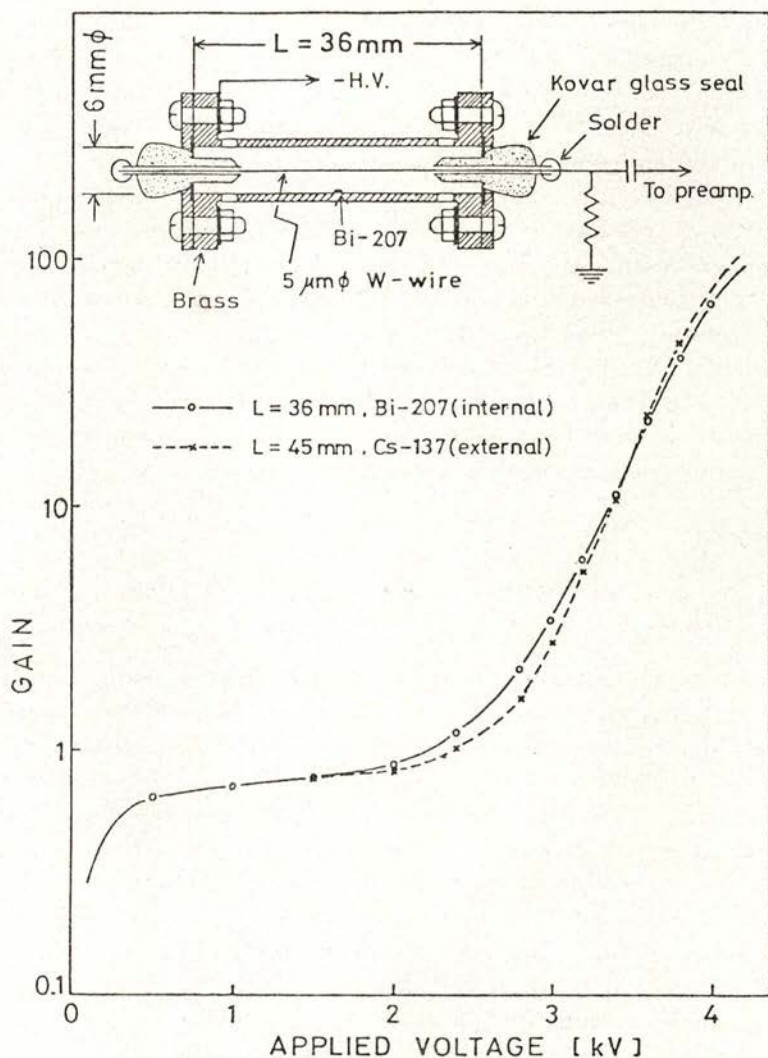


Fig. 3 — Charge gain versus applied voltage for a proportional counter having a center wire of $5 \mu\text{m}$ in diameter, as shown in the inserted figure. The solid line represents the gain for an internal ^{207}Bi source and the dashed line for external irradiation with collimated ^{137}Cs gamma-rays.

local irregularities of the surface of the center wire. In practical applications of such a counter, this fact should be taken into consideration.

Derenzo et al. also tried to estimate the first Townsend coefficient in liquid xenon from their experimental data [3]. Namely they firstly derived the analytical formula for the variation of the charge gain with the applied voltage and fitted the curves obtained from the formula to the experimental data for three center wires of different diameter, by adjusting the values of W , recombination constant, attachment probability and first Townsend coefficient as unknown parameters. Then it was found that the first Townsend coefficient was 27 times larger than that in xenon gas with the same density as that of liquid xenon. However, this figure seems to be wrong, because the W -value and the recombination constant obtained as well as the first Townsend coefficient are inconsistent with those accurately measured by us [22, 23]. Therefore, we are trying to estimate the real value of the first Townsend coefficient by treating the W -value and the recombination constant as known parameters.

3 — RECOMBINATION AND ATTACHMENT

When an ionization chamber is used as an energy spectrometer for nuclear radiation, the charge produced by the ionizing radiation must be collected completely in the collector electrode in order to determine its intrinsic energy resolution. In the electron pulse chamber, the characteristics of electron charge collection are firstly determined by recombination between electrons and ions. In addition, the electrons attaching to electronegative gas during the drift to the collector can not effectively contribute to the induced voltage in the collector within the short measuring time, of the order of μ sec. Therefore, the existence of electronegative gases in a liquid rare gas deteriorates the characteristics of the charge collection in an electron pulse chamber.

Here, we describe the present status in our understanding about the recombination and the attachment processes in liquid rare gases.

3.1 — *Recombination between electrons and ions*

If the electron-ion pairs produced by a minimum ionizing particle with low specific ionization are independent of each other, we can understand the recombination process between electrons and ions by Onsager's theory [49]. When an electron originated by ionization is slowed down to thermal energy, according to the theory, if the electron is within a certain distance from its parent ion where the Coulomb energy is equal to thermal energy, it can not escape from the influence of the parent ion and the electron-ion pair recombines. Conversely, if the thermalizing point of the electron is outside that critical distance, it is free from the influence of the parent ion even if the external electric field is zero. Actually, it seems that there exists a large number of free electrons, without recombination with the parent ion or other ions, during a considerably long time ($>$ msec) in absence of electric field. However, it is difficult to completely understand the recombination process between electrons and ions in liquid rare gases only by Onsager's theory, because the mean interval of electron-ion pairs produced by ionizing radiation in liquids is comparable to the critical distance even for minimum ionizing particle and, under such a condition, the assumption of the existence of ion pairs which are independent of each other becomes unreal. Nevertheless, we consider that a rough explanation of the characteristics of charge collection in liquid rare gases is possible by Onsager's theory.

Figure 4 shows the characteristics of charge collection in liquid argon and liquid xenon observed by using internal conversion electrons of ^{207}Bi [50]. In the figure, the solid curves are the theoretical ones obtained by fitting Onsager's theory to the experimental data and the agreement is good. According to Onsager's theory also, the initial slope of the charge collection curve in liquid xenon is smaller than in liquid argon.

However, the rise of the charge collection curve in liquid xenon is steeper than in liquid argon for electric fields lower than 1 kV/cm. This is different from the above prediction of Onsager's theory. Such a difference is caused by the effect of columnar recombination which occurs between electrons and ions other than the parent ion and the attachment of electrons to

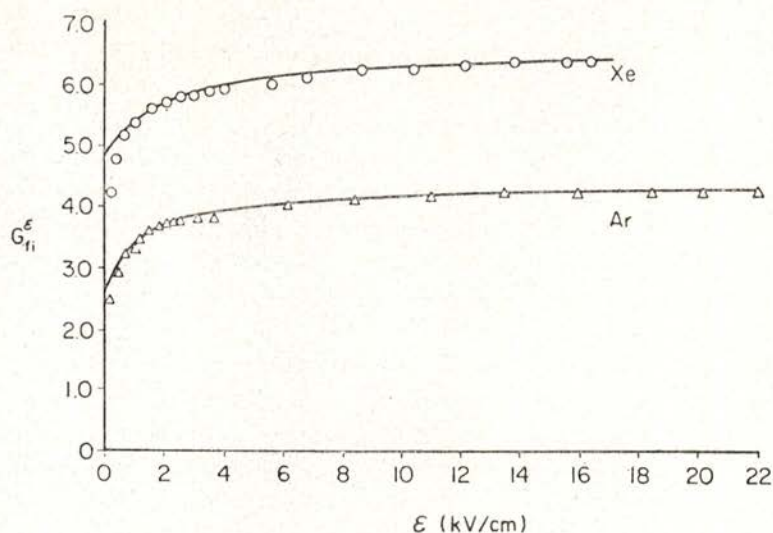


Fig. 4 — Saturation characteristics of collected charge versus electric field for liquid argon and xenon. G_{fi}^{ϵ} is the free ion yield per 100 eV of absorbed energy at the field strength ϵ .

electro-negative impurities in the rare gas liquid. By extrapolating the theoretical charge collection curve, obtained from the fitting to the experimental data for electric fields larger than 1 kV/cm, to the low electric field region, we can estimate the fraction of recombination free electrons to the total number of electrons produced by the radiation for zero electric field. The values obtained in this way are 0.53 ± 0.04 for liquid argon and 0.73 ± 0.04 for liquid xenon, respectively [50]. These values seem to be an overestimate, because of the ambiguity in the low electric field region. This problem will be again discussed in the section on direct scintillation.

3.2 — *Electron Attachment*

In an ionization chamber with a large sensitive volume, such as total absorption chambers or time projection chambers for neutrino detection, the electrons produced by ionizing radiation are required to drift a long distance without losses due to electron attachment to electro-negative impurities in the liquid

rare gases. From the point of view of the liquid argon time projection chamber, Chen et al. made an experiment to estimate how long electron drift lengths can be achieved in liquid argon supplied through a purifier, using a drift distance of a few centimeters, and showed that attenuation lengths longer than 35 cm are achievable at the electric field of 2 kV/cm [17]. Recently, they constructed a 50 liter liquid argon test chamber with a maximum drift distance of 30 cm and showed that an attenuation length of 55 cm is achievable at a drift field of 1.6 kV/cm [18]. Now, let us consider oxygen molecules as a typical electro-negative gas in liquid argon. Its cross section for electron attachment (or attenuation coefficient of drifting charge) in liquid argon at the electric field of 10^2 to 10^4 V/cm has already been measured by Zaklad [51], Hofmann et al [52] and Bakale et al [53].

Their results are shown in Figure 5 as well as the results in liquid xenon obtained by Bakale et al [53]. The values of

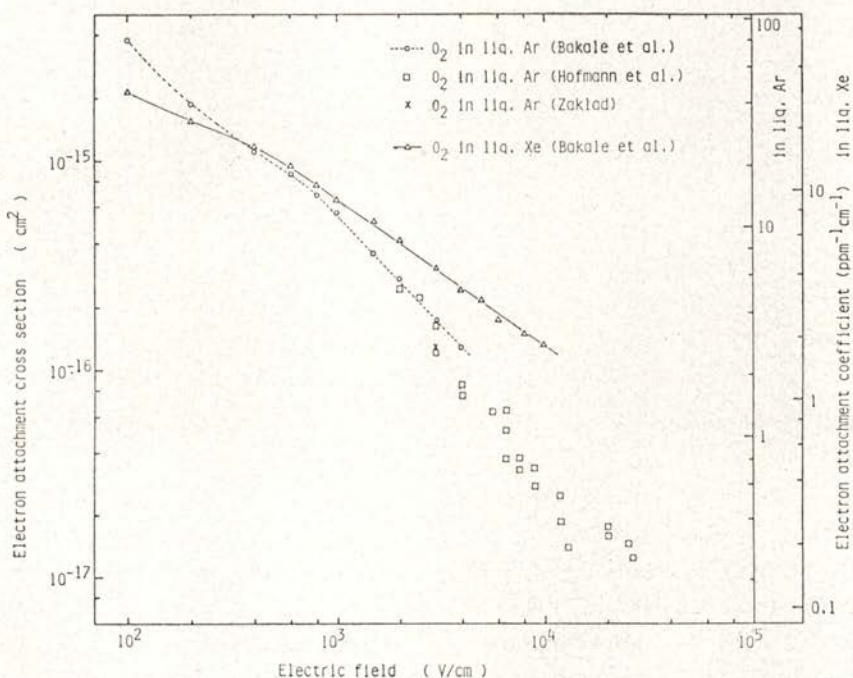


Fig. 5 — Variation of the electron attachment cross section with the electric field in liquid argon and xenon.

the electron attachment cross section in liquid argon are in good agreement. Using these values, the upper limit of the concentration of oxygen molecule in liquid argon used in Chen's experiment

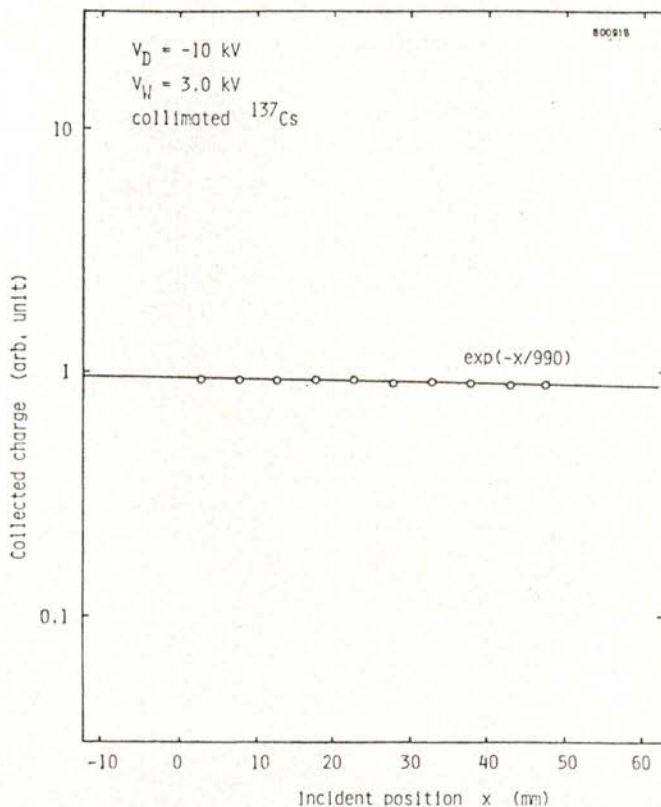


Fig. 6 — Attenuation of collected charge versus drifting distance in liquid xenon.

periment is estimated to be 2.6 ppb. Such a purity was obtained by passing a sequence of a Hydrox purifier and molecular sieves maintained at 196 K.

Complete collection of the charge produced by ionizing radiation in liquid xenon is more difficult than that in liquid argon, because a larger amount of electro-negative impurities are dissolved in liquid xenon due to a temperature higher than that

of liquid Ar [51]. In addition, the cross section for electron attachment by oxygen molecules is about one and a half times larger than that in liquid argon as seen in Fig. 5. Recently, we observed the reduction of the ionization pulse height for the drift distance of 5 cm in a liquid xenon drift chamber using collimated gamma-rays [30]. The result is shown in Figure 6. In this case, the attenuation length of electrons in liquid xenon was one meter. Assuming the cross section of electron attachment shown in Fig. 5, we can estimate the concentration of oxygen molecules in the liquid xenon used in our experiment to be 1.8 ppb, which is better than that obtained in liquid argon by Chen et al., in spite of the difficulty in purification of xenon. This shows that our test chamber and gas purification systems, in which a titanium-barium getter [48] is used, are superior to the systems of Chen et al.

4 — ELECTRON DRIFT VELOCITY AND DIFFUSION

The drift velocity of electrons determines the time response of radiation detectors and the diffusion of electrons in the detector medium gives the limit of the accuracy of position determination. From the analogy with the mixing effect on the electron drift velocity in gaseous state, several years ago, we studied electron drift velocities in liquid argon mixed with small amounts of molecular gases and found a remarkable increase of the drift velocity for mixtures with methane or ethylene [23]. If the diffusion coefficient and the drift velocity of electrons in liquids are experimentally obtained as a function of the electric field strength, we can estimate the momentum transfer cross sections and the agitation (random) energies of electrons in the liquid state. This information gives us not only the spread of electrons drifting under an electric field in liquids, but also the understanding of the mixing effect as mentioned above. Therefore, we also tried to measure the diffusion coefficients of electrons in liquid argon [26, 57] and liquid xenon [57].

In this section, these results are shown and some relevant considerations are made.

4.1 — Electron drift velocities

As mentioned above, we measured the variations of electron drift velocities by admixing various kinds of molecular gases (200 to 5000 ppm) into liquid argon [23]. These results are shown in Figure 7 as well as the variation of the electron drift

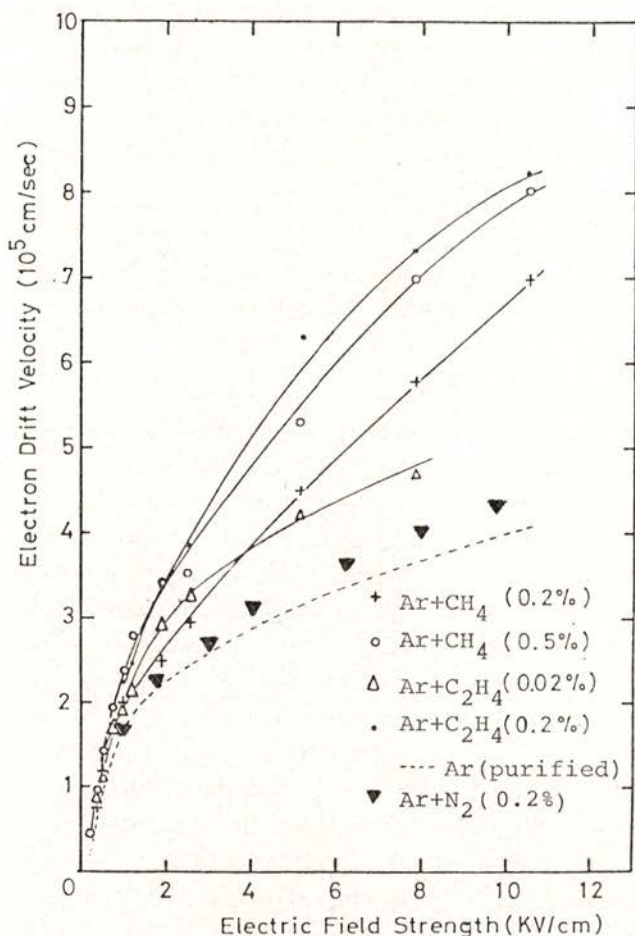


Fig. 7 — Variation of the drift velocity of electrons in liquid argon, liquid argon-nitrogen, - methane and - ethylene mixtures as a function of the electric field.

velocity for pure liquid argon as a function of electric field. As seen from the figure, in the liquid argon-nitrogen mixture, no significant change in the electron drift velocity was observed, while in liquid argon-methane and -ethylene mixtures, a considerable increase was observed. The degree of the increase in the electron drift velocity, however, is not so large as

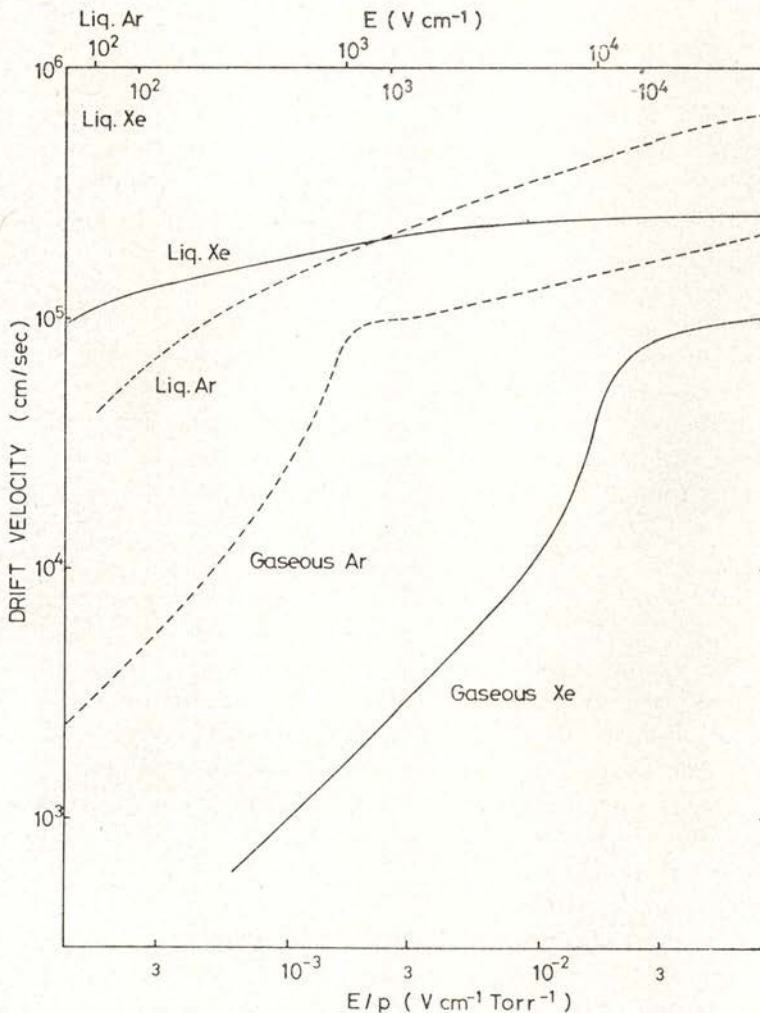


Fig. 8 — Variation of the drift velocity of electrons in liquid argon and xenon, and in gaseous argon and xenon with the same atomic density as in liquid state, with the reduced electric field.

expected directly from the analogy with the mixing effect in the gaseous state. This fact is due to the lack of the Ramsauer-Townsend effect in liquid argon as shown in the next section. Here, it should be noted that admixing of molecular gases into liquid rare gases results in a considerable reduction of pulse height. This is attributed to attachment of drifting electrons to electronegative gases included in the mixing molecular gas or in the rare gas itself. In applications of mixtures of liquid rare gases and molecular gases to detector media, great care must be taken regarding this problem.

Figure 8 shows the variations of the electron drift velocities in liquid xenon and liquid argon with the electric field for a wide range, as well as in gaseous argon and xenon with densities corresponding to the liquid state. These curves are drawn on the basis of the data recently obtained by several investigators [54, 55, 56]. From the figure, it is clear that the electron drift velocity in liquid is larger than that in gas over the whole region. In particular, the difference is remarkable in xenon. From the view-point of radiation detectors it should also be noted that liquid xenon is suitable as detector medium of drift chambers, because the electron drift velocity in liquid xenon is almost constant for electric fields higher than 3 kV/cm.

4.2 — *Diffusion coefficient of electrons*

The group of electrons produced by the ionizing radiation in liquid rare gas gradually spreads during drifting along the lines of electric force by the diffusion process. The process is determined by the agitation velocity of electrons $V_{ag} (\propto \langle \epsilon \rangle^{1/2})$, $\langle \epsilon \rangle$ being the agitation energy) and the momentum transfer cross section of electrons σ in the liquid. If the spread of the electron group ($\propto (Dt)^{1/2} = (Dd/\mu E)^{1/2} \propto (D/\mu)^{1/2}$, where D is the diffusion coefficient, d the drift distance, μ the mobility and E the electric field strength) in the liquid is measured as a function of the electric field, we can get the agitation energy of electrons from Einstein's relation $eD/\mu = kT = 2\langle \epsilon \rangle/3$. If we know the electron drift velocity or the electron mobility in the liquid, we can also get the diffusion coefficient of electrons by using that relation. Figure 9(a) and 9(b) show the variation

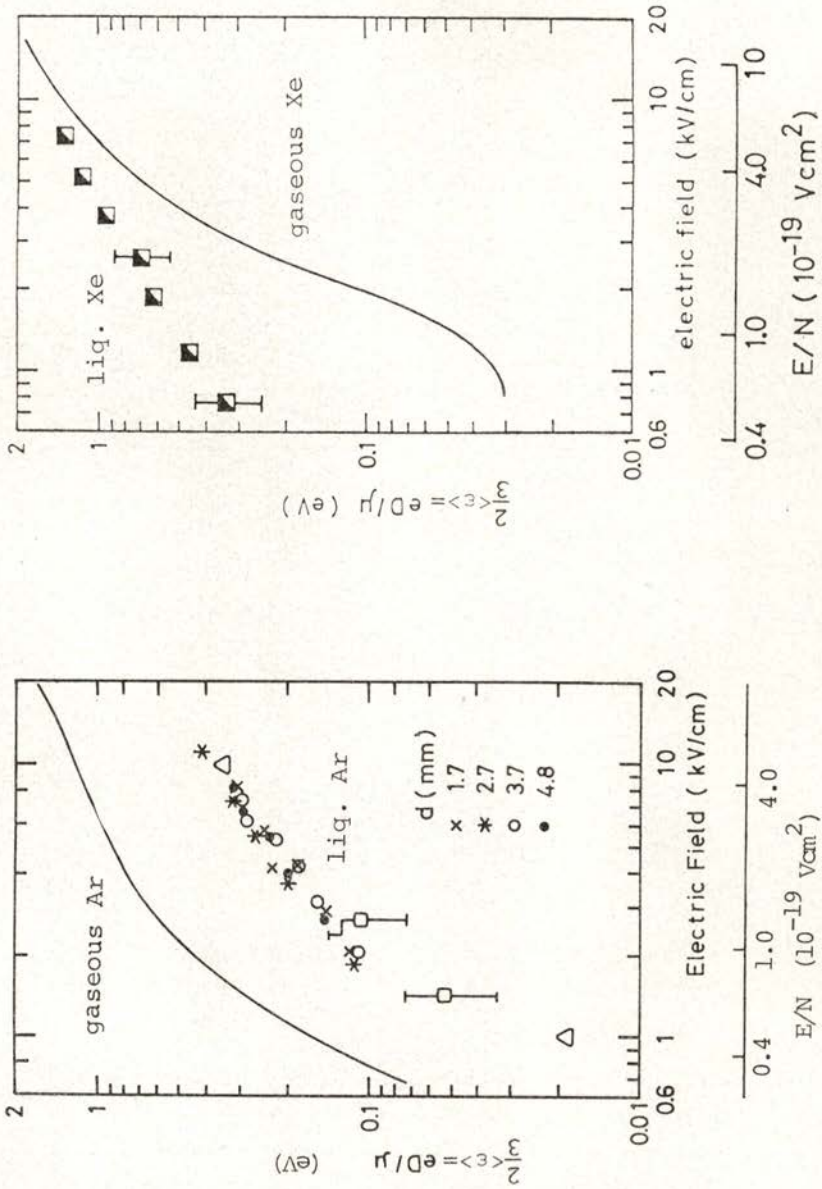


Fig. 9 — Field dependence of $\frac{2}{3} \langle \epsilon \rangle = eD/\mu$ (eV) in liquid argon (a), and liquid xenon (b). Solid curves show the results for the gaseous states, respectively. N , in the lower horizontal scale, is the atomic density in the liquid state.

of $\langle \epsilon \rangle$ in liquid argon and liquid xenon with the electric field strength obtained from measurements of the spread of electrons as mentioned above [26, 57]. For comparison with the agitation energy of electrons in gas, the curve for argon or xenon gas

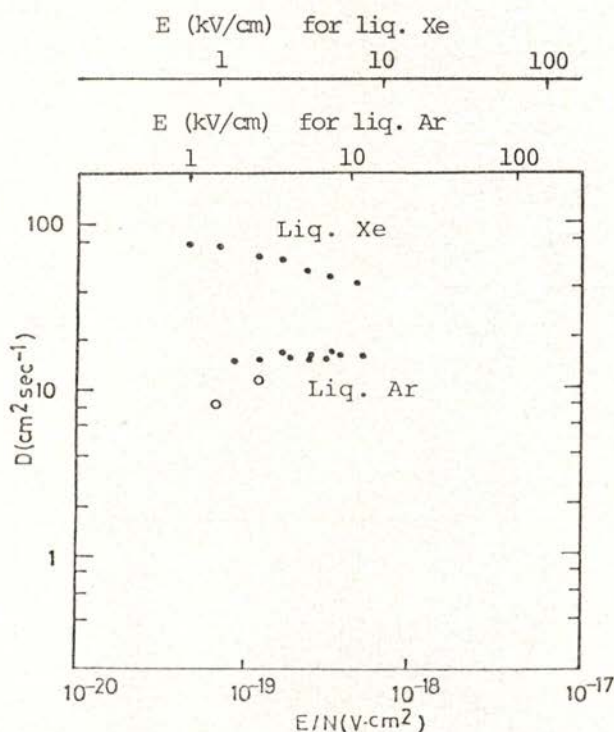


Fig. 10 — Field dependence of the diffusion coefficients of electrons.

with the same density as in the liquid state is also shown in each figure. As seen from the figures, the values of $\langle \epsilon \rangle$ of electrons in liquid argon is several times lower than in gaseous argon, while those in liquid xenon is a few to ten times larger than in gaseous xenon.

Figure 10 shows the variation of diffusion coefficients of electrons in liquid argon and liquid xenon with the electric field

strength, which was obtained from the data of Fig. 9 (a) and (b). The diffusion coefficients in liquid argon are 10 to 20 cm²/sec for the electric field of 2 to 11 kV/cm and clearly smaller than those (17 to 37 cm²/sec) in gaseous argon with the same density as in the liquid state. This shows that liquid argon is superior to high pressurized gaseous argon as a detector medium for

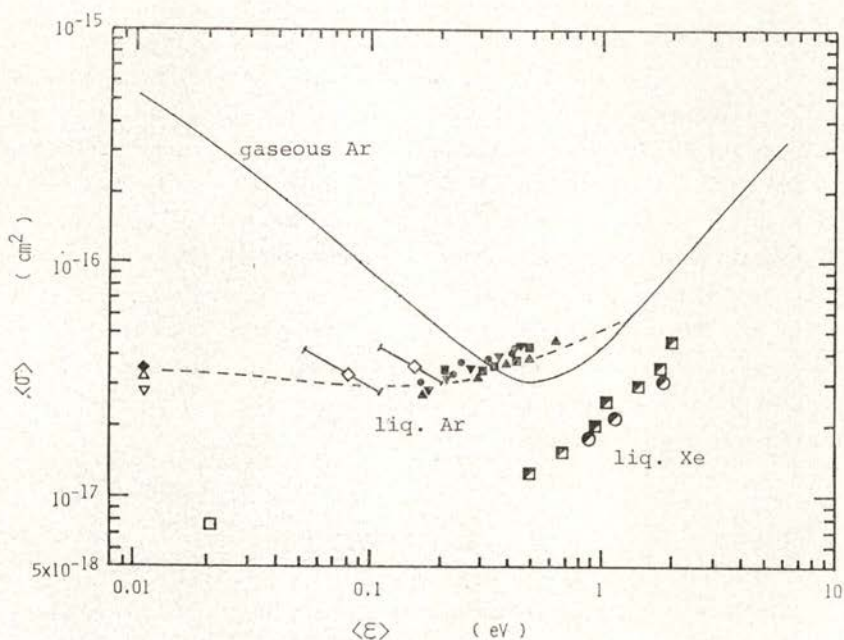


Fig. 11 — Variation of the momentum transfer cross section as a function of $\langle E \rangle$ in liquid argon and xenon. The solid line shows the result for gaseous argon and the dashed line the result obtained by Lekner's theory.

position sensitive detectors. On the other hand, the diffusion coefficients in liquid xenon are several times larger than those in liquid argon. This means that the diffusion coefficient in liquid xenon is larger than that in gaseous xenon with the same density as in the liquid state, because the diffusion coefficient in gaseous xenon is smaller than in gaseous argon. Nevertheless, the diffusion coefficient in liquid xenon is still fifty times smaller

than that in xenon gas at one atmosphere and small enough to make negligible the fluctuation of the center of gravity of the electron cloud distribution, less than $1 \mu\text{m}$ for the drift distance of 2 mm.

From the agitation energy $\langle \epsilon \rangle$ of electrons and the electron drift velocity w or electron mobility μ , we can estimate the momentum transfer cross section by using the simple formula $\sigma_t = eE/Nw(2m\langle \epsilon \rangle)^{1/2}$, derived from the relation $w = eE\lambda/m\langle v \rangle$, where N is the atomic density, e and m are the charge and mass of the electron, respectively, λ is the mean free path and $\langle v \rangle$ is the average agitation velocity of the electrons. Figure 11 shows the variation of the momentum transfer cross sections of electrons in liquid argon and liquid xenon with the electric field strength, which was obtained from the above formula using the data shown in Fig. 9 (a) and (b). For comparison, the variation of the cross section with the electric field in gaseous argon with the same density as that of liquid argon is also shown by the solid line in the figure. This figure clearly shows the lack of the Ramsauer-Townsend minimum in liquid argon and liquid xenon as predicted by Lekner [58], compared with the curve for gaseous argon.

5 — SCINTILLATION

The scintillations in liquid rare gases due to ionizing radiations were studied by Northrop and Gursky [59], about twenty years ago. After that, however, such scintillations have been scarcely used in the field of nuclear experiments. Although it is sure that its application is not so easy as implied by Northrop and Gursky, the decay time of the scintillations from liquid rare gases such as liquid argon or xenon is very fast [64-68], and so they are useful as triggering pulses in the case of fast counting. Recently, furthermore, we found the so called proportional scintillation in liquid xenon [27, 28], which is the same phenomenon as that in rare gases. This finding will open the way to applications wider than that at the present. In this section, we describe some results on the direct scintillation and the proportional scintillation obtained in our experiments.

5.1 — *Direct scintillation*

Excited atoms R^* produced by ionizing radiation form excited molecules R_2^* through collision with other atoms on the ground state and ultraviolet photons are emitted in transitions from the lowest excited molecular state of R_2^* to the dissociative ground state. On the other hand, ionized atoms R^+ produced by ionizing radiation also form excited molecules through the following processes: i) $R^+ + R \rightarrow R_2^+$, ii) $R_2^+ + e \rightarrow R^{**} + R$, iii) $R^{**} \rightarrow R^*$ and iv) $R^* + R \rightarrow R_2^*$ and then the excited molecules also give rise to ultraviolet photons. We call this type of scintillation «recombination scintillation». The mean wave lengths of these photons are 1300 Å for liquid argon, 1500 Å for liquid krypton and 1750 Å for liquid xenon, respectively.

The intensity ratio of scintillation from excited atoms to recombination scintillation will be given as N_{ex}/N_i if there is no radiationless transition process of the excited molecular state to the dissociative ground state, which does not seem to be theoretically probable for low temperatures as in liquid argon or liquid xenon. To justify such a theoretical consideration, we measured the variations of the scintillation intensities in liquid argon and liquid xenon as a function of electric field using internal conversion electrons from ^{207}Bi . The results are shown in Figure 12 [60]. From this figure, it is clear that the scintillation intensity decreases with increase of the applied electric field, but even under electric fields higher than 10 kV/cm the scintillation intensities remain 32 % of that without the electric field for liquid argon and 26 % for liquid xenon. These values are larger than the theoretical values of 17 % for liquid argon and 5.7 % for liquid xenon, which are estimated from $N_{ex}/N_i + N_{ex}$. This discrepancy may be explained by taking into consideration the existence of recombination free electrons as mentioned in section 3. Namely, the recombination rate between recombination free electrons and ions is very slow and as the result, we can not observe the scintillation produced from such a recombination by the fast pulse techniques, which are widely used in the field of nuclear experiments. So, assuming that the recombination free electrons do not contribute to the scintillation, we can estimate the reduction factor of scintillation light to be 31 % for liquid argon and

18 % for liquid xenon, using the fractions of recombination free electrons obtained by the analysis on the basis of Onsager's theory [50]. These values roughly agree with the experimental ones.

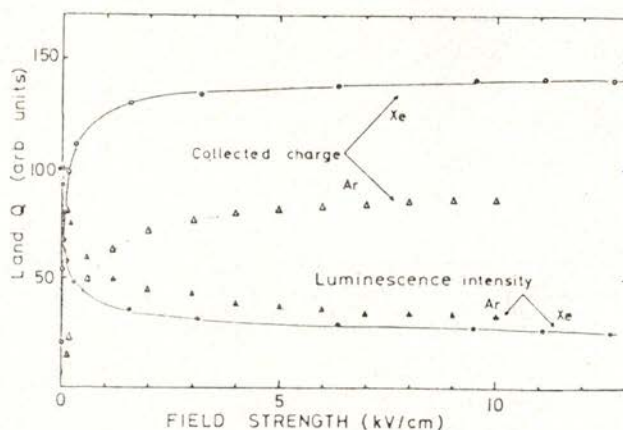


Fig. 12 — Variation of the relative luminescence intensity L and collected charge Q in liquid argon and liquid xenon with the applied electric field strength for 1 MeV electrons.

If the effect of recombination free electrons on the scintillation intensity in liquid rare gases is clear for fast electrons, it is considered that the scintillation yield per unit absorbed energy due to fast electrons may be smaller than that due to alpha-particles, which produce comparatively higher specific ionizations along the track where recombination efficiently occurs. To make sure of the matter, we tried to measure the dE/dx dependence of the scintillation yield in liquid argon using several kinds of ionizing particles [61, 62]. Figure 13 shows the results obtained. The data in the figure are normalized to the scintillation yield due to alpha-particles and show that the scintillation yield due to fast electrons is about 15 % lower than that due to alpha-particles. However, we could not observe the reduction of one-third in the scintillation yield due to alpha-particles. By using fission fragments from ^{252}Cf , on the other hand, we found a great reduction of the scintillation yield in the high specific ionization region [61]. To compare with NaI (Tl) crystals, the

variation of the scintillation yield with the energy loss rate of the incident particle for those scintillators [63] is also shown by a solid curve in the same figure. As seen from

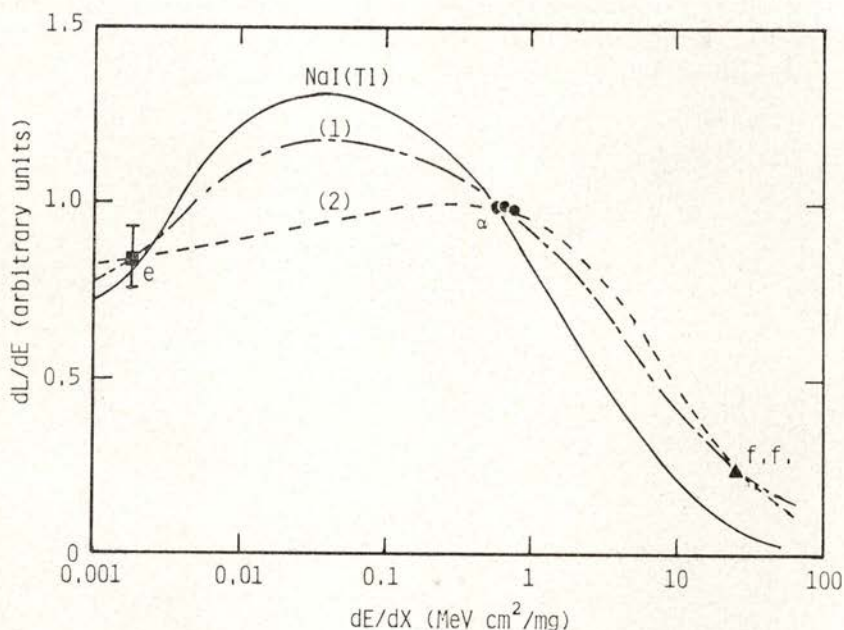


Fig. 13 — Scintillation yield per unit absorbed energy dL/dE as a function of the specific ionization dE/dx in liquid argon. Solid curve shows the dE/dx -dependence of scintillation yield in NaI(Tl) crystals. Scintillation yields in the figure are normalized to that due to alpha-particles. For dashed curves (1) and (2), see the text.

this figure, it seems that the experimental data naturally fit to the curve (1), like that for NaI (Tl) crystals, rather than to the curve (2), which is comparatively flat compared with curve (1). The peak seen in curve (1) may be explained by considering the effect of recombination free electrons in the low specific ionization region and the quenching effect in the high specific ionization region; and by the same considerations, the question why the scintillation yield due to fast electrons is only 15% lower than that due to alpha-particles may be

solved. To justify such a consideration, at present, we are planning to measure the scintillation yields due to protons of several tens MeV and other heavy ions.

Apart from the theoretical view point as mentioned above, let us compare the dE/dx -dependence of the scintillation yield in liquid argon with that in NaI (Tl) crystals. As a whole, the curve of scintillation yield versus dE/dx for liquid argon is comparatively flat compared with the curve for NaI (Tl) crystals.

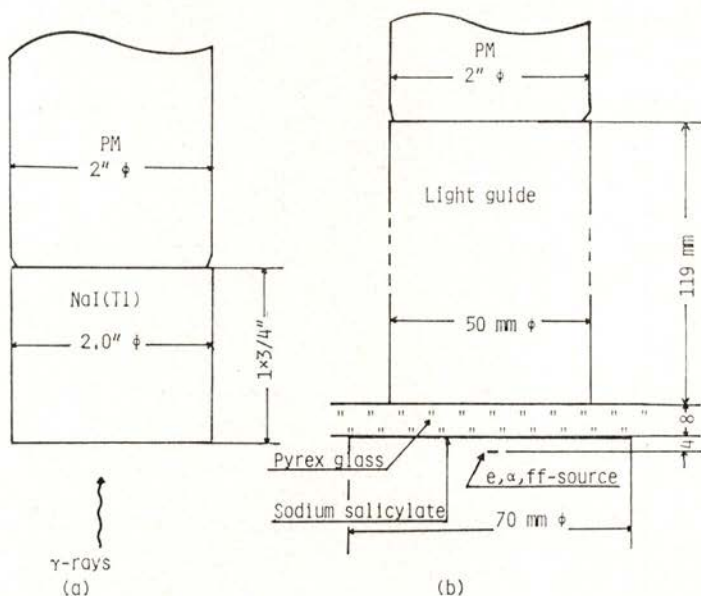


Fig. 14 — Geometrical arrangements of the apparatus for liquid argon and xenon (a), and for NaI(Tl) crystal detector (b) used in the measurements for Table 5.

In particular, the reduction of scintillation yield due to fission fragments in NaI (Tl) crystals is remarkable compared with that in liquid argon. This means that the quenching effect in the high specific ionization region in liquid argon is smaller than that in NaI (Tl) crystals.

For comparison of the scintillation yield in liquid argon with that in NaI (Tl) crystals, let us try to estimate the rela-

tive light yields from the widths of the pulse height distributions of scintillations from liquid argon, liquid xenon and NaI (Tl) crystals. The apparatus used for observation of scintillation from liquid rare gases is shown in Figure 14 as well as one used for the NaI (Tl) detector. As seen from the figure, we used sodium salicylate film, whose conversion efficiency to visible photons is nearly constant over a wide range of wave lengths, coated on the surface of a Pyrex glass window as wave length shifter. The resolution (fwhm) of scintillation light due to alpha-particles expressed in % for liquid argon and liquid xenon are shown in Table 5 as well as that of 1 MeV gamma-

TABLE 5—Comparison of the energy resolution and the light yield for liquid argon or liquid xenon scintillation counters and NaI (Tl) detectors.

Scintillator	Energy resolution (fwhm) for 6 MeV alpha-particles	Energy resolution (fwhm) for 1 MeV electrons	Relative light yield
Liquid Ar	$10.3 \pm 0.5 \%$	(25.2 %) (*)	$1.08 \begin{matrix} + 1.92 \\ - 0.52 \end{matrix}$ (**)
Liquid Xe	$9.1 \pm 0.5 \%$	(22.3 %) (*)	$1.37 \begin{matrix} + 2.44 \\ - 0.67 \end{matrix}$ (**)
NaI (Tl)		6.0 %	1.00

(*) These values were estimated from the energy resolutions for 6 MeV alpha-particles.

(**) These errors arise from the uncertainties of light reduction factors in the light guide and conversion efficiencies of sodium salicylate used in the measurement.

-rays in the NaI (Tl) detector. From these values, the relative photon intensity ratio for argon and xenon, S_{Xe}/S_{Ar} is estimated to be 1.27, assuming that the resolution is proportional to the square root of the number of emitted photons. This value is in fairly good agreement with the theoretical one estimated from N_{ex}/N_i and W_{liq} (*). Also, the last column in the table shows the relative scintillation yields of liquid argon and liquid xenon,

$$(*) \text{ Namely, } \frac{S_{Xe}}{S_{Ar}} = \frac{W_{liqAr} (1 + N_{ex}/N_i)_{Xe}}{W_{liqXe} (1 + N_{ex}/N_i)_{Ar}} = 1.32$$

when the scintillation yield of NaI (T1) crystal is assumed to be unity. In this estimation, also, we assumed that the fraction of photons incident upon the surface of sodium salicylate to the total number of photons is 0.42, the conversion efficiency of sodium salicylate to visible photons is 0.5 ± 0.2 and the reduction factor of light in the light guide is 0.5 ± 0.2 . These results show that the relative scintillation yields per unit absorbed energy for liquid argon and liquid xenon are comparable to that of NaI (T1) crystals.

TABLE 6— τ_1 , τ_2 and A_1/A_2 for scintillations from liquid argon, krypton and xenon, excited by fast electrons and alpha particles.

Liquid (Temperature)	Excitation (Ref. n.º)	Electric field (kV/cm)	τ_1 (ns)	τ_2 (ns)	A_1/A_2
Liquid Ar (94K)	e(Ref. 64)	6	5.0	860	7.8
»	e(»)	0	6.3	1020	13.5
»	e(Ref. 67)	0	2.4	1100	14.6
(90-100K)	e(Ref. 68)	0	4.6	1540	
» »	α (»)	0	4.4	1100	
Liquid Kr (120K)	e(Ref. 64)	4	2.1	80	0.9
»	e(»)	0	2.0	91	0.4
»	e(Ref. 67)	0	2.0	85	0.49
Liquid Xe (179K)	e(Ref. 64)	4	2.2	27	0.6
»	e(»)	0		34	
»	α (Ref. 67)	0	3.0	22	25
»	α (Ref. 66)	0	4.0	27	

The counting rate capability of scintillation counters is limited by the decay time of the scintillation. The scintillation from liquid rare gases has two decay components of a few nano-seconds and a few microseconds, which correspond to the life times of the singlet state and the triplet state of the excited molecule, respectively. Table 6 shows both decay time constants τ_1 and τ_2 for scintillations from liquid argon, liquid krypton and liquid xenon, excited by fast electrons or alpha-particles, and the ratio between both amplitudes when the decay is expres-

sed by $A_1 \exp(-t/\tau_1) + A_2 \exp(-t/\tau_2)$ [64-68]. The time constants quoted in the table show small variations for the various measurements. However, the difference in τ_2 in liquid xenon excited by fast electrons and alpha-particles is caused by recombination between electrons and ions. In the case of electron excitation, the time required for recombination τ_r is longer than τ_1 and comparable to τ_2 in liquid xenon. So, if a high electric field is applied, the component due to recombination does not appear. For the alpha-particle excitation, such a slow component does not appear because the recombination rapidly occurs due to the high density of electron-ion pairs produced by this particle. On the other hand, in liquid argon, this phenomenon is not seen because τ_r is shorter than τ_1 even for the electron excitation.

Recently, Kubota et al. [67] observed a decrease in the decay times for the slow component with an addition of Xe (>1ppm), N₂ (~2 %) or CO₂ (~1 %) in liquid argon excited by fast electrons. Such a mixing effect is promising for application to scintillation counters with fast time response.

The scintillation yields in liquid argon and liquid xenon are comparable to those in NaI (Tl) crystals and the dE/dx-dependence of the scintillation yield is smaller. Also, these liquid scintillators have a faster time response than NaI (Tl) detectors. However, a considerable percentage of the photons emitted in the scintillators is absorbed by surrounding materials, because there are no good reflectors for ultraviolet photons. At present, therefore, we can not achieve a good energy resolution by liquid rare gas scintillators. If a wave length shifter that can be doped into liquid rare gases without any quenching effect is found the above difficulty may be overcome.

5.2 — *Proportional scintillation*

In the gas scintillation proportional counter «photon-multiplication» occurs along the path of a drifting electron in the region of high electric field around the center wire. This is called «proportional scintillation», because the intensity is proportional to the number of electrons initially produced by ionizing radiation. In liquid rare gases, we found that such a proportional scintilla-

tion occurs only in liquid xenon. The photons in the proportional scintillation are emitted from deexcitation of excited molecules to the dissociative ground state, as in the direct scintillation. The proportional scintillation is produced only in the region very close to the surface of the center wire. Therefore, the rise time of the scintillation is comparable to or slightly longer than that of the direct scintillation, if the range of an incident particle is negligibly small. Accordingly, a counting rate of 10^5 counts/sec will be achievable in proportional scintillation as in direct scintillation. These properties show that the proportional scintillation counter is suitable as a position sensitive detector with fast time response as well as a proportional counter. If the gain of photon-multiplication is sufficient, furthermore, it is expected that in principle a good energy resolution for gamma-rays, as determined only by the Fano factor, is achievable as in gas proportional scintillation counters for X-ray detection [69]. This means that by the use of the proportional scintillation, a liquid xenon gamma-ray spectrometer with a high energy resolution, which is not affected by the electronic noise of the preamplifier, can be developed.

From the same point of view, we measured the light gain versus the voltage applied to the center wire for liquid xenon proportional scintillation counters with different center wires of 4, 6, 8.5, 10, 11 and 20 μm in diameter [28]. The results are shown in Figure 15 as well as the curves of charge gain. From the analysis of these results, we found that the increase in the photon gain with the applied voltage in liquid xenon is approximately explained by assuming the linear relation between the photon gain and the electric field strength as in gaseous xenon; and the threshold field strength for production of photons in liquid xenon ($4 - 7 \times 10^5$ V/cm) is nearly equal to the value calculated by considering liquid xenon as gaseous xenon of 520 atm. Also, the number of photons emitted by one electron in the proportional scintillation process was estimated to be about five for a 20 μm wire at the applied voltage of 5 kV. This means that if a center wire of 50 μm in diameter is used in a proportional counter and 12 kV is applied the photon gain per one electron is expected to be about 30 [70]. This value is large enough to make the electronic noise effect negligible.

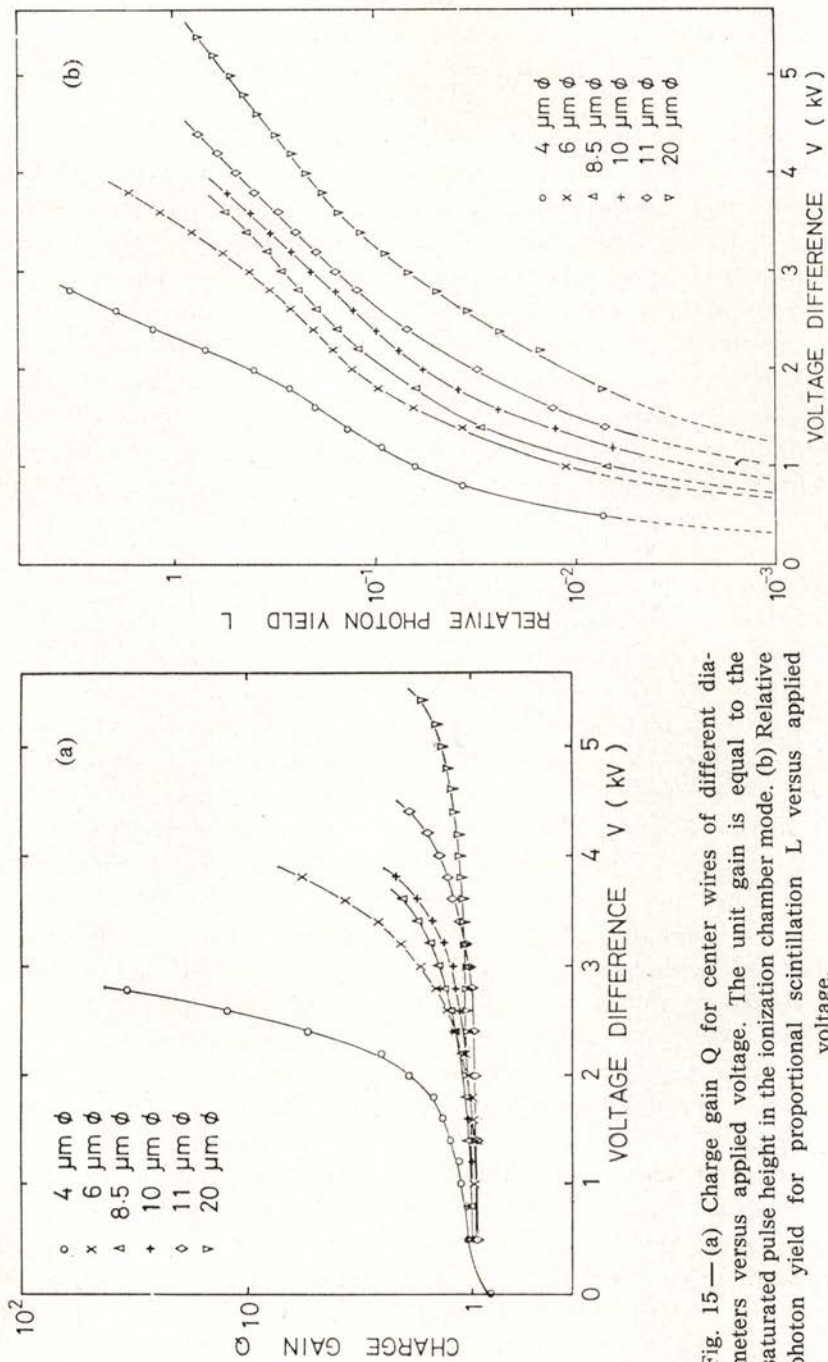


Fig. 15—(a) Charge gain Q for center wires of different diameters versus applied voltage. The unit gain is equal to the saturated pulse yield in the ionization chamber mode. (b) Relative photon yield for proportional scintillation L versus applied voltage.

6 — POSSIBILITIES OF APPLICATION TO NUCLEAR RADIATION DETECTORS

Some possibilities of application of liquid rare gases to nuclear radiation detectors have already been described in each section. Here, they are summarized as a whole and some ideas for developing liquid rare gases detectors are presented. Liquid rare gases can be used as detector media in the following four detector modes as in gaseous detectors; i) ionization mode, ii) scintillation mode, iii) proportional scintillation mode and iv) proportional ionization mode. In the modes, i) and iii) they will be used as energy spectrometers with good energy resolution or as position sensitive detectors with good position resolution for minimum ionizing particles or gamma-rays. Mode ii) will correspond to fast counters or detectors for heavy ions. In the mode iv) they will be used only as position sensitive detectors, because its signals are useful only for timing.

Now, let us consider in detail the possibilities of application to nuclear radiation detectors of liquid argon and liquid xenon.

In liquid argon, the photon- and electron-multiplications do not occur as mentioned before, and so, liquid argon can be used only as detector medium in the ionization and scintillation modes. Nevertheless, it is expected to be a good detector medium in large size detectors, such as calorimeters for energy measurement of high energy gamma-rays or high energy electrons and time projection chambers for neutrino detection, because of its cheapness and the easiness of its treatment. Recently, the possibility of «photo-ionization detectors» in liquid phase was suggested by Policarpo [70]. The most practical medium for this type of detector is liquid argon doped by a small amount (~ several ten ppm) of organic compounds with low ionization potential. Such a liquid photo-ionization detector (LPID) is expected to have a large detection efficiency over a wide wavelength range of ultra-violet photons and a better position resolution than gaseous PID.

On the other hand, it is not so easy to construct a large size liquid xenon detector as compared with liquid argon, because of its high cost and its high sensitivity to impurities. However, liquid xenon is suitable as detector medium for gamma-ray detectors, because of its high atomic number and

its high atomic density. As a gamma-ray spectrometer with good energy resolution, a gridded ionization chamber or a proportional scintillation chamber filled with liquid xenon may be used. Also, liquid xenon is suitable as detector medium in the drift chamber, because the drift velocity of electrons in liquid xenon is almost constant for electric fields higher than 3 kV/cm. If a liquid xenon proportional scintillation chamber is used with a liquid xenon PID, we can use the detector system as a position sensitive detector as well as an energy spectrometer for gamma-rays. Furthermore, it is possible to construct a kind of time projection chamber for gamma-rays by combining drift chambers and gridded ionization techniques.

Finally, we would like to suggest a new type liquid rare gas detector, which uses both signals of ionization and scintillation. Considerable part of the scintillation from liquid rare gases arises from recombination between electrons and ions. In particular, this is remarkable for heavy ions. On the other hand, only a small amount of charge produced by a heavy ion is observable. Thus, the scintillation signal and charge signal are complementary for heavy charged particles and it is considered that some linear combination of scintillation signal and charge signal will be proportional to the energy of the particle. Such a detector will be useful as a total absorption detector for high energy heavy ions. Also, the ratio of the scintillation signal to the charge signal depends on the kind of particle. Therefore, such a technique may be used for particle identification of heavy ions.

ACKNOWLEDGMENT

The author would like to express his thanks to Professor A. J. P. L. Policarpo for having made possible the realization of this review article.

REFERENCES

- [1] L. W. ALVAREZ, *Lawrence Radiation Laboratory Physics Note*, No. 672 (1968).
- [2] R. A. MULLER, S. E. DERENZO, G. SMADJA, B. SMITH, R. G. SMITS, H. ZAKLAD and L. W. ALVAREZ, *Phys. Rev. Letters*, **27**, 532 (1971).
- [3] S. E. DERENZO, T. S. MAST, H. ZAKLAD and R. A. MULLER, *Phys. Rev.*, **A9**, 2582 (1974).

- [4] S. E. DERENZO, A. R. KIRSCHBAUM, P. H. EBERHARD, R. R. ROSS and F. T. SOLMITZ, *Nucl. Instr. Meth.*, **122**, 319 (1974).
- [5] M. C. GADENNE, A. LANSIART and A. SEIGNEUR, *Nucl. Instr. Meth.*, **124**, 521 (1975).
- [6] J. PRUNIER, R. ALLEMAND, M. LAVAL and G. THOMAS, *Nucl. Instr. Meth.*, **109**, 257 (1973).
- [7] A. LANSIART, A. SEIGNEUR, J. MORETTI and J. MORUCCI, *Nucl. Instr. Meth.*, **135**, 47 (1976).
- [8] B. A. DOLGOSHEIN, V. N. LEBEDENKO and B. U. RODIONOV, *JETP Letters*, **11**, 351 (1970).
- [9] B. A. DOLGOSHEIN, A. A. KRUGLOV, V. N. LEBEDENKO, V. P. MIROSHICHENKO and B. U. RODIONOV, *Sov. J. Particles Nucl.*, **4**, 70 (1973).
- [10] G. KNIES and D. NEUFFER, *Nucl. Instr. Meth.*, **120**, 1 (1974).
- [11] J. ENGLER, B. FRIEND, W. HOFMANN, H. KLEIN, R. NICKSON, W. SCHMIDT-PARZEFALL, A. SEGAR, M. TYRRELL, D. WEGENER, T. WILLARD and K. WINTER, *Nucl. Instr. Meth.*, **120**, 157 (1974).
- [12] W. J. WILLIS and V. RADEKA, *Nucl. Instr. Meth.*, **120**, 221 (1974).
- [13] D. HITLIN, J. F. MARTIN, C. C. MOREHOUSE, G. S. ABRAMS, D. BRIGGS, W. CARITHERS, S. COOPER, R. DEVOE, C. FRIEDBERG, D. MARSH, S. SHANNON, E. VELLA and J. S. WHITAKER, *Nucl. Instr. Meth.*, **137**, 225 (1976).
- [14] C. J. FABJAN, W. STRUCZINSKI, W. J. WILLIS, C. KOURKOUHELIES, A. J. LANKFORD and P. REHAK, *Nucl. Instr. Meth.*, **141**, 61 (1977).
- [15] C. CERRI and F. SERGIAMPRIETRI, *Nucl. Instr. Meth.*, **141**, 207 (1977).
- [16] C. RUBBIA, *CERN EP Internal Report*, 77-8 (1977).
- [17] H. H. CHEN and J. F. LATHROP, *Nucl. Instr. Meth.*, **150**, 585 (1978).
- [18] H. H. CHEN and P. J. DOE, *IEEE Transaction on Nucl. Sci.*, **NS-28** 454 (1980).
- [19] S. KONNO and S. KOBAYASHI, *Sci. Pap. Inst. Phys. Chem. Res.*, **67**, 57 (1973).
- [20] T. TAKAHASHI, S. KONNO and T. DOKE, *J. Phys.* **C7**, 230 (1974).
- [21] M. MIYAJIMA, T. TAKAHASHI, S. KONNO, T. HAMADA, S. KUBOTA, E. SHIBAMURA and T. DOKE, *Phys. Rev.*, **A9**, 1438 (1974).
- [22] T. TAKAHASHI, S. KONNO, T. HAMADA, S. KUBOTA, A. NAKAMOTO, A. HITACHI, E. SHIBAMURA and T. DOKE, *Phys. Rev.*, **A12**, 1771 (1975).
- [23] E. SHIBAMURA, A. HITACHI, T. DOKE, T. TAKAHASHI, S. KUBOTA and M. MIYAJIMA, *Nucl. Instr. Meth.*, **131**, 249 (1975).
- [24] S. KUBOTA, A. NAKAMOTO, T. TAKAHASHI, S. KONNO, T. HAMADA, M. MIYAJIMA, E. SHIBAMURA, A. HITACHI and T. DOKE, *Phys. Rev.*, **B13**, 1649 (1976).
- [25] T. DOKE, A. HITACHI, S. KUBOTA, A. NAKAMOTO and T. TAKAHASHI, *Nucl. Instr. Meth.*, **134**, 353 (1976).
- [26] E. SHIBAMURA, S. KUBOTA, T. TAKAHASHI and T. DOKE, *Phys. Rev.*, **A20**, 2547 (1979).
- [27] M. MIYAJIMA, K. MASUDA, Y. HOSHI, T. DOKE, T. TAKAHASHI, T. HAMADĀ, S. KUBOTA, A. NAKAMOTO and E. SHIBAMURA, *Nucl. Instr. Meth.*, **160**, 239 (1979).

- [28] K. MASUDA, S. TAKASU, T. DOKE, T. TAKAHASHI, A. NAKAMOTO, S. KUBOTA and E. SHIBAMURA, *Nucl. Instr. Meth.*, **160**, 247 (1979).
- [29] K. MASUDA, A. HITACHI, Y. HOSHI, T. DOKE, A. NAKAMOTO, E. SHIBAMURA and T. TAKAHASHI, *Nucl. Instr. Meth.*, **174**, 439 (1980).
- [30] K. MASUDA, T. TAKAHASHI and T. DOKE, *Nucl. Instr. Meth.* (to be published).
- [31] H. A. ULLMAIER, *Phys. Med. Biol.*, **11**, 95 (1966).
- [32] N. V. KLASSEN and W. F. SCHMIDT, *Can. J. Chem.*, **47**, 4286 (1969).
- [33] M. G. ROBINSON and G. R. FREEMAN., *Can. J. Chem.*, **51**, 641 (1973).
- [34] S. HUANG and G. R. FREEMAN, *Can. J. Chem.*, **55**, 1838 (1977).
- [35] R. L. PLATZMAN, *Int. J. Appl. Rad. Isotopes*, **10**, 116 (1961).
- [36] W. SHOCKLEY, *Czech. J. Phys.*, **B11**, 81 (1961).
- [37] C. A. KLEIN, *J. Appl. Phys.*, **39**, 2029 (1968).
- [38] G. BALDINI and R. S. KNOX, *Phys. Rev. Letters*, **11**, 127 (1963).
G. BALDINI, *Phys. Rev.*, **137**, A508 (1965).
- [39] U. ROSSLER, *Phys. Status Solidi* **B42**, 345 (1970), **B45**, 483 (1971).
- [40] G. KEITEL, DESY F41-70/7 (1970).
P. SCHREBER, DESY F1-70/5 (1970).
- [41] U. FANO, *Phys. Rev.*, **72**, 26 (1947).
- [42] G. D. ALKHAZOV, A. P. KOMAR and A. A. VOROBEV, *Nucl. Instr. Meth.*, **48**, 1 (1967).
- [43] H. A. BETHE and J. ASHKIN, *Experimental Nuclear Physics* (ed. E. Segre, Wiley, New York, 1973) Vol. 1, Part 2.
- [44] I. M. OBODOVSKY and S. G. POKACHALOV, *Low Temp. Phys.*, **5**, 829 (1979).
- [45] A. P. PISAREV, *Sov. Phys. JETP*, **36**, 823 (1973).
- [46] E. SHIBAMURA, A. HITACHI, M. MIYAJIMA, S. KUBOTA, A. NAKAMOTO, T. TAKAHASHI, S. KONNO and T. DOKE, *Bull. Sci. Eng. Res. Lab. Waseda Univ.*, **69**, 104 (1975).
- [47] S. E. DERENZO, D. B. SMITH, R. G. SMITS, H. ZAKLAD, L. W. ALVAREZ and R. A. MULLER, UCRL-20118 (1970).
- [48] M. MIYAJIMA, K. MASUDA, A. HITACHI, T. DOKE, T. TAKAHASHI, S. KONNO, T. HAMADA, S. KUBOTA, A. NAKAMOTO and E. SHIBAMURA, *Nucl. Instr. Meth.*, **134**, 403 (1976).
- [49] L. ONSAGER, *Phys. Rev.*, **54**, 554 (1938).
- [50] T. TAKAHASHI, S. KONNO, A. HITACHI, T. HAMADA, A. NAKAMOTO, M. MIYAJIMA, E. SHIBAMURA, Y. HOSHI, K. MASUDA and T. DOKE, *Sci. Pap. Inst. Phys. Chem. Res.*, **74**, 65 (1980).
- [51] H. ZAKLAD, UCRL-20690 (1971).
- [52] W. HOFMANN, U. KLEIN, M. SCHULZ, J. SPENGLER and D. WEGENER, *Nucl. Instr. Meth.*, **135**, 151 (1976).
- [53] G. BAKALE, U. SOWADA and W. F. SCHMIDT, *J. Phys. Chem.*, **80**, 2556 (1976).
- [54] J. L. PACK, R. E. VOSHALL and A. V. PHELPS, *Phys. Rev.*, **127**, 2084 (1962).
- [55] L. S. MILLER, S. HOWE and W. E. SPEAR, *Phys. Rev.*, **166**, 871 (1968).
- [56] Y. YOSHINO, U. SOWADA and W. F. SCHMIDT, *Phys. Rev.*, **A14**, 438 (1976).

- [57] E. SHIBAMURA, S. KUBOTA, T. TAKAHASHI and T. DOKE, *Proc. Int. Seminar on Swarm Experiments in Atomic Collision Research*, Tokyo, 47 (1979).
- [58] J. LEKNER, *Phys. Rev.*, **158**, 130 (1967).
- [59] J. A. NORTHROP and J. C. GURSKY, *Nucl. Instr. Meth.*, **3**, 207 (1958).
- [60] S. KUBOTA, A. NAKAMOTO, T. TAKAHASHI, T. HAMADA, E. SHIBAMURA, M. MIYAJIMA, K. MASUDA and T. DOKE, *Phys. Rev.* **B17**, 2762 (1978).
- [61] A. HITACHI, T. TAKAHASHI, T. HAMADA, E. SHIBAMURA, A. NAKAMOTO, N. FUNAYAMA, K. MASUDA and T. DOKE, *Phys. Rev.*, **B23**, (1981) in press.
- [62] A. HITACHI, T. TAKAHASHI, T. HAMADA, E. SHIBAMURA, N. FUNAYAMA, K. MASUDA, J. KIKUCHI and T. DOKE, *Proc. INS Intern. Symposium on Nuclear Radiation Detectors*, Tokyo, (1981) in press.
- [63] R. B. MURRAY and A. MEYER, *Phys. Rev.*, **122**, 815 (1961).
- [64] S. KUBOTA, M. HISHIDA and J. RUAN, *J. Phys.*, **C11**, 2645 (1978).
- [65] S. KUBOTA, M. HISHIDA, M. SUZUKI and J. RUAN, *Phys. Rev.*, **B20**, 3486 (1979).
- [66] S. KUBOTA, M. SUZUKI and J. RUAN, *Phys. Rev.* **B21**, 2632 (1980).
- [67] S. KUBOTA, M. HISHIDA, M. SUZUKI and J. RUAN, *Proc. INS Intern. Symposium on Nuclear Radiation Detectors*, Tokyo, (1981) in press.
- [68] M. J. CARVALHO and G. KLEIN, *J. Luminescence*, **18/19**, 487 (1979).
- [69] A. J. P. L. POLICARPO, M. A. F. ALVES, M. C. M. DOS SANTOS and M. J. T. CARVALHO, *Nucl. Instr. Meth.*, **102**, 337 (1972).
- [70] A. J. P. L. POLICARPO, *Proc. INS Intern. Symposium on Nuclear Radiation Detectors*, Tokyo, (1981) in press.

THE ESTIMATED INTENSITY VARIANCE AS A MEAN OF EXPECTED AND SAMPLE VARIANCES

WALTER GONSCHOREK (*)

Departamento de Física da Universidade de Coimbra

3000 Coimbra, Portugal

(Received 19 January 1981)

ABSTRACT—Two estimates for the variance $\sigma^2(I)$ of repeatedly measured integrated intensities I are given, one based on the sample variance the other one based on Poisson statistics. The weighted mean of both is taken as the final estimate of $\sigma^2(I)$. The ratio of this final estimate to the «sample variance» of symmetry dependent intensities plotted once against I and once against $\sin \theta/\lambda$ and alternatively a χ^2 -test can help to detect systematic errors inherent in the intensities or errors of the final estimates of $\sigma^2(I)$

1 — INTRODUCTION

Weighting, in least squares procedures, can considerably influence the refined parameters. Given a set of observations x_i to be compared with calculated values x_{ci} , the function to be minimized is [1]

$$Q = \sum (x_i - x_{ci})^2 \sigma_i^{-2} \quad (1)$$

σ_i^2 is the variance of x_i . Its reciprocal σ_i^{-2} is called the weight of the observation x_i . Repeated observations x_i of the same quantity under equal conditions have the same variance σ_i^2 . Therefore in (1) they can be replaced by their mean with the variance of the mean σ_i^2/n if n values x_i are observations of the same quantity [2]. This can be understood without applying the rules of

(*) On leave from Institut für Kristallographie, T. H. Aachen, Germany.

statistics by simply considering the normal equations to be derived from (1) [3]. The problem is how to determine the variances σ_i^2 .

Undoubtedly the processes of generating and diffracting X-rays or neutrons obey Poisson statistics so that the variance of an integrated intensity I is known in principle [4]. In practice, however, sample variances $s^2(I)$, which in statistics serve as estimates for the population variances $\sigma^2(I)$, often are considerably larger than $\sigma_p^2(I)$ of Poisson distributions [5] [6] (*). McCandlish, Stout & Andrews [6] describe a procedure by which, through the use of somewhat modified sample variances derived from repeatedly-measured standard intensities, two correction terms are added to the variance obtained from the Poisson distribution. Abrahams [7] emphasizes the experiment as the best proof for any error estimation. He gives a list of some presumed error sources and proposes to estimate the contribution of each individual error source to the total error if it is not accessible either to experiment or to theory, as for example intensity drift of the primary beam or statistical variances are. On the other side Hamilton [8] (p. 148) strictly gives preference to theoretical variances over sample variances at least for small samples just as Schulz & Schwarz [9] practise.

In electron density work the reliability of the variances $\sigma^2(I)$ (or their estimates) seems to be as important as the reliability of the integrated intensities I themselves. The variances $\sigma^2(I)$ in least squares refinements besides their action through weights via the goodness of fit parameters serve as an indicator if either the model is inadequate or the data are burdened by some hidden errors or if both situations occur. In Fourier methods reliable estimates of $\sigma^2(I)$ are indispensable to decide whether the experimentally determined electron densities are significant or not.

Regarding the «instability constant» [6] it must be noticed that in X-ray diffraction the strongest reflections are low order reflections and these contain most of the information on bonding electrons. If therefore the deformation of the atoms or ions caused by bonding effects are not taken into account the differences $\Delta = |I_{\text{obs}} - I_{\text{calc}}|$ naturally will be larger for strong reflections than

(*) Schulz in his expression for the variance of the corrected intensity already took into account a term representing the uncertainty of the scaling parameter deduced from control or standard reflections.

for weak ones. Furthermore strong reflections are most affected by extinction and counting losses through dead time of the counting devices. The correction of these effects introduces additional errors whose magnitudes must be estimated and taken into account.

If, however, the estimation of $\sigma^2(I)$ through sample variances reveals a linear dependence of $\sigma^2(I)$ upon I^2 this error can be kept small using small crystals or weaker primary intensities. Some other error sources which preferably affect strong reflections like weakening filters or movable β -filters can be easily avoided.

In this paper it is assumed that all intensities have been corrected for time drifts according to McCandlish et al. [6] if this turned out to be necessary. The variances $\sigma_{P_{ji}}^2$ are thought of to have the form $\sigma_{P_{ji}}^2 = \sigma_P^2 + \sigma_K^2$ where σ_P^2 is the variance derived from Poisson statistics and σ_K^2 is the variance which takes into account the uncertainty of the scale parameter.

In the following two estimates of the intensity variances shall be given, the first one based on sample variances according to (8), the second one derived from Poisson variances. The weighted mean of both shall be taken as the final estimate of $\sigma^2(I)$.

2 — CONFIDENCE LIMITS AND WEIGHTS

Suppose (with close reference to Hamilton [8] (p. 40)) that m samples each with n_j observations all having the same population mean μ led to m means \bar{x}_j with variances $\sigma^2(\bar{x}_j)$. Then it is reasonable to take the weighted mean \bar{x} :

$$\bar{x} = \sum_{j=1}^m w_j \bar{x}_j \quad (2)$$

$$w_j = \sigma^{-2}(\bar{x}_j) / \sum_i^m \sigma^{-2}(\bar{x}_i) \quad (3)$$

In w_j , the quantity $\sigma(\bar{x}_j)$, considered as a confidence limit, guarantees a certain probability P_j for the interval $(\bar{x}_j - \sigma(\bar{x}_j), \bar{x}_j + \sigma(\bar{x}_j))$ to include the population mean μ . For normally distributed observations this probability has the value $P_G = 0.682689$.

Therefore it is proposed to replace the $\sigma(\bar{x}_j)$ in (3) by confidence limits s_{ij} for the probability P_G if the $\sigma(\bar{x}_j)$ are unknown :

$$s_{ij} = t_\alpha (n_j - 1) s_j / n_j^{1/2} \quad (4)$$

$t_\alpha(\nu)$ = fractile (percentage point) of Student's t-distribution for the probability $\alpha = 1 - P_G$ and the degree of freedom ν , s_j^2 = sample variance of the j-th sample. Table I gives the fractiles $t_\alpha(\nu)$.

TABLE I—Fractiles of Student's t-distribution for the two-tailed probability $\alpha = 1 - P_G$, $P_G = 0.682689$ (*). ν is the number of degrees of freedom.

ν	$t_\alpha(\nu)$	ν	$t_\alpha(\nu)$	ν	$t_\alpha(\nu)$
1	1.837	7	1.077	13	1.040
2	1.321	8	1.067	14	1.037
3	1.197	9	1.059	15	1.034
4	1.142	10	1.053	20	1.026
5	1.111	11	1.048	25	1.020
6	1.091	12	1.043	30	1.017

(*) P_G is the value of the integral taken over the Gaussian density function from $-\sigma$ to $+\sigma$, $\mu = 0$. The integration was carried out by the quadrature method of Gauss once with 24 and once with 26 grid points for the integration from 0 to σ . Both results (with 24 and with 26 grid points) agreed to within the 10th digit after the decimal point. The fractiles were obtained by integration of Student's t-distribution function again using the quadrature method of Gauss with 26 grid points. The limits of integration were varied until the value of the integral deviated less than $4.10 \cdot 10^{-6}$ from $P_G = 0.6826894921$. That last limit of integration was taken as $t_\alpha(\nu)$.

3—TWO ESTIMATES OF $\sigma^2(\bar{I}_j)$

Suppose the integrated intensity of the j-th reflection repeatedly has been measured n_j times yielding the integrated intensities I_{ji} and variances $\sigma_{ji}^2 = \sigma_P^2 + \sigma_K^2$: The weighted mean

$$\bar{I}_j = \sum_i^{n_j} w_i I_{ji} \quad (5)$$

is taken as the integrated intensity of that reflection. Here the weights w_i have the form

$$w_i = \frac{n_j}{\sum_k \sigma_{jk}^{-2}} \sigma_{ji}^{-2} \quad (6)$$

3.1 — Estimate of $\sigma^2(\bar{I}_j)$ through the sample variance

According to (4) the first estimate of $\sigma^2(\bar{I}_j)$ takes the form

$$s_{ij}^2 = t_\alpha^2 (n_j - 1) s_j^2 / n_j \quad (7)$$

with $\alpha = 1 - P_G$ and

$$s_j^2 = (n_j - 1)^{-1} \sum_i^{n_j} w_i (I_{ji} - \bar{I}_j)^2 \quad (8)$$

with w_i as defined in (6).

The variance of s_j^2 is derived in Appendix A. With that result the variance of s_{ij}^2 is

$$\sigma^2(s_{ij}^2) = t_\alpha^4 (n_j - 1) 2 (n_j - 1)^{-1} / \left(\sum_i^{n_j} \sigma_{ji}^{-2} \right)^2 \quad (9)$$

σ_{ji}^2 is the (unknown) variance of I_{ji} . If in (9) σ_{ji}^2 is replaced by σ_{Pji}^2 and if the definition (12) is used, $\sigma^2(s_{ij}^2)$ takes the form

$$\sigma_P^2(s_{ij}^2) = t_\alpha^4 (n_j - 1) 2 (n_j - 1)^{-1} \sigma_P^4(\bar{I}_j) \quad (10)$$

3.2 — Estimate of $\sigma^2(\bar{I}_j)$ through Poisson statistics

For m repeatedly measured reference reflections, the weighted means according to (5) and (6) and the quantities s_i^2 (eq. (8)) $j = 1, \dots, m$ are taken. The variances of \bar{I}_j derived from (5) are

$$\sigma^2(\bar{I}_j) = \sum_i^{n_j} w_i^2 \sigma_{ji}^2 \quad (11)$$

Here σ_{ji}^2 is replaced by σ_{Pji}^2 . This leads to

$$\sigma_P^2(\bar{I}_j) = \left(\sum_i^{n_j} \sigma_{Pji}^{-2} \right)^{-1} \quad (12)$$

Now the ratios v_j are taken

$$v_j = s_{ij}^2 / \sigma_P^2(\bar{I}_j) \quad (13)$$

Their weighted mean is

$$\bar{v} = \frac{\sum_i^m s_i^{-2}(v_j) v_j}{\sum_k^m s_i^{-2}(v_k)} \quad (14)$$

with $s_i^2(v_j)$ as derived in Appendix B.

Then as the second estimate of $\sigma^2(\bar{I}_j)$ for each repeatedly measured intensity the quantity $s_j'^2$ is taken:

$$s_j'^2 = \bar{v} \sigma_P^2(\bar{I}_j) \quad (15)$$

4 — THE FINAL ESTIMATE OF $\sigma^2(\bar{I}_j)$

The final estimate of $\sigma^2(\bar{I}_j)$ is

$$s'^2(\bar{I}_j) = (\sigma_P^{-2}(s_{ij}^2) s_{ij}^2 + s_i^{-2}(s_j'^2) s_j'^2) / (\sigma_P^{-2}(s_{ij}^2) + s_i^{-2}(s_j'^2)) \quad (16)$$

with $\sigma_P^2(s_{ij}^2)$ as defined in (10) and with $s_i^2(s_j'^2)$ as derived in Appendix C.

An estimate of the variance of $s'^2(\bar{I}_j)$ is

$$s^2(s'^2(\bar{I}_j)) = (\sigma_P^{-2}(s_{ij}^2) + s_i^{-2}(s_j'^2))^{-1} \quad (17)$$

If for some j -th reflection there exists only one single measurement I_{ji} its variance is estimated as

$$s'^2(I_{ji}) = \bar{v} \sigma_{Pji}^2 \quad (18)$$

An estimate of the variance of $s'^2(I_{ji})$ is

$$s^2(s'^2(I_{ji})) = s_i^2(\bar{v}) \sigma_{Pji}^4 \quad (19)$$

with $s_i^2(\bar{v})$ as defined in (C6).

Often \bar{I}_j is corrected by some factor c_j (e. g. absorption): $\bar{I}_{jc} = c_j \bar{I}_j$. In the following $s'^2(\bar{I}_j)$ must then be replaced by the appropriate estimate of $\sigma^2(c_j \bar{I}_j)$.

5 — SYMMETRY DEPENDENT INTENSITIES

For symmetry dependent intensities \bar{I}_j , $j = 1, \dots, n_D$ the weighted mean is taken :

$$\bar{I} = \sum_j^{n_D} w_j \bar{I}_j \quad (20)$$

with weights

$$w_j = s'^{-2}(\bar{I}_j) / \sum_k^{n_D} s'^{-2}(\bar{I}_k) \quad (21)$$

An estimate of the variance of \bar{I} deduced from (20) is

$$s'^2(\bar{I}) = \left(\sum_j^{n_D} s'^{-2}(\bar{I}_j) \right)^{-1} \quad (22)$$

and this should be taken as the estimate of $\sigma^2(\bar{I})$. The estimated variance $s'^2(\bar{I})$ can be compared with the weighted scatter of \bar{I}_j :

$$s^2(\bar{I}) = (n_D - 1)^{-1} \sum_j^{n_D} w_j (\bar{I}_j - \bar{I})^2 \quad (23)$$

The ratios of $s_i^2(\bar{I}) = t_a^2 (n_D - 1) s^2(\bar{I})$ to $s'^2(\bar{I})$ plotted once against \bar{I} and once against $\sin \vartheta / \lambda$ may help to reveal systematic dependences if they exist. Alternatively a χ^2 -test according to van der Waerden ([1] p. 222) can be applied. This will be done in a paper which is in preparation.

A considerable part of this work was done at the Institut für Kristallographie der T. H. Aachen. The author, therefore, is deeply indebted to Prof. Th. Hahn. Thanks are due to Prof. Alte da Veiga who gave the opportunity to complete this work. The grant of a research and teaching fellowship by Deutscher Akademischer Austauschdienst is highly appreciated.

APPENDIX A

The variance of the quantity s_j^2 (8) is to be derived. For that purpose the intensities I_{ji} , with constant j , are assumed to be normally and independently distributed with variances σ_{ji}^2 and all with the same (population) mean μ . Then the weights w_i instead of (6) have the form

$$w_i = \sigma_{ji}^{-2} / \sum_k^{n_j} \sigma_{jk}^{-2} \quad (A1)$$

Correspondingly the variances of \bar{I}_j instead of (12) are

$$\sigma^2(\bar{I}_j) = \left(\sum_i^{n_j} \sigma_{ji}^{-2} \right)^{-1} \quad (A2)$$

Now the quantity

$$\chi^2 = (n_j - 1) s_j^2 / \sigma^2(\bar{I}_j) \quad (A3)$$

shall be shown to be χ^2 -distributed with $(n_j - 1)$ degrees of freedom. For that purpose according to van der Waerden [1], (p. 111) I_{ji} is replaced by

$$x_i = (I_{ji} - \mu) / \sigma_{ji}; \quad (A4)$$

x_i is normally distributed with mean zero and unit variance. Equation (8) can be rewritten as

$$s_j^2 = (n_j - 1)^{-1} \left[\sum_i^{n_j} w_i I_{ji}^2 - \left(\sum_i^{n_j} w_i I_{ji} \right)^2 \right] \quad (A5)$$

or, taking (A4) into account,

$$s_j^2 = (n_j - 1)^{-1} \left[\sum_i^{n_j} w_i (\sigma_{ji} x_i + \mu)^2 - \left(\sigma^2(\bar{I}_j) \sum_i^{n_j} \sigma_{ji}^{-1} x_i + \mu \right)^2 \right] \quad (A6)$$

This leads to

$$s_j^2 = \sigma^2(\bar{I}_j) (n_j - 1)^{-1} \left[\sum_i^{n_j} x_i^2 - \left(\sum_i^{n_j} w_i^{1/2} x_i \right)^2 \right] \quad (A7)$$

The quantity in square brackets in (A7) is identical with χ^2 defined by (A3). Now the transformation

$$y_1 = \sum_i^{n_j} w_i^{1/2} \bar{x}_i \quad (\text{A8})$$

is considered. The sum of the squares of its coefficients is equal to unity. Therefore this equation can replace the first row of the linear equations in van der Waerden ([1], p. 112) or the last row of the corresponding equations in Martin ([10], p. 59), and the conclusions drawn in these works concerning χ^2 as defined there apply also to χ^2 defined in (A3). Therefore χ^2 (A3) assumes a χ^2 -distribution with $(n_j - 1)$ degrees of freedom and the variance of s_j^2 is

$$\sigma^2 (s_j^2) = 2 (n_j - 1)^{-1} \sigma^4 (\bar{I}_j) \quad (\text{A9})$$

APPENDIX B

The variance $\sigma^2 (v_j)$ with v_j as defined in (13) according to Hamilton ([8] p. 32) is given by

$$\sigma^2 (v_j) = \sigma^2 (s_{ij}^2) \sigma^2 (\sigma_P^{-2} (\bar{I}_j)) + \sigma_P^{-4} (\bar{I}_j) \sigma^2 (s_{ij}^2) + s_{ij}^4 \sigma^2 (\sigma_P^{-2} (\bar{I}_j)) \quad (\text{B1})$$

Here it is assumed that s_{ij}^2 and $\sigma_P^{-2} (\bar{I}_j)$ are statistically independent. $\sigma^2 (s_{ij}^2)$ is estimated through (10). $\sigma^2 (\sigma_P^{-2} (\bar{I}_j))$ is found using a formula again given by Hamilton ([8], p. 32):

$$\sigma^2 (\sigma_P^{-2} (\bar{I}_j)) \approx \sigma^2 (\sigma_P^2 (\bar{I}_j)) / \sigma_P^8 (\bar{I}_j) \quad (\text{B2})$$

To find an estimate of $\sigma^2 (\sigma_P^{-2} (\bar{I}_j))$ the weighted mean of $\sigma_{P_{ji}}^2$ as defined in (6) is considered

$$\sigma_{P_{ji}}^2 = \sum_i^{n_j} w_i \sigma_{P_{ji}}^2 = n / \sum_i^{n_j} \sigma_{P_{ji}}^{-2} \quad (\text{B3})$$

$\sigma_{P_j}^2$ is an estimate of the variance of the observations I_{ji} for constant j . Therefore an estimate of the variance of \bar{I}_j is $\sigma_{P_j}^2/n_j$ which is identical with (12):

$$\sigma_P^2(\bar{I}_j) = \sigma_{P_j}^2/n_j \quad (B4)$$

Now $\sigma_{P_j}^2$ (B3) being the weighted mean of $\sigma_{P_{ji}}^2$ an estimate of its variance is given by

$$s^2(\sigma_{P_j}^2) = (n_j - 1)^{-1} \sum_i^{n_j} w_i (\sigma_{P_{ji}}^2 - \sigma_{P_j}^2)^2 \quad (B5)$$

With (B4) this leads to an estimate of $\sigma_P^2(\bar{I}_j)$:

$$s^2(\sigma_P^2(\bar{I}_j)) = s^2(\sigma_{P_j}^2) / n_j^2 \quad (B6)$$

Now an estimate of $\sigma^2(v_j)$ (B1) can be given. First in (B2) $\sigma^2(\sigma_P^2(\bar{I}_j))$ is replaced by (B6). $s^2(\sigma_P^2(\bar{I}_j))$ (B6) according to (4) is multiplied by $t_\alpha^2(n_j - 1)$. s_{ij}^4 in the last term of (B1) according to (13) is replaced by $v_j^2 \sigma_P^4(\bar{I}_j)$. Then the estimate of $\sigma^2(v_j)$ is

$$s_i^2(v_j) = t_\alpha^2(n_j - 1) \left[s^2(\sigma_{P_j}^2) n_j^{-2} \sigma_P^{-4}(\bar{I}_j) \right. \\ \left. (2t_\alpha^4(n_j - 1)/(n_j - 1) + v_j^2) + 2t_\alpha^2(n_j - 1)/(n_j - 1) \right] \quad (B7)$$

with $s^2(\sigma_{P_j}^2)$ as defined in (B5) and $\sigma_P^2(\bar{I}_j)$ as defined in (12).

APPENDIX C

The variance $\sigma^2(s_j''^2)$ according to Hamilton ([8], p. 32) has the form

$$\sigma^2(s_j''^2) = \sigma^2(\bar{v}) \sigma^2(\sigma_P^2(\bar{I}_j)) + \sigma_P^4(\bar{I}_j) \sigma^2(\bar{v}) + \bar{v}^2 \sigma^2(\sigma_P^2(\bar{I}_j)) \quad (C1)$$

Here \bar{v} and $\sigma_P^2(\bar{I}_j)$ are considered to be statistically independent. An estimate of $\sigma^2(\sigma_P^2(\bar{I}_j))$ is given through (B6). For $\sigma^2(\bar{v})$ two estimates can be derived:

1. \bar{v} as defined in (14) has the variance

$$\sigma^2(\bar{v}) = \sum_j^m w_j^2 \sigma^2(v_j) \quad (C2)$$

with

$$w_j =: s_i^{-2}(v_j) / \sum_k^m s_i^{-2}(v_k) \quad (C3)$$

In (C2) $\sigma^2(v_j)$ is replaced by $s_i^2(v_j)$ (B7) yielding

$$\sigma_i^2(\bar{v}) = \left(\sum_j^m s_i^{-2}(v_j) \right)^{-1} \quad (C4)$$

2. An alternative estimate of $\sigma^2(\bar{v})$ is the weighted scatter of v_j

$$s^2(\bar{v}) = (m-1)^{-1} \sum_j^m w_j (v_j - \bar{v})^2 \quad (C5)$$

with weights as defined in (C3). As the final estimate of $\sigma^2(\bar{v})$ the maximum

$$s_i^2(\bar{v}) = \text{Max} \left(\sigma_i^2(\bar{v}); t_\alpha^2 (m-1) s^2(\bar{v}) \right) \quad (C6)$$

shall be taken. Finally the estimate of $\sigma^2(s_j'^2)$ (C1) to be used in (16) is

$$s_i^2(s_j'^2) = t_\alpha^2 (n_j - 1) s^2(\sigma_{p_j}^2) n_j^{-2} \left[s_i^2(\bar{v}) + \bar{v}^2 \right] + \sigma_p^4(\bar{I}_j) s_i^2(\bar{v}) \quad (C7)$$

REFERENCES

- [1] VAN DER WAERDEN, B. L. (1965). *Mathematische Statistik*. Berlin: Springer.
- [2] CRUICKSHANK, D. W. J. (1965). *Computing Methods in Crystallography*, edited by J. S. Rollett, pp. 99-106. Oxford: Pergamon Press.
- [3] ROLLETT, J. S. (1970). *Crystallographic computing*, edited by F. R. Ahmed, pp. 167-181.
- [4] SCHULZ, H. & HUBER, P. H. (1971). *Acta Cryst.* **A27**, 536-539.
- [5] SCHULZ, H. (1971). *Acta Cryst.* **A27**, 540-544.

- [6] McCANDLISH, L. E., STOUT, G. H. & ANDREWS, L. C. (1975). *Acta Cryst.* **A31**, 245-249.
- [7] ABRAHAMS, S. C. (1969). *Acta Cryst.* **A25**, 165-173.
- [8] HAMILTON, C. H. (1964). *Statistics in Physical Science*. New York: Ronald Press.
- [9] SCHULZ, H. & SCHWARZ, K. H. (1978). *Acta Cryst.* **A34**, 999-1005.
- [10] MARTIN, B. R. (1971). *Statistics for Physicists*. London: Academic Press.

THE THERMAL AND MAGNETIC PROPERTIES OF SOME RARE EARTH-Pd₃ PHASES OF THE AuCu₃ STRUCTURE

J. M. MACHADO DA SILVA *

Clarendon Laboratory, Parks Road, Oxford OX13PU U.K.

W. E. GARDNER

Materials Physics Division, AERE, Harwell, Oxon, U. K.

I. R. HARRIS

Department of Physical Metallurgy and Science of Materials, Birmingham University, Birmingham B15 2TT, UK.

(Received 30 June 1981)

Abstract—Heat capacity and magnetization measurements have been made on LaPd₃, PrPd₃, TbPd₃ and ErPd₃. Values of $\gamma = 0.33 \pm 0.02$ mJ/(K². g atom) and $\Theta_D = 171 \pm 1$ K were found for LaPd₃. In the other phases specific heat contributions from both magnetic ordering and crystal field levels were observed: $T_N = 0.6$ K and $E(\Gamma_3) - E(\Gamma_5) = 4$ K for PrPd₃; $T_N = 3.7$ K and $E(\Gamma_5) - E(\Gamma_3) = 8$ K for TbPd₃; $T_N < 0.22$ K and $E(\Gamma_8^{(3)}) - E(\Gamma_6) = 2$ K for ErPd₃.

Saturation moments at 1.2 K and in effective fields of 37 kOe of 0.97, 6.60 and 7.52 μ_B were observed for PrPd₃, TbPd₃ and ErPd₃ respectively. The results have been analysed using a crystal field Hamiltonian and compared with the predictions of a simple point-charge model.

1 — INTRODUCTION

Rare earth metals form intermetallic compounds of the AuCu₃ type (L1₂) with Al, Pd, In, Sn, Pt, Tl and Pb [1]. The magnetic properties of several of these compounds [2], [3], [4] have been reported and it is noticeable that, for a given rare earth atom, the ordering temperature is about an order of magnitude smaller

(*) Now at Centro de Física da Universidade do Porto (INIC), Faculdade de Ciências, 4000 Porto, Portugal.

for the palladium-based phases. Thus these phases offer the opportunity to examine the properties of the rare earth atoms in environments where the crystal field interaction predominates over the exchange interaction. Both heat capacity and magnetic measurements can lead to estimates of the crystal field and exchange interactions.

2 — EXPERIMENTAL

The details of sample preparation have been given previously by Gardner *et al* [2]. The magnetic measurements have been made using a Sartorius electronic microbalance and a superconducting solenoid with gradient coils [5] in fields up to 42 kOe and at temperatures between 1 and 50 K. Heat capacity measurements have been made using the technique and equipment described previously [6].

3 — THEORY

3.1. Heat Capacity

For a metallic lattice with 4 atoms / unit cell the heat capacity / g molecule at low temperature is given by

$$C_v = 7776 (T/\theta_D)^3 + 4\gamma T \quad \text{J mole}^{-1} \text{K}^{-1} \quad (1)$$

where θ_D is the Debye temperature and γ the coefficient of the electronic heat capacity of 1 g atom [7].

Although the 4f electron is not localized in CePd₃ [2] the magnetic evidence suggests that the 4f electrons are localized in the succeeding phases of the rare earth series. All the other rare earth ions, including europium, are trivalent in the RPd₃ phases and the 4fⁿ free ion ground level is split in these AuCu₃ intermetallic phases by the cubic crystalline field from the neighbours. These splittings can be calculated by solving the crystal field Hamiltonian.

The crystal field Hamiltonian can be written in many equivalent forms using various related parameters. For a rare earth

ion in a cubic crystalline field we have chosen to express the Hamiltonian in angular momentum operators with respect to a polar axis of quantization z , which can have 2 - ($\langle 110 \rangle$ direction), 3 - ($\langle 111 \rangle$ direction) or 4 - ($\langle 100 \rangle$ direction) fold symmetry :

$$\mathcal{H} = B_4 (O_4^0 + 5 O_4^4) + B_6 (O_6^0 - 21 O_6^4) \quad (2)$$

where

$$B_4 = A_4 \langle r^4 \rangle \beta, \quad B_6 = A_6 \langle r^6 \rangle \gamma \quad (3)$$

i.e.

$$\mathcal{H} = A_4 \langle r^4 \rangle \beta (O_4^0 + 5 O_4^4) + A_6 \langle r^6 \rangle \gamma (O_6^0 - 21 O_6^4) \quad (4)$$

where the O_n^m are Stevens operator equivalents, and β and γ are Stevens multiplicative factors [8], [9].

The quantities $A_4 \langle r^4 \rangle$ and $A_6 \langle r^6 \rangle$ are the crystal field parameters which determine the magnitude of the splittings and the matrix elements.

These parameters can be regarded as empirical ones or calculated from a point charge model. For the RPd₃ phases the simple point charge model can be evaluated in terms of the unit cell dimension a and charges Z_1 on the 12 nearest-neighbors Pd atoms at a distance $a/\sqrt{2}$ and Z_2 on the 6 R-neighbors at distance a . The appropriate relations are [10] (hereafter denoted by LLW)

$$B_4 = (7/16) (e^2/a^5) (2\sqrt{2} Z_1 - Z_2) \langle r^4 \rangle \beta \quad (5)$$

$$B_6 = (3/64) (e^2/a^7) (26\sqrt{2} Z_1 - Z_2) \langle r^6 \rangle \gamma \quad (6)$$

LLW use the two alternative parameters W , which is the energy scale factor, and x , which measures the relative size of the fourth- and sixth-degree terms, where

$$B_4 F(4) = W x \quad (7)$$

$$B_6 F(6) = W (1 - |x|) \quad (8)$$

F(4) and F(6) are numerical factors introduced for convenient pictorial representation and tabulated by LLW.

LLW have essentially diagonalized eq. (4) for all values of x and all J and have reported the energies of the crystal field states and their wave functions. (The energies are, of course, independent of the choice of axis of quantization but the wave functions are not). Thus if the energies of these states are measured, x and W may be obtained from LLW and the fourth and sixth-degree terms from equations (7) and (8).

Now the energies of such states can be determined from heat capacity measurements since an additional contribution — the so-called Schottky anomaly — occurs from changes in their population with temperature. In order to resolve this contribution the heat capacity of the lattice has to be removed and frequently this proves troublesome. However if the Schottky anomaly occurs at low temperatures the errors involved are considerably reduced. This additional contribution to the heat capacity from N rare earth ions at temperature T thermally populating $(n + 1)$ states of energy E_i (K) and degeneracy g_i [7] is given by

$$C_V/R = Z^{-1} \left\{ \sum_{i=0}^n g_i (E_i/T)^2 \exp (-E_i/T) - \right. \\ \left. - Z^{-1} \left[\sum_{i=0}^n g_i (E_i/T) \exp (-E_i/T) \right]^2 \right\} \quad (9)$$

where E_0 is assumed to be zero and the partition function Z is given by

$$Z = \sum_{i=0}^n g_i \exp (-E_i/T) \quad (10)$$

The additional entropy associated with the removal of the degeneracy of the entire ground level is

$$\Delta S/R = \ln \left(\sum_{i=0}^n g_i \right) - \ln g_0$$

Frequently the separation of the states is such that it is very instructive to begin the interpretation of the results by con-

sidering the contribution from a two state system. Equation (9) then reduces to

$$C_V/R = (E_1/T)^2 (g_0/g_1) \exp (E_1/T) [1 + (g_0/g_1) \exp (E_1/T)]^{-2} \quad (11)$$

Since the most obvious feature of a Schottky anomaly is its maximum value we would like to draw attention to the frequently neglected use that can be made of this feature, namely that from it E_1 and g_1/g_0 can be deduced immediately. Thus the maximum value (C_m) of eq (11) does not depend on E_1 but is a simple function of g_1/g_0 [11] and is given by the relations

$$C_m/R = 4 (g_1/g_0) \exp (E_1/T_m) [\exp (E_1/T_m) - (g_1/g_0)]^{-2} \quad (12)$$

$$E_1/T_m = 2 [\exp (E_1/T_m) + (g_1/g_0)] [\exp (E_1/T_m) - (g_1/g_0)]^{-1} \quad (13)$$

C_m/R and E_1/T_m are plotted as a function of g_1/g_0 in figure 1.

However if splitting of the states by the crystal field is small the interpretation is less straightforward and some initial consideration of the order of the states predicted by theory provides useful guidance.

In the phases where exchange interaction is small the energies can be determined from equation (4) but in many instances the effects of exchange are important and allowance has to be made for them in the Hamiltonian. Therefore let us consider the extra term needed in the Hamiltonian when there is both an applied magnetic field and exchange interaction.

3.2. *The effects of a magnetic field*

Assume that only the lowest level of the multiplet is significantly populated (this is a reasonable assumption for all the phases except SmPd_3 and EuPd_3) and that the exchange interac-

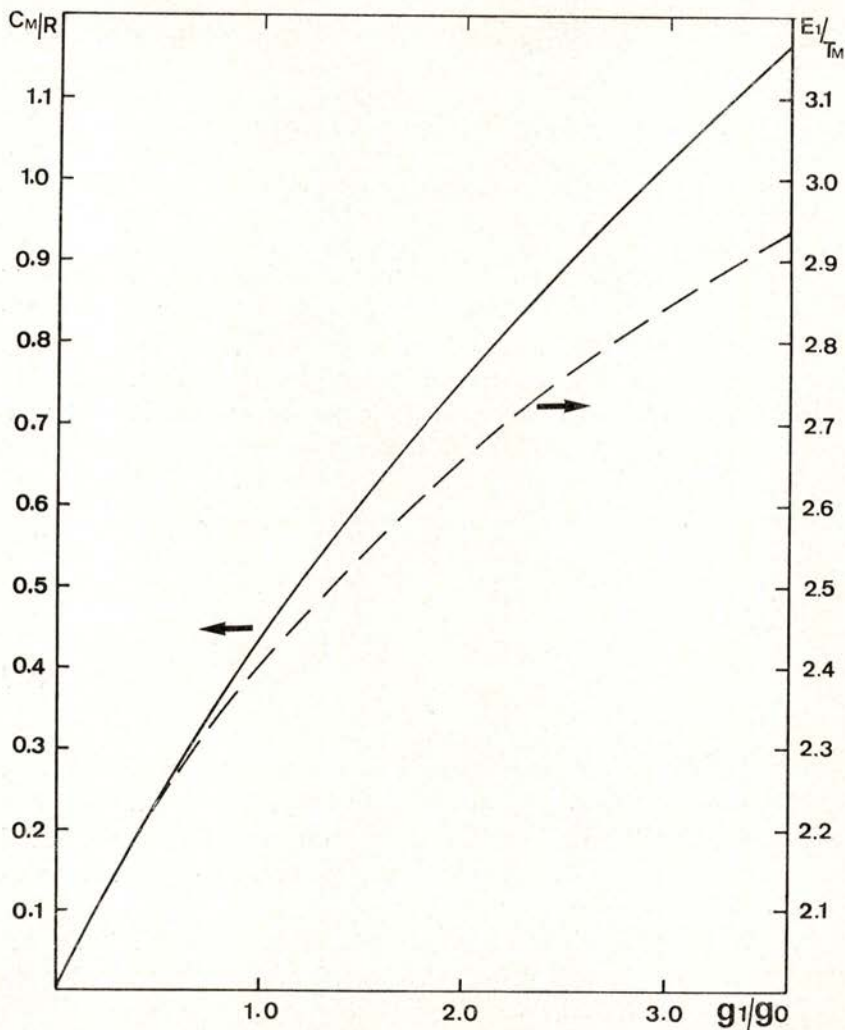


Fig. 1 — Maximum heat capacity/g atom of a two-level system of ions (—) and ratio of the energy separation of the levels (E_1) and the temperature of the maximum (T_m) (---) as a function of the ratio of the degeneracies of the two levels.

tion acts only on the spin-component of J . Then the extra term in the Hamiltonian can be written

$$\mathcal{H}_m = \mu_B [(\mathbf{H}_{ex} + \mathbf{H}_a) \cdot 2 \mathbf{S} + \mathbf{H}_a \cdot \mathbf{L}] \quad (14)$$

where H_{ex} is the exchange field and H_a is the applied field i.e. the external field corrected for the demagnetizing field. Since the crystal field and magnetic interactions are small compared to the spint-orbit interaction \mathcal{H}_m can be rewritten

$$\mathcal{H}_m = \mu_B g J \cdot \{ H_a + 2 [(g - 1)/g] H_{ex} \} = \mu_B g J \cdot H \quad (15)$$

where g is the Landé factor. Thus the exchange interaction need not be treated separately but can be simply added to the applied field.

In order to diagonalize the Hamiltonian modified by this additional term it is simplest if the magnetic field is assumed to be along the axis of quantization. Using equations (2) — (4), solutions can be obtained for the three major symmetry directions. However for a polycrystalline sample all orientations of H with respect to the crystal axes have to be evaluated and an average obtained. This is not necessary in order to determine the magnetic susceptibility (χ_m) since this is a scalar quantity in a crystal with cubic symmetry and therefore a calculation along any of the crystal axes is sufficient to determine it. However the magnetization does depend on direction and a full calculation is necessary. Since this involves excessive computing time we have been forced to approximate and we have only made calculations in the three principal symmetry directions and obtained an estimate of the polycrystalline magnetization (M_p) from their weighted average:

$$M_p = (1/26) [6 M < 100 > + 8 M < 111 > + 12 M < 110 >] \quad (16)$$

In order to make a comparison with the experimental results we assume some values for the crystal field parameters (or x and W) and the magnetic field and diagonalize the Hamiltonian in the 3 principal directions to obtain the energy states and wave functions. Use is then made of these to calculate the heat capacity, entropy, magnetization and susceptibility. Expressions for the heat capacity and entropy have been given above. The expressions used to determine the magnetization and susceptibility are

$$M_z = N \sum_{2J+1} \mu(i) \exp [- E(i)/T] / \sum_{2J+1} \exp [- E(i)/T] \quad (17)$$

$$\chi_m = N \sum_{2J+1} \{ [W_1(i)^2/T] - 2 W_2(i) \} \exp [-W_0(i)] / \sum_{2J+1} \exp [W_0(i)/T] \quad (18)$$

$$E(i) = W_0(i) + W_1(i) H_Z + W_2(i) H_Z^2$$

$$W_1(i) = \langle \psi_i | g \mu_B J_Z | \psi_i \rangle$$

$$W_2(i) = \sum_{n \neq i} | \langle \psi_n | g \mu_B J_Z | \psi_i \rangle |^2 [E_i - E_n]^{-1}$$

In order to interpret magnetization data it is useful to consider the limiting values of these expressions. At $T = 0$ K only the ground state is populated, and, neglecting exchange interaction and the temperature-independent contributions from the excited states, its magnetic properties are

$$\mu_{\text{sat}} = \langle \Gamma_s | g \mu_B J_Z | \Gamma_s \rangle \quad (19)$$

$$\mu_{\text{eff}}^2 = 3 \sum_r | \langle \Gamma_r | g \mu_B J_Z | \Gamma_r \rangle |^2 g_0^{-1} \quad (20)$$

where the 'largest' wave function is chosen for Γ_s and the summation for μ_{eff}^2 is over all the g_0 states composing the ground state.

Simply by using the known degeneracy of the crystal field states and equations (19) and (20) it can be shown [12] that the following relations hold for μ_{eff} :

$$\mu_{\text{eff}} = \sqrt{2} \mu_{\text{sat}} \quad \text{if } \Gamma_4 \text{ (or } \Gamma_5) \text{ is the lowest state;} \quad (21)$$

$$\mu_{\text{eff}} = \sqrt{3} \mu_{\text{sat}} \quad \text{if } \Gamma_6 \text{ (or } \Gamma_7) \text{ is the lowest state;} \quad (22)$$

$$\sqrt{3/2} \mu_{\text{sat}} < \mu_{\text{eff}} < \sqrt{3} \mu_{\text{sat}} \quad \text{if } \Gamma_8 \text{ is the lowest state.} \quad (23)$$

When $T \gg$ crystal field splittings, equation (18) becomes Curie's law

$$\chi_m = g^2 J(J+1) / 3T = \mu_{\text{eff}}^2 / 3T \quad (24)$$

Therefore in the absence of exchange the susceptibility obeys Curie's law at high temperatures i.e. $1/\chi$ is a linear function of T but departures from the straight line occur as $T \rightarrow 0$, as the value of μ_{eff}^2 changes. In the case of non-magnetic ground states

the value of $1/\chi_m$ becomes constant as $T \rightarrow 0$, this constant value being determined by the temperature independent contributions from the excited states (see eq. (18)). In the rare earth compounds, where the overall crystal field splittings are ~ 200 K, a plot of $1/\chi_m$ as a function of T which only includes data taken over a small temperature interval can be misleading since it frequently appears linear with a positive or negative intercept. This intercept is often taken as an indication of the presence of an exchange interaction. However from the above discussion it is clear that it may simply be associated with temperature dependent effects due to the crystal field.

The effects of exchange interaction can be taken into account using the molecular field approximation,

$$H_{\text{ex}} = \lambda M \quad (25)$$

It is simple to show that when M is linear in H_a [13]

$$H_a / M = \chi_{\text{obs}}^{-1} = \chi_m^{-1} - 2 [(g - 1) / g] \lambda \quad (26)$$

where χ_m is given by equation (18). Thus the effect of the exchange interaction on the magnetic susceptibility is to increase (or decrease) $1/\chi_m$ by an amount independent of temperature above the ordering temperature. If χ_m satisfies eq (24) we obtain the Curie-Weiss law

$$\chi_{\text{obs}} = \mu_{\text{eff}}^2 / 3 (T - \Theta) \quad (27)$$

where

$$\Theta = (2/3) [(g - 1) / g] \lambda \mu_{\text{eff}}^2 \quad (28)$$

At low temperatures M is no longer linear in H_a but shows signs of saturation. This behaviour can be calculated using equations (16) and (17), but some simple comments are helpful. For an isolated crystal field state the saturation moment is seen, from equations (21), (22) and (23), to be independent of the direction of \mathbf{H} relative to the crystal axes except for Γ_8 . In the case of Γ_8 the maximum value depends on direction and varies considerably with the wave-functions. For illustration consider

Er³⁺ [14]*; the saturation moment in the three principal directions is given in table 5 (page 84) for the three Γ_8 states, for a fourth-degree field only. It will be noticed that the maximum value occurs in either the $\langle 100 \rangle$ or the $\langle 111 \rangle$ direction in agreement with the predictions of Trammel [15]. Trammel has shown that if only fourth-order fields are present the easy axis depends on the sign of the anisotropy and can be in either the $\langle 100 \rangle$ or $\langle 111 \rangle$ direction. Sixth-order fields have to be present if the $\langle 110 \rangle$ is the easy direction.

In phases where crystal state splittings are small it is important to consider the mixing of the crystal field states by a magnetic field. For example separation of the first excited state in ErPd₃ is only 2 K from the ground state and energy changes of this magnitude are readily achieved in rare earth phases since a field of 10⁴ Oe lowers the energy of a state of magnetic moment $1 \mu_B$ by 0.675 K. Thus it is possible to have not only strong mixing produced between the states but also actual crossing-over of states. Bleaney [13] in his pioneer paper in this area produced quantitative results for some simple situations such as T = 0 K and field mixing of only the two lowest states. He showed that the maximum possible moment at T = 0 K for the mixed state with **H** in the z direction is given by

$$\mu_{\text{sat}} (\text{max}) = (1/2) g \mu_B \{ a + b + [(a-b)^2 + 4c^2]^{1/2} \} \quad (29)$$

where $a = \langle \psi_0 | J_z | \psi_0 \rangle$, $b = \langle \psi_1 | J_z | \psi_1 \rangle$, $c = \langle \psi_1 | J_z | \psi_0 \rangle$.

As an example, equation (29) is very useful in considering the maximum effect of an excited state on a non-magnetic ground state.

Finally although we have not made measurements of heat capacity in an applied field the results obtained in zero field are affected by the exchange field. This will produce a large magnetic contribution to the heat capacity at the ordering temperature which will take the typical λ - form.

(*) Many of the results of this paper given in their table 2 need correcting as a spectroscopic stability check will indicate.

The additional heat capacity is associated with a change in separation and loss of degeneracy in the crystal field states. The detailed behaviour depends on the approximation used for describing the exchange interaction and will not be calculated in this paper. However if the ground state has a degeneracy g_0 there will be an associated entropy change

$$\Delta S / R = \ln g_0 \quad (30)$$

4 — HEAT CAPACITY RESULTS *

4.1. LaPd₃

The heat capacity of a 9.454 g sample of LaPd₃ (MW = 458.1) was measured from 1.6 to 6.9 K and the results are given in figure 2 where C_V/RT is plotted versus T^2 . It can be seen imme-

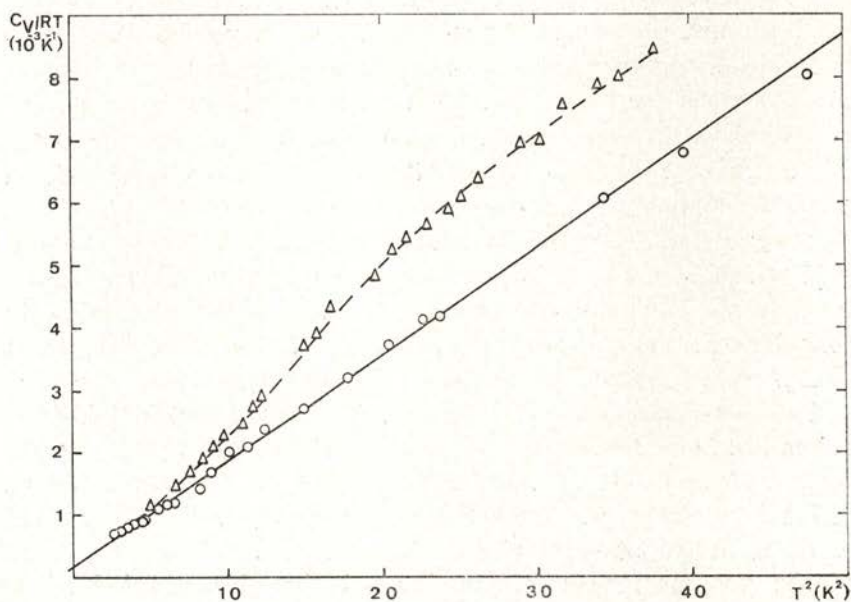


Fig. 2 — Heat capacity/g molecule of LaPd₃: o — this investigation; Δ — Hutchens et al. [4]

(*) A previous account of the heat capacity results has been published in [16], [17].

diately that the data are described by equation (1) with $\gamma = 0.33 \pm 0.02$ mJ/(K². g atom) and $\Theta_D = 171 \pm 1$ K. Hutchens *et al* [18] have also measured the heat capacity of a LaPd₃ sample, and their data are also plotted in figure 2. The agreement between the two sets of data is rather poor although there is coincidence at about 2 K. It is physically impossible to describe the data of Hutchens *et al* [4] by equation (1) since such a fit for the lowest temperature results would lead to a negative value for γ . Hutchens *et al* [4] overcome this difficulty by the introduction into the specific heat of a contribution from a postulated conduction electron spin fluctuation interaction [19]. The possibility of such a contribution will be considered in the discussion of the results.

4.2. PrPd₃

The heat capacity of a 17.975 g sample of PrPd₃ (MW = 460.1) has been measured from 0.35 to 10.7 K and the results* are given in figure 3, together with the heat capacity of LaPd₃. There are three obvious features: (i) a λ - type maximum with $C_v/R \sim 0.7$ at 0.6 K which suggests the occurrence of magnetic ordering, (ii) a broad maximum at 2 K with $C_v/R \sim 0.3$ which is a Schottky anomaly from the two 4f electrons of Pr³⁺, (iii) the crossing of the heat capacity curves of LaPd₃ and PrPd₃ at about 9 K which indicates a larger Debye temperature for the latter. In order to calculate the observed behaviour we have first to consider the crystal field states of Pr³⁺. The *ab initio* point charge model predicts a predominant fourth-degree field (table 1) and the energies of the 4 states involved are given in table 2a, column 3. Note firstly that the ground state is a triplet state Γ_5 with a doublet state Γ_3 at 51 K. If such a configuration existed in PrPd₃ it would produce a Schottky anomaly with a maximum of C_v/K of 0.3 at ~ 22 K (see figure 1) *i.e.* outside the range of the present measurements. Instead the observed behaviour suggests that the separation of the two lowest states is ~ 5 K, rather than 51 K, and that the threefold degeneracy of the Γ_5

(*) In order to plot the results for PrPd₃ a correction was required since the magnetic measurements (Section 5.1) showed that the sample only contained $22.0 \pm 0.5\%$ Pr.

TABLE 1

	a (Å)	$\langle r^4 \rangle$ (a.u.) ⁴	$\langle r^6 \rangle$ (a.u.) ⁶	x	W (K)	$A_4 \langle r^4 \rangle$ (K)	$A_6 \langle r^6 \rangle$ (K)
Pr	4.129	2.822	15.726	-0.983	-1.81	-40.5	-0.40
Tb	4.068	1.419	5.688	-0.992	0.162	-21.9	-0.16
Er	4.045	1.126	3.978	0.935	-0.051	-17.9	-0.12
Yb	4.027	0.960	3.104	-0.909	-1.64	-15.6	-0.09
Nd	4.118	2.401	12.396	0.952	0.6407	-34.9	-0.32
Dy	4.061	1.322	5.102	-0.972	-0.0753	-20.6	-0.15
Ho	4.054	1.224*	4.540*	0.9429	0.0406	-19.2	-0.13
Tm	4.039	1.043*	3.541*	-0.9735	0.1721	-17.1	-0.11

* Interpolated values.

TABLE 2 (a) — The energies of the crystal field states of Pr^{3+} derived from the ground level 3H_4

State	Degeneracy	Calculated Energy (K) Schemes		
		(i) Point charge model	(ii) Best experimental fit	(iii) A possible fit
Γ_5	3	0	0	1.52
Γ_3	2	51	5.0	0
Γ_4	3	71	100	4.02
Γ_1	1	98	(233)	12.54

state is removed at 0.6 K. However it is possible to fit the peak value at 0.6 K with a Schottky contribution assuming a 2-fold degenerate ground state and 3-fold level at 1.50 K (see figure 1). However using eq. (9) and the energy levels of column 5 table 2a it can be seen (figure 3) that the overall contribution between 0.6 and 3 K is much too large when a fit to the broad maximum at 2 K is also attempted. Thus the λ - type maximum is undoubtedly associated with a magnetic transition in which the degeneracy of the ground state is removed.

This broad interpretation is unaffected by estimates of the lattice and electronic specific heats but in order to obtain a

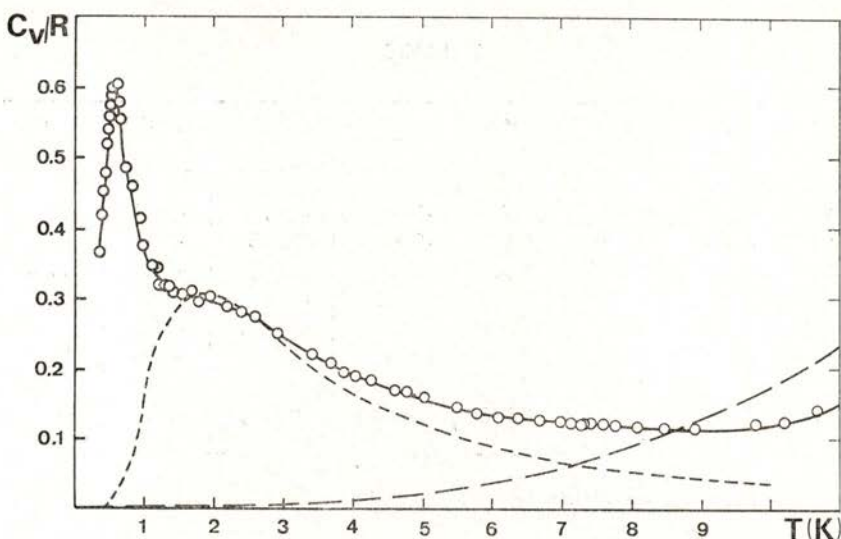


Fig. 3 — Heat capacity/g molecule of PrPd_3 as a function of temperature: o experimental results; ---- theoretical curve for energy scheme (ii) of table 2a; — LaPd_3 .

detailed fit above 4 K these terms must be considered. If we ignored their contribution entirely a second excited state at ~ 60 K would fit the observed value at 10.5 K which therefore sets a lower limit on the energy of this state. Now the lattice and the electronic contributions are represented by equation (1) and we anticipated that since the two compounds LaPd_3 and PrPd_3 have similar metallic lattices and, probably, similar melting points, the lattice (from the Lindemann equation) and conduction electron terms of PrPd_3 would be very similar to those of LaPd_3 (given in 4.1). The results above 9 K (figure 3) show that this is clearly untrue and we have assumed instead that although the electronic contribution is unchanged and given by equation (1) the lattice contribution is halved. The specific heat at 10.5 K can now be fitted with a second excited state ~ 100 K. The calculated curve which gives the best experimental fit to the overall data is shown in figure 3. It is derived from equation (9) using the energy levels of column 4, table 2a. The fit is sensitive to the choice of energy of Γ_3 and acceptable fits are obtained for $\Gamma_3 = 5.0 \pm 0.5$ K, $\Gamma_4 = 100 \pm 10$ K. When

$\Gamma_3 = 5.5$ K the theoretical curve slightly exceeds the experimental points above about 3 K. Our choice of 5.0 K permits the possibility of a short range contribution up to about 9 K. In fact the error in Γ_3 (± 0.5 K) mainly lies in trying to estimate this contribution whereas the error in Γ_4 (± 10 K) lies in the assumption made about the lattice specific heat. Further light on the interpretation can be made by considering the entropy variation up to 10.7 K. The observed entropy variation between 0.35 and 10.7 K is $S/R = 1.142 \pm 0.020$.

The calculated entropy variation associated with the best theoretical fit is 0.523 ± 0.010 . The difference represents the magnetic contribution above 0.35 K. In order to calculate the total magnetic contribution it is necessary to estimate the entropy change below 0.35 K. The temperature dependence of the heat capacity is unknown but the entropy at 0.35 K is 0.139 for a T^3 dependence and 0.415 for a T dependence. We will take 0.27 ± 0.1 as a reasonable estimate and therefore the total entropy change associated with the magnetic ordering up to 11 K is 0.89 ± 0.1 .

This magnetic entropy is significantly smaller than $\ln 3$ (1.099) even though the temperature interval considered should have included most of the contribution from short range ordering above the ordering temperature [20]. This discrepancy could be explained if the praseodymium content was 16.5% instead of 22% but this difference far exceeds experimental error. We believe that the discrepancy occurs because the magnetic ordering commencing at 0.6 K is incomplete. The lack of entropy does not indicate, as discussed above, that the anomaly is a non-magnetic one.

The energy values deduced above to fit the specific heat data can be used to determine the fourth and sixth degree terms. An examination of the diagram of energy states (figure 4 (a) LLW) for Pr^{3+} shows that Γ_5 and Γ_3 cross at $x \sim -0.74$. The observed energy values show that x has to be less than but close to this value. In fact knowing the energy (and degeneracies) of the first two excited states with respect to the ground state, W and x (or $A_4 \langle r^4 \rangle$ and $A_6 \langle r^6 \rangle$, or Z_1 and Z_2) can be determined immediately from the solution of two simple simultaneous equations. The results are given in table 2b. It can be seen that the simple point charge model estimate of

TABLE 2 (b) — The parameters associated with the crystal field states of Pr³⁺

	x	w	A ₄ <r ⁴ > (K)	A ₆ <r ⁶ > (K)	Z ₁	Z ₂
(i)	-0.983	-1.81	-40.5	-0.40	0	3
(ii)	-0.747	-4.20	-71.1	-13.8	-2.92	-2.99
(iii)	-0.645	-0.145	-2.12	-0.66	-0.147	-0.259

both crystal field terms was low and that in particular the sixth degree term is large and significant in PrPd₃, being about 20 % of the fourth degree term. The values obtained for Z₁ and Z₂ do not appear to have a simple explanation. In conclusion, this analysis of the heat capacity results of PrPd₃ has produced the crystal field parameters A₄ <r⁴> = - 71 ± 10 K and A₆ <r⁶> = - 14 ± 2 K, where the errors correspond to the limit of acceptable fits. The errors are primarily associated with the uncertainty in the lattice contribution and if the data had been taken to 20 K the above errors would have been reduced considerably, and become comparable to those obtained using neutron scattering techniques [21]. Thus we are able to refute the conclusion [21] that «only direct spectroscopic measurements can yield parameters of sufficient accuracy to be of any use in evaluating models for the microscopic origins of crystal fields in metals». In fact the proper conclusion is that the determination of crystal field parameters of sufficient accuracy depends on whether the energy levels that are affecting the observations are associated with a wide or narrow range of crystal field values. It seems evident that, since the variation of the energy levels of the various rare earths as a function of the two crystal field parameters is somewhat complicated, broad sweeping conclusions of the above kind are always liable to be wrong.

4.3. TbPd₃

The heat capacity of a 5.207 g sample of TbPd₃ (MW = 478.1) has been measured from 2.1 to 8.6 K and the results (*) are given in

(*) The alloy composition was checked using standard chemical techniques and agreed (± 0.48 %) with the nominal composition.

figure 4 where C_v/R is plotted versus temperature. The results have been plotted on two scales, which differ by a factor of 10, in order to show the features fully. The heat capacity shows a typical λ -anomaly with a maximum value of C_v/R of ~ 7.0 at

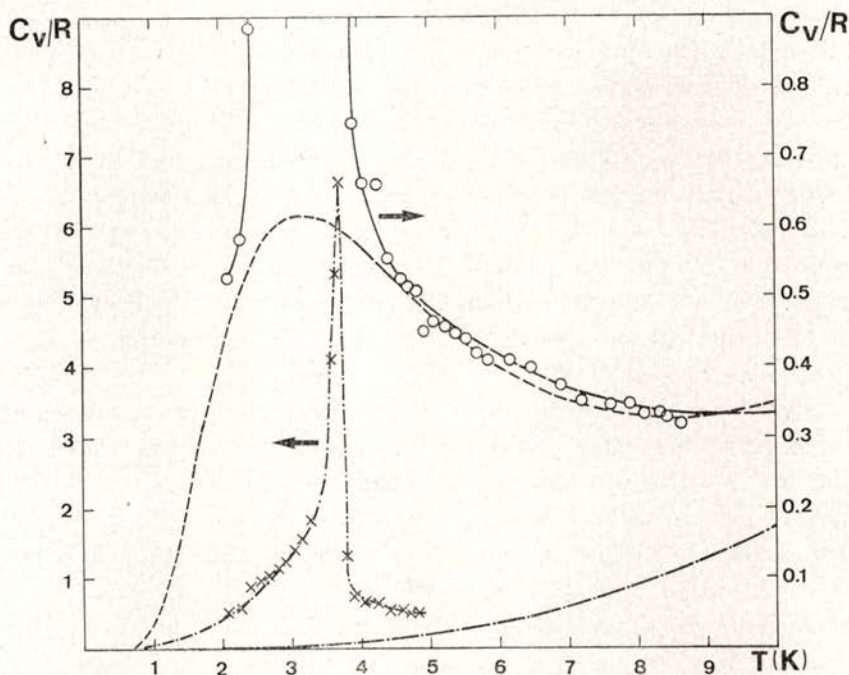


Fig. 4 — Heat capacity/g molecule of $TbPd_3$ as a function of temperature. The dashed curves in the figure (except that of $LaPd_3$) represent theoretical fits: — · — a T^3 curve fitted at 2.5 K; - - - 0,8,60 + lattice heat capacity of $LaPd_3$; — — — 0,8,33 + lattice heat capacity deduced for $PrPd_3$; — · — the heat capacity of $LaPd_3$. The ordering temperature is 3.75 K

a temperature of 3.75 K indicating that magnetic ordering occurs at this temperature. In addition, the heat capacity up to 8.6 K is always greater than that of $LaPd_3$ (figure 4) indicating either that above 3.75 K there is a continuing contribution from the magnetic interaction or that there is a crystal field contribution also occurring. If the latter situation applies to $TbPd_3$, then, unlike $PrPd_3$, where the magnetic and Schottky anomalies were almost resolved, in $TbPd_3$ there is considerable overlap. Despite this

greater complexity a consideration of the entropy as a function of temperature, the heat capacity above the λ -point and the predictions of the point charge model lead to a reasonable interpretation of the data.

As a consequence of experimental difficulties during the measurement of TbPd₃, the heat capacity results commence at 2.1 K and thus an estimate of the entropy below this temperature is necessary. This has been obtained by assuming no further anomalies occur below the λ -point and that the heat capacity below 2.5 obeys a T^3 law. We believe that the error involved in these assumptions is small and is $\Delta (S/R) \sim \pm 0.05$. The calculated entropy at the ordering temperature (3.75 K) is 1.10 ± 0.10 and the values obtained between 4 and 9 K are given in table 3a. It is immediately evident that the entropy at the ordering temperature is close to $\ln 3$ (1.099) and at 9 K lies between $\ln 4$ (1.386) and $\ln 5$ (1.609).

We have not attempted to fit the heat capacity data below the λ -point but have considered its behaviour between 4.5 K and 8.6 K. The *ab initio* point charge model ($Z_1 = 0$, $Z_2 = 3$) predicts, as in PrPd₃, a predominant fourth degree term (table 1). The resulting energies of the 6 crystal field states obtained from the 7F_6 ground level of Tb³⁺ are given in table 3b, column 5. The predicted ground state is the non-magnetic doublet Γ_3 with a triplet state $\Gamma_5^{(1)}$ at 1.9 K and a singlet state Γ_2 at 7.9 K. The calculated heat capacity from such a configuration bears no resemblance either to the entropy or the heat capacity data above 4.5 K. We have therefore calculated the change in heat

TABLE 3 (a) — The entropy S/R of TbPd₃

T(K)	Observed	Observed—ln2	(i)	(ii)
4	1.15 ± 0.10	0.45 ± 0.10	0.527	0.526
5	1.28	0.58	0.645	0.644
6	1.36	0.66	0.725	0.727
7	1.42	0.73	0.782	0.787
8	1.47	0.77	0.827	0.835
9	1.50	0.81	0.866	0.874

TABLE 3 (b) — The energies of the crystal field states of Tb³⁺, ground level ⁷F₆

State	Degeneracy	Observed Energy (K)		Calculated Energy (K)
		(i)	(ii)	(iii)
Γ ₃	2	0	0	0
Γ ₅ ⁽¹⁾	3	8	8	1.9
Γ ₂	1	60	33	7.9
Γ ₅ ⁽²⁾	3	—	(116)	27.5
Γ ₄	3	—	(139)	32.9
Γ ₁	1	—	(159)	37.6

capacity associated with these 3 states upon varying their separation and order. We find that the heat capacity results are sensitive both to the separation and order of the two lowest states and that, irrespective of any assumptions about the lattice specific heat, a good fit is possible only if the ground state is Γ₃ and the energy of Γ₅⁽¹⁾ is 8.0 ± 0.5 K. On the other hand, the calculated energy of the Γ₂ state does depend on the choice made for the lattice heat capacity. If we assume that this is the same as LaPd₃ a good fit to experimental values is obtained (see figure 4) if the energy of Γ₂ is 60 ± 10 K, whereas if the lattice heat capacity adopted for PrPd₃ is assumed an equally good fit can be achieved (see figure 4) if the energy of Γ₂ is 33 ± 5 K.

The entropy values have also been calculated for these two cases and are given in table 3a. These values have to be compared with the observed values less the magnetic entropy associated with the Γ₃ ground state (ln 2) which are also given in table 3a. The agreement is good and in fact improves when the separation of Γ₃ and Γ₅⁽¹⁾ is taken as 8.5 K. We think that, in spite of the assumptions necessary to compare calculation with experiment, the results show clearly that the ground state cannot be Γ₅⁽¹⁾, with short range order contributions above the ordering temperature, nor could we find a satisfactory configuration of states that would produce a reasonable fit with this ground state. Instead our analysis shows that the ground state

is Γ_3 and that if we ignore short range order effects above the ordering temperatures, then the first excited state is $\Gamma_5^{(1)}$ at 8 K and that the second excited state Γ_2 lies at 33 K or 60 K (or perhaps an intermediate value) depending on the magnitude of the lattice heat capacity. These energy values deduced to fit the heat capacity data can be used to determine the fourth- and sixth-degree terms. An examination of the energy diagram for TbPd₃ (figure 6b in Lea, Leask and Wolf [10]) shows that the separation of Γ_3 and $\Gamma_5^{(1)}$ only varies slightly between $x = -1$ and -0.7 and that these states cross at $x \sim -0.5$, whereas the energy separation of Γ_2 and Γ_3 varies linearly with x . Consequently, we can fit a second excited state at ~ 33 K with a value of x close to -1.0 , whereas if Γ_2 is at 60 K a value of $x \sim -0.75$ is required; the corresponding values of the crystal field parameters, W and Z_1

TABLE 3 (c)

	x	W	$A_4 \langle r^4 \rangle$	$A_6 \langle r^6 \rangle$	Z_1	Z_2
(i)	-0.75	0.582	-59.5	-18.0	-9.58	-18.95
(ii)	-0.99	0.682	-92.0	-0.84	-0.09	12.3
(iii)	-0.992	0.162	-21.9	-0.160	0	3

- (i) lattice heat capacity based on the LaPd₃ results, energy states 0,8,60.
 (ii) lattice heat capacity based on the PrPd₃ results, energy states 0,8,33.

and Z_2 are given in table 3c. For energy scheme (ii) we allowed x to take the point charge value and the calculated value of W is roughly 4 times greater than the point charge value. Energy scheme (i) involves a large sixth degree term and the values of $A_4 \langle r^4 \rangle$ and $A_6 \langle r^6 \rangle$ are very similar to those obtained for PrPd₃ (table 2b). The two proposed energy schemes correspond to very different values of x namely $x = -0.99$ and -0.75 . The corresponding crystal field parameters, W and Z_1 and Z_2 are given in table 3c. Inelastic neutron scattering results on TbPd₃ [22] exhibit a transition peak at ~ 6 meV. This might well suggest that the energy of Γ_2 is indeed ~ 60 K.

Finally, the effects of the exchange energy on the crystal field states should be considered. The observed entropy at the ordering temperature is close to $\ln 3$ and our analysis has shown that this corresponds to the removal of the twofold degeneracy of the Γ_3 state and the depopulation of the excited states below 3.75 K. We have also obtained good agreement above 3.8 K by assuming that the short range ordering is small and this is perhaps not surprising since the magnetism of the Γ_3 ground state depends on the presence of an exchange field which, at least in the molecular field model disappears at the ordering temperature. In order to determine the effect of an exchange field we have calculated energies of the crystal field states as a function of magnetic field and have found that the Γ_3 and $\Gamma_5^{(1)}$ states do not cross for fields up to 200 kOe. Second order perturbation theory shows that Γ_3 magnetizes in second order because of the different mixing terms in the $\langle 100 \rangle$ direction, so that the state which mixes with $\Gamma_5^{(1)}$ falls faster than the state mixing with Γ_4 . However in the $\langle 111 \rangle$ direction the degeneracy of the Γ_3 state is not removed in second order and therefore it seems likely [15] that ordering will occur in the $\langle 100 \rangle$ direction. Thus TbPd_3 is an example of a system which orders in a non-magnetic ground state by exchange induced mixing with higher states.

4.4. ErPd_3

The heat capacity of a 1.700 g sample of ErPd_3 ($MW = 486.46$) has been measured from 0.2 to 0.9 K and the results are shown in figure 5 where C_v/R is plotted as a function of temperature. Unfortunately, the experimental results are over a brief temperature interval and therefore the analysis we can carry out is somewhat restricted. However a Schottky anomaly with a maximum at about 0.75 K with $C_v/R \sim 0.74$ is clearly visible and it is evident that magnetic ordering does not occur in ErPd_3 above 0.2 K.

ErPd_3 is a system in which magnetic interactions are clearly unimportant and therefore we would anticipate good agreement between the observed data and calculations based on the crystal field energy states. Agreement should be particularly good below

1 K since there is an almost negligible contribution from the lattice and electronic terms.

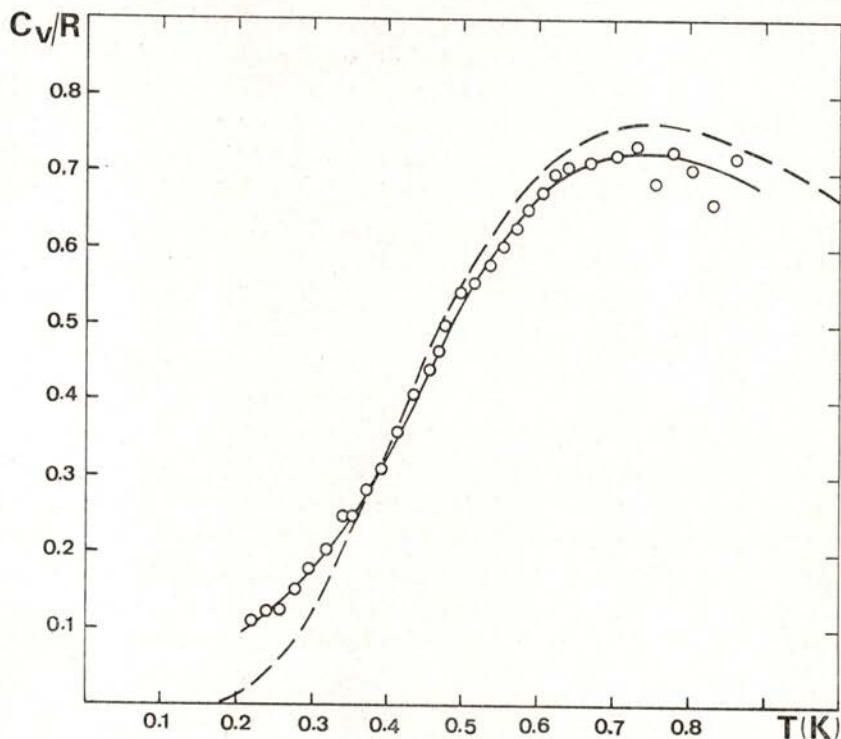


Fig. 5 — Heat capacity / g molecule of ErPd_3 as a function of temperature. The dashed curve is derived from equation (8) using $g_1 / g_0 = 2$ and $E_1 = 2.0$ K.

In the case of Er^{3+} the ground level is $^4J_{15/2}$ and the ab initio point charge model predicts that this level will split into 5 states with the degeneracies and energies given in table 4a. Thus the ground state is the magnetic doublet Γ_6 with the four-fold degenerate $\Gamma_8^{(3)}$ state at 0.7 K, and the two-fold degenerate state Γ_7 at 14.1 K. The specific heat data only gives information about the two lowest states. From figure 1 using $g_1/g_0 = 2$ we anticipate that $C_m/R = 0.76$ and $E_1/T_m = 2.66$. Since $T_m = 0.75$ K this corresponds to the $\Gamma_8^{(3)}$ state at 2.0 K. The calculated curve for this energy separation is shown in figure 5 and the agreement is reasonable. The extra specific heat below 0.4 K is probably

TABLE 4 (a) — The energies of the crystal field states of Er^{3+}

State	Degeneracy	Observed Energy (K)	Calculated Energy (K)				
			(i)	(ii)	(iii)	(iv)	(v)
Γ_6	2	0	0	0	0	0	0
$\Gamma_8^{(3)}$	4	2	0.7	2.0	2.0	2.0	2.0
Γ_7	2		14.1	34.4	59.9	23.0	33.4
$\Gamma_8^{(2)}$	4		17.8	44.7	72.9	31.4	43.0
$\Gamma_8^{(1)}$	4		22.7	58.0	93.2	39.8	54.8

ground level $^4J_{15/2}$ $x = 0.935$ $W = -0.051$ K

due to short range order effects suggesting that ordering occurs below 0.2 K. The observed specific heat at 0.7-0.9 K is somewhat lower than theory but the difference may well be experimental since the results obtained showed considerable scatter. Unfortunately the data are insufficient to enable us to determine the energy of the Γ_7 state. However the results clearly show that $x \sim 0.85$ since below this value the states $\Gamma_8^{(3)}$ and Γ_6 cross [10]. Such a crossing has not occurred since the value of C_m/R would have been only 0.26 (see figure 1) for $g_1/g_0 = 0.5$.

Since the separation of Γ_6 and $\Gamma_8^{(3)}$ is 2.0 K for a given value of x between 1.0 and 0.85 the corresponding value of W can be calculated using the variation of energy of these states given by LLW. The corresponding values of $A_4 \langle r^4 \rangle$ and $A_6 \langle r^6 \rangle$

TABLE 4 (b)

	x	W	$A_4 \langle r^4 \rangle$	$A_6 \langle r^6 \rangle$
(i) *	0.935	-0.051	-17.9	-0.12
(ii)	0.935	-0.121	-42.5	-0.27
(iii)	0.90	-0.190	-64.2	-0.662
(iv)	1.0	-0.072	-27.2	0
(v)	0.95	-0.105	-37.4	-0.182

* point charge model.

can then be determined from eqs (7) and (8). In table 4b these pairs of values are given for $x = 1.0, 0.95, 0.935$ and 0.90 . The effect of decreasing x is to increase the separation of the higher levels and the total splitting changes from $E = 40$ K for $x = 1.0$ to $E = 93$ K for $x = 0.90$.

5 — MAGNETIZATION RESULTS

5.1. *PrPd₃*

The magnetization of a 68.1 sphere of *PrPd₃* has been measured from 1.2 to 50 K in magnetic fields varying from 2 to 42 kOe. The inverse of the observed magnetic susceptibility as a function of temperature is shown in figure 6. The results lie on a curve which does not pass through the origin and suggest the presence of an antiferromagnetic interaction.

The ground level of *PrPd₃* is 3H_4 . Specific heat measurements (4.2) have shown that crystal field effects are important, that the ground state is Γ_8 and the first excited state is Γ_3 at 5.0 K and that *PrPd₃* orders magnetically at 0.6 K. Using the crystal field parameters of table 2b line (ii) the magnetic susceptibility has been calculated using eq (18) and its inverse is shown as a function of temperature in figure 6. For comparison purposes the free ion behaviour of the ground level is also shown. The difference between the observed behaviour and calculated behaviour is due to the exchange interaction present which should produce a displacement independent of T (eq (2)). Such behaviour is not observed experimentally as shown in the plot (figure 6)

TABLE 5 — The saturation moment (μ_B) in the three principal directions for isolated Γ_8 states of Er^{3+} in a fourth-degree crystal field

State	$\langle 100 \rangle$	$\langle 110 \rangle$	$\langle 111 \rangle$
$\Gamma_8(1)$	5.50	6.23	6.40
$\Gamma_8(2)$	4.78	4.92	4.96
$\Gamma_8(3)$	5.67	5.13	4.84

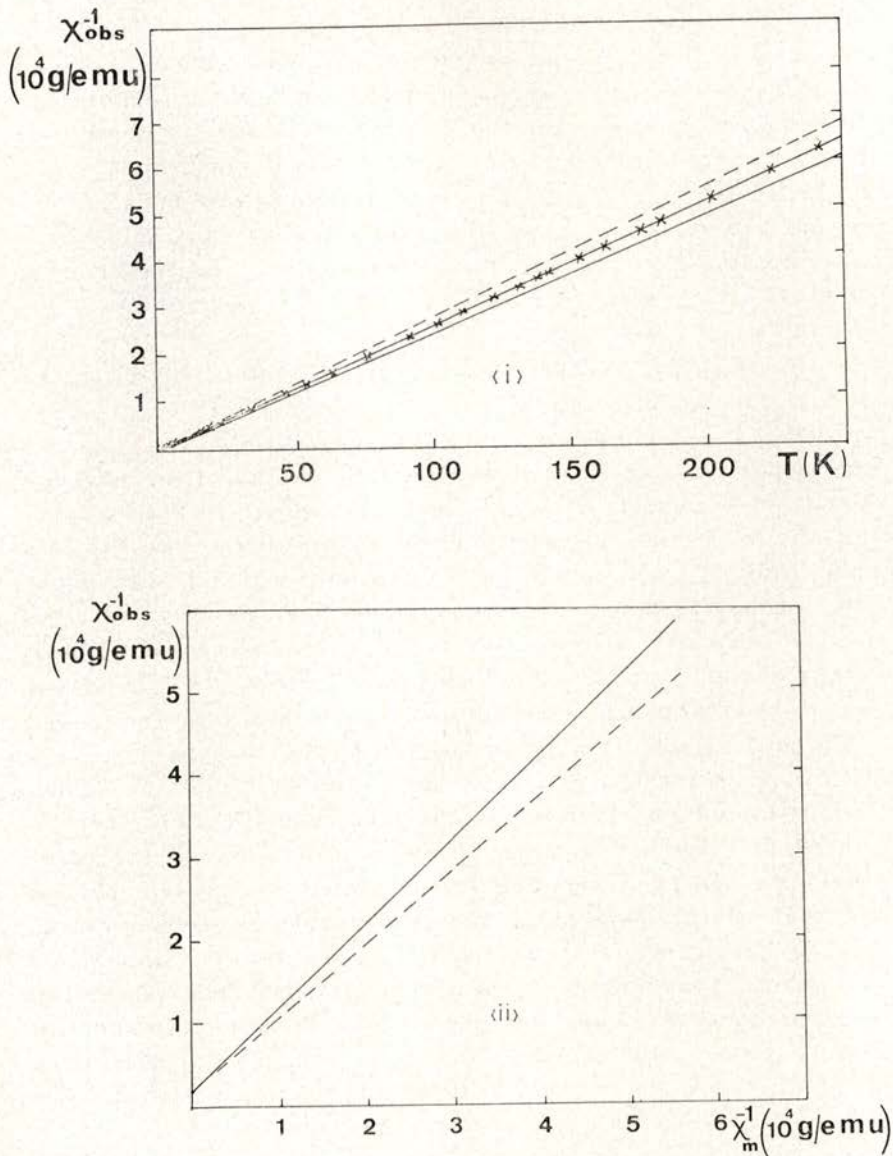


Fig. 6 — (i) The inverse magnetic susceptibility of PrPd_3 as a function of temperature: x observed results; — — free ion behaviour; — crystal field behaviour. (ii) The inverse magnetic susceptibility of PrPd_3 , χ_{obs}^{-1} as a function of the calculated value χ_m^{-1} : — observed results; — — slope for 25% Pr^{3+} ions / mole.

of the inverse of the observed susceptibility $(\chi_{\text{obs}})^{-1}$ as a function of the inverse of the calculated susceptibility $(\chi_{\text{m}})^{-1}$: If the sample contained 25 % of praseodymium the observed points would lie on the interrupted line instead of the line drawn through them. It is simple to show that the ratio of the slopes of these two lines gives the actual praseodymium content of the sample which is 22.0 ± 0.5 %. The specific heat results given in 4.2 were normalized to 25 % using this value as are the subsequent magnetization results. In addition the value of λ can be deduced from figure 6 using eq (26) and $g = 0.8$; we find $\lambda = 9.0$ g mole/emu.

The magnetic moment/Pr atom, obtained after correcting the results for the diamagnetism of the matrix (-0.15 emu/g [2]), of PrPd₃ at 4.2 and 1.2 K is shown in figure 7 as a function of the applied magnetic field H_a , ie the external field less the demagnetizing field. It can be seen that up to 42 kOe at both 1.2 and 4.2 K the magnetic moment varies almost linearly with field, and shows none of the saturation behaviour that might have been anticipated. The theoretical behaviour of the magnetization calculated as indicated in 3.2 using the best fit crystal field parameters of table 2b is shown in figure 7 at 4.2 and 1.2 K for the three principal crystal directions and their average, derived from equation (16). The ground state of PrPd₃ is Γ_5 which has a saturation moment of $2\mu_B$ in isolation. In the $\langle 100 \rangle$ direction this is approximately true in PrPd₃ (see figure 7) since there is no mixing with the Γ_3 state. However the mixing in the other directions causes a significant dependence of the moment on direction above about $1\mu_B$. This effect is unimportant in the analysis of our magnetization data since our results, summarised in table 6, are limited to moments less than this value. The discrepancy between the theoretical curves and the experimental results is due to the exchange field which can be evaluated from eq. (15). Using the molecular field approximation and eq (25), values of λ of 10.00 and 11.6 g atom/emu at 4.2 and 1.2 K respectively have been deduced from the data in figure 7. These values are significantly greater than the value deduced from the susceptibility results and suggest that a breakdown of the molecular field approximation occurs as the ordering temperature of 0.6 K is approached. If we use eq. (28) to determine Θ from these values of λ we obtain $\Theta \sim -5$ K, so that Θ is an order of magnitude

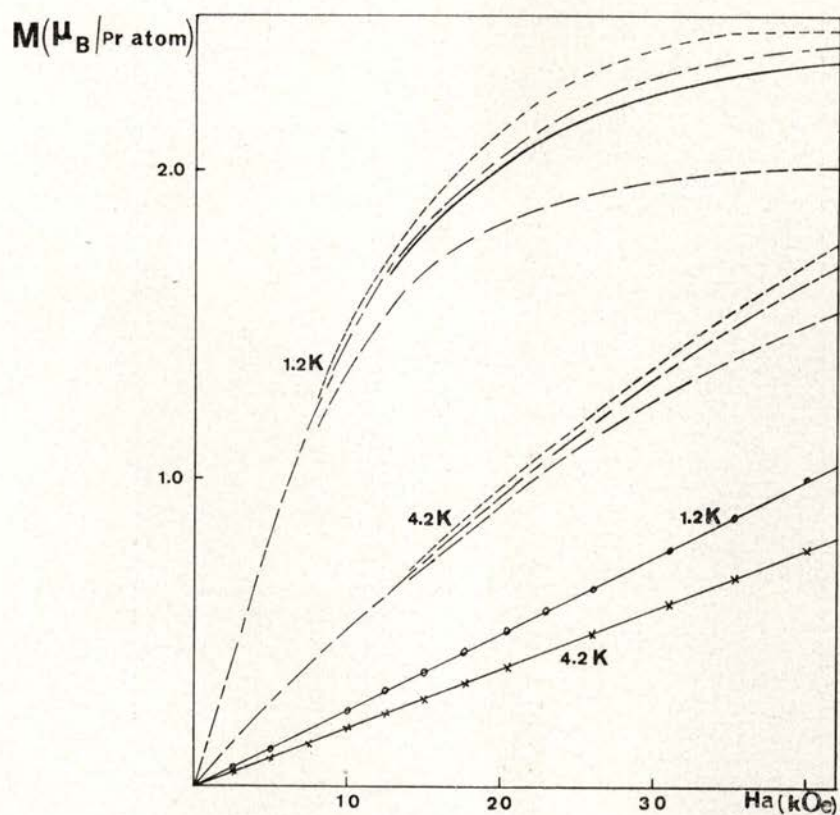


Fig. 7 — The magnetic moment / Pr atom (μ_B) of PrPd_3 as a function of applied field, H_a : x (4.2 K), o (1.2 K). The calculated values of M_{100} (—); M_{110} (- - -); M_{111} (- · -) and M_p (—) at 4.2 K and 1.2 K are also shown. At 4.2 K M_p (not represented) virtually coincides with M_{110} .

greater than the ordering temperature. It is possible to account for such a ratio using molecular field arguments. If the ordering was type 1, ie antiferromagnetic chains, the nearest neighbour interaction would be ~ 0.36 K and the nnn interaction ~ 0.13 K whereas if the ordering was type 3 ie ferromagnetic planes, both interactions would be ~ 0.21 K. Type 2 ordering is excluded.

A previous sample of PrPd_3 [2] containing more than 25 % Pr, since its μ_{eff} above 50 K was greater than the free ion value, was observed to have a value of $\theta = 0$ K. This suggests that the

TABLE 6

Compound	Ground State	μ_{eff} (μ_B)	μ_{sat} (μ_B)	Excited State	μ_{eff} (μ_B)	μ_{sat} (μ_B)	Energy of excited state (K)	Compound ground state max ^m μ_{sat} (μ_B)	Free ion		Observed μ_{sat} at 38 KOe		Observed		
									μ_{eff}	μ_{sat}	4.2 K	1.2 K	μ_{eff} 4.2 K	μ_{eff} 1.2 K	Θ (K)
PrPd_3	Γ_5	2.83	2.0	Γ_3	0	0	5	2.0	3.58	3.2	0.77	0.98	2.92	2.83	-5
TbPd_3	Γ_3	0	0	$\Gamma_5^{(1)}$	1.28	0.906	8	$<100>$ 7.62 $<111>$ 5.85	9.72	9.0	6.31	6.60	13.0	5.7	0
ErPd_3	Γ_6	5.19	3.0	$\Gamma_8^{(3)}$	6.97	$<100>$ 5.67 $<111>$ 4.84	2	$<100>$ 8.97 $<111>$ 7.42	9.58	9.0	7.20	7.52	9.60	7.45	0

value of Θ for Pr-Pd alloys depends critically on the Praseodymium content in the region of 25 % Pr.

5.2. *TbPd₃*

The magnetization of a 16.3 mg sphere of *TbPd₃* has been measured from 1.2 to 10 K in applied magnetic fields varying from 2 to 42 kOe. The inverse of the observed magnetic susceptibility obtained in an applied field of 2.3 kOe as a function of temperature is shown in figure 8. An antiferromagnetic transition clearly occurs at ~ 3.5 K in good agreement with the ordering observed at 3.75 K in the heat capacity results. This transition is more clearly marked than the shallow minimum observed previously [2] in this temperature region but on a different sample. Since the Tb content of both samples is close to 25 % the magnetic behaviour below 4 K must be sensitive to the details of the preparation. The ground level of *TbPd₃* is 7F_6 . Specific heat measurements have shown (section 4.3) that in addition to the exchange interaction which produces antiferromagnetism there is a crystal field present which splits the level into the states given in table 3b. Using the crystal field parameters of table 3c and eq. (18) the magnetic susceptibility as a function of temperature has been calculated. The calculated values of $1/\chi_m$ are greater than $1/\chi_{obs}$ between 1 and 10 K but a good fit can be achieved by using eq. (26). In figure 8 the theoretical curve for crystal field parameters of table 3c line (ii) was displaced using $g = 1.5$ and $\lambda = 0.49$ g mole/emu; the equivalent high temperature Θ being 3.9 K. An equally good fit can be obtained from the crystal field parameters of table 3c line (i) with $\lambda = 0.50$ g mol/emu. Thus the large exchange displacement makes the observed values insensitive to the choice of crystal field parameters presented by the heat capacity analysis.

The magnetic moment/Tb atom, obtained after correcting the results for the diamagnetism of the matrix, at 4.2 and 1.2 K is shown in figure 9 as a function of the applied magnetic field. Although the curves show that saturation occurs the magnetization is still rising slowly above 40 kOe. The magnetization at 1.2 K exceeds that of 4.2 K above a field of 5 kOe. The value of $6.2 \mu_B$ at 40 kOe and 1.2 K lies well below the free ion value of $9 \mu_B$ and clearly reveals the effect of the crystal field.

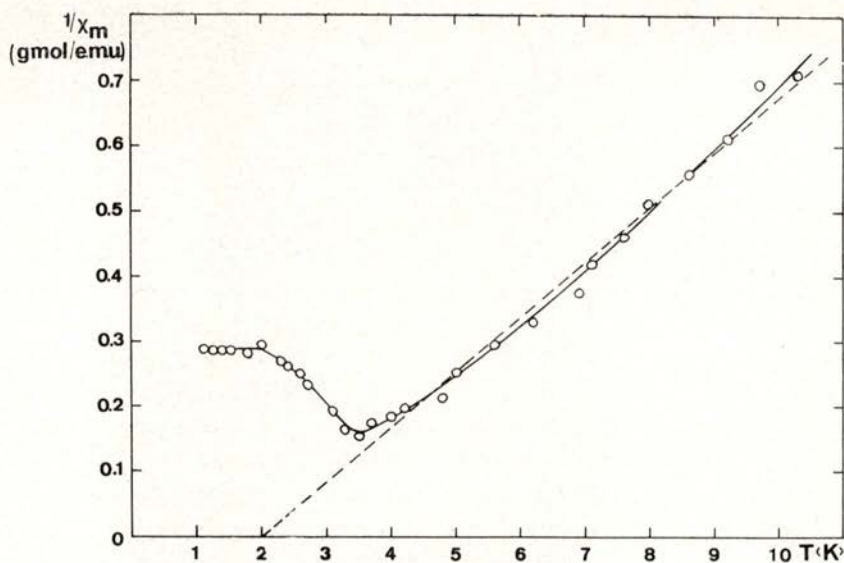


Fig. 8 — The reciprocal of the molar susceptibility (χ_m^{-1}) of TbPd_3 as a function of temperature from measurements in an applied field of 2.3 kOe; — — — free ion Curie-Weiss relation, $\Theta = 2$ K.

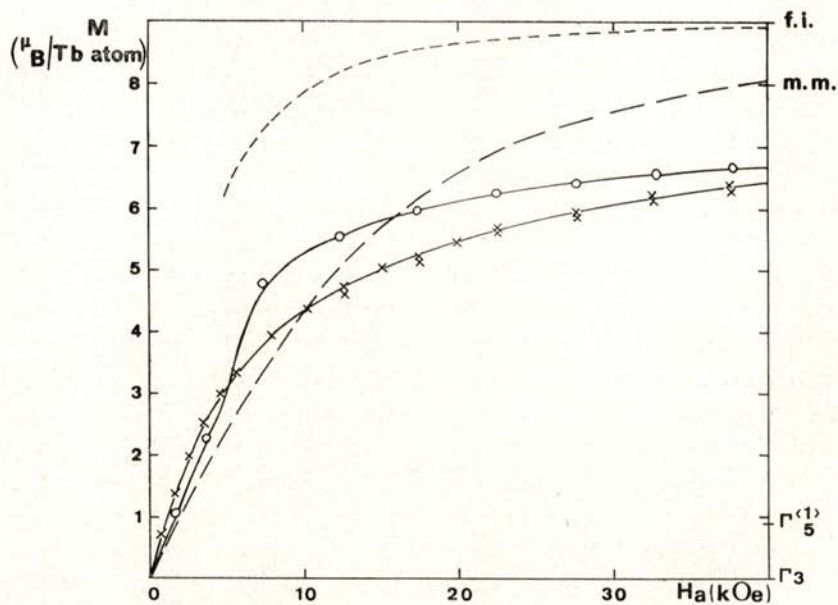


Fig. 9 — The magnetic moment/Tb atom (μ_B) as a function of effective field, H_a : \times (4.2 K); \circ (1.2 K). The curves represent the Brillouin function for $J = 6$; $g = 3/2$ at 4.2 K (—) and 1.2 K (---); f.i. = free ion, m.m. = mixed maximum (Bleaney [13]).

5.3. ErPd_3

The magnetization of a 16.9 mg sphere of ErPd_3 has been measured at 4.2 and 1.2 K in effective fields up to 38 kOe and the results are shown in figure 10.

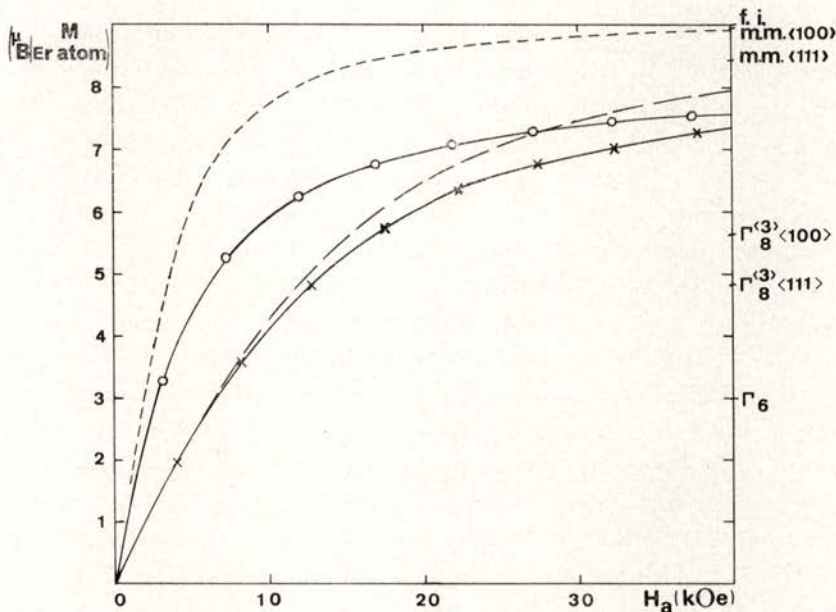


Fig. 10—The magnetic moment/Er atom as a function of effective field H_a : \times (4.2 K); o (1.2 K). The curves represent the Brillouin function for $J = 15/2$, $g = 6/5$, at 4.2 K (—) and 1.2 K (---); f.i. = free ion, m.m. = mixed maximum (Bleaney [13]).

The magnetic susceptibility of ErPd_3 closely follows Curie's law from 4 to 300 K [2] with μ_{eff} close to the free ion value; the initial slope at 4.2 K for this sample agrees with this behaviour but departure occurs at 1.2 K. For $H_a = 38$ kOe the magnetizations at 4.2 and 1.2 K fall well below the Brillouin values for the free ion. This behaviour suggests that exchange interaction effects are unimportant and the departures are associated with the crystal field. In section 4.4 the specific heat

results also showed that exchange interactions are weak and that any magnetic ordering occurs below 0.22 K. They also showed that the ground state is Γ_6 and that the first excited state $\Gamma_8^{(3)}$ is at 2.0 K. However no information was obtained about the energies of higher levels so that from the knowledge of the separation of Γ_6 and $\Gamma_8^{(3)}$ it was only possible to calculate pairs of corresponding values of x and W (or $A_4 \langle r^4 \rangle$ and $A_6 \langle r^6 \rangle$) (table 4b).

Since the overall separation increases as x decreases the magnetization in a given direction will take its maximum value for $x = 1.0$. In figure 10 only the calculated curves for $x = 1.0$ and $x = 0.90$ are shown, since the other values produce intermediate curves. It is obvious that even the smallest energy separation of the higher levels corresponding to $x = 1.0$ does not produce a large enough magnetization at either 4.2 or 1.2 K for $H_a = 38$ kOe. We cannot improve this fit by decreasing their separation further without lowering the energy separation of Γ_6 and $\Gamma_8^{(3)}$ and hence spoiling the fit to the specific heat results. Thus it is apparent that the discrepancy is a real effect. In figs 11 and 12 the separate curves of $x = 1.0$ and 0.90 for the three major crystalline directions are shown and it can be seen that there is considerable anisotropy, with the value in the $\langle 100 \rangle$ direction exceeding that in the $\langle 111 \rangle$ direction by 50% at 40 kOe. In addition the magnetization saturates most easily in the $\langle 100 \rangle$ direction but the change between 20 kOe and 40 kOe at 1.2 K for the harder directions is only $\sim 0.4 \mu_B$, compared with an observed change $\sim 0.8 \mu_B$.

Thus the discrepancy between the theoretical curves and the experiment at 38 kOe could be associated with the method used to calculate M_p . However, it cannot simply be attributed to the approximation adopted for M_p , since the theoretical curve at 4.2 K lies below the observed values at all fields whereas at 1.2 K it exceeds the observed values for fields less than 15 kOe and at both temperatures in fields over 20 kOe the observed values of M/H are greater than the calculated ones. This suggests that there may be effects due to crystalline field anisotropy and that the moments may not rotate freely at low temperatures, but may well prefer the $\langle 100 \rangle$ direction.

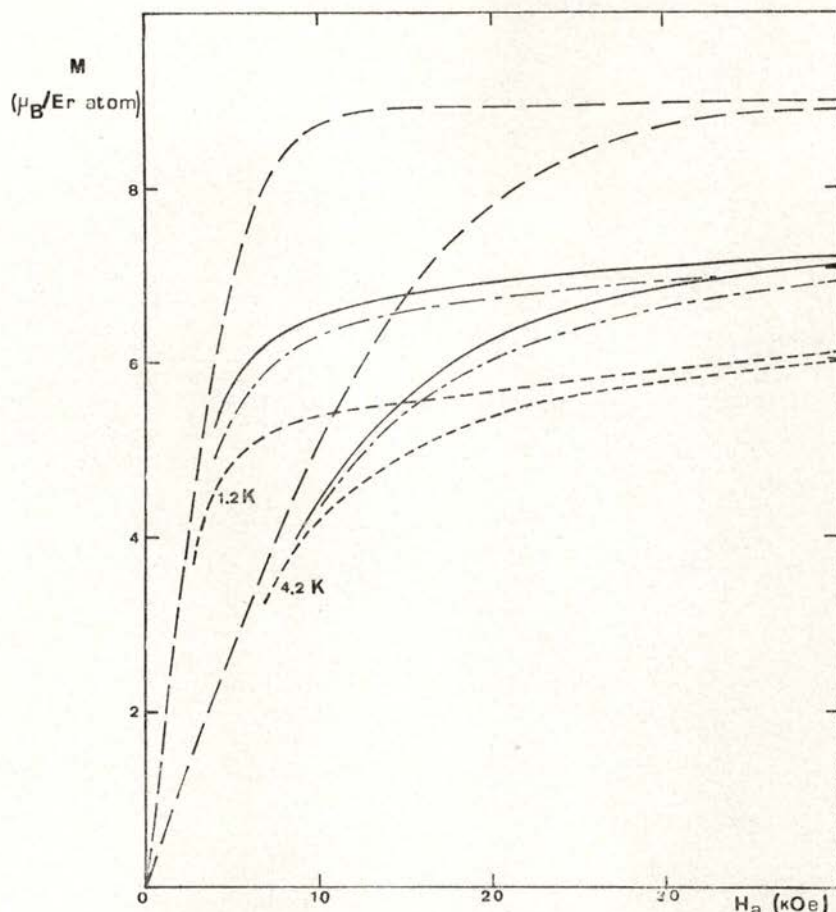


Fig. 11 — Calculated values of M_{100} (---); M_{110} (- · -); M_{111} (·····) and M_p (—) at 4.2 K and 1.2 K for ErPd_3 ; $x = 1.0$, $W = -0.072$.

Thus the magnetization results on a polycrystalline sample are unable to determine the appropriate pair of crystalline field parameters from table 4b. Clearly measurements on a single crystal of ErPd_3 are required.

6 — DISCUSSION

The magnetic susceptibility measurements of Gardner *et al* [2] showed that the exchange interaction was unimportant in several

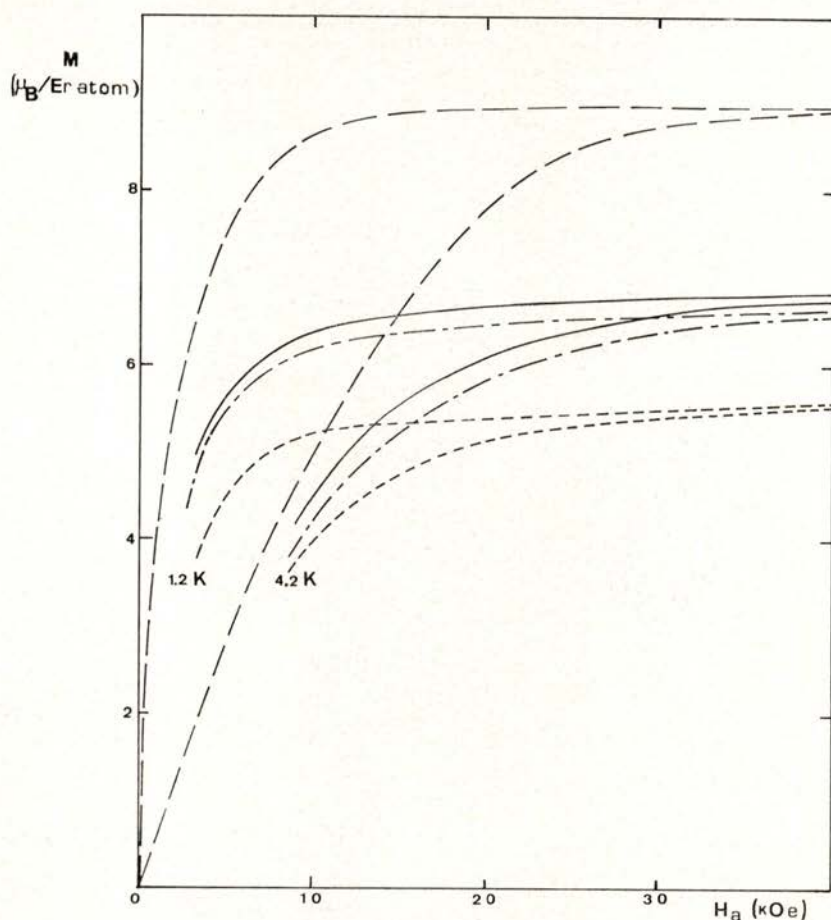


Fig. 12 — Calculated values of M_{100} (— — —); M_{110} (— · —); M_{111} (· · · · ·) and M_p (—) at 4.2 K and 1.2 K for $ErPd_3$: $x = 0.9$, $W = -0.19$.

RPd_3 phases above 1 K and that the point charge model correctly predicted the ground state if the fourth order term was assumed predominant. Electrical resistivity measurements [23] confirmed the absence of magnetic order above 1 K in many of the phases but the suggestion that $PrPd_3$ and $SmPd_3$ magnetically ordered between 3 and 5 K is incorrect and associated with impurities, as suspected by these authors.

Elliot and Hill [23] also considered the possible existence of a Kondo effect in $LaPd_3$ since they observed a weak minimum in the resistivity at about 4 K. They were inclined to associate

this with the effects of impurities but were unable to rule out the possibility that it might be induced by the Pd atoms.

The magnetic susceptibility measurements [2] which show that LaPd₃ is a diamagnet clearly rule out this latter possibility and the weak minimum must therefore be associated with impurities (as is the observed rise in magnetic susceptibility at low temperatures). Thus instead of introducing the concept of spin fluctuations to account for the anomalous heat capacity behaviour of LaPd₃ observed by Hutchens *et al* [18] we would simply associate it with the presence of impurities. It is not difficult to obtain the small effects observed ($C_V/R \sim 10^{-2}$ at 5 K) from the presence of rare earth impurities since the specific heat of the magnetic RPd₃ phases is very much greater ($C_V/R \sim 0.5$ at 5 K).

Now simple point charge calculations have been successful, rather surprisingly, in predicting the crystal field parameters determined from neutron scattering measurements [21] in rare earth compounds. This success has been repeated by Nowik *et al* [24] in YbPd₃ using Mossbauer effect studies. Nowik *et al* [24] reproduced experimental observations of the dependence of the magnetic hyperfine field (and quadrupole interaction) of the ¹⁷⁰Yb nucleus with applied field. These authors used a crystal field calculation to determine the magnetic hyperfine field along three $\langle 100 \rangle$, $\langle 110 \rangle$ and $\langle 111 \rangle$ crystalline symmetry axes as a function of applied field and, since the anisotropy was only $\sim 10\%$, averaged over these directions, instead of all orientations of applied field, to determine the crystal field parameters for their powder sample. A best fit was achieved using $B_4/\beta = -12 \pm 1 \text{ cm}^{-1}$ and $B_6/\gamma = 0.6 \pm 0.6 \text{ cm}^{-1}$.

Perhaps we should point out that this analysis is identical with the analysis for the magnetisation as a function of applied field and that the experimental observations are equivalent to the measurement of magnetization from 0 to 45 kOe at 4.2 and 1.4 K.

A simple point-charge model calculation (the details are described in section 3) using equations (3) and (4) with $Z_1 = 0$ (a neutral Pd atom) and with $Z_2 = 3$ (an unscreened Yb³⁺ ion), produces [24] the values $B_4/\beta = -10.7 \text{ cm}^{-1}$ and $B_6/\gamma = 0.065 \text{ cm}^{-1}$. The energy levels from the two determinations are given in

table 7. The agreement between the two sets of values is good, although in the light of our additional comparisons, it may well be fortuitous.

TABLE 7—The energies of the crystal field states of Yb³⁺

State	Degeneracy	Mossbauer Calculated Energy (K)	Point-charge Calculated Energy (K)
Γ_7	2	0	0
Γ_8	4	42	32
Γ_6	2	56	52
Ground level $^2F_{7/2}$			
		x	W(K)
		Mossbauer	0.92
		point-charge	0.99
			1.96
			- 1.61

This excellent agreement has not been observed using a similar analysis to fit the specific heat and magnetization results obtained on PrPd₃, TbPd₃ and ErPd₃. Nor has it proved possible by varying the assumptions about the charges on the neighbouring atoms to obtain satisfactory agreement. Junod *et al* [25] also failed to obtain good agreement with a simple point charge model calculation and the crystal field parameters determined for RN compounds. However, the specific heat results confirmed that the point charge model correctly predicts the ground state, if the fourth order term is predominant. They also showed that probably the exchange field mixes the two lowest states in TbPd₃ so as to produce in second order a magnetic Γ_3 ground state in the $\langle 100 \rangle$ direction.

Mossbauer measurements on TbPd₃ (Longworth, private communication) also show that ordering takes place below 4 K. Details of the ordering have been investigated using neutron scattering (Wedgwood, private communication) and it has been established that it is much more complex than that observed in TbPt₃ [26]. In addition, using neutron techniques similar to

those of Turberfield *et al* [21], Wedgwood (private communication) has been able to make a detailed study of the states produced by the crystalline field and thus complement the results obtained from these measurements.

ACKNOWLEDGEMENTS

We would like to thank T F Smith, in particular, for his vital support, B Bleaney, R W Hill, G Longworth, R Levi and F A Wedgwood for valuable discussions, and D Kells and N Nambudripad for assistance with the measurements and analysis of the results. We would also like to thank B D Dunlop for sending us a preprint of ref [24]. One of us (JMMS) would like to thank the Science Research Council (UK) for a post doctoral grant.

REFERENCES

- [1] McMASTERS, O. D. and GSCHNEIDER, JR, K. A., *Nuclear Metallurgy*, **10**, 93 (1964).
- [2] GARDNER, W. E., PENFOLD, J., SMITH, T. F., HARRIS, I. R., *J. Phys.*, **F2**, 133 (1972).
- [3] BUSCHOW, K. H. J., DE WIJN, H. W., and VAN DIEPEN, A. H., *J. Chem. Phys.*, **50**, 137 (1969).
- [4] HUTCHENS, R. D., and WALLACE, W. E., *J. Solid State Chem.*, **3**, 564 (1971).
- [5] GARDNER, W. E., and SMITH, T. F., *Progr. Vacuum Microbalance Tech.*, **1**, 155, edited by T. Gast and E. Robins, Heyden and Son Limited (1972).
- [6] MACHADO DA SILVA, J. M., D. Phil Thesis, Oxford (1970).
- [7] KEESOM, P. H. and PEARLMAN, N., *Encyclopaedia of Physics*, **14**, 282 (1956).
- [8] STEVENS, K. W. H., *Proc. Phys. Soc. (London)*, **A65**, 209 (1952).
- [9] HUTCHINGS, M. T., *Solid State Physics*, **16**, 277 (1964).
- [10] LEA, K. R., LEASK, M. J. M., and WOLF, W. P., *J. Phys. Chem. Solids*, **23**, 1381 (1962).
- [11] HILL, R. W., D. Phil Thesis, Oxford University, p. 26 (1952).
- [12] CHAN, S. K., *J. Phys. Chem. Solids*, **32**, 1111 (1971).
- [13] BLEANEY, B., *Proc. Roy Soc. (London)*, **A276**, 19 (1963).
- [14] SCHUMACHER, D. P., and HOLLINGSWORTH, C. A., *J. Phys. Chem. Solids*, **27**, 749 (1966).
- [15] TRAMMELL, G. T., *Phys. Rev.*, **131**, 932 (1963).
- [16] MACHADO DA SILVA, J. M., *Solid State Comm.*, **28**, 857 (1978).
- [17] MACHADO DA SILVA, J. M., *Journal de Physique*, **152**, 40 (1979).

- [18] HUTCHENS, R. D., RAO, V. U. S., GREEDAN, J. E., and CRAIG, R. S, *Proc., 9th Rare Earth Research Conference*, Blacksburg, Virginia (Editor P. E. Field), 680 (1971).
- [19] DONIACH, S., and ENGELSBERG, S., *Phys., Rev. Lett*, **17**, 750 (1960).
- [20] ROBINSON, W. K., and FRIEDBERG, S. A., *Phy. Rev.*, **117**, 402 (1960).
- [21] TURBERFIELD, K. C., PASSEL, L., BIRGENAU, R. J. and BUCHER, E., *J. App. Phys.*, **42**, 1746 (1971).
- [22] FURRER, A. and PURWINS, H. G., *J. Phys.*, **C9**, 1491 (1976).
- [23] ELLIOTT, R. O. and HILL, H. H., *Proc. 9th Rare Earth Research Conference*, Blacksburg, Virginia (Editor P. E. Field), (1971).
- [24] NOWIK, I., DUNLOP, B. D. and KALVIUS, G. M., *Phys. Rev.*, **B6**, 1048 (1972).
- [25] JUNOD, P., MENTH, A. and VOGT, O., *Phys. Kondens Materie*, **8**, 323 (1969).
- [26] NERESON, N. and ARNOLD, G., *J. Chem. Phys.*, **53**, 2818 (1970).

AN EPITOME OF CONFIGURATIONAL DATA ON CONNECTED CLUSTERS

J. A. M. S. DUARTE

Departamento de Física — Faculdade de Ciências do Porto, 4000 Porto, Portugal

(Received 26 June 1981)

ABSTRACT — New lattice data on configurational histograms are given for bond and site clusters grouped by fixed percolation perimeter, fixed energy perimeter and fixed cluster size. The latter are illustrated by several combinations of interest of cyclomatic number discriminations.

INTRODUCTION

It has long been recognized that configurational studies are a fundamental tool in the theory of critical phenomena. Recently, however, powerful techniques (like transfer-matrix renormalization and field theoretical methods [17]) have surged on to the statistics of lattice clusters in the percolation and animal problems (see e. g. ref [18]) and significant advances in the knowledge of the critical exponents for both problems have been brought close to a virtually «exact» solution. There is, however, still open a rich field of specializations (valence, cyclomatic number, specific connectivity requirements, restricted sets of clusters (animals) defined through topological constraints). Our aim in this paper is twofold: written in mid-81 it should concentrate on selected topics referring to the cluster topology which are likely to assume physical relevance in the future, and where series expansions and configurational studies will remain competitive. On the other hand, it should unify various treatments that have remained scattered in the literature without any systematic exploration (like bond or site content in percolation). We have divided the data in 5 broad groups: fixed energy groupings, fixed percolation perim-

eter groupings, fixed size percolation groupings, cyclomatic number distributions (in percolation) and fixed size energy groupings. Each one of them is preceded by a succinct description of the graph theoretical procedures used in its derivation.

The notation to be consistently applied throughout the paper is:

- s — denotes the number of cluster sites
- b — denotes the number of cluster bonds
- $c = b - s + 1$ denotes the cyclomatic number of a connected cluster
- e — denotes the external bond (energy) perimeter
- t — denotes the perimeter in the percolation sense

g_{se} ; g_{sbt} — give the number of geometrically different cluster configurations with a given label s, e or s, b, t .

Note that the normalization of the various $g_{s...}$ may occasionally vary for convenience. We have indicated in each case the factor relative to a normalization per lattice site.

A — *Fixed energy groupings*

Whenever the bond perimeter of connected site clusters is fixed, the resulting distributions according to the variable number of sites enclosed within a given configuration of boundary bonds can easily be translated topologically into a fixed perimeter — enclosed area problem by considering the dual lattice (Sykes et al [1], [2]). Consider figure 1 for the triangular — honeycomb system: in Fig. 1 A, the connected cluster of 8 sites and 11 bonds on the triangular lattice is the *dual* of the honeycomb configuration with 26 sides and area 8. Denoting the number of sites by s , the number of (*internal*) bonds by b and external bonds by e , the following linkage rule for site clusters (strongly embedded clusters)

$$e = zs - 2b \qquad \text{A. 1}$$

is valid on any lattice (coordination number z). For configurations of the type in Fig. 1A there are no sites enclosed within

the configuration and not belonging to it but Fig. 1B indicates the possibility of such configurations: all clusters that can be derived from the fully compact cluster limited by the outermost boundary through the exclusion of any combination of hexagonal faces marked with (x) are still duals of connected clusters on the triangular lattice, but, unlike the case of Fig. 1A, their boundary is no longer singly-connected (it is no longer a simple polygon).

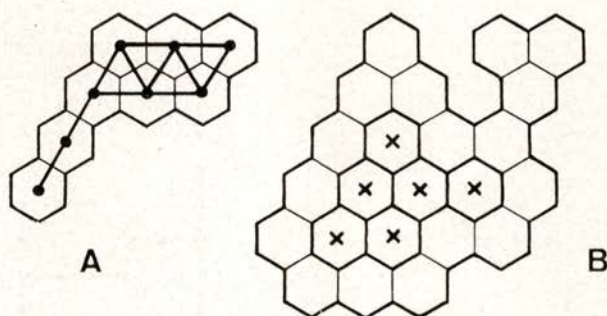


Fig 1

- A.—Site cluster on the triangular lattice and its dual on the honeycomb lattice. The triangular configuration is compact (no inner perimeter sites) and its dual is bounded by a simple polygon.
- B.—Another example of a honeycomb configuration. Exclusion of any face marked with (x) generates a connected dual from the larger simple polygon.

The situation recurs for the simple quadratic lattice, which is well known to be self-dual (Fig. 2). Fig. 2C is a compact configuration bounded by a simple polygon (it is, in fact, the isoperimetric solution for perimeter 18, Duarte and Marques [3] — and area 20). Once again, exclusion of any combination of square faces marked with (x) generates a connected area (alternative examples are drawn in 2A and 2B), which is still a dual of some site cluster on the same lattice. Fig. 2D shows, explicitly, a square site tree (17 sites) and its connected dual.

Now all perimeter distributions of site clusters contribute to the low temperature ferromagnetic polynomials for the Ising

model [1]. It is, however, required, for their isolation, to separate the contribution of multicomponent graphs as described in [4]. To go one stage further and separate the simple polygons from the nonpolygonal connected duals, we note that on the honeycomb lattice (Fig. 1) it is impossible to have more than 3 ele-

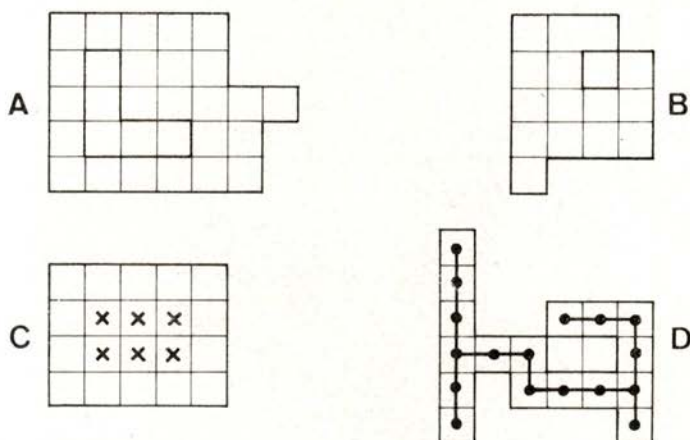


Fig. 2

- A, B — Examples of connected duals on the square lattice.
 C — Simple polygon on the square lattice. Exclusion of any face marked with (x) generates a connected dual from the larger configuration.
 D — A square lattice tree and its dual.

mentary hexagonal faces meeting at a site and, therefore, the contribution from those configurations can be singled out from clusters discriminations on the triangular lattice taking into account the number of elementary triangular faces f (as well as s and b). Isolated inner boundary sites will then occur for all clusters where f does not account for the total cyclomatic number:

$$b - s + 1 \neq f \quad \text{A. 2}$$

and this inequality identifies the non-polygonal connected duals: all inner boundaries will be separate from the outermost boundary.

It is impossible to proceed in this way for the square lattice: a tree like in Fig. 2D does not verify A.2 and yet its dual is not a polygon. In general the problem of determining the connected duals up to a reasonable order is lessened by simple conversion of fixed s distributions (b groupings), like those below in section D. Earlier results for the square polygons can be found in Hiley and Sykes [5].

The additional data should sum to the known results for the total number of polygons (fixed perimeter), greatly extended in a recent paper by Enting [6] through the use of transfer matrix techniques.

We give new data for polygons on the honeycomb ($e \leq 42$) and square lattices ($e \leq 22$) as well as for the corresponding connected duals.

B — *Fixed percolation perimeter groupings*

When the perimeter is measured in the percolation sense, i.e. by the number of sites (bonds) t necessary for the isolation of a given cluster on a lattice, the perimeter groupings suffer considerable rearrangement of the various cluster contributions. The usual perimeter method can, of course, be used for obtaining these groupings — once again, they can be obtained through a straightforward conversion of the fixed size percolation distributions, although such information must be completed (for detailed descriptions see Sykes et al [4], Blease et al [7]).

In this paper we present results for these groupings on the square ($t \leq 16$) and honeycomb ($t \leq 13$) lattices (site problem) as well as for the Kagomé site problem ($t \leq 16$). As in section A, the problem is equivalent to the enumeration of the histograms g_{st} or g_{bt} at fixed t ; g_{st} or g_{bt} gives the number of geometrically different cluster configurations per site (or per bond) with a given perimeter value t (here t refers to bond and site perimeter for bond and site percolation respectively).

In addition, we have used inequality A.2 (and further discrimination through b , s , t and f) to isolate all the non-polygonal connected duals of the triangular lattice according to their percolation weight. The resulting perimeter polynomials are given

through order 21 (they should be compared with the complete set of perimeter groupings for the problem, given in Sykes et al [4] ($t \leq 22$)).

C — *Fixed size percolation groupings*

The g_{st} (fixed size s) are the best illustrated groupings in the literature. They have been listed for 2, 3 and higher dimensions [8], [9], for both site and bond [10] problems on most usual lattices. The interested reader should refer to those papers for an outline of the method and detailed considerations on the applicability of the corresponding series expansions. We have added in this paper the groupings for the site problem on the 2 archimedean lattices of coordination number 5, (3,3,3,4,4) and (3,3,4,3,4) ($s \leq 12$). Both lattices (their Ising points are known exactly) provide good testing ground for the variation of the perimeter — to — size ratio and its connection with criticality (Duarte [11]). The well known sum rule to be verified by the g_{st} is

$$p = \sum_{s,t} s g_{st} p^s (1-p)^t \quad \text{C. 1}$$

D — *Cyclomatic number distributions in percolation*

A different type of configurational weighting which has been the object of much recent interest is the set of three — indexed discriminations of clusters by their site, bond content and perimeter (in the percolation sense). Through Euler's law these discriminations lead to the expansions of the average cyclomatic number $\langle c \rangle$ (Cherry [12], Gaunt et al [13]).

$$\langle c \rangle = \langle b \rangle - \langle s \rangle + \langle l \rangle \quad \text{D. 1}$$

and from expansion of the higher moments of the cluster size distribution of the type

$$\langle s^k \rangle = \sum_{s,b,t} s^k g_{sbt} p^b (1-p)^t \quad \text{D. 2}$$

for bond percolation and

$$\langle b^k \rangle = \sum_{s,b,t} b^k g_{sbt} p^s (1-p)^t \quad \text{D. 3}$$

for site percolation, new quantities of interest, paralleling the moments in the usual cluster size distribution are obtained. They are expected to belong to the same universality class as normal percolation and therefore constitute alternative ways of calculating the critical exponents for percolation. For $k=2$, D.2 and D.3 lead to «susceptibility» series diverging near p_c with a critical exponent γ , like the mean cluster size

$$p \rightarrow p_c^-, \langle s^2 \rangle_{\text{bond}} \sim |p_c - p|^{-\gamma}, \langle b^2 \rangle_{\text{site}} \sim |p_c - p|^{-\gamma}, \quad \text{D. 4}$$

This property has been occasionally used in the literature (Dunn et al [14], Agrawal et al [15]). A systematic study for 2 dimensional percolation (p_c lattices) is reported in [16].

We present results for the set of histograms $\sum_b b g_{sbt}$ for the triangular, square matching, Kagomé, honeycomb and archimedean (3,3,3,4,4) and (3,3,4,3,4) site problems and for $\sum_s s g_{sbt}$ for the square and honeycomb bond problems, as well as for $\sum_b b^2 g_{sbt}$ for the Kagomé site problem. We recall that for the first moment distributions the sum rules

$$\sum_{b,s,t} b g_{sbt} p^s (1-p)^t = (z/2) p^2 \quad \text{D. 5}$$

for site percolation and

$$\sum_{b,s,t} s g_{sbt} p^b (1-p)^t = 1 - (1-p)^z \quad \text{D. 6}$$

for bond percolation, should be verified.

It also seems adequate to mention that the use of detailed valence discriminations constitute an alternative way of determining their cyclomatic number distributions. Since they represent an expansion from 3-indexed to z-indexed discriminations it is usually more cumbersome to take this line of procedure (it was however followed in refs [12], [13]). If the sites in a connected cluster are partitioned according to the number of

site neighbours in the cluster (their valence) the following linkage rules are verified

$$\sum_v s_v = s \quad \text{D. 7}$$

$$\sum_v v s_v = 2b \quad \text{D. 8}$$

with s_v the number of sites with valence v and where the summations run from 1 to z . Equations D. 7 and D. 8 are unwieldy for bond percolation (valence considerations apply equally to bond and site percolation clusters), since b is usually fixed and any cyclomatic number mixing in a given g_{bt} must be disentangled from a combination of different s as well as from all compatible combinations of s_v 's. It is generally more direct to start from bond percolation distributions and exploit the following properties of the yield factor generation (see Blease et al [7] for an exposition of the method):

a) For a given space-type strongly embeddable on the specific lattice under investigation, the number of bonds that can be transferred from the bond content to the bond perimeter is not greater than the cyclomatic number, if connectivity is to be preserved.

b) The number of transferable bonds is zero for strongly embedded trees.

c) The length of the bond tree percolation polynomial (with $b = s - 1$ bonds) is $c_{\max} + 1$, where c_{\max} is the maximum cyclomatic number of s -site clusters.

d) Strongly embedded clusters always maximise the bond perimeter for given values of b and c . Recalling that the linkage rule for strongly embedded clusters is $e = t = zs - 2b$, it can be seen that the difference in bond perimeter between clusters with successive cyclomatic numbers (same b) is z . These properties enable a separation of the cyclomatic number contributions in bond perimeter polynomials of not too high b (like those in Sykes et al [10]). In every case the sum rule D. 6 acts as a check on such graph theoretical manipulations and use of valence discriminations is thereby avoided.

E — *Fixed size energy groupings*

These enumerations are converse of those considered in section A. For site clusters, these groupings constitute (through eq. A. 1) a strict partition according to the cyclomatic number (or alternatively, according to the number of bonds b in the cluster). No data exist in the literature regarding this specific partition, which has emerged in recent times as a very relevant tool for the study of branched polymers in the dilute limit (mainly through the studies of Lubensky and coworkers [17], [18]). Clearly, in this partition the 3-indexed discriminations in D. 2 and D. 3, the g_{sbt} , are summed over the perimeter index, so that with the resulting g_{sb} (which are equivalent to the g_{se}) new moments of the «animal distribution» [17] can be defined and numerically investigated.

We present data on the three 2-dimensional regular lattices. The first noticeable difference with respect to the g_{ts} is that the corresponding histograms evolve very slowly in shape, so that it might be argued that for this specific partition the lattices are not very effectively sampled. Now, in each case, the maximum bond perimeter corresponds to the minimum number of bonds in the cluster, so that the last value in each of the g_{se} histograms just gives the total number of site trees on each lattice. As we have mentioned, in the previous section, this total number will also appear as the maximum perimeter configuration value in the bond percolation polynomial of bond size $b = s - 1$. Hence, the present data represent an extension over the data of ref [10].

Unfortunately the following term in g_{se} (corresponding to the total number of polygons, tadpoles and other configurations of cyclomatic number 1) does not grow sufficiently fast for a non-degenerate histogram to occur for loose-packed lattices. Consideration of the bond case only worsens the balance of the histogram: A. 1 is no longer valid, so that the g_{sb} with $s = b + 1$, gives the total number of bond trees and through the use of the yield factor generation all site clusters of $b + 1$ sites give non-zero contributions to $g_{b+1, b}$.

In order to avoid these problems one must concentrate on high coordination number (site) lattices where the strong embeddability «propagates» the distributions towards lower e values. But,

better still, the careful exploitation of local linkage rules and consideration of both site and bond valence and the changes they undergo in bond-to-site transformations have enabled Duarte and Ruskin [19] to identify the valence structure on lattices which are covering lattices of bond problems. For the site trees ($g_{b+1, b}$) are always neighbour avoiding walks, belonging to a totally different universality class from branched trees and with a comparatively smaller growth parameter. The same happens for the terms of the form g_{bb} which originate from the corresponding bond polygons and bond trees with one single site of valence 3. Hence the g_{se} for the corresponding site covering problem shows a rapid evolution towards non-degenerate configurational histograms. We illustrate this point with the square covering g_{se} ($s \leq 13$).

This research was funded, at various stages, by I.N.I.C. (Portugal), The Royal Society — Academia das Ciências (Lisboa) and the Gulbenkian Foundation. The author is greatly indebted to Prof. J. M. Araújo for assistance with the manuscript. H. J. Ruskin and R. Cherry made an invaluable contribution towards the computing proficiency of the author.

APPENDIX

FIXED ENERGY GROUPINGS

A — Honeycomb polygons

	$e = 6$	$g_{es} (\times 1)$	$e = 20$	
1		1	5	60
	$e = 10$		6	42
2		3	7	30
	$e = 12$		8	6
3		2	$e = 22$	
	$e = 14$		5	99
3		9	6	129
4		3	7	105
	$e = 16$		8	69
4		12	9	27
5		6	10	3
	$e = 18$		$e = 24$	
4		29	6	280
5		21	7	276
6		14	8	246
7		1	9	160

10	86	17	1368
11	24	18	606
12	2	19	198
	$e = 26$	20	42
6	348	21	6
7	726		$e = 34$
8	720	8	4644
9	609	9	18786
10	432	10	27627
11	249	11	33405
12	117	12	32061
13	27	13	29097
14	3	14	23553
	$e = 28$	15	18597
7	1242	16	13128
8	1710	17	8877
9	1812	18	5412
10	1458	19	2943
11	1164	20	1401
12	702	21	507
13	414	22	147
14	168	23	27
15	42	24	3
16	6		$e = 36$
	$e = 30$	9	23472
7	1260	10	54148
8	3759	11	76662
9	4611	12	88378
10	4769	13	86860
11	3870	14	78978
12	3163	15	67134
13	2126	16	53826
14	1320	17	40866
15	729	18	29076
16	290	19	19672
17	87	20	12006
18	14	21	6936
19	1	22	3424
	$e = 32$	23	1458
8	5436	24	496
9	9804	25	128
10	12186	26	24
11	12030	27	2
12	10476		$e = 38$
13	8406	9	17382
14	6336	10	90924
15	4134	11	160131
16	2622	12	218436

13	240579	27	13128
14	242613	28	6060
15	219816	29	2412
16	193602	30	798
17	158682	31	216
18	126099	32	42
19	93948	33	6
20	68019		
21	45531	e = 42	
22	29049	10	65822
23	17115	11	431448
24	9138	12	897289
25	4338	13	1369834
26	1719	14	1691994
27	579	15	1865164
28	147	16	1873893
29	27	17	1778925
30	3	18	1601354
	e = 40	19	1397388
10	100740	20	1168533
11	287838	21	951897
12	464580	22	742157
13	604434	23	564297
14	661206	24	410122
15	669792	25	288397
16	619944	26	192099
17	553584	27	122932
18	469290	28	73674
19	384144	29	41040
20	300192	30	21083
21	226296	31	9632
22	163500	32	3918
23	111960	33	1341
24	73266	34	392
25	44646	35	87
26	25626	36	14
		37	1

A — *Square polygons*

e = 4	} (see Hiley, Sykes [5])	9	656
e = 6		10	482
e = 8		11	310
e = 10		12	151
e = 12		13	68
e = 14		14	22
e = 16	$g_{se} (\times 1)$	15	6
7	566	16	1
8	676		

	e = 18		21	187
8	1868		22	68
9	2672		23	22
10	2992		24	6
11	2592		25	1
12	2086			
13	1392		e = 22	
14	864		10	21050
15	456		11	39824
16	218		12	56162
17	88		13	61032
18	30		14	60864
19	8		15	54032
20	2		16	45936
			17	35952
	e = 20		18	26858
9	6237		19	18744
10	10376		20	12456
11	13160		21	7648
12	12862		22	4472
13	11717		23	2408
14	9332		24	1208
15	7032		25	560
16	4748		26	238
17	3010		27	88
18	1728		28	30
19	914		29	8
20	426		30	2

A — *Honeycomb duals*

e = 6	} Same as polygons		e = 26	
e = 10			6	348
e = 12			7	732
e = 14			8	720
e = 16			9	609
e = 18			10	432
e = 20			11	249
e = 22		12	117	
e = 24	$g_{se} (\times 1)$	13	27	
6	281	14	3	
7	276		e = 28	
8	246	7	1248	
9	160	8	1737	
10	86	9	1818	
11	24	10	1458	
12	2	11	1164	
		12	702	
		13	414	

14	168	23	27
15	42	24	3
16	6	e = 36	
e = 30		9	23662
7	1260	10	54411
8	3795	11	78990
9	4697	12	91389
10	4817	13	89680
11	3876	14	81183
12	3163	15	68294
13	2126	16	54261
14	1320	17	40950
15	729	18	29083
16	290	19	19672
17	87	20	12006
18	14	21	6936
19	2	22	3424
e = 32		23	1458
8	5472	24	496
9	9990	25	128
10	12453	26	24
11	12264	27	2
12	10557	e = 38	
13	8418	9	17382
14	6336	10	92205
15	4134	11	165144
16	2622	12	226125
17	1368	13	250641
18	606	14	252177
19	198	15	227970
20	42	16	199110
21	6	17	161712
e = 34		18	127287
8	4644	19	94242
9	19014	20	68067
10	28305	21	45531
11	34263	22	29049
12	32901	23	17115
13	29601	24	9138
14	23721	25	4338
15	18627	26	1719
16	13128	27	579
17	8877	28	147
18	5412	29	27
19	2943	30	3
20	1401	e = 40	
21	507	10	101679
22	147	11	295356

12	482850	13	1431751
13	631218	14	1782600
14	694122	15	1971774
15	702816	16	1985091
16	648951	17	1879842
17	575856	18	1685370
18	484095	19	1458954
19	392556	20	1210437
20	303741	21	975901
21	227472	22	753821
22	163743	23	568761
23	111990	24	411402
24	73266	25	288661
25	44646	26	192123
26	25626	27	122932
27	13128	28	73674
28	6060	29	41040
29	2412	30	21083
30	798	31	9632
31	216	32	3918
32	42	33	1341
33	6	34	392
e = 42		35	87
10	65822	36	14
11	438264	37	1
12	929414		

A — *Square duals*

e = 4		$g_{se} (\times 1)$	8	134
1		1	9	72
e = 6			10	30
2		2	11	8
e = 8			12	2
3		6	e = 16	
4		1	7	570
e = 10			8	677
4		18	9	656
5		8	10	482
6		2	11	310
e = 12			12	151
5		55	13	68
6		40	14	22
7		22	15	6
8		6	16	1
9		1	e = 18	
e = 14			8	1908
6		174	9	2708
7		168	10	3008

11	2596	23	22
12	2086	24	6
13	1392	25	1
14	864	e = 22	
15	456	10	22202
16	218	11	42012
17	88	12	58742
18	30	13	63256
19	8	14	62396
20	2	15	54908
e = 20		16	46352
9	6473	17	36112
10	10724	18	26906
11	13456	19	18756
12	13034	20	12456
13	11789	21	7468
14	9354	22	4472
15	7036	23	2408
16	4748	24	1208
17	3010	25	560
18	1728	26	238
19	914	27	88
20	426	28	30
21	187	29	8
22	68	30	2

PERCOLATION PERIMETER GROUPINGS

B — *Square lattice*

	t = 4	$g_{st} (\times 1)$	6	54
1		1	7	22
	t = 6		8	4
2		2	t = 11	
	t = 7		5	12
3		4	6	80
	t = 8		7	136
3		2	8	80
4		9	9	28
5		1	10	4
	t = 9		t = 12	
4		8	5	2
5		20	6	60
6		4	7	252
	t = 10		8	388
4		2	9	291
5		28	10	154

11	52	11	11772
12	9	12	12502
13	1	13	10480
	$t = 13$	14	7508
6	16	15	4608
7	228	16	2406
8	777	17	1104
9	1152	18	396
10	986	19	124
11	644	20	28
12	325	21	4
13	112		$t = 16$
14	28	7	2
15	4	8	152
	$t = 14$	9	2089
6	2	10	9750
7	100	11	24472
8	818	12	38694
9	2444	13	44574
10	3676	14	41408
11	3530	15	33046
12	2644	16	23311
13	1660	17	14385
14	828	18	8146
15	332	19	3982
16	106	20	1730
17	22	21	651
18	4	22	206
	$t = 15$	23	52
7	20	24	9
8	480	25	1
9	2804		
10	7612		

B — *Honeycomb lattice*

	$t = 3$	$g_{st} (\times 1)$		$t = 7$	
1		1		5	15
	$t = 4$			6	15
2		1.5		7	3
	$t = 5$			$t = 8$	
3		3		6	31.5
	$t = 6$			7	60
4		7		8	37.5
5		3		9	12
6		0.5		10	1.5

	t = 9		12	7078
7	62		13	11181
8	177		14	12937.5
9	190		15	11758
10	111		16	8895
11	39		17	5796
12	9		18	3258
13	1		19	1522
	t = 10		20	565.5
8	123		21	164
9	471		22	37
10	744		23	6
11	705		24	0.5
12	449.5			
13	207		t = 13	
14	69	11	11	1029
15	15	12	12	6927
16	1.5	13	13	20160
	t = 11		14	37635
9	246		15	52311
10	1167		16	57960
11	2361		17	53949
12	3006		18	43728
13	2721		19	31536
14	1902		20	20355
15	1083		21	11689
16	492		22	5889
17	162		23	2541
18	33		24	894
19	3		25	234
	t = 12		26	39
10	503		27	3
11	2874			

B — *Kagomé lattice*

	t = 4	$g_{st} (\times 1)$		t = 8	
1		1		5	31
	t = 5			6	12
2		2		8	9
	t = 6			11	1
3		14/3			
6		1/3		t = 9	
	t = 7			6	81 1/3
4		12		7	54
5		2		9	36 2/3
7		2		10	11

12	8	15	5952
15	2/3	16	3974
t = 10		17	5770
7	216	18	2190
8	220	19	1780
9	35	20	2318
10	133	21	468
11	88	22	748
13	45	23	674
14	10	25	258
16	9	26	126
19	1	28	70
t = 11		29	10
8	576	31	14
9	798	34	2
10	280	t = 14	
11	454	11	11522
12	496	12	28524
13	58	13	30774
14	212	14	28078
15	138	15	38372
17	66	16	33712
18	19	17	21063
20	14	18	27850
23	2	19	18925
t = 12		20	10303
9	1550 $\frac{1}{3}$	21	14744
10	2724	22	6903
11	1576	23	3946
12	1620	24	6058
13	2344	25	1542
14	804	26	1729
15	877	27	1904
16	1020	28	139
17	153	29	639
18	371	30	430
19	270	32	195
21	118 $\frac{2}{3}$	33	68
22	46	35	49
24	29	38	9
27	4 $\frac{2}{3}$	41	1
30	1/3	t = 15	
t = 13		12	317770 $\frac{2}{3}$
10	4210	13	89636
11	8940	14	117736
12	7432	15	120652 $\frac{2}{3}$
13	6536	16	151052
14	9726	17	162910

18	119496	19	637131
19	128790	20	608309
20	120932	21	645568
21	69820 $\frac{2}{3}$	22	472456
22	78394	23	418304
23	62468	24	425165
24	29484 $\frac{2}{3}$	25	247522
25	40976	26	237541
26	23430	27	216930
27	10837 $\frac{1}{3}$	28	99805
28	17521	29	122492
29	6096	30	86467
30	4432	31	36226
31	6050	32	55156
32	1082	33	27197
33	1763 $\frac{1}{3}$	34	12362
34	1689	35	21294
36	612	36	681
37	342	37	5339
39	179 $\frac{1}{3}$	38	6868
40	41	39	800
42	42 $\frac{2}{3}$	40	2052
45	8	41	1778
48	2/3	43	693
t = 16		44	360
13	88129	46	203
14	279000	47	32
15	427488	49	49
16	500865	52	9
17	608253	55	1
18	716926		

B — *Triangular lattice (without holes)*

t = 6	$g_{st} (\times 1)$	t = 12	
1	1	4	29
t = 8		5	21
2	3	6	14
t = 9		7	1
3	2	t = 13	
t = 10		5	66
3	9	6	42
4	3	7	30
t = 11		8	6
4	12	t = 14	
5	6	5	93
		6	153

7	105		t = 19
8	69	8	5310
9	27	9	13488
10	3	10	18006
	t = 15	11	18732
6	298	12	14892
7	360	13	11310
8	264	14	7764
9	160	15	4614
10	86	16	2712
11	24	17	1374
12	2	18	606
	t = 16	19	198
6	306	20	42
7	840	21	6
8	918		t = 20
9	717	8	3408
10	444	9	20469
11	249	10	41673
12	117	11	51822
13	27	12	52992
14	3	13	45129
	t = 17	14	33981
7	1290	15	24900
8	2316	16	16188
9	2382	17	10023
10	1884	18	5676
11	1308	19	2879
12	720	20	1401
13	414	21	507
14	168	22	147
15	42	23	27
16	6	24	3
	t = 18		t = 21
7	1014	9	21372
8	4299	10	71644
9	6486	11	125448
10	6641	12	153614
11	5160	13	152658
12	3913	14	136014
13	2354	15	106416
14	1356	16	79446
15	729	17	55440
16	290	18	36576
17	87	19	22708
18	14	20	12912
19	1	21	7116

22	3442	25	128
23	1458	26	24
24	496	27	2

SIZE PERCOLATION GROUPINGS

C — Archimedean (3, 3, 4, 3, 4) (site problem)

	s = 4	$g_{st} (\times 4)$	14	2926
5		4	15	6680
	s = 2		16	8164
6		2	17	4632
7		8	18	848
	s = 3		19	32
8		20		
9		12	s = 9	104
	s = 4		13	612
8		2	14	2960
9		28	15	8780
10		66	16	20116
11		16	17	29908
	s = 5		18	25312
9		8	19	9888
10		48	20	1266
11		180	21	36
12		156		
13		20	s = 10	24
	s = 6		13	372
10		28	14	1998
11		108	15	9156
12		432	16	27284
13		676	17	62016
14		304	18	103726
15		24	19	110440
	s = 7		20	68554
10		4	21	19204
11		72	22	1836
12		316	23	40
13		1092		
14		2180	s = 11	8
15		1928	13	128
16		528	14	1308
17		28	15	7104
	s = 8		16	28436
11		20	17	86612
12		204	18	198268
13		988	19	350032

20	437312	17	91972
21	356728	18	279622
22	166292	19	645560
23	34668	20	1183662
24	2556	21	1639860
25	44	22	1606806
s = 12		23	1032628
12	2	24	368306
13	40	25	59220
14	660	26	3452
15	4816	27	48
16	24572		

C — Archimedean (3, 3, 3, 4, 4) (site problem)

s = 1		$g_{st} (\times 2)$	13	504
5		2	14	832
s = 2			15	1084
6		2	16	464
7		2	17	110
8		1	s = 8	
s = 3			11	4
7		2	12	120
8		4	13	504
9		10	14	1523
s = 4			15	2750
8		2	16	3791
9		10	17	2906
10		33	18	1294
11		10	19	118
12		2	20	8
s = 5			s = 9	
9		2	12	36
10		34	13	346
11		72	14	1512
12		68	15	4496
13		36	16	9004
s = 6			17	13046
10		7	18	13130
11		90	19	8992
12		172	20	2300
13		254	21	314
14		254	s = 10	
15		36	12	5
16		4	13	158
s = 7			14	1080
11		34	15	4758
12		204		

16	13604	23	55766
17	28980	24	9696
18	45462	25	854
19	52606		$s = 12$
20	45831	13	4
21	21304	14	247
22	5518	15	2310
23	358	16	12693
24	16	17	48018
	$s = 11$	18	137623
13	42	19	306124
14	608	20	541719
15	3670	21	755720
16	14956	22	828850
17	42802	23	676978
18	93434	24	392305
19	157478	25	123404
20	202272	26	21028
21	200886	27	1024
22	133464	28	32

CYCLOMATIC NUMBER DISTRIBUTIONS IN PERCOLATION

D — *Triangular lattice*

$s = 2$	$\sum_b bg_{sbt} (\times 1)$	$s = 7$	
8	3	12	12
	$s = 3$	13	330
9	6	14	1098
10	18	15	3198
	$s = 4$	16	6504
10	15	17	8802
11	48	18	6084
12	87		$s = 8$
	$s = 5$	13	84
11	42	14	897
12	126	15	3420
13	324	16	10230
14	372	17	22494
	$s = 6$	18	37251
12	126	19	41430
13	342	20	23856
14	1047		$s = 9$
15	1746	14	432
16	1530	15	2478
		16	10962

17	32550	23	12435252
18	77244	24	19008123
19	142686	25	23432184
20	196716	26	22557609
21	187836	27	15089856
22	92496	28	5218950
s = 10		s = 13	
14	57	16	702
15	1548	17	10626
16	8256	18	67356
17	33522	19	322320
18	107844	20	1241400
19	258930	21	3838218
20	528585	22	10430136
21	822762	23	23661498
22	991227	24	46122252
23	826092	25	76516392
24	356391	26	105213888
s = 11		27	118095138
15	504	28	103613454
16	5088	29	63161082
17	28686	30	19879872
18	106518	s = 14	
19	354294	16	87
20	882774	17	4704
21	1886160	18	40776
22	3269094	19	254682
23	4492410	20	1112547
24	4797486	21	4240902
25	3559656	22	13165455
26	1366230	23	35992752
s = 12		24	83918157
15	48	25	169687884
16	2691	26	297846975
17	17442	27	446213892
18	97686	28	560840964
19	358230	29	578723592
20	1154871	30	467147454
21	3044358	31	261616854
22	6663264	32	75562266

D — *Square matching site problem*

	$s = 2$	$\Sigma_b b_{g_{sbt}} (\times 1)$		$s = 7$
10		2	16	292
12		2	17	224
	$s = 3$		18	1960
12		16	19	4120
14		16	20	7968
15		8	21	12092
16		4	22	21732
	$s = 4$		23	22660
12		6	24	26520
14		78	25	24704
15		32	26	21956
16		96	27	13352
17		64	28	7820
18		72	29	3096
19		24	30	840
20		6	31	120
	$s = 5$		32	12
14		64		$s = 8$
15		24	16	100
16		332	17	72
17		336	18	1986
18		568	19	3872
19		452	20	10910
20		612	21	24892
21		336	22	51134
22		208	23	73640
23		48	24	119744
24		8	25	153072
	$s = 6$		26	177006
14		22	27	172104
16		396	28	168700
17		476	29	127632
18		1422	30	86776
19		2164	31	46364
20		3682	32	21414
21		3064	33	6580
22		4178	34	1400
23		3264	35	168
24		2338	36	14
25		1180		$s = 9$
26		460	16	20
27		80	18	1360
28		10	19	2528
			20	11440

21	32760	37	1800604
22	75996	38	879220
23	146044	39	341348
24	304820	40	101672
25	473628	41	21060
26	700344	42	3204
27	942580	43	288
28	1158604	44	18
29	1203972		
30	1200980	s = 11	
31	1031344	18	208
32	810160	19	372
33	519744	20	7300
34	294132	21	21692
35	135616	22	81332
36	49920	23	247844
37	12224	24	646804
38	2176	25	1492640
39	224	26	3236880
40	16	27	6180136
		28	11020012
s = 10		29	17637232
18	670	30	26672100
19	968	31	36246008
20	10406	32	45860536
21	31096	33	53549768
22	82660	34	57479148
23	219324	35	56049244
24	510996	36	50716588
25	948612	37	41178380
26	1795748	38	30463740
27	2903344	39	19695760
28	4335128	40	11292320
29	5806280	41	5528144
30	7281978	42	2318500
31	8178288	43	756984
32	8407562	44	190168
33	7738904	45	33960
34	6627886	46	4520
35	4895912	47	360
36	3241420	48	20

D — *Kagomé lattice site problem*

	$s = 2$	$\sum_b \text{bg}_{\text{stb}} (\times 3)$	12	71826
5		6	13	296724
	$s = 3$		14	1141584
6		30	15	1241916
	$s = 4$		$s = 13$	
7		120	10	2376
	$s = 5$		11	2682
7		24	12	113640
8		426	13	306876
	$s = 6$		14	1349736
6		6	15	3912288
8		204	16	3762834
9		1416	$s = 14$	
	$s = 7$		10	546
7		48	11	12126
9		1140	12	40842
10		4548	13	511212
	$s = 8$		14	1397292
8		258	15	5612268
10		5496	16	13185468
11		14220	17	11375370
	$s = 9$		$s = 15$	
9		1206	9	42
10		936	11	8190
11		23052	12	53886
12		43860	13	329904
	$s = 10$		14	2159004
9		378	15	6383382
10		4932	16	21974364
11		8880	17	43892388
12		88956	18	34321086
13		134250	$s = 16$	
	$s = 11$		10	612
8		42	12	65484
10		3504	13	255342
11		18636	14	2012856
12		56616	15	9002940
13		325044	16	28199694
14		408894	17	82526616
	$s = 12$		18	144709680
9		384	19	103371816
11		21972	$s = 17$	
			11	4824
			12	10158

13	396048	17	118643394
14	1397940	18	301417152
15	10394394	19	473127060
16	38126082	20	310901274

D — *Honeycomb lattice site problem*

	$s = 2$	$\sum_b b g_{stb} (\times 2)$		$s = 12$
4		3	9	234
	$s = 3$		10	10797
5		12	11	68670
	$s = 4$		12	156972
6		42	13	152394
	$s = 5$		14	46530
6		24		$s = 13$
7		120	9	30
	$s = 6$		10	5616
6		6	11	69870
7		150	12	275772
8		315	13	486714
	$s = 7$		14	395352
7		42	15	104496
8		720		$s = 14$
9		744	10	2097
	$s = 8$		11	54420
8		552	12	354312
9		2478	13	998700
10		1722	14	1457295
	$s = 9$		15	1001676
8		216	16	234312
9		3126		$s = 15$
10		7536	10	510
11		3936	11	34248
	$s = 10$		12	355644
8		33	13	1524900
9		2166	14	3428742
10		13623	15	4197072
11		21006	16	2500512
12		9054	17	524244
	$s = 11$			$s = 16$
9		882	10	57
10		14862	11	17130
11		47766	12	295326
12		57480	13	1849878
13		20580	14	6028185
			15	11161506

16	11757504		$s = 19$	
17	6162480		11	138
18	1171950		12	64644
	$s = 17$		13	1285596
11	6198		14	10333392
12	209940		15	47614188
13	1876770		16	137698308
14	8488092		17	258202302
15	22152534		18	311675004
16	34968960		19	227833902
17	32137488		20	87704424
18	15050304		21	12997152
19	2616288		$s = 20$	
	$s = 18$		12	25860
11	1386		13	892020
12	128046		14	9492018
13	1650396		15	55892538
14	10041624		16	206922024
15	35364792		17	506625396
16	77356395		18	832200162
17	105800778		19	896996238
18	86255844		20	593959458
19	36453678		21	209710524
20	5835012		22	28922142

D — Archimedean lattice (3, 3, 4, 3, 4) site problem

	$s = 2$	$\sum_b bg_{stb} (\times 4)$	12	2652
6		2	13	3680
7		8	14	1560
	$s = 3$		15	120
8		44	$s = 7$	
9		24	10	36
	$s = 4$		11	656
8		8	12	2644
9		104	13	8220
10		210	14	15100
11		48	15	12272
	$s = 5$		16	3240
9		48	17	168
10		248	$s = 8$	
11		832	11	224
12		644	12	2190
13		80	13	9696
	$s = 6$		14	26442
10		208	15	55872
11		724	16	63322

17	33960	14	21148
18	6056	15	107820
19	224	16	407184
s = 9		17	1168464
12	1344	18	2518668
13	7436	19	4211012
14	33664	20	5012660
15	92464	21	3902412
16	196812	22	1753036
17	275136	23	357472
18	218848	24	25948
19	82256	25	440
20	10396	s = 12	
21	288	12	38
s = 10		13	768
12	356	14	12156
13	5408	15	84764
14	27408	16	409734
15	117676	17	1453032
16	327452	18	4178896
17	697796	19	9142376
18	1100140	20	15939366
19	1110356	21	21095484
20	656814	22	19821760
21	178864	23	12241136
22	16796	24	4242200
23	360	25	669848
s = 11		26	38508
12	136	27	528
13	2140		

D — Archimedean lattice (3, 3, 3, 4, 4) site problem

s = 2	$\sum_b \text{bg}_{\text{stb}} (\times 2)$	s = 5	
6	2	9	14
7	2	10	184
8	1	11	318
s = 3		12	280
7	6	13	144
8	8	s = 6	
9	20	10	56
s = 4		11	626
8	10	12	1028
9	38	13	1378
10	102	14	1292
11	30	15	180
12	6	16	20

	$s = 7$		19	524380
11	322		20	435309
12	1724		21	196808
13	3826		22	50046
14	5708		23	3222
15	6828		24	144
16	2832			
17	660		$s = 11$	
			13	754
	$s = 8$		14	10084
11	48		15	56894
12	1322		16	216292
13	5008		17	579562
14	13914		18	1189958
15	22892		19	1893344
16	29028		20	2301600
17	21208		21	2177084
18	9158		22	1396480
19	826		23	569130
20	56		24	97684
			25	8540
	$s = 9$			
12	488		$s = 12$	
13	4316		13	84
14	17404		14	4770
15	47576		15	41758
16	88356		16	215426
17	118700		17	764342
18	112864		18	2066141
19	74098		19	4346780
20	18600		20	7293506
21	2512		21	9678184
			22	10131540
	$s = 10$		23	7961512
12	81		24	4476120
13	2390		25	1382338
14	15100		26	232628
15	61894		27	11264
16	163962		28	352
17	326878			
18	480335			

D — *Square bond problem*

	$s = 1$	$\sum_s sg_{stb} (\times 2)$	10	72
6		4		
	$s = 2$		$s = 4$	
8		18	8	4
	$s = 3$		11	160
9		16	12	275

	s = 5		19	97920
10		40	20	58257
12		180		s = 9
13		960	13	480
14		1044	14	1072
	s = 6		15	1476
11		84	16	24984
12		240	17	42516
14		2324	18	84992
15		4704	19	273920
16		3990	20	460040
	s = 7		21	432200
10		12	22	222020
13		1092		s = 10
14		1176	12	48
15		2688	14	558
16		16240	15	6552
17		21696	16	5904
18		15264	17	53080
	s = 8		18	188160
12		154	19	281096
14		1824	20	809612
15		7664	21	1636008
16		7144	22	2281884
17		36576	23	1867624
18		89748	24	845746

D — *Honeycomb bond problem*

	s = 1	$\sum_s \text{sg}_{\text{stb}} (\times 1)$	10	5184
4		6		s = 8
	s = 2		8	216
5		18	10	5940
	s = 3		11	15552
6		56		s = 9
	s = 4		9	990
7		180	10	1050
	s = 5		11	23940
7		36	12	46510
8		558		s = 10
	s = 6		9	330
6		6	10	3990
8		252	11	9240
9		1708	12	89892
	s = 7		13	138930
7		42		s = 11
9		1296	8	30

10	2904		s = 15	
11	14982		9	26
12	56736		11	5796
13	321840		12	36834
14	414792		13	267840
	s = 12		14	1730016
9	264		15	5652390
11	17856		16	20519424
12	58712		17	41415840
13	289848		18	33004544
14	1112436			s = 16
15	1239056		10	378
	s = 13		12	45900
10	1620		13	180702
11	2262		14	1618176
12	91416		15	7296948
13	260268		16	25115160
14	1292508		17	76400448
15	3764712		18	135462936
16	3701418		19	98498952
	s = 14			s = 17
10	390		11	2970
11	8268		12	7344
12	33768		13	276960
13	408492		14	1037808
14	1218804		15	8308410
15	5298120		16	31418934
16	12555000		17	105743982
17	11054610		18	277089606
			19	439782480
			20	293866272

D — *Kagomé lattice site problem*

s = 2	$\sum_b b^2 g_{sbt} (\times 3)$	s = 7	
5	6	7	384
	s = 3	9	8088
6	66	10	32232
	s = 4		s = 8
7	408	8	2472
	s = 5	10	46104
7	96	11	117972
8	1980		s = 9
	s = 6	9	13266
6	36	10	8406
8	1164	11	223344
9	8316	12	416466

	s = 10		15	89507916
9	4344		16	208467996
10	61158		17	176236950
11	94416		s = 15	
12	973692		9	882
13	1435470		11	162306
	s = 11		12	1105230
8	588		13	6111624
10	46632		14	40617600
11	255828		15	113174922
12	681552		16	377802300
13	3958824		17	746740380
14	4861974		18	572993958
	s = 12		s = 16	
9	6144		10	13878
11	325416		12	1403460
12	1066932		13	5488974
13	3967332		14	40162224
14	15296832		15	179523264
15	16256316		16	531568206
	s = 13		17	1520199504
10	41856		18	2636009496
11	41490		19	1850067696
12	1841832		s = 17	
13	4835928		11	117576
14	19813620		12	225234
15	57146988		13	9075648
16	53773968		14	31074372
	s = 14		15	221592582
10	9954		16	799876968
11	231498		17	2375467950
12	693798		18	5918963946
13	8980896		19	9187911360
14	23326068		20	5937914886

FIXED SIZE ENERGY GROUPINGS

E — Honeycomb lattice

	s = 1	$g_{sc} (\times 2)$		s = 5	
3		2		7	36
	s = 2			s = 6	
4		3		6	1
	s = 3			8	93
5		6		s = 7	
	s = 4			7	6
6		14		9	244

s = 8		s = 16	
8	27	10	3
10	648	12	1113
s = 9		14	36405
9	110	16	428955
11	1728	18	2062784
s = 10		s = 17	
8	3	11	42
10	399	13	5340
12	4651	15	127170
s = 11		17	1318254
9	24	19	5794056
11	1362	s = 18	
13	12630	12	356
s = 12		14	22941
10	135	16	433941
12	4468	18	4035356
14	34566	20	16325904
s = 13		s = 19	
9	2	11	6
11	636	13	2244
13	14244	15	91622
15	95312	17	1456674
s = 14		19	12310578
10	27	21	46133390
12	2631	s = 20	
14	44706	12	87
16	264387	14	11838
s = 15		16	348120
11	198	18	4830054
13	10050	20	37445847
15	138938	22	130703016
17	736974		

E — *Square lattice*

s = 1		12	55
4	$g_{se} (\times 1)$	s = 6	
	1	10	2
s = 2		12	40
6	2	14	174
s = 3		s = 7	
8	6	12	22
s = 4		14	168
8	1	16	570
10	18	s = 8	
s = 5		12	6
10	8		

14	134	18	864
16	677	20	9354
18	1908	22	62396
s = 9		24	297262
12	1	26	1056608
14	72	28	2448760
16	656	30	3329608
18	2708	s = 15	
20	6473	16	6
s = 10		18	456
14	30	20	7036
16	482	22	54908
18	3008	24	317722
20	10724	26	1359512
22	22202	28	4401192
s = 11		30	9436252
14	8	32	11817582
16	310	s = 16	
18	2596	16	1
20	13456	18	218
22	42012	20	4748
24	76886	22	46352
s = 12		24	303068
14	2	26	1563218
16	151	28	6095764
18	2086	30	18173796
20	13034	32	36285432
22	58742	34	42120340
24	163494	s = 17	
26	268352	18	88
s = 13		20	3010
16	68	22	36112
18	1392	24	276464
20	11789	26	1603984
22	63256	28	7477928
24	250986	30	26922156
26	633748	32	74496544
28	942651	34	139297108
s = 14		36	150682450
16	22		

E — *Triangular lattice*

s = 1		$g_{se} (\times 1)$	s = 3	
6		1	12	2
s = 2				
10		3	14	9

	$s = 4$		30	4817
14	3		32	12453
16	6		34	28305
18	29		36	55411
	$s = 5$		38	92205
16	6		40	101679
18	21		42	65822
20	60		$s = 11$	
22	99		24	24
	$s = 6$		26	249
18	14		28	1164
20	42		30	3876
22	129		32	12264
24	281		34	34263
26	348		36	78990
	$s = 7$		38	165144
18	1		40	295356
20	30		42	438264
22	105		44	434784
24	276		46	251655
26	732		$s = 12$	
28	1248		24	2
30	1260		26	117
	$s = 8$		28	702
20	6		30	3163
22	69		32	10557
24	246		34	32901
26	720		36	91389
28	1737		38	226125
30	3795		40	482850
32	5472		42	929414
34	4644		44	1531383
	$s = 9$		46	2050899
22	27		48	1852892
24	160		50	969819
26	609		$s = 13$	
28	1818		26	27
30	4697		28	414
32	9990		30	2126
34	19014		32	8418
36	23662		34	29601
38	17382		36	89680
	$s = 10$		38	250641
22	3		40	631218
24	86		42	1431751
26	432		44	2845248
28	1458		46	5093199

48	7761168	38	252177
50	9484524	40	694122
52	7876554	42	1782600
54	3762517	44	4157097
	$s = 14$	46	8736174
26	3	48	16309377
28	168	50	27275403
30	1320	52	38620725
32	6336	54	43453965
34	23721	56	33417534
36	81183	58	14680890

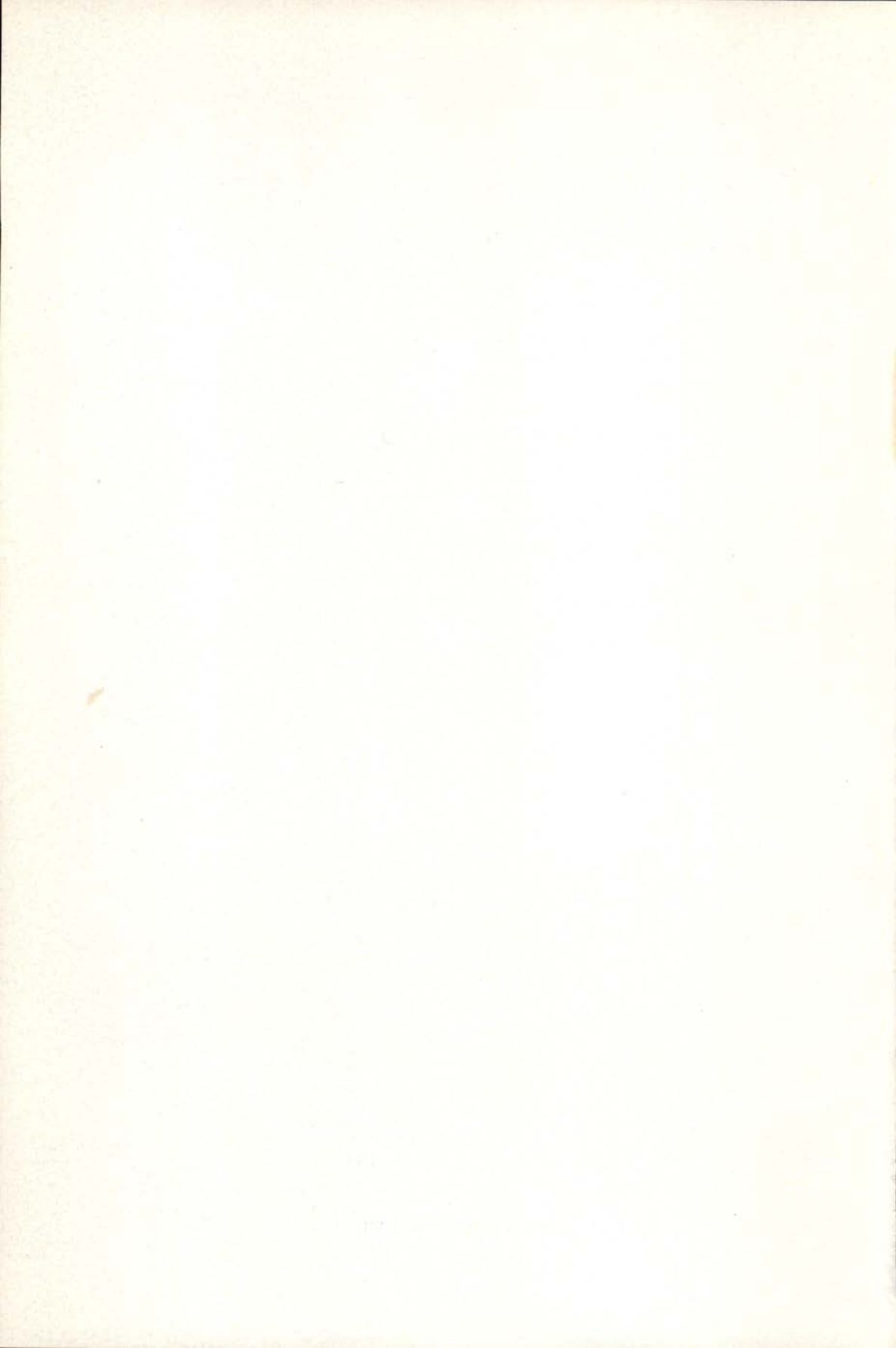
E — *Square covering site problem*

	$s = 1$	$g_{se} (\times 2)$	24	344
6		2	26	1924
	$s = 2$		28	4035
10		6	30	10858
	$s = 3$		32	13259
12		4	34	2958
14		18		$s = 9$
	$s = 4$		22	26
12		1	24	168
16		37	26	1076
18		50	28	3336
	$s = 5$		30	13512
16		12	32	25240
18		26	34	56634
20		192	36	47320
22		142	38	8134
	$s = 6$			$s = 10$
18		16	22	4
20		102	24	58
22		246	26	580
24		874	28	2266
26		390	30	9360
	$s = 7$		32	29444
18		2	34	83758
20		24	36	152964
22		226	38	266710
24		640	40	163340
26		1826	42	22050
28		3508		$s = 11$
30		1086	24	16
	$s = 8$		26	236
20		6	28	1372
22		82	30	6260

32	23720	46	4832436
34	74098	48	1784168
36	222372	50	162466
38	493862		
40	869372	s = 13	
42	1169136	26	12
44	545580	28	316
46	60146	30	2122
		32	11448
		34	42428
24	1	36	170104
26	76	38	520236
28	743	40	1612728
30	3704	42	3966084
32	17174	44	9399652
34	58860	46	15765404
36	208354	48	23066864
38	553224	50	19101104
40	1507761	52	5711504
42	2822608	54	440750
44	4625299		

REFERENCES

- [1] SYKES M. F., WATTS M. G., GAUNT D. S., *J. Phys.*, **A8**, 1448 (1975).
- [2] SYKES M. F., GAUNT D. S., MARTIN J., MATTINGLY S. R., ESSAM J. W. *J. Math. Phys.*, **14**, 1071 (1973).
- [3] DUARTE J. A. M. S., MARQUES M. C. A. M., *Nuovo Cim.* **B54**, 508 (1979).
- [4] SYKES M. F., GAUNT D. S., GLEN M., *J. Phys.*, **A9**, 715 (1976).
- [5] HILEY B. J., SYKES M. F., *J. Chem. Phys.*, **34**, 1531 (1961).
- [6] ENTING I. G., *J. Phys.*, **A13**, 3713 (1980).
- [7] BLEASE J., ESSAM J. W., PLACE C. M., *J. Phys.*, **C11**, 4009 (1978).
- [8] SYKES M. F., GLEN M., *J. Phys.*, **A9**, 87 (1976).
GAUNT D. S., SYKES M. F., RUSKIN H. J., *J. Phys.*, **A9**, 1899 (1976).
GAUNT D. S., RUSKIN H. J., *J. Phys.*, **A11**, 1369 (1978).
- [9] PETERS H. P., STAUFFER D., HOLTERS H. P., LOEWENICH L., *Zeit f. Phys.* **B35**, 399 (1979).
- [10] SYKES M. F., GAUNT D. S., GLEN M., *J. Phys.*, **A14**, 287 (1981).
- [11] DUARTE J. A. M. S., *J. Physique*, **40**, 845 (1979).
- [12] CHERRY R. J., PH. D. THESIS, London, unpublished (1979).
- [13] GAUNT D. S., MIDDLEMISS K. M., TORRIE G., WHITTINGTON S. G., *J. Phys.*, **A13**, 3029 (1980).
- [14] DUNN A. G., ESSAM J. W., RITCHIE D. S., *J. Phys.*, **C8**, 4219 (1975).
- [15] AGRAWAL P., REDNER S., REYNOLDS P. J., STANLEY H. E., *J. Phys.*, **A12**, 2073 (1979).
- [16] DUARTE J. A. M. S., RUSKIN, H. J., *Zeit. f. Phys.*, **B**, in press (1981).
- [17] LUBENSKY T. C., ISAACSON, J., *Phys. Rev.*, **A20**, 2130 (1979).
- [18] HARRIS A. B., LUBENSKY T. C., *Phys. Rev.*, **B23**, 3591 (1981).
- [19] DUARTE J. A. M. S., RUSKIN H. J., *J. Physique* in press (1981).



SOCIEDADE PORTUGUESA DE FÍSICA
AV. REPÚBLICA 37-4.º, 1000 LISBOA, PORTUGAL

PORTUGALIAE PHYSICA publishes articles or research notes with original results in theoretical, experimental or applied physics; invited review articles may also be included.

Manuscripts, with an abstract, may be written in English or French; they should be typewritten with two spaces and in duplicate. Figures or photographs must be presented in separate sheets and be suitable for reproduction with eventual reduction in size; captions should make the figures intelligible without reference to the text. Authors are requested to comply with the accepted codes concerning references.

There is no page charge. Author(s) will get 50 free reprints (without covers); these are to be shared among all the authors of the article. Authors interested in more reprints should say so when sending their manuscripts; quotations shall be sent with the proofs.

Subscription rates for volume 12:

1,200 Escudos (US\$20) — individuals

3,000 Escudos (US\$50) — libraries

PORTUGALIAE PHYSICA may also be sent on an exchange basis; we welcome all suggestions to such effect.

All mail to be addressed to

PORTUGALIAE PHYSICA

C/O LABORATÓRIO DE FÍSICA, FACULDADE DE CIÊNCIAS
PRAÇA GOMES TEIXEIRA
4000 PORTO PORTUGAL

PORTUGALIAE PHYSICA

VOL. 12 · NUMB 1/2 · 1981

CONTENTS

NUCLEAR PHYSICS

Time-Dependent Generator Coordinate Method and the N-N Interaction

L. P. BRITO and C. A. SOUSA 1

Fundamental Properties of Liquid Argon, Krypton and Xenon as Radiation Detector Media.

T. DOKE 9

CONDENSED MATTER PHYSICS

The Estimated Intensity Variance as a Mean of Expected and Sample Variances.

W. GONSCHOREK 49

The Thermal and Magnetic Properties of Some Rare Earth-Pd₃ Phases of the AuCu₃ Structure

J. M. MACHADO DA SILVA, W. E. GARDNER, I. R. HARRIS 61

GENERAL AND MATHEMATICAL PHYSICS

An Epitome of Configurational Data on Connected Clusters

J. A. M. S. DUARTE 99

PORTUGALIAE PHYSICA

VOLUME 12
FASCÍCULO 3-4
1981

SOCIEDADE PORTUGUESA DE FÍSICA

PORTUGALIAE PHYSICA

Fundada em 1943 por A. Cyrillo Soares, M. Telles Antunes, A. Marques da Silva e M. Valadares

Director

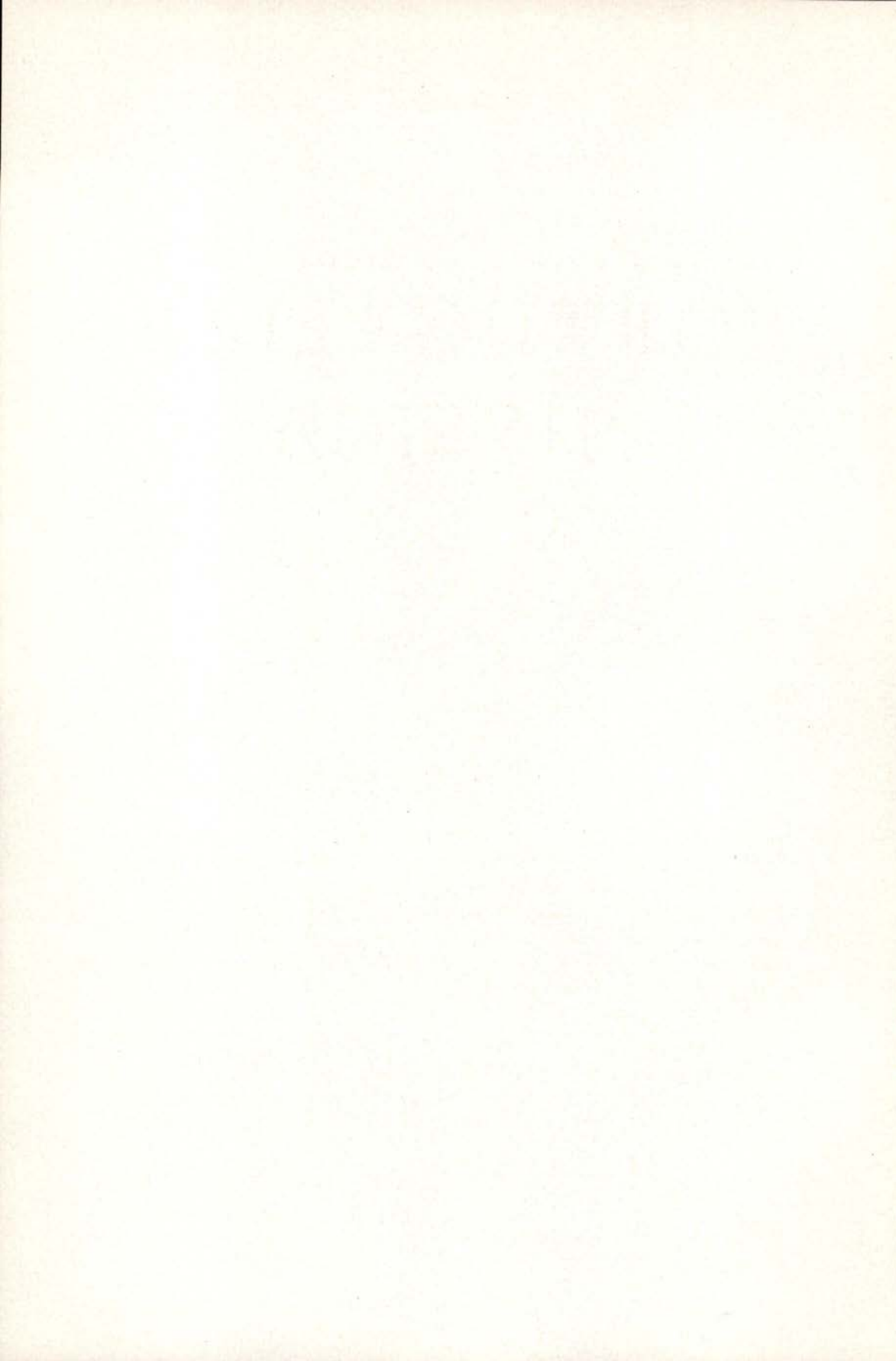
J. M. Araújo (Faculdade de Ciências, Universidade do Porto)

Comissão Redactorial

- J. M. Araújo (Faculdade de Ciências, Universidade do Porto)
J. Gomes Ferreira (Faculdade de Ciências, Universidade de Lisboa)
F. Bragança Gil (Faculdade de Ciências, Universidade de Lisboa)
M. F. Laranjeira (Faculdade de Ciências e Tecnologia, Universidade Nova de Lisboa)
F. D. S. Marques (Universidade do Minho)
A. Farinha Martins (Centro de Física da Matéria Condensada, Lisboa)
R. Vilela Mendes (Centro de Física da Matéria Condensada, Lisboa)
A. M. C. Moutinho (Centro de Física Molecular, Lisboa)
J. Pinto Peixoto (Faculdade de Ciências, Universidade de Lisboa)
A. Policarpo (Faculdade de Ciências e Tecnologia, Universidade de Coimbra)
J. da Providência (Faculdade de Ciências e Tecnologia, Universidade de Coimbra)
F. Carvalho Rodrigues (Laboratório de Física e Engenharia Nucleares, Sacavém).
F. D. Santos (Faculdade de Ciências, Universidade de Lisboa)
E. Ducla Soares (Faculdade de Ciências, Universidade de Lisboa)
O. D. D. Soares (Faculdade de Ciências, Universidade do Porto)
J. B. Sousa (Faculdade de Ciências, Universidade do Porto)
A. T. Rocha Trindade (Instituto Superior Técnico, Lisboa)
L. Alte da Veiga (Faculdade de Ciências e Tecnologia, Universidade de Coimbra)

PORTUGALIAE PHYSICA

VOLUME 12
FASCÍCULO 3-4
1981



THE ASYMPTOTIC APPROXIMATION IN HEAVY ION TRANSFER REACTIONS (*)

A. M. GONÇALVES and F. D. SANTOS

Laboratório de Física, Faculdade de Ciências da Universidade de Lisboa
1294 Lisboa Codex, Portugal

(Received 14 December 1981)

ABSTRACT — Finite range effects in heavy ion transfer reactions are discussed using a previously developed formalism where the bound state wave functions are represented by the asymptotic spherical Hankel functions. Using the asymptotic approximation and a local recoil momentum a DWBA computer code was developed which has the simplicity of a zero-range program and allows the inclusion of finite range and recoil effects. Good agreement is obtained with results from full finite range calculations for one nucleon transfer reactions. The effects of the Coulomb terms in the interaction are discussed.

1 — INTRODUCTION

Finite range and recoil effects are known to be generally very important in transfer reactions induced by heavy-ions. Various approximate methods [1]-[11] have been proposed for treating these effects in the distorted wave Born approximation (DWBA). By using them we obtain a more detailed understanding of the reaction mechanism, particularly of those aspects which are specifically related with the finite range of the interaction. Furthermore they are useful since full finite range calculations are time consuming, specially when it is necessary to include multi-step contributions to the reaction cross section.

Here we report on an extension of the Buttle and Goldfarb approximation [1] in which the recoil effects associated with the

(*) Research supported by Centro de Física Nuclear (INIC).

finite mass of the transferred particle can be easily included. From another point of view our model for the transition amplitude is a generalization of the zero range approximation to states with orbital angular momentum different from zero. The reaction form factor, which may include the effects of recoil, is calculated using analytical methods and the DWBA calculation retains the simplicity of a zero-range code.

Results of calculations using this model for various reactions, including cases where the contribution from unnatural parity processes is important, are compared with full finite range calculations. The significance and reliability of the model is discussed. In the present calculation and also in those of a preceding short paper [12] the recoil momentum is obtained using a local momentum approximation.

With the same model and approximations that are described here in detail we have performed calculations for the cross section and analysing powers of the $^{58}\text{Ni}(^7\text{Li}, ^6\text{Li})^{59}\text{Ni}$ reaction at an incident energy of 20.3 MeV. In this work, published elsewhere [13], [14], it was shown that the agreement between the DWBA predictions and the observed Q-value dependence of the vector analysing power was greatly improved when the recoil momentum is generated using a semi-classical model proposed by Brink [15], [16].

2 — DWBA FORMALISM

The DWBA transition amplitude for the transfer reaction $A(a,b)B$ where $a = b + x$ and x is the transferred cluster is given by

$$T_{ba} = \int dr_{xA} \, dr_{bx} \, \chi_b^{(-)*}(\mathbf{r}_b) \langle Bb | V | Aa \rangle \chi_a^{(+)}(\mathbf{r}_a), \quad (1)$$

where the coordinates \mathbf{r}_{xA} , \mathbf{r}_{bx} , \mathbf{r}_a and \mathbf{r}_b are illustrated in Fig. 1 and $\chi_a^{(+)}$ and $\chi_b^{(-)}$ are elastic scattering wave functions in the entrance and exit channels. Using a fractional parentage expansion of the internal states of a and B into states of x and performing the integration over the internal coordinates of b ,

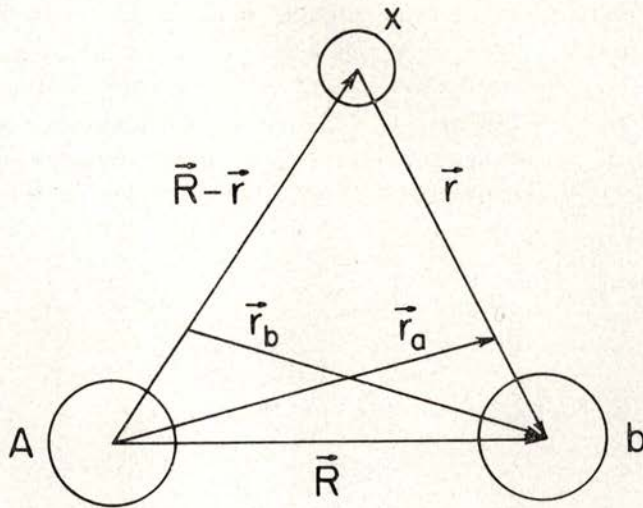


Fig. 1 — The coordinate vectors for a general transfer reaction.

A and X the transition matrix can be written, using essentially the notation of ref [10], as

$$\begin{aligned}
 & \langle J_B M_B s_b \sigma_b | V | J_A M_A s_a \sigma_a \rangle = \\
 & \sum_{L j_1 j_2} (J_A M_A j_2 \xi_2 | J_B M_B) (L \Lambda j_1 \xi_1 | j_2 \xi_2) \\
 & \cdot (-1)^{S_b - \sigma_b} (s_a \sigma_a s_b - \sigma_b | j_1 \xi_1) \hat{L} \sum_{l_1 l_2} A_{L j_1 j_2}^{l_1 l_2} \beta_{j_1 j_2}^{l_1 l_2 L \Lambda}, \quad (2)
 \end{aligned}$$

where $\hat{L} = (2L + 1)^{1/2}$,

$$A_{L j_1 j_2}^{l_1 l_2} = \Theta_{l_1 j_1} \Theta_{l_2 j_2} \hat{s}_a \hat{L} (-1)^{j_1 + s_x} \begin{Bmatrix} L & j_1 & j_2 \\ s_x & l_2 & l_1 \end{Bmatrix}, \quad (3)$$

and the reduced amplitude β is given by

$$\beta_{j_1 j_2}^{l_1 l_2 L \Lambda} = \frac{i^{-L}}{\hat{L}} \int d\mathbf{r}_{xA} d\mathbf{r}_{bx} \chi_b^{(-)*}(\mathbf{r}_b) f_{L j_1 j_2 \Lambda}^{l_1 l_2}(\mathbf{r}_{xA}, \mathbf{r}_{bx}) \chi_a^{(+)}(\mathbf{r}_a). \quad (4)$$

Here L is the total orbital angular momentum transfer in the reaction and the spins of A, a, B, b and x are denoted by J_A, s_a, J_B, s_b and s_x . The quantities $\Theta_{l_1 j_1}$ and $\Theta_{l_2 j_2}$ are fractional parentage coefficients corresponding to a bound x with angular momentum quantum numbers $l_1 j_1$ and $l_2 j_2$. The form factor of the reduced amplitude is given by

$$f_{l_1 j_1 l_2 j_2}^{l_1 l_2 L \Lambda}(\mathbf{r}_{xA}, \mathbf{r}_{bx}) = i^{L+l_1-l_2} \sum_{\lambda_1 \lambda_2} (l_2 \lambda_2 l_1 \lambda_1 | L \Lambda) \cdot R_{l_2 j_2}(\mathbf{r}_{xA}) Y_{l_2}^{\lambda_2*}(\hat{\mathbf{r}}_{xA}) V R_{l_1 j_1}(\mathbf{r}_{bx}) Y_{l_1}^{\lambda_1*}(\hat{\mathbf{r}}_{bx}), \quad (5)$$

where $R_{l_1 j_1}$ and $R_{l_2 j_2}$ are the normalized radial wave functions of x in the projectile and residual nucleus. In the conventional form of the DWBA the interaction V responsible for the transfer is assumed to be V_{bx} in the post representation and V_{Ax} in the prior representation.

It is well known that there is a strong localization of the integrand in eq. (4), as a function of the separation \mathbf{R} between the heavy ion cores, due to combined action of the Coulomb barrier and of large absorption for small R , with the lack of overlap between the bound state wave functions at large R . It is therefore appropriate to treat the deviations from \mathbf{R} in the arguments of the distorted waves in an approximate way. To discuss such approximations it is useful to perform Taylor expansions of $\chi_a^{(+)}$ and $\chi_b^{(-)}$. Representing \mathbf{r}_{bx} by \mathbf{r} we can write

$$\beta_{l_1 j_1 l_2 j_2}^{l_1 l_2 L \Lambda} = \frac{i^{-L}}{\tilde{L}} \int d\mathbf{R} d\mathbf{r} e^{i\mathbf{r} \cdot \mathbf{0}} f_{l_1 j_1 l_2 j_2}^{l_1 l_2 L \Lambda}(\mathbf{R}-\mathbf{r}, \mathbf{r}) \chi_b^{(-)*}(\gamma\mathbf{R}) \chi_a^{(+)}(\mathbf{R}), \quad (6)$$

where $\gamma = M_A/M_B$,

$$\mathbf{0} = \frac{M_x}{M_A} \nabla_b - \frac{M_x}{M_a} \nabla_a, \quad (7)$$

and ∇_a (∇_b) is the gradient with respect to \mathbf{R} and acts only on the function $\chi_a^{(+)}$ ($\chi_b^{(-)*}$). Notice that we could have used \mathbf{r}_{xA} instead of \mathbf{r}_{bx} as integration variable. A similar derivation gives

$$\beta_{j_1 j_2}^{l_1 l_2 L \Lambda} = \frac{i^{-L}}{\hat{L}} \int d\mathbf{R} d\mathbf{r} e^{\mathbf{r} \cdot \mathbf{Q}} f_{L j_1 j_2 \Lambda}^{l_1 l_2}(\mathbf{r}, \mathbf{R}-\mathbf{r}) \chi_b^{(-)*}(\mathbf{R}) \chi_a^{(+)}(\mu\mathbf{R}), \quad (8)$$

where \mathbf{r}_{xA} was also represented by \mathbf{r} , $\mu = M_b/M_a$ and

$$\mathbf{Q} = \frac{M_x}{M_b} \nabla_a - \frac{M_x}{M_B} \nabla_b. \quad (9)$$

Both eqs. (6) and (8) are exact and will be used as the starting point for our analysis.

When comparing eqs. (6) and (8) we notice that the vector \mathbf{r} in the translation operator is the argument of the projectile and residual nucleus bound state wave functions, respectively. In relation with our model this makes the expression (6) more convenient to use in the post form of the DWBA transition amplitude while the expression (8) is more convenient to use in the prior form of the DWBA transition amplitude.

In eqs. (6) and (8) the effects due to recoil are described by the operators $\exp(\mathbf{r} \cdot \mathbf{0})$ and $\exp(\mathbf{r} \cdot \mathbf{Q})$. These operators become equal to the identity operator if we assume that the transferred particle has no mass. This approximation, known as the no-recoil approximation, is described in ref. [1]. We can take into account the recoil effects to all orders in our expansion of the translation operator by assuming a local momentum approximation when operating with $\exp(\mathbf{r} \cdot \mathbf{0})$ or $\exp(\mathbf{r} \cdot \mathbf{Q})$ on the distorted waves. In this approximation the operator $\mathbf{0}$ in eq. (7) is replaced by the recoil momentum,

$$\mathbf{p} = - \left(\frac{M_x}{M_B} \mathbf{k}_b + \frac{M_x}{M_a} \mathbf{k}_a \right), \quad (10)$$

where \mathbf{k}_a and \mathbf{k}_b represent local momenta in the entrance and exit channels, respectively. The usual procedure is to choose the direction of \mathbf{p} along the bisector of the scattering angle corresponding to the distance of closest approach for a Coulomb orbit

in the exit channel. It has been shown by Braun-Munzinger *et al.* [17], that the reduced transition amplitude depends weakly on that direction.

We can follow a different approach in which the recoil momentum \mathbf{p} is generated using a semiclassical model [15], [16]. This has been described in references [13], [14]. We obtain

$$\mathbf{p} = -\mathbf{n} \left(\frac{Q}{v} + \frac{1}{2} M_x v \right) \quad (11)$$

where \mathbf{n} is a unit vector in the reaction plane tangent to the projectile trajectory at the point where the transfer is more probable, v is the relative velocity between the heavy ions at that point and Q is the reaction Q -value.

3 — USE OF SPHERICAL HANKEL FUNCTIONS

The most simple way to represent the bound states in a heavy ion transfer reaction is to use the Hankel function which describes the asymptotic behaviour for large r . In this approximation, which we shall call the asymptotic approximation, the form factor of the reduced amplitude in the post representation is

$$f_{L_j i_1 i_2 \Lambda}^{1 1/2}(\mathbf{R}-\mathbf{r}, \mathbf{r}) = i^{L+1-i_2} \sum_{\lambda_1 \lambda_2} (1_2 \lambda_2 1_1 \lambda_1 | L \Lambda) N'_0 i^{1/2} h_{i_2}^{(1)}(i\beta | \mathbf{R}-\mathbf{r}) \\ Y_{i_2}^{\lambda_2*}(\hat{\mathbf{R}}-\hat{\mathbf{r}}) \frac{\hbar^2}{2M_x \mu} (\nabla^2 - \alpha^2) N_0 i^{i_1} h_{i_1}^{(1)}(i\alpha r) Y_{i_1}^{\lambda_1}(\hat{\mathbf{r}}), \quad (12)$$

where we have used the Schrödinger equation of nucleus a to replace the V_{bx} interaction and assumed $\alpha_0 = \alpha$ and $\beta_0 = \beta$. Using a recoil momentum \mathbf{p} the \mathbf{r} integration in eq. (6) is given by

$$\int d\mathbf{r} e^{i\mathbf{p}\cdot\mathbf{r}} f_{L_j i_1 i_2 \Lambda}^{1 1/2}(\mathbf{R}-\mathbf{r}, \mathbf{r}) = \frac{\hbar^2}{2M_x \mu} N'_0 N_0 i^L (-1)^{i_1+i_2} \\ \sum_{\lambda_1 \lambda_2} (1_2 \lambda_2 1_1 -\lambda_1 | L \Lambda) (-1)^{\lambda_1} H_{i_1 \lambda_1 i_2 \lambda_2}(\mathbf{R}, \mathbf{p}, \alpha, \beta), \quad (13)$$

where

$$H_{l_1 \lambda_1 l_2 \lambda_2}(\mathbf{R}, \mathbf{p}, \alpha, \beta) = \int d\mathbf{r} [h_{l_2}^{(1)}(i\beta|\mathbf{R}-\mathbf{r}|) Y_{l_2}^{\lambda_2}(\hat{\mathbf{R}}-\hat{\mathbf{r}})]^* (\nabla^2 \cdot \alpha^2) h_{l_1}^{(1)}(i\alpha r) Y_{l_1}^{\lambda_1}(\hat{\mathbf{r}}) e^{i\mathbf{p}\cdot\mathbf{r}}. \quad (14)$$

The procedure which is usually followed to calculate this type of integral is to separate variables in $h_{l_2}^{(1)}(i\beta|\mathbf{R}-\mathbf{r}|) Y_{l_2}^{\lambda_2}(\hat{\mathbf{R}}-\hat{\mathbf{r}})$ using the well known addition theorem for Hankel functions [1], [18]. This, however, involves an expansion that in general does not converge uniformly and requires further approximations in the calculation of the folding integral. As shown in the Appendix 3 of ref [10] the intergral (14) can be calculated analitically without the above shortcomings. Using this result and eqs. (6), (13) and (14) we finally obtain for the reduced amplitude in the asymptotic approximation

$$\beta_{i_1 j_2}^{l_1 l_2 L \Lambda} = \frac{4\pi}{\hat{L}} \sum_{l_r \lambda_r} (l_r \lambda_r L_c \Lambda_c | L \Lambda) \int d\mathbf{R} Y_{L_c}^{\Lambda_c*}(\mathbf{R}) y_{l_r}^{\lambda_r*}(\mathbf{ip}) \cdot F_{l_1 l_2 L L_c l_r}(\mathbf{R}, \mathbf{p}^2) \chi_b^{(-)*}(\gamma\mathbf{R}) \chi_a^{(+)}(\mathbf{R}), \quad (15a)$$

where

$$F_{l_1 l_2 L L_c l_r}(\mathbf{R}, \mathbf{p}^2) = \Gamma_{l_1 l_2 L_r L L_c l_r} X_{l_1 l_2 L_r L_c l_r}(\mathbf{R}) \quad (15b)$$

$$\Gamma_{l_1 l_2 L_r L L_c l_r} = (-1)^{L_r} \hat{l}_1 \hat{L}_r \hat{L}_c \hat{l}_r \left\{ \begin{matrix} l_1 l_2 L \\ L_c l_r L_r \end{matrix} \right\} (1_1 0 1_r 0 | L_r 0) (L_r 0 L_c 0 | l_2 0), \quad (15c)$$

$$X_{l_1 l_2 L_r L_c l_r} = \frac{\hbar^2}{2M_{x\mu}} \frac{(2l_1+1)!!}{(2l_r+1)!! (2L_r+1)!!} N_0 N'_0 \frac{\beta^{L_r}}{\alpha^{l_1+1}} i^{L_c} h_{L_c}^{(1)}(i\beta R), \quad (15d)$$

$$(2l+1)!! = (2l+1)(2l-1) \dots \text{ and}$$

$$L_r = l_1 - l_r . \quad (16)$$

The orbital angular momenta l_r and L_c have a very simple physical interpretation [11]: l_r is the part of the total balance of orbital angular momentum in the transfer process which is due to the

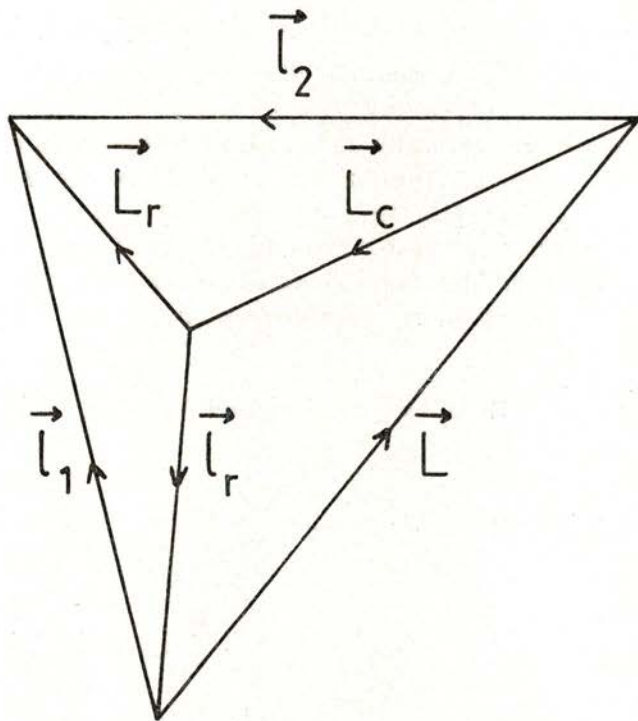


Fig. 2 — Vector coupling of the orbital angular momentum operators in a transfer reaction. The vectors are defined in the text.

finite mass of x and is usually called the recoil angular momentum. From the angular momentum coupling in eqs (15) we conclude that L_c is the orbital angular momentum transferred from the relative motion of the heavy ion cores A and b in the entrance channel to the relative motion of A and b in the exit channel. The coupling of orbital angular momentum in a transfer reaction is illustrated in Fig. 2, where the sum $l_r + l_1$ (equal to

$l_2 - L_c$) is represented by L_r . The no-recoil approximation is obtained with $l_r = 0$, which implies $L_c = L$ and $l_1 = L_r$. With this approximation the eqs. (15) reproduce the radial form factor of ref. [1],

$$F_{l_1 l_2 L L_c l_r} (R, p^2) = (-1)^{l_1} \hat{l}_1 (1_1 0 L 0 | 1_2 0) \frac{\hbar^2}{2M_{x\mu}} \cdot N_0 N'_0 \frac{\beta^{l_1}}{\alpha^{l_1+1}} i^L h_L^{(1)}(i\beta R). \quad (17)$$

This result shows that the present model can be considered as a natural extension of the Buttke and Goldfarb approximation [1].

The most general selection rule due to parity conservation in the reaction involves the quantum numbers L_c and l_r . The particular form of angular momentum coupling in eq. (15c) implies that [11]

$$l_r + L_c + l_1 + l_2 = \text{even}. \quad (18)$$

In the exact DWBA matrix element there is no restriction on the values of l_r . However due to the small mass of the transferred cluster relative to the heavy ion cores only the first few values of l_r are likely to give important contributions to the transition amplitude. This has been shown, for instance, in the work of Braun-Munzinger *et al.* [17]. In the asymptotic approximation there is an upper limit for the allowed values of l_r , since according with eq. (16) $l_r \leq l_1$. Eq. (16) means that l_r is anti-parallel to l_1 . This selection rule is a consequence of our description of the bound state wave function of x in the projectile as one Hankel function. With this approximation we assume that the transfer process is insensitive to the finite range of the binding potential of x in a . In fact for one Hankel function the product $V_{bx} R_{l_1 j_1} Y_{l_1}^{\lambda_1}$, present in the form factor, has zero range (see eq. (A.23) of ref. [10]) and therefore it cannot generate an orbital angular momentum larger than l_1 . For a finite range interaction we can have $l_r > l_1$. Notice that the asymptotic approxi-

mation allows for the inclusion of recoil effects and at the same time maintains the radial form factor X , for each l_r , proportional to $N_0 N'_0$. It is therefore particularly suited to study the dependence of the cross section on $N_c N'_0$ which is a well defined quantity in heavy ion transfer reactions, particularly at sub-Coulomb energies [19], [20].

Following essentially the same type of derivation we can readily obtain from eq. (8) the reduced transition amplitude for the asymptotic approximation in the prior form

$$\beta_{j_1 j_2}^{l_1 l_2 L \Lambda (\text{prior})} = (-1)^{l_1 + l_2 + L} \frac{4\pi}{\hat{L}} \sum_{l_r \lambda_r} (l_r \lambda_r L_c \Lambda_c | L \Lambda) \int d\mathbf{R} Y_{L_c}^{\Lambda_c*}(\hat{\mathbf{R}}) \cdot y_{l_r}^{\lambda_r*}(\mathbf{i}\mathbf{p}) F_{l_1 l_2 L L_c l_r}^{(\text{prior})}(\mathbf{R}, p^2) \chi_b^{(-)*}(\mathbf{R}) \chi_a^{(+)}(\mu\mathbf{R}), \quad (19a)$$

where

$$F_{l_1 l_2 L L_c l_r}^{(\text{prior})}(\mathbf{R}, p^2) = \Gamma_{l_1 l_2 L_r L L_c l_r} X_{l_1 l_2 L_r L_c l_r}^{(\text{prior})}(\mathbf{R}), \quad (19b)$$

$$X_{l_1 l_2 L_r L_c l_r}^{(\text{prior})} = (-1)^{l_r} \frac{\hbar^2}{2M_{XY}} \frac{(2l_2 + 1)!!}{(2l_r + 1)!! (2L'_r + 1)!!} N_0 N'_0 \frac{\alpha^{l_r}}{\beta^{l_2 + 1}} i^{L_c} h_{L_c}^{(1)}(i\alpha\mathbf{R}), \quad (19c)$$

and

$$L'_r = l_2 - l_r. \quad (19d)$$

This selection rule, involving the angular momentum $L'_r = l_2 - l_r$ (equal to $l_1 + L_c$), implies that in the prior representation $l_r \leq l_2$.

We emphasize that as regards the bound states the asymptotic approximation is equivalent to a generalization to states with $l_1 > 0$ of what is usually called a zero range approximation in a transfer from an s-state. In fact notice that for $l_1 = 0$ the expression (12) implies that V_{bx} is proportional to a δ -function.

4 — COULOMB EFFECTS

In the preceding analysis we have assumed that the interaction V in the DWBA matrix element is purely nuclear. Here we consider the effects of the Coulomb terms of this interaction. In the post representation these Coulomb terms are of the form [21]

$$\Delta V_c = \frac{Z_b Z_A e^2}{R} - \frac{Z_b Z_B e^2}{r_b}, \quad (20)$$

where Z_i is the charge of nucleus i and $r_b = \gamma R + (1-\gamma)r$. Since ΔV_c has a weak dependence on r ($\gamma \approx 1$) we can write

$$\Delta V_c \approx \frac{Z_b Z_A e^2}{R} (1 - 1/\gamma) - \frac{Z_x Z_B e^2}{\gamma R}. \quad (21)$$

In the prior representation the analogous approximation yields

$$\Delta V_c^{(\text{prior})} \approx \frac{Z_b Z_A e^2}{R} (1 - 1/\mu) - \frac{Z_x Z_A e^2}{\mu R}. \quad (22)$$

The calculation of the effects of ΔV_c on the transition matrix is straightforward using eqs. (21) and (22) although it involves integrals of the type

$$J_{l_1 \lambda_1 l_2 \lambda_2}(\mathbf{R}, \mathbf{p}, \alpha, \beta) = \int d\mathbf{r} [h_{l_2}^{(1)}(i\beta|\mathbf{R}-\mathbf{r}|) Y_{l_2}^{\lambda_2}(\hat{\mathbf{R}}-\hat{\mathbf{r}})]^* \cdot h_{l_1}^{(1)}(i\alpha r) Y_{l_1}^{\lambda_1}(\hat{\mathbf{r}}) e^{i\mathbf{p}\cdot\mathbf{r}}. \quad (23)$$

These integrals can be easily calculated for $\mathbf{p} = 0$ and were discussed in ref. [10]. For $\mathbf{p} \neq 0$ the analytic calculation of $J_{l_1 \lambda_1 l_2 \lambda_2}$ is considerably more difficult as it is shown in the Appendix, where an approximate expression is also derived.

5 — NUMERICAL RESULTS

A DWBA computer program called HYDRA [22] has been coded in FORTRAN which generates the distorted waves and calculates the reduced transition amplitudes using eqs. (15) and (19) in the post and prior representations. To illustrate the validity of the asymptotic approximation we performed calculations for angular distributions which were previously analyzed with other DWBA codes in particular with full finite range programs. Fig. 3 shows results for the one neutron transfer reaction $^{12}\text{C} (^{14}\text{N}, ^{13}\text{N}) ^{13}\text{C}_{g.s.}$ at $E_{\text{Lab}} = 78$ MeV obtained using the same optical model parameters as in ref. [24]. Since this is a transfer between two $p\frac{1}{2}$ states the recoil effects can be quite large. The calculations of Fig. 3 compare the usual no-recoil Buttle and Goldfarb approximation with the asymptotic approximation described in this work and given by eqs. (15) and (19). We emphasize that in both cases the bound state wave functions are described by one Hankel function and depend exclusively on the parameters N_0, α_0 and N'_0, β_0 . The constants N_0 and N'_0 were extracted from bound state wave function generated in a Woods-Saxon well with geometry parameters $r_0 = 1.25$ fm and $a = 0.65$ fm.

We find that in this reaction the asymptotic approximation provides an accurate description of the recoil effects. This can be seen in Fig. 4 where it is compared with full finite range results obtained with the code LOLA for the same optical model and bound state parameters and for incident energies of 78 and 100 MeV. Both curves agree well in shape and in absolute value. The product of spectroscopic factors for the initial and final states $S_1 S_2$ differs by less than 18% at both energies. In fact we obtain in the post representation $S_1 S_2 = 0.50$ and 0.60 at 78 and 100 MeV, while the full finite range calculations [23], [26] give $S_1 S_2 = 0.53$ and 0.51 , respectively. The result of DWBA calculations using the code BRUNHILD [17] are also shown in Fig. 4 and give $S_1 S_2 = 0.47$ and 0.44 at 48 and 100 MeV respectively.

Calculations using the asymptotic approximation for the proton transfer reaction $^{12}\text{C} (^{14}\text{N}, ^{13}\text{C}) ^{13}\text{N}$ at 78 MeV are shown in Fig. 5. Good agreement is obtained in shape and magnitude

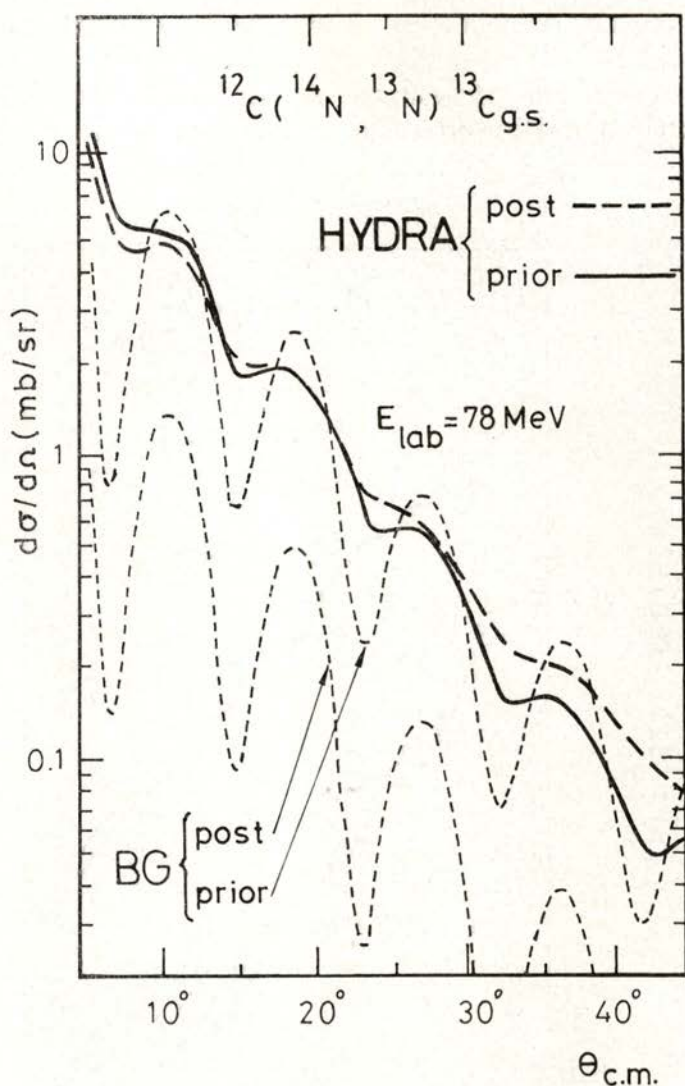


Fig. 3 — Comparison of the DWBA curves for the $^{12}\text{C} (^{14}\text{N}, ^{13}\text{N}) ^{13}\text{C}_{\text{g.s.}}$ reaction at $E_{\text{Lab}} = 78 \text{ MeV}$ obtained with HYDRA using the asymptotic approximation and with the no-recoil Buttle and Goldfard (BG) approximation in the post and prior representations. The optical potentials correspond to the set 3 of ref. [24].

with full finite range calculations [23], [25] performed with the same optical model and bound state parameters. These results indicate that the degree of convergence of the sum over the

recoil angular momentum l_r is well described by the selection rule $l_r \leq l_1$.

A test of the dependence of our results on the recoil momentum \mathbf{p} was performed for the same reaction as in Fig. 4.

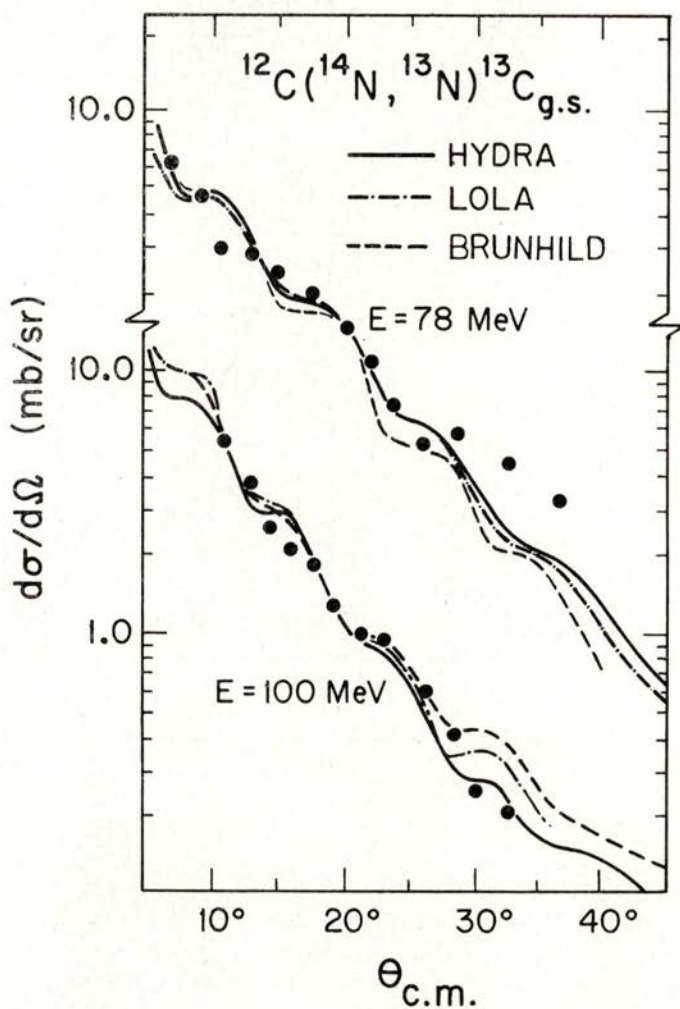


Fig. 4 — Comparison of the DWBA curves for the $^{12}\text{C}(^{14}\text{N}, ^{13}\text{N})^{13}\text{C}_{\text{g.s.}}$ reaction at incident energies of 78 and 100 MeV obtained, with the code HYDRA (full curve) using the asymptotic approximation, with the code LOLA [23], [26] (point-dash curve) and with the code BRUNHILD [17] (dash curve).

Using the local momentum approximation we find that the differential cross section is almost insensitive the modulus of \mathbf{p} . The dependence on the direction of \mathbf{p} is small and weaker in the post representation than in the prior representation. This is probably due to the presence of the $(-1)^l$ factor in eq. (19c), which for the dominant recoil term in this reaction is -1.

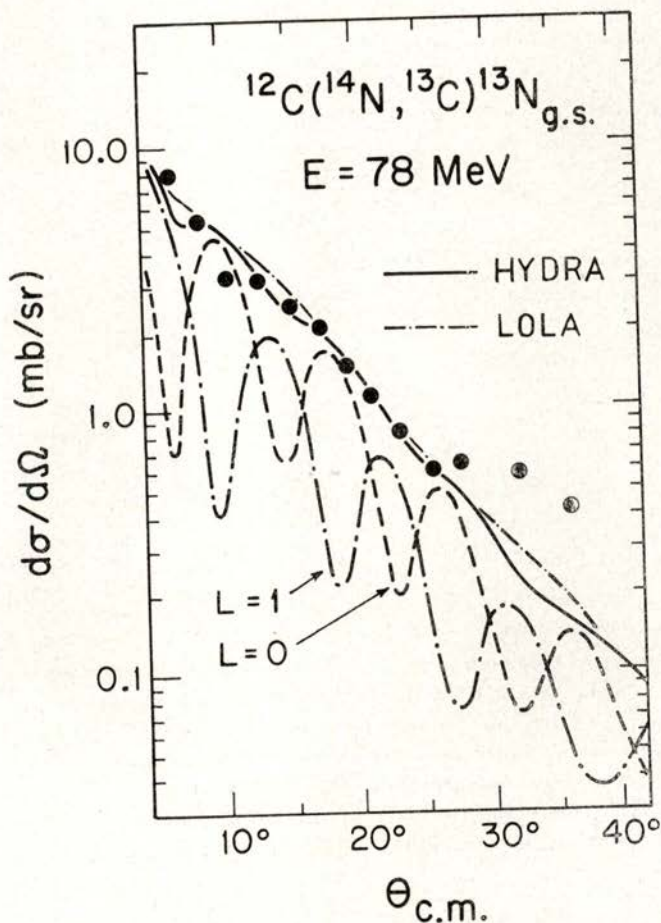


Fig. 5 — Same as in Fig. 5 for the $^{12}\text{C}(^{14}\text{N}, ^{13}\text{C})^{13}\text{N}_{\text{g.s.}}$ reaction at 78 MeV. The dashed curves show the angular distributions of the $L=0$ and $L=1$ transitions separately calculated with HYDRA. The sum is given by the full curve. The experimental values are from ref. [24].

In order to study the relative importance of recoil effects in the contributions from different values of the total orbital angular momentum L we have chosen the $^{26}\text{Mg}(^{16}\text{O}, ^{15}\text{N})^{27}\text{Al}_{\text{g.s.}}$ reaction at $E_{\text{lab}} = 45$ MeV since l_1 is different from l_2 and also because our results can be compared with previous full finite range DWBA calculations [27]. This is a transfer from a $p^{1/2}$ state to a $d^{5/2}$ state and therefore $L = 2, 3$. The DWBA curves of Fig. 6

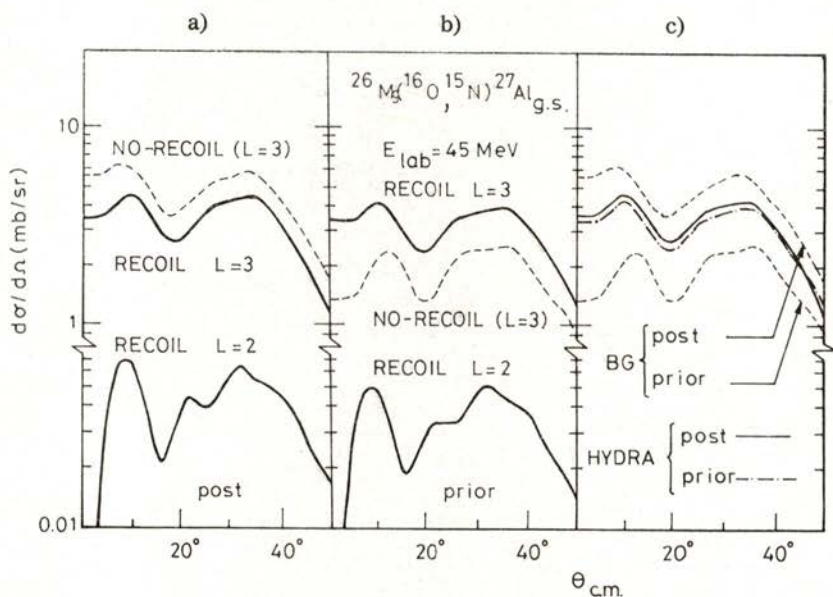


Fig. 6 — DWBA calculations for the $^{26}\text{Mg}(^{16}\text{O}, ^{15}\text{N})^{27}\text{Al}_{\text{g.s.}}$ reaction at 45 MeV. Part a) shows a comparison in the post representation between the contribution from $L = 2$ and $L = 3$ calculated with HYDRA using the asymptotic approximation and the cross section calculated in the no-recoil Buttle and Goldfarb (BG) approximation which only allows $L = 3$. Part b) shows the same comparison in the prior representation. Part c) shows the total cross section predicted by HYDRA and by the no-recoil BG approximation in both representations. The optical potentials are from ref. [27].

were obtained using the asymptotic approximation and the same optical model and bound state parameters as in ref. [27]. We find that the effects of recoil is either to increase or to decrease the cross section whether it is calculated in the prior or post

representations, respectively. As a result the discrepancy between the post and prior representations in the no-recoil approximation is strongly reduced. Fig. 7 shows that there is good agreement between the asymptotic and the full finite range calculations of Buttler [27] using the code DAISY for both $L = 2$ and $L = 3$

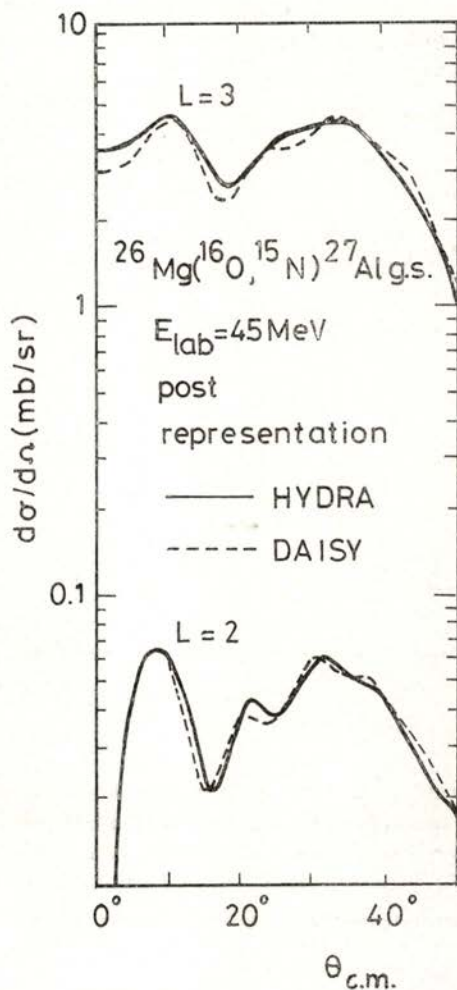


Fig. 7 — DWBA calculations for the $^{26}\text{Mg}(^{16}\text{O}, ^{15}\text{N})^{27}\text{Al}_{\text{g.s.}}$ reaction at 45 MeV. Comparison between calculations obtained with the code HYDRA (full curve) and with the full finite range code DAISY [27] (broken curve), for the $L = 2$ and $L = 3$ in the post representation.

although there is a factor of about 2 orders of magnitude between these two contributions to the cross section. The difference in the absolute magnitude of the differential cross section at the main peak is less than 10% in the two calculations.

In the $^{26}\text{Mg} (^{16}\text{O}, ^{15}\text{N}) ^{27}\text{Al}$ g.s. reaction the selection on the recoil angular momentum is $l_r \leq 1$ and $l_r \leq 2$ in the post and prior representations, respectively. This difference however does not have a marked effect on the cross section, because the contribution from $l_r = 2$ is very small, as shown in Fig. 8. Thus

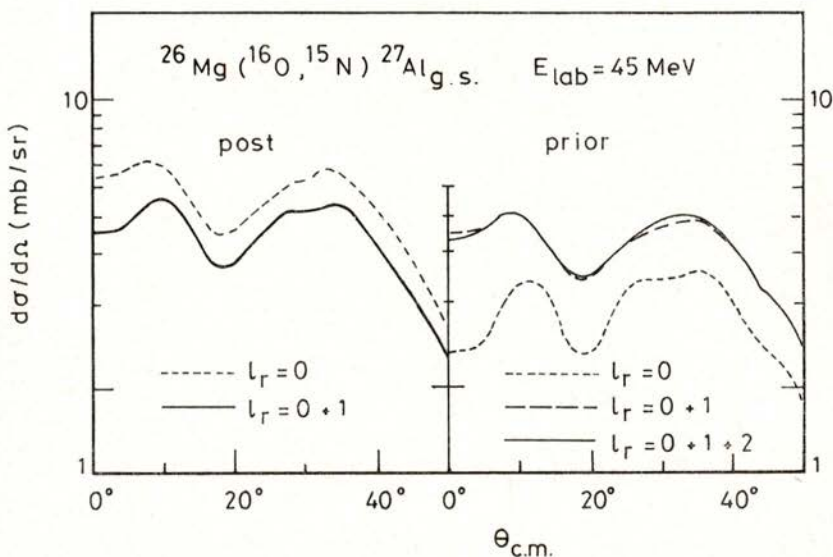


Fig. 8—DWBA calculations for the same reaction as in Fig. 6 and 7 with HYDRA using the asymptotic approximation. The left hand side shows the contributions to the cross section in the post representation from the allowed values of $l_r = 0$ and 1. The right hand side shows the analogous contributions in the prior representation where l_r varies from 0 to 2.

although l_1 is different from l_2 the degree of convergence of the sum over l_r is well described by the asymptotic selection rule in both the prior and post representations.

5 — DISCUSSION

Using the formalism presented in ref. [10] for the approximate treatment of finite range and recoil effects a DWBA program was developed and applied to the analysis of quasi-elastic heavy ion transfer reactions.

In our approach the DWBA calculation is reduced to a zero-range type calculation since the form factor, which may include the effects of recoil, is calculated analytically. The simplification is obtained through the representation of the bound state wave functions by the asymptotic spherical Hankel functions. This representation provides an accurate description of the reaction due to the strong localization of the transfer process outside the nuclear surfaces. In this asymptotic approximation the cross section is proportional to the product of the squares of the normalization of the tail of the bound state wave functions which is a well defined quantity in heavy ion transfer reactions [19], [20].

We obtain good agreement with the results of full finite range calculations [23], [25], [26], [27] in all one-nucleon transfer reactions investigated so far, using considerably smaller computing times. Also we find that the inclusion in the asymptotic approximation of the Coulomb terms, that are present in the interaction responsible for the transfer, improves considerably the agreement with the spectroscopic factors extracted from full finite range calculations.

Our approximation can be expected to break down in cases where a substantial part of the cross section comes from the nuclear interior and also in multinucleon transfer reactions where the local momentum approximation may be inadequate to account for the recoil effects. Within its region of applicability the present approach gives a reliable description of finite range and is particularly simple to use. It can be useful in coupled reaction channel calculations to include finite range and recoil effects with a very small increase in the computing time.

From another point of view we note that the integral on the left hand side of eq. (13), which gives the reaction form factor in the DWBA, is formally similar to the transfer amplitude in

the Brink semi-classical model of transfer reactions (compare for instance with eq. (6.16) of ref. [15]). This means that the asymptotic approximation can also be applied in the context of semi-classical models of transfer reactions. Finally we note that the development of approximate methods to deal with finite range and recoil effects is made particularly significant by recent results [28] where it is shown that the usual form of the DWBA is often unable to interpret the transfer reaction data.

We wish to thank Dr. D. M. Brink, Dr. P. J. A. Buttle and Dr. R. C. Johnson for many interesting and valuable discussions during the course of this work. The computer time provided at the IBM-360/44 of the Centro de Cálculo das Universidades de Lisboa, where the calculations were done, is gratefully acknowledged.

APPENDIX

FOLDING INTEGRAL WITH TWO HANKEL FUNCTIONS

The integral

$$J_{l_1 \lambda_1 l_2 \lambda_2}(\mathbf{R}, \mathbf{p}, \alpha, \beta) = \int d\mathbf{r} [h_{l_1}^{(1)}(i\beta|\mathbf{R}-\mathbf{r}|) Y_{l_2}^{\lambda_2}(\hat{\mathbf{R}}-\hat{\mathbf{r}})]^* \cdot h_{l_1}^{(1)}(i\alpha r) Y_{l_1}^{\lambda_1}(\hat{\mathbf{r}}) e^{i\mathbf{p}\cdot\mathbf{r}}. \quad (\text{A.1})$$

can be written in momentum space as

$$J_{l_1 \lambda_1 l_2 \lambda_2}(\mathbf{R}, \mathbf{p}, \alpha, \beta) = \int d\mathbf{k} e^{i\mathbf{R}\cdot\mathbf{k}} F_{l_2 \lambda_2}(\mathbf{k}, \beta)^* F_{l_1 \lambda_1}(\mathbf{p}-\mathbf{k}, \alpha), \quad (\text{A.2})$$

where $F_{l\lambda}(\mathbf{k}, \beta)$ is the Fourier transform of $h_l^{(1)}(i\beta r) Y_l^\lambda(\hat{\mathbf{r}})$. The calculation of this integral is considerably simplified if we neglect the dependence on the angle between \mathbf{k} and \mathbf{p} in the

denominator of the radial part of $F_{1\lambda_1}$. Assuming \mathbf{p} perpendicular to \mathbf{k} we get

$$F_{1\lambda_1}(\mathbf{p}-\mathbf{k}, \alpha) \cong - \left(\frac{2}{\pi}\right)^{1/2} \frac{1}{\alpha_1^{l_1+1}} \frac{1}{\alpha_p^2+k^2} Y_{1\lambda_1}^{\lambda_1}(\mathbf{p}-\mathbf{k}). \quad (\text{A.3})$$

where $\alpha_p = (p^2 + \alpha^2)^{1/2}$. This approximation is reasonable as long as p is sufficiently smaller than α . Otherwise we can use the expansion

$$\frac{1}{(\mathbf{p}-\mathbf{k})^2 + \alpha^2} = \frac{4\pi}{2pk} \sum_{lm} Q_l(z) Y_l^{m*}(\hat{\mathbf{p}}) Y_l^m(\hat{\mathbf{k}}). \quad (\text{A.4})$$

where Q_l are Legendre functions of the second kind and

$$z = (p^2 + k^2 + \alpha^2)/2pk.$$

Using the well known addition theorem

$$Y_{1\lambda_1}^{\lambda_1}(\mathbf{p}-\mathbf{k}) = \sum_{l_r} a_{1\lambda_1 l_r} (1_r \lambda_r L_r \Lambda_r | 1\lambda_1) Y_{l_r}^{\lambda_r}(\mathbf{p}) Y_{l_r}^{\Lambda_r}(-\mathbf{k}) \quad (\text{A.5})$$

where $L_r = l_1 - l_r$,

$$a_{1\lambda_1 l_r} = (4\pi)^{1/2} (-1)^{l_r} \hat{l}_r \frac{(2l_1+1)!!}{(2l_r+1)!!(2L_r+1)!!} (1_1 0 1_r 0 | L_r 0) \quad (\text{A.6})$$

and eqs. (A.2) and (A.3), we can write

$$J_{1\lambda_1 l_2 \lambda_2}(\mathbf{R}, \mathbf{p}, \alpha, \beta) \cong \sum_{l_r} a_{1\lambda_1 l_r} (1_r \lambda_r L_r \Lambda_r | 1\lambda_1) \frac{\alpha_p^{l_r+1}}{\alpha^{l_r+1}} Y_{l_r}^{\lambda_r}(\mathbf{p}) \cdot \int d\mathbf{k} e^{i\mathbf{R}\cdot\mathbf{k}} F_{l_2 \lambda_2}^*(\mathbf{k}, \beta) F_{L_r \Lambda_r}(\mathbf{k}, \alpha_p). \quad (\text{A.7})$$

This integral is given in eq. (A.36) of Ref. [10]. With this result we obtain

$$\begin{aligned}
 J_{l_1 \lambda_1 l_2 \lambda_2}(\mathbf{R}, \mathbf{p}, \alpha, \beta) = & \\
 & \sum_{l_r \lambda_r l_c \lambda_c} i^{l_2 - l_1 + L_c} (-1)^{\lambda_1} (l_2 \lambda_2 l_1 - \lambda_1 | L \Lambda) (l_r \lambda_r l_c \lambda_c | L \Lambda) \\
 & Y_{L_c}^{\Lambda^*}(\hat{\mathbf{R}}) Y_{l_r}^{\lambda_r^*}(\mathbf{i}\mathbf{p}) \Gamma_{l_1 l_2 l_r l_c}^{L L l_r} \frac{(2l_1 + 1)!!}{(2l_r + 1)!! (2L_r + 1)!!} \\
 & \cdot \frac{\alpha_p^{L_r + 1}}{\beta^{l_1 + 1}} f_{l_r l_c l_2}(\mathbf{R}, \alpha_p, \beta). \tag{A.8}
 \end{aligned}$$

where $L_r = l_1 - l_r$, $\Gamma_{l_1 l_2 l_r l_c}^{L L l_r}$ has been defined in eq. (28c) and

$$f_{l_r l_c l_2}(\mathbf{R}, \alpha_p, \beta) = \frac{1}{\alpha_p^2 - \beta^2} \left[\frac{\alpha_p^{l_2}}{\beta^{l_2 + 1}} h_{L_c}^{(l)}(\mathbf{i}\alpha_p \mathbf{R}) - \frac{\beta^{L_r}}{\alpha_p^{L_r + 1}} h_{L_c}^{(l)}(\mathbf{i}\beta \mathbf{R}) \right]. \tag{A.9}$$

REFERENCES

- [1] P. J. A. BUTTLE and L. J. B. GOLDFARD, *Nucl. Phys.* **78** (1966), 409; *Nucl. Phys.* **A115** (1968), 461; *Nucl. Phys.* **A176** (1971), 229.
- [2] F. SCHMITTROTH, W. TOBOCMAN and A. A. GOLESTANEH, *Phys. Rev.* **C1** (1970), 377.
- [3] M. A. NAGARAJAN, *Nucl. Phys.* **A196** (1972), 34; *Nucl. Phys.* **A209** (1973), 485.
- [4] P. S. HAUGE, *Nucl. Phys.* **A223** (1974), 394; *Nucl. Phys.* **A236** (1974), 61.
- [5] L. A. CHARLTON, *Phys. Rev.* **C8** (1973), 146; *Nucl. Phys.* **A241** (1975), 144.
- [6] N. K. GLENDENNING and M. A. NAGARAJAN, *Nucl. Phys.* **A236** (1974), 13.
- [7] A. J. BALTZ and S. KAHANA, *Phys. Rev.* **C9** (1974), 2243.
- [8] A. J. BALTZ, *Phys. Rev.* **C13** (1976), 668.
- [9] P. BRAUN-MUNZINGER and H. L. HARNEY, *Nucl. Phys.* **A223** (1974), 381.
- [10] F. D. SANTOS, *Nucl. Phys.* **A212** (1973), 341.
- [11] F. D. SANTOS, *Phys. Lett.* **48B** (1974), 193.
- [12] A. M. GONÇALVES and F. D. SANTOS, *Portgal. Phys.* **10** (1979), 129.
- [13] F. D. SANTOS and A. M. GONÇALVES, *Phys. Lett.* **101B** (1981), 219.
- [14] F. D. SANTOS and A. M. GONÇALVES, *Phys. Rev.* **C24** (1981), 156.

- [15] D. M. BRINK, *Les Houches, Session xxx* North-Holland, Amsterdam (1978), p. 1.
- [16] H. HASAN and D. M. BRINK, *J. Phys.* G5 (1979), 771.
- [17] P. BRAUN-MUNZINGER, H. L. HARNEY and S. WENNEIS, *Nucl. Phys.* A235, (1974), 190.
- [18] M. DANOS and L. C. MAXIMON, *J. Math. Phys.* 6 (1965), 766.
- [19] J. L. DURELL, P. J. A. BUTTLE, L. J. B. GOLDFARD, W. R. PHILLIPS, G. D. JONES, B. W. HOSTON and M. IVANOVICH, *Nucl. Phys.* A269 (1976), 443.
- [20] H. P. GUBLER, G. R. PLATTNER, I. SICK, A. TRABER and W. WEISS, *Nucl. Phys.* A284 (1977), 114.
- [21] R. M. DEVRIES, G. R. SATCHLER and J. G. CRAMER, *Phys. Rev. Lett.* 32 (1974), 1377.
- [22] A. M. GONÇALVES, *Ph. D. Thesis*, Lisbon 1979 (unpublished).
- [23] R. M. DEVRIES and K. I. KUBO, *Phys. Rev. Lett.* 30 (1973), 325.
- [24] W. VON OERTZEN, M. LIU, C. CAVERZASIO, J. C. JACMART, F. POUGHEON, M. RIOU, J. C. ROYNETTE and C. STEPHAN, *Nucl. Phys.* A143 (1970), 34.
- [25] R. M. DEVRIES, M. S. ZISMAN, J. G. CRAMER, K. L. LIU, F. D. BECCHETTI, B. G. HARVEY, H. HOMEYER, D. G. KOVAR, J. MAHONEY and W. VON OERTZEN, *Phys. Rev. Lett.* 32 (1974), 683.
- [26] R. M. DEVRIES, *Phys. Rev.* C8 (1973), 951.
- [27] P. J. A. BUTTLE, *Comp. Phys. Comm.* 14 (1978), 133.
- [28] J. R. SHEPARD, E. ROST and P. D. KUNZ, *Proceedings of the Fifth International Symposium on Polarization Phenomena in Nuclear Physics*, Santa Fé, 1981 (Edited by G. G. Ohlsen *et al.*), American Institute of Physics, New York, 1981, p. 361.

1870

1871

1872

1873

1874

1875

1876

1877

1878

1879

1880

1881

1882

1883

1884

1885

1886

1887

1888

ABSOLUTE CROSS SECTIONS FOR THE $^{64}\text{Zn}(^{12}\text{C}, X)$ AND $^{58}\text{Ni}(^{12}\text{C}, X)$ REACTIONS

H. KAWAKAMI ⁽¹⁾, A. P. DE LIMA ⁽²⁾, J. H. HAMILTON, A. V. RAMAYYA,
R. M. RONNINGEN ⁽³⁾

Physics Department ⁽⁴⁾, Vanderbilt University, Nashville, TN 37235, U.S.A.

M. D. BARKER ⁽⁵⁾, G. D. GALAMBOS ⁽⁶⁾

Physics Department, Emory University, Atlanta, GA 30322, U.S.A.

A. C. RESTER

Space Astronomy Laboratory, University of Florida
Gainesville, FL 32601, U.S.A.

H. K. CARTER, R. L. MLEKODAJ, E. H. SPEJEWSKI

UNISOR ⁽⁷⁾, Oak Ridge, TN 37830, U.S.A.

(Received 30 December 1981)

ABSTRACT — With a He-jet transport system at UNISOR, the absolute cross section for the ^{12}C induced reactions on ^{64}Zn and ^{58}Ni targets from 64 to 93 MeV were obtained from the yields for γ -rays from the decays of the resulting radioactivities.

Strong experimental cross sections are observed with the following outgoing particles: $2p_n$, $\alpha(2p_2n)$, αp , $3p_n$, αp_n and $\alpha 2p_n$ for ^{64}Zn and $2p$, p_n , $3p_n$, αp , αp_n and $\alpha 2p_n$ for ^{58}Ni . Experimental values are compared with theoretical calculations based on a statistical model.

[NUCLEAR REACTIONS $^{64}\text{Zn}(^{12}\text{C}, X)$ and $^{58}\text{Ni}(^{12}\text{C}, X)$, $E_{^{12}\text{C}} = 64.0$ to 93.3 MeV; measured E_γ , I_γ ; deduced $\sigma(E)$.]

(1) On leave from Institute for Nuclear Study, University of Tokyo, Japan.

(2) On leave from Physics Department, University of Coimbra, Portugal.

(3) Present address: Cyclotron Laboratory, Michigan State University.

(4) Work supported in part by a grant from the Energy Research and Development Administration.

(5) Present address: Physics Department, University of Wisconsin.

(6) Present address: Department of Nuclear Engineering, University of Illinois.

(7) UNISOR is a consortium of fourteen institutions and is supported by them and by the US Energy Research and Development Administration.

1 — INTRODUCTION

There is presently considerable research activity centered in the mass region $A = 60-80$ by in-beam spectroscopy and reaction experiments. Evidence has been found for the coexistence of both spherical and deformed shapes in ^{72}Se and ^{74}Se , refs. [1], [2], and more recently in $^{74,76}\text{Kr}$ where these nuclei exhibit very large ground state deformation with the 0_2^+ level in ^{76}Kr associated with near-spherical shape [3]. In $^{68,70}\text{Ge}$ evidence [4], [5] for the importance of the $g_{9/2}$ orbital is reported at spins 8^+ and this structure seems to occur in $^{72,74}\text{Se}$ also. In odd- A nuclei in this region evidence for the role of the $g_{9/2}$ orbital is also seen [6], [7], [8]. Rotational like bands built on this and other orbitals are seen [6]. In ^{65}Ga the data are best fitted by an asymmetric rotor model [6]. To further test this model in ^{65}Ga more data are needed on the $\Delta I = 1$ transitions in the $g_{9/2}$ and $f_{5/2}$ bands. The odd-odd nuclei in this region have been studied very little but a few high and low spin isomers are now known for example in ^{74}Br , refs. [9], [10]. For the first time levels built on the 4^- isomer in ^{74}Br have been identified and their structure is very rotational [11]. There should be similar isomers in the other odd-odd Br isotope and perhaps in the odd-odd As and Ga isotopes. Information about low spin states and high spin states from high spin isomers can provide valuable data to extend our understanding of the above nuclei. Experimental data on the radioactive decay of isotopes, particularly off the stability line, in this region with an on-line isotope separator would provide valuable and complementary information to these data, including the identification of new isomers. Levels built on such isomers may go unidentified as was first the case in our ^{74}Br work without knowledge of the radioactive decays.

In order to explore the feasibility of the use of the Unisor facility to obtain neutron deficient isotopes in this mass region we investigated the absolute cross sections of the reactions induced by bombardment of ^{64}Zn and ^{58}Ni targets with ^{12}C beams. The experimental results presented here show that neutron deficient isotopes can indeed be produced in sufficient quantity for good experiments with heavy ion beams with energies in the range studied. Strong experimental cross sections were observed

for the following outgoing particles: 2pn, $\alpha(2p2n)$, αp , 3pn, αpn , and $\alpha 2pn$ for ^{64}Zn and 2p, pn, 3pn, αp , αpn , and $\alpha 2pn$ for ^{58}Ni .

There have been various theoretical calculations of the cross sections for heavy ion induced reactions [12]-[15]. There are of course various uncertainties in these calculations as discussed by Robinson *et al.* [16]. This group has already carried out some measurements of absolute cross sections to test these calculations in this nuclear region up to energies 51 MeV [16]-[18]. Our present results extend these measurements to test the calculations at higher energies. The experimental cross sections obtained in this work are compared with theoretical calculations obtained with the computer code ALICE developed by Blann and Plasil [15].

2 — EXPERIMENTAL PROCEDURE AND RESULTS

Enriched targets of ^{64}Zn of 4.3 mg/cm² (enrichment >99 %) and ^{58}Ni of 3.2 mg/cm² (enrichment >99 %) were bombarded by ^{12}C ions from the Oak Ridge Isochronous Cyclotron with beam energies from 64.0 to 93.3 MeV. The recoiling nuclei were transported with a He-jet system [19] through a teflon tubing of about 20 m length and deposited on a collection tape at UNISOR. After collecting for 144 seconds, the collected activities were moved to a counting chamber and γ -rays were detected with a Ge(Li) detector. Singles γ -ray measurements were performed in the multiscaling mode with 12 planes of each 12 s, in order to extract half-lives of the parent nuclei. The efficiency of the He-jet system was calibrated by a direct catch method, in which the recoil nuclei were collected for 10 min on Mylar film located 5 mm behind the target. After collection, the Mylar film was pulled out from the target chamber and the activities were counted at the same position as used with He-jet system from 6 min to 11 min after bombardment. This procedure was performed for the He-jet system, too. From the comparison of γ -ray intensities, obtained with both methods, of the 594, 604, 743, 1112, 1707, 1780 and 2018 keV transitions from ^{70}As ($T_{1/2}=52.5$ min), the efficiency was determined to be 22 ± 3 %. In this estimation it was assumed that the efficiency of the direct catch method was 100 %. The absolute efficiency of the Ge(Li) detector used was determined with an IAEA standard source.

Each singles γ -ray spectrum taken in the multiscaling mode was analyzed, and γ -rays were identified by the half-life of the known parent nuclei and relative intensities. Residual nuclei resulting from emitting xn , pxn , $2pxn(\alpha x'n)$, $3pxn(\alpha px'n)$, $2\alpha xn$ and $2\alpha pxn$ were surveyed, where x or $x' = 0$ to 3.

Absolute cross sections were estimated with equation (A - 8), as shown in the Appendix, by taking into account β -decay feeding from parent nuclei, if necessary. In the estimation of absolute cross sections, we made the three following assumptions:

- 1) The Faraday cup is 100 % efficient in catching the cyclotron beam.
- 2) The charge state for ions captured in the Faraday cup is 6^+ .
- 3) The efficiency of the He-jet system is independent of projectile energy and independent of Z .

Although the charge state of the ^{12}C beam is originally 4^+ , passage of ions through the target and the helium atmosphere (pressure of 0.8 atm) ionize them further to a most probably 6^+ charge state. The uncertainty of the energy-dependence of the He-jet system was less than 20 %, which was taken from ref. [20]. Uncertainties of 20 % were thus included in the errors of absolute cross sections.

The experimental cross sections along with the γ -ray energies and metimes used in the analysis are listed in Table I for ^{64}Zn . The beam energies are corrected for the energy losses in the target material. Unidentified γ -rays are listed in Table II, corrected for beam intensities, efficiencies and times.

The feeding corrections from β -decay were deduced to be less than 1 % of the total cross sections for every case. The largest value of F_β that we expect is the case with very small $T_{1/2}(p)$, compared with $T_{1/2}(d)$. Here F_β is the feeding correction factor from β -decay and a function of only the lifetimes of the parent nucleus ($T_{1/2}(p)$) and of the daughter nucleus ($T_{1/2}(d)$) (details in the Appendix).

In the present experiment the largest correction factor F_β could be for $^{64}\text{Zn}(^{12}\text{C}, p3n)^{72}\text{Br}$ ($T_{1/2}(p) = 78$ s) and $^{64}\text{Zn}(^{12}\text{C}, 2p2n)^{72}\text{Se}$ ($T_{1/2}(d) = 8.4$ d). There F_β is 0.59, but since, even at

90 MeV the absolute value $\sigma_p = 0.26 \pm 0.06$ is very small compared with $\sigma_d = 36 \pm 8$, therefore the β -feeding correction had a negligible influence on σ_d .

3 — DISCUSSION

The experimental absolute cross sections were compared with theoretical calculations obtained with the ALICE program developed by Blann and Plasil [15]. These comparisons are illustrated in Figs. 1-3 for ^{64}Zn and Figs. 4-5 for ^{58}Ni . In the Figs. 1 and 3, excitation curves for the $^{64}\text{Zn}(^{12}\text{C}, \alpha p \text{ and/or } 3p2n)^{71}\text{As}$ and $^{64}\text{Zn}(^{12}\text{C}, \alpha n \text{ and/or } 2p3n)^{71}\text{Se}$ reactions show that the cross section for both reactions decreases initially with increasing projectile energy and increases again above an energy of ~ 80 MeV. The first decreasing part is interpreted as due to the αn and αp component, and the increasing part due to the $2p3n$ and $3p2n$ reaction channels, respectively. This interpretation is seen to be reasonable by taking

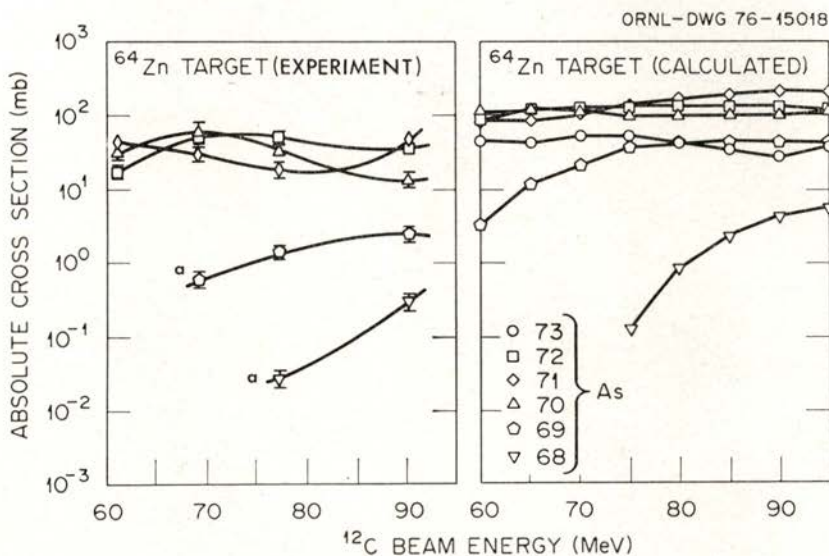


Fig. 1 — Experimental and calculated cross sections for the $^{64}\text{Zn}(^{12}\text{C}, 3pxn \text{ or } \alpha pxn)\text{As}$ reactions. The a indicates that the data for $\alpha p2n$ and $\alpha p3n$ channels are not corrected for absolute γ -ray abundances (η), since the ground state feeding is not known.

into account the Q values, $Q(\alpha n) = -9.9$, $Q(2p3n) = -41.9$, $Q(\alpha p) = -7.8$ and $Q(3p2n) = -36.1$ MeV. The theoretically calculated curves for ^{71}As and ^{71}Se of Figs. 1 and 3 also present similar rising for higher energies. However in the ^{71}Se case the experimental cross sections are one order of magnitude smaller than the calculated ones.

The experimental and theoretical values are reasonably close within factors of three to ten for the $^{64}\text{Zn}(^{12}\text{C}, \alpha$ and/or $2p2n)^{72}\text{Se}$, and within factors of two to six for $^{64}\text{Zn}(^{12}\text{C}, 3pn)^{72}\text{As}$, $^{64}\text{Zn}(^{12}\text{C}, \alpha p)^{71}\text{As}$ and $^{64}\text{Zn}(^{12}\text{C}, \alpha pn)^{70}\text{As}$ reactions. For other reactions the general features, but not the absolute values, are reproduced by the theoretical calculations. The agreement for the $^{64}\text{Zn}(^{12}\text{C}, \alpha 2pn)^{69}\text{Ge}$, and $^{64}\text{Zn}(^{12}\text{C}, 2\alpha n)^{67}\text{Ge}$ reactions is better than a factor of two but here the experimental data are not corrected for the absolute γ -ray abundances since the ground state feedings are not known. The agreement as shown in Fig. 2 suggests that the ground state feeding is probably negligible.

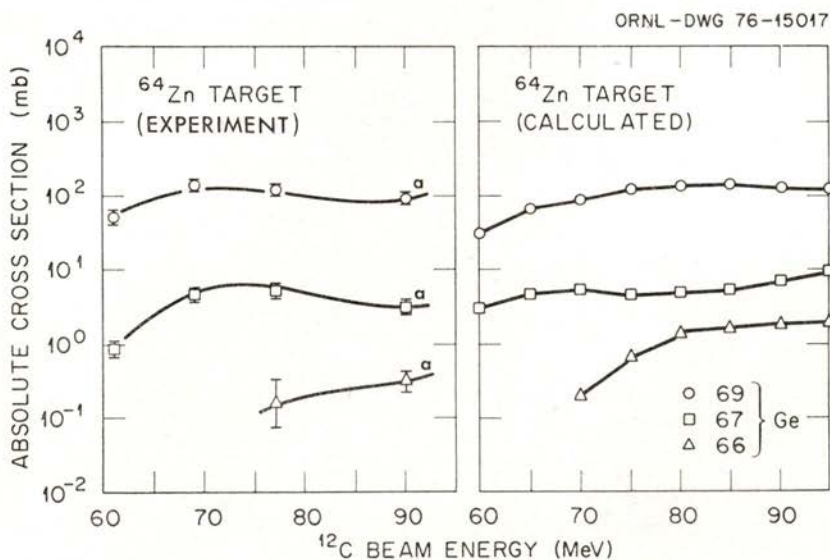


Fig. 2 — Experimental and calculated cross sections for the $^{64}\text{Zn}(^{12}\text{C}, \alpha 2pxn$ or $2\alpha n)^{\text{Ge}}$ reactions. The α indicates each of these cross sections are uncorrected for the absolute γ -ray abundances (η), (see Discussion in the text).

For the $^{58}\text{Ni}(^{12}\text{C}, X)Y$ reactions, the experimental values are: smaller than the calculated ones for ^{68}As by a factor of five to one hundred; for ^{67}Ge from agreement to a factor of 20 lower; in near agreement for ^{60}Ga ; a factor of five to ten smaller for $^{65,64}\text{Ga}$; near agreement for ^{63}Zn ; lower by factors of two to ten for ^{61}Zn — as shown in Figs. 4-6. Even though the cross section for production of ^{68}Ge is large, we could not observe ^{68}Ge because of its pure β -decay to the ground state of ^{68}Ga .

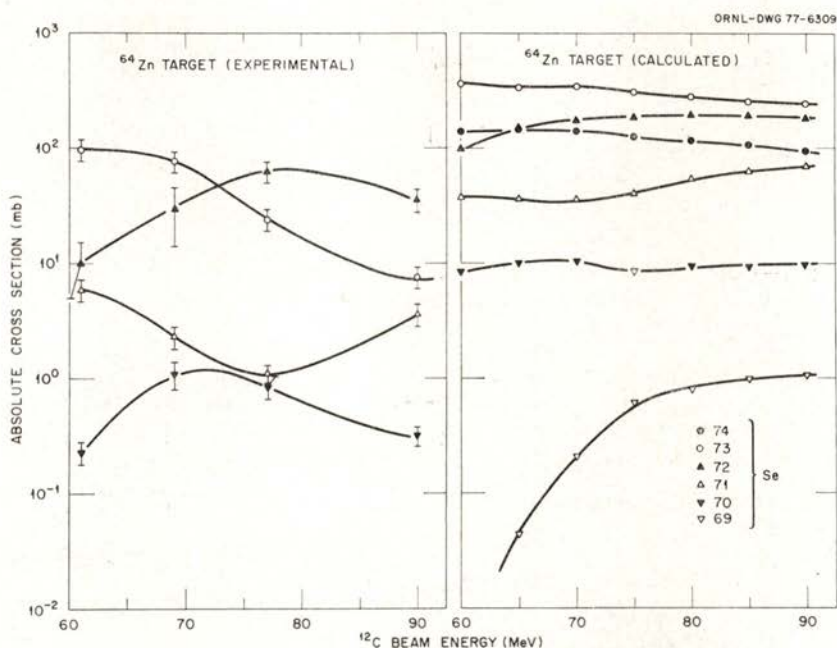


Fig. 3 — Experimental and calculated cross sections for the $^{64}\text{Zn}(^{12}\text{C}, 2\text{pxn or } \alpha\text{xn})\text{Se}$ reactions.

On the other hand, large discrepancies in the absolute values are found in the cases of $^{64}\text{Zn}(^{12}\text{C}, \text{pxn})\text{Br}$ reactions. The ratios of the theoretical to experimental cross sections at 90 MeV are 2.4×10^3 and 4.5×10^2 for pn and p2n reactions respectively. The data of Robinson *et al.* [16] for the same compound nucleus, $^{60}\text{Ni} + ^{16}\text{O} \rightarrow ^{76}\text{Kr}^* \rightarrow \text{Br} + \text{pxn}$, yield an absolute pn cross section

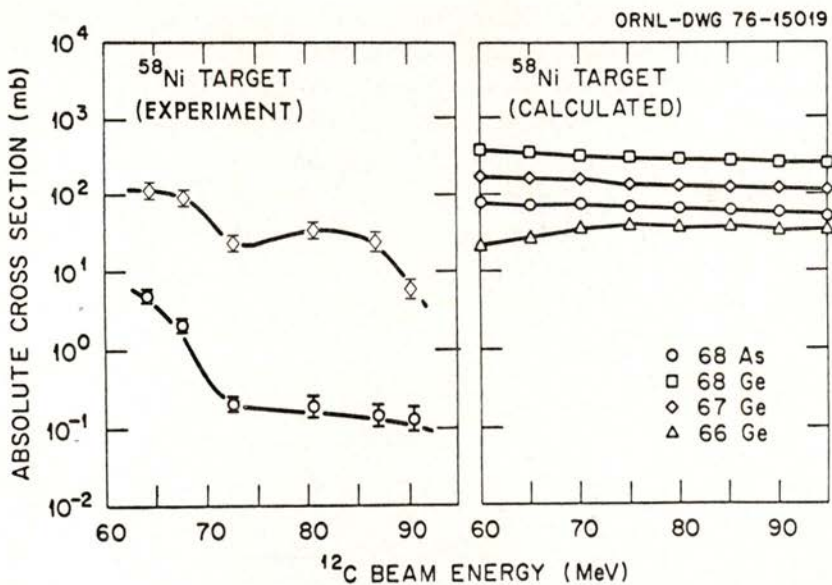


Fig. 4 — Experimental and calculated cross sections for the $^{58}\text{Ni}(^{12}\text{C}, \text{pn})^{68}\text{As}$ and $^{58}\text{Ni}(^{12}\text{C}, 2\text{pxn})\text{Ge}$ reactions.

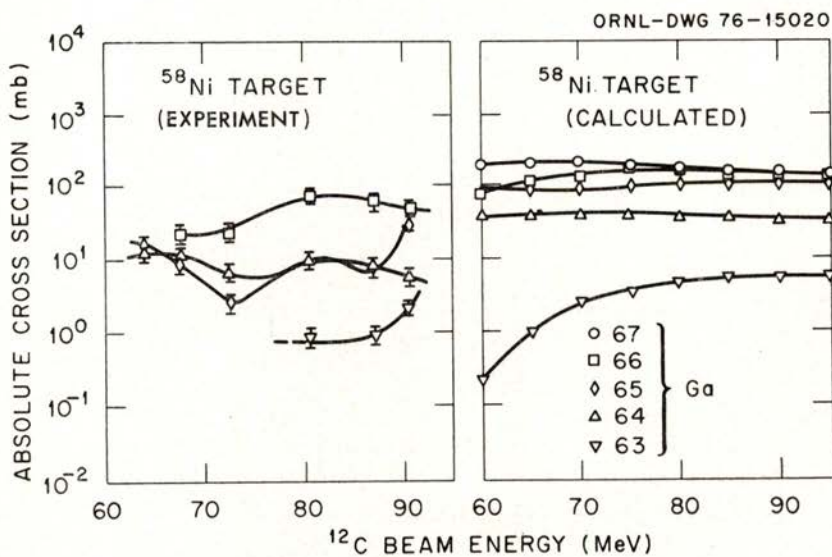


Fig. 5 — Experimental and calculated cross section for the $^{58}\text{Ni}(^{12}\text{C}, 3\text{pxn}$ or $a\text{pxn})\text{Ga}$ reactions.

of 95 mb at 46 MeV. The present value is 1.2 mb at 60.7 MeV. If outgoing particles p and n are emitted after formation of the compound nucleus, both reaction cross sections of $^{60}\text{Ni}(^{16}\text{O}, \text{pn})^{74}\text{Br}$ and $^{64}\text{Zn}(^{12}\text{C}, \text{pn})^{74}\text{Br}$ should have nearly the same values, like the αp , 2pn and αn cross sections as shown in Fig. 7. The large discrepancies between the experimental and the theoretical values and also with the $^{60}\text{Ni}(^{16}\text{O}, \text{pn})$ reaction are thus rather surprising. One source of the discrepancies might be some experimental problem which we failed to take into account. For example, the Br isotopes may have been selectively absorbed by some of the materials used in the experiment. Such absorption can be the primary cause of the discrepancy observed.

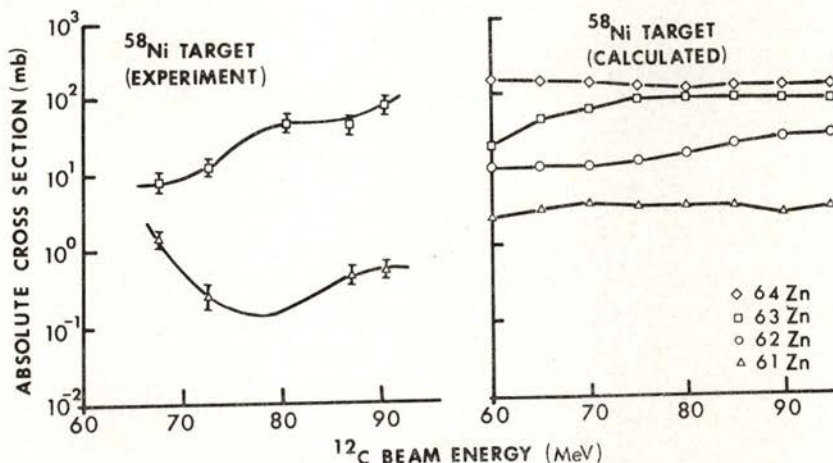


Fig. 6 — Experimental and calculated cross section for the $^{58}\text{Ni}(^{12}\text{C}, \alpha\text{pXn})\text{Zn}$ reactions.

The strong reactions are $^{64}\text{Zn}(^{12}\text{C}, 2\text{pn})^{73}\text{Se}$, $2\text{p}2\text{n})^{72}\text{Se}$, $3\text{pn})^{72}\text{As}$, $\alpha\text{p})^{71}\text{As}$, $\alpha\text{pn})^{70}\text{As}$, $\alpha 2\text{pn})^{69}\text{Ge}$ [with moderate cross sections for the production of ^{71}Se and ^{67}Ge] and $^{58}\text{Ni}(^{12}\text{C}, 2\text{p})^{68}\text{Ge}$, $3\text{pn})^{66}\text{Ga}$, $3\text{p}2\text{n}$ or $\alpha\text{p})^{65}\text{Ga}$, $3\text{p}3\text{n}$ or $\alpha\text{pn})^{64}\text{Ga}$ and $\alpha 2\text{pn})^{63}\text{Zn}$ [with moderate cross sections for the production of ^{68}As and ^{61}Zn and an indication that the cross section for the production of ^{63}Ga may be good at higher energies]. We conclude that neutron deficient isotopes in

this mass region can be produced in sufficient quantity for good experiments with heavy ion beams with energies in the range studied.

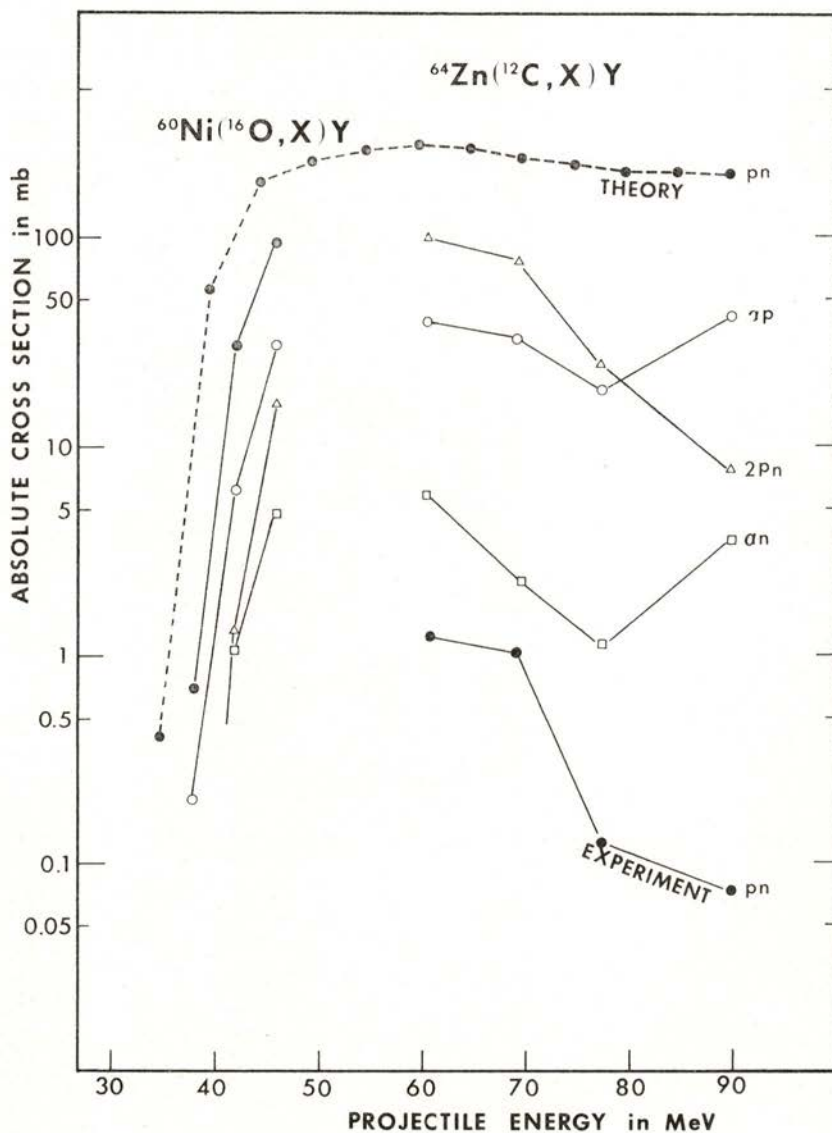


Fig. 7 — Comparison between $^{60}\text{Ni}(^{16}\text{O}, X)Y$ [16] and $^{64}\text{Zn}(^{12}\text{C}, X)Y$ reaction cross sections.

APPENDIX

In this appendix we derive the equations used for estimation of the absolute cross section. A derivation for the general case, as shown in Fig. 8, in which the isotope is produced both directly and through beta decay from a parent nucleus is presented below.

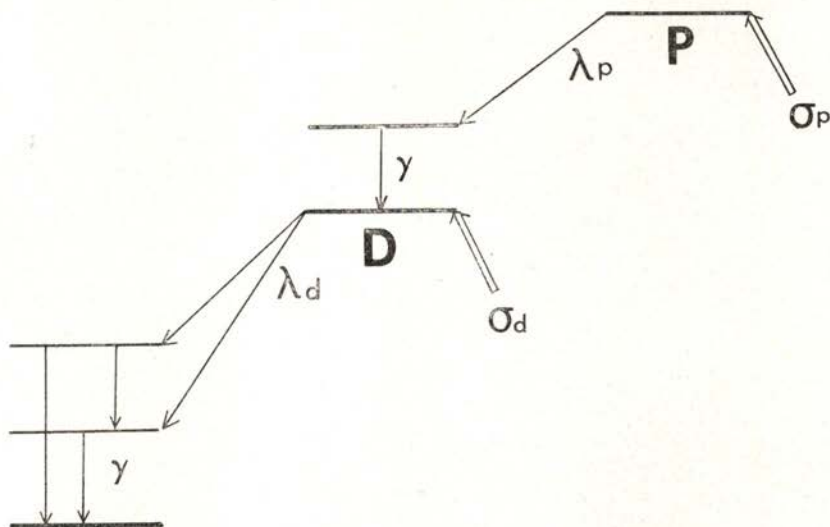


Fig. 8 — General scheme for the derivation of absolute cross sections.

Bombardment

The decay rates of parent and daughter nuclei, $P(t)$ and $D(t)$, at time t are given by

$$\frac{d P(t)}{dt} = - \lambda_p P(t) + \sigma_p N n_b \tag{A-1}$$

$$\frac{d D(t)}{dt} = - \lambda_d D(t) + \sigma_d N n_b + \lambda_p P(t) \tag{A-2}$$

where, $\lambda_{p,d}$ are the decay constants and σ the absolute cross sections in which we are interested; n_b is the beam intensity (atom/sec) which is related to the current integrator reading and charge state of the beam; and N is the number of atoms in the

target (atom/cm²). The solutions of the coupled differential equations are

$$P(t) = \frac{\sigma_p N n_b}{\lambda_p} (1 - e^{-\lambda_p t}) \quad (\text{A-3})$$

$$D(t) = \frac{(\sigma_p + \sigma_d) N n_b}{\lambda_d} (1 - e^{-\lambda_d t}) + \frac{\sigma_p N n_b}{\lambda_d - \lambda_p} (e^{-\lambda_d t} - e^{-\lambda_p t}) \quad (\text{A-4})$$

Measurement

A source is collected on the tape for T_b seconds, so the source initially has $P(T_b)$ "P" nuclei and $D(T_b)$ "D" nuclei. The number of nuclei "D" is given by

$$\frac{dD'(t)}{dt} = -\lambda_d D'(t) + \lambda_p P'(t) \quad (\text{A-5})$$

where

$$P'(t) = P(T_b) e^{-\lambda_p t}$$

By using the initial condition at $t = 0$, $D'(0) = D(T_b)$, we find

$$D'(t) = N n_b \left\{ \left[\frac{P}{\lambda_d - \lambda_p} (1 - e^{-\lambda_p T_b}) \right] e^{-\lambda_p t} + \left[(1 - e^{-\lambda_d T_b}) \left(\frac{\sigma_d}{\lambda_d} - \frac{\lambda_p \sigma_p}{\lambda_d (\lambda_d - \lambda_p)} \right) \right] e^{-\lambda_d t} \right\} \quad (\text{A-6})$$

Therefore, the counting rate R of a detector is

$$R(t) = \eta \varepsilon \omega \lambda_d D'(t) \quad (\text{A-7})$$

where $\varepsilon \omega$ is the total efficiency of the system, and η is the γ -ray abundance.

Knowing the number of counts (n) detected in the counting time T_c , we can calculate the cross section,

$$\sigma_d = \frac{n}{\eta \varepsilon \omega N n_b} \cdot \frac{\lambda_d}{(1 - e^{-\lambda_d T_b})(1 - e^{-\lambda_d T_c})} - F_\beta \sigma_p \quad (\text{A-8})$$

where, the β -feeding correction factor F_β is

$$F_\beta = \frac{\lambda_d}{\lambda_d - \lambda_p} \left\{ \frac{\lambda_d}{\lambda_p} \frac{(1 - e^{-\lambda_p T_b})}{(1 - e^{-\lambda_d T_b})} \frac{(1 - e^{-\lambda_p T_c})}{(1 - e^{-\lambda_d T_c})} - \frac{\lambda_p}{\lambda_d} \right\} \quad (\text{A-9})$$

Experimental σ_p values are obtained from the same equation (A-8) by putting $F_\beta = 0$ and substituting σ_p and λ_p for σ_d and λ_d . Now we can estimate the optimum counting or collection time at UNISOR.

For simplicity; let $\sigma_p = 0$; $T_b = T_c = t$ and the total time of an experiment T , then the total counts are given by

$$n'(t) = n \cdot \frac{T}{t} \propto \frac{(1 - e^{-\lambda_d t})^2}{\lambda_d t}$$

Fig. 9 shows the relation of n' vs $t/T_{1/2}$. The maximum counts are obtained at $t = 1.8 T_{1/2}$.

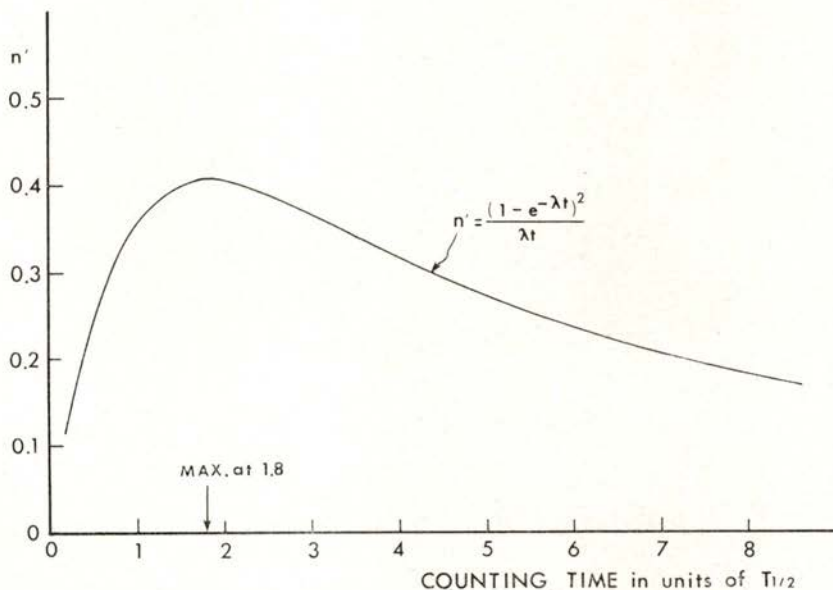


Fig. 9 — The relation of counting time vs. total counts in the isotope separator experiment. The maximum counts are obtained at $t = 1.8 T_{1/2}$.

TABLE I — Absolute Cross Section for $^{64}\text{Zn}(^{12}\text{C}, X)Y$ Reactions. The γ -ray energies and the half-lives used in this analysis are also listed. In some cases the γ -ray abundance, η , is unknown and so enters σ_{ab} as a parameter.

Out-Going Particle	Residual	E_γ (keV)	$T_{1/2}$ (Parent)	$T_{1/2}$ (Parent)	σ_{ab} (mb)	Energy (MeV)	η
n	^{75}Kr	133, 157	5.5 m	60.7	69.3	77.5	90.0
p	^{75}Br	286.8	1.68 h				
pn	^{74}Br	634.8	25 m (1 ⁻) or 42 m (4)*		1.03 ± 0.22	0.122 ± 0.054	0.072 ± 0.027
p2n	^{73}Br	64.4, 335.6	3.3 m		2.00 ± 0.42	0.86 ± 0.18	0.141 ± 0.030
p3n	^{72}Br	862.3	78 s		0.037 ± 0.008	0.18 ± 0.04	0.26 ± 0.06
2p	^{74}Se		STABLE				
2pn	$^{73}\text{Se}(9/2^+)$ $^{73}\text{Se}(1/2^-)$	67.0 84.5, 393.4, 1078.6	7.2 h 39 m 3.3 m		98 ± 21	24 ± 5 14	7.6 ± 1.6 4.8
2p2n	^{72}Se	45.9	8.4 d				
α n or	^{71}Se	147.1, 723.3, 830.8, 870.8, 1095.8	4.9 m		30 ± 16	63 ± 13	36 ± 8
2p3n					5.9 ± 1.2	1.1 ± 0.2	3.6 ± 0.8
α 2n	^{70}Se	49.2, 202.6, 376.7, 426.0	41 m		1.1 ± 0.3	0.84 ± 0.18	0.32 ± 0.06

* We took a mean value of 25 m and 42 m, even though the high spin isomer should be more strongly populated. The error assigned overlaps the results if $T_{1/2} = 42$ m is assumed.

TABLE I — (cont'd)

Out-Going Particle	Residual	E_γ (keV)	$T_{1/2}$	$T_{1/2}$ (Parent)	σ_{ab} (mb)		
					60.7	69.3	Energy (MeV) 77.5
$\alpha 3n$	^{69}Se	98, 66.4	27.3 s				90.0
3p	^{73}As	53.3	80.3 d				
3pn	^{72}As	834.5	26 h	8.4 d	17 ± 4	52 ± 11	42 ± 9
αp or							
3p2n	^{71}As	175.3	62 h	4.9 m	39 ± 8	33 ± 8	41 ± 9
αpn	^{70}As	595.2, 905.9, 1114.0	52.5 m	41 m	30 ± 6	68 ± 13	15 ± 3
$\alpha p 2n$	^{69}As	146.0, 232.8	15 m	27.3 s	0.57 ± 0.13/ η	1.5 ± 0.3/ η	2.6 ± 0.6/ η
$\alpha p 3n$	^{68}As	1016.2, 651.5, 761.9, 1778.5	2.7 m			0.029 ± 0.015/ η	0.32 ± 0.06/ η
$\alpha 2p$	^{70}Ge		STABLE				
$\alpha 2pn$	^{69}Ge	1106.5	39.2 h	15 m	54 ± 12/ η	151 ± 33/ η	96 ± 20/ η
2α	^{68}Ge		288 d	2.7 m			
$2\alpha n$	^{67}Ge	166.8	19.0 m				
$2\alpha 2n$	^{66}Ge	382.0	2.27 h				
$2\alpha 3n$	^{65}Ge	649.7	30.9 s				
$2\alpha p$	^{67}Ga	93.3, 184.6	78.3 h	19.0 m	0.93 ± 0.20/ η	4.9 ± 1.1/ η	3.4 ± 0.7/ η
$2\alpha pn$	^{66}Ga	1039.3	9.4 h	2.27 h			
		833.6					
$2\alpha p 2n$	^{65}Ga	115.0	15.2 m	30.9 s			1.4 ± 0.30

TABLE II— Unidentified γ -rays observed in the $^{64}\text{Zn}(^{12}\text{C}, \text{X})\text{Y}$ reactions. Raw total counts are divided by efficiencies (ϵ and ω), beam intensities (n_b), and times (T_b and T_c).

E_γ	I_γ				
	60.7	69.3	77.5	90.0	
74.7	43	35	26		30
121.9	10	7.4	2.4		
143.2	155	43	29		68
180.9	67	64	21		22
358.8	101	98			37
514.7	368	473			
626.6					71
637.8	24	66			
657.9	409	193	95		245
659.1	419	99			209
812.3			66		81
828.1	45	115	81		56
843.4	65				29
925.1	75	18			
937.4	60	44	11		16
962.7			26		44
1073.4		16			35
1179.8	54	173	70		30
1255.1	42		78		
1295.7	62		30		27
1307.6			17		22
1317.4			17		19
1378.6					10
1381.0					27
1382.2	55				13
1443.2	24	52			17
1527.1					23
1535.2					45
1550.6	156	273	157		117
1552.1	101	321	160		
1605.8	77	33	11		
1625.3	48	165	65		
1640.4			37		37
1680.8			27		44
1714					
1767.4		21	40		53
1850.9		82	43		
1923.2		59	31		
1934.6	37				19
1945.8		48	36		
2001.2		8.2	34		48
2014.8			16		23
2033.8		36	14		

REFERENCES

- [1] J. H. HAMILTON, A. V. RAMAYYA, W. T. PINKSTON, R. M. RONNINGEN, G. GARCIA-BERMEDEZ, R. L. ROBINSON, H. J. KIM, R. O. SAYER and H. K. CARTER, *Phys. Rev. Letters*, **32**, 239 (1974); J. H. HAMILTON, H. L. CROWELL, R. L. ROBINSON, A. V. RAMAYYA, W. E. COLLINS, R. M. RONNINGEN, V. MARUHN-REZWANI, J. MARUHN, N. C. SINGHAL, H. J. KIM, R. O. SAYER, T. MAGEE and L. C. WHITLOCK, *Phys. Rev. Letters*, **36**, 340 (1976).
- [2] R. M. RONNINGEN, A. V. RAMAYYA, J. H. HAMILTON, W. LOURENS, J. LANGE, H. K. CARTER and R. O. SAYER, *Nucl. Phys.*, **A261**, 439 (1976).
- [3] R. B. PIERCEY, J. H. HAMILTON, R. SOUNDREANAYAGAM, A. V. RAMAYYA, C. F. MAGUIRE, X. J. SUN, Z. Z. ZHAO, R. L. ROBINSON, H. J. KIM, S. FRAUENDORF, J. DÖRING, L. FUNKE, G. WINTER, J. ROTH, L. CLEEMANN, J. EBERTH, W. NEUMANN, M. NOLTE, J. C. WELLS, J. LIN, A. C. RESTER and H. K. CARTER, *Phys. Rev. Lett.*, **47**, 1514 (1981).
- [4] A. P. DE LIMA, A. V. RAMAYYA, J. H. HAMILTON, B. VAN NOOLJEN, R. M. RONNINGEN, H. KAWAKAMI, R. B. PIERCEY, E. DE LIMA, R. L. ROBINSON, H. J. KIM, L. K. PEKER, F. A. RICKEY, R. POPLI, A. J. CAFFREY and J. C. WELLS, *Phys. Rev.*, **C23**, 213 (1981).
- [5] R. L. ROBINSON, H. J. KIM, R. O. SAYER, J. C. WELLS, R. M. RONNINGEN and J. H. HAMILTON, *Phys. Rev.*, **C16**, 2268 (1977); C. MORAND, M. AGARD, J. F. BRUANDET, A. GIORNI, J. P. LONGEQUEUE and T. U. CHAN, *Phys. Rev.*, **C13**, 2182 (1976).
- [6] H. KAWAKAMI, A. P. DE LIMA, R. M. RONNINGEN, A. V. RAMAYYA, J. H. HAMILTON, R. L. ROBINSON, H. J. KIM and L. K. PEKER, *Phys. Rev.*, **C21**, 1311 (1980).
- [7] G. F. NEAL, Z. P. SAWA, F. P. VENEZIA and P. R. CHAGNON, *Nucl. Phys.*, **A280**, 161 (1977).
- [8] B. HEITS, H. G. FRIEDERICKS, A. GELBERG, K. P. LIEB, A. PEREGO, R. RASCHER, K. O. ZELL, P. VON BRENTANO, *Phys. Lett.*, **61B**, 33 (1976).
- [9] A. COBAN, J. C. LISLE, G. MURRAY and J. C. WILLMOTT, *Part. Nucl.*, **4**, 108 (1972).
- [10] A. COBAN, *J. Phys. A: Math Nucl. Gen.*, **7**, 1705 (1974).
- [11] R. B. PIERCEY, J. H. HAMILTON, R. M. RONNINGEN, A. V. RAMAYYA, R. L. ROBINSON, and H. J. KIM, *Bull. Am. Phys. Soc.*, **22**, 488 (1977); R. B. PIERCEY, A. V. RAMAYYA, J. H. HAMILTON, L. CLEEMANN, J. ROTH and J. EBERTH, *Bull. Am. Phys. Soc.*, **25**, 578 (1980).
- [12] F. S. STEPHENS, J. R. LEIGH and R. M. DIAMOND, *Nucl. Phys.*, **A170**, 321 (1971).
- [13] J. R. GROVER and J. GILAT, *Phys. Rev.*, **157**, 802 (1967) and *ibid.*, **C3**, 734 (1971).
- [14] M. BLANN, *Phys. Rev.*, **157**, 860 (1967).
- [15] M. BLANN and F. PLASIL, «ALICE, A Nuclear Evaporation Code», US Atomic Energy Commission Report No. COO-3494-10, 1973 (unpublished).

- [16] R. L. ROBINSON, H. J. KIM and J. L. C. FORD, Jr., *Phys. Rev.*, **C9**, 1402 (1974).
- [17] J. C. WELLS, Jr., R. L. ROBINSON, H. L. KIM and J. L. C. FORD, Jr., *Phys. Rev.*, **C12**, 1529 (1975).
- [18] J. C. WELLS, Jr., R. L. ROBINSON, H. J. KIM and J. L. C. FORD, Jr., *Phys. Rev.*, **C11**, 879 (1975) and *ibid.*, **C13**, 2588 (1976).
- [19] W. D. SCHMIDT-OTT, R. L. MLEKODAJ, E. H. SPEJEWSKI and H. K. CARTER, *Nucl. Inst. Method*, **124**, 83 (1975).
- [20] W. D. SCHMIDT-OTT and K. S. TOTH, *Nucl. Inst. Method*, **121**, 97 (1974).

TEMPERATURE DEPENDENCE OF THE MAGNETIC SUSCEPTIBILITY OF SOME $AgMn$ ALLOYS

J. M. MACHADO DA SILVA *, H. ABE and H. MIYAJIMA

The Institute for Solid State Physics

The University of Tokyo, Roppongi, Minato-ku, Tokyo, Japan

and

J. M. ARAÚJO

Centro de Física (INIC), Faculdade de Ciências

Universidade do Porto, 4000 Porto, Portugal

(Received 9 November 1981)

ABSTRACT—The susceptibility of three alloys of $AgMn$ ($c = 4.96, 6.35$ and 13.00 at %) has been investigated around its maximum in terms of a distribution of blocking temperatures.

1 — INTRODUCTION

The nature of the transition of a spin glass has been a point of great controversy. The sharpness of the temperature dependence of the magnetic susceptibility around its maximum depends on the experimental conditions. A.C. susceptibility (χ_a) measurements reveal a sharp cusp at the transition temperature T_0 . This maximum of the susceptibility is frequency dependent, although in some cases the shift in T_0 is small and hard to detect [1]. The presence of a D.C. field depresses χ_a and simultaneously rounds up the cusp [2]. D.C. susceptibility measurements as well as A.C. measurements are further complicated by time effects.

A great deal of effort has been concentrated on the theoretical explanation of the spin glass behaviour [3], [4], based on the exchange interaction between the impurity spins. Substantial

(*) On leave of absence from Centro de Física (INIC), Faculdade de Ciências, Universidade do Porto, 4000 Porto, Portugal.

analytical and computational work has been done, but in most cases it does not quite agree with experiments.

Recently Wohlfarth [5] has put forward a phenomenological model based on the original idea of Néel [6], which assumed clustering of the impurity spins in fine particles. Frequency and time effects will be natural consequences, as was discussed by Néel [6] himself.

One of the crucial assumptions in Wohlfarth's model [5] is that the intrinsic Curie temperature of the cluster material is well above the transition temperature T_0 (for Mn, $T_C \approx 95$ K). According to the model, the susceptibility of the clusters is zero below a blocking temperature T_B and given by $\chi = C/T$ for T greater than T_B . If $f(T_B)$ is the distribution function for the blocking temperatures, the susceptibility of the spin glass will be given by

$$\chi(T) = 1/T \int_0^T C f(T_B) dT_B \quad (1)$$

In his calculation, Wohlfarth [5] treated C as constant (independent of T_B); however, the analysis may be carried out, to a certain extent, without making any such assumption. In fact, introducing the average

$$\bar{C} = \int_0^\infty C(T_B) f(T_B) dT_B \quad (2)$$

and defining a new function

$$g(T) = C(T) f(T) / \bar{C} \quad (3)$$

it is straightforward to check that, as in [5],

$$g(T) = (d(\chi T) / dT) / \lim_{T \rightarrow \infty} (\chi T) \quad (4)$$

The temperature T_0 at which the susceptibility has a maximum is given by

$$T_0 g(T_0) = \int_0^{T_0} g(T) dT \quad (5)$$

which is identical to eq. (8) of ref. [5] after replacing $f(T)$ by $g(T)$. It appears, thus, possible to extract from the experimental data, $\chi(T)$, both the function $g(T)$ and the temperature T_0 , *without any assumption about $C(T)$.*

It is also possible to express the second derivative of the susceptibility (eq. (12) of ref. [5]) at T_0 in terms of the function $g(T)$; one gets

$$\left(\frac{d^2 \chi}{dT^2} \right)_{T_0} = \left(\bar{C} / T_0 \right) \left(dg / dT \right)_{T_0} \quad (6)$$

This expression may be used to verify the consistency of the analysis.

2 — EXPERIMENTAL

We measured the D.C. susceptibility of three Ag Mn alloys of atomic compositions 4.96, 6.35 and 13.00 at % respectively. These alloys were zero field cooled, the measuring field being 1.3 kOe. The measurements were performed on a very sensitive magnetic pendulum developed by Matsui *et al.* [7]. The samples were made by mixing the two components under a vacuum better than 10^{-5} Torr in a high frequency induction furnace. The ingots obtained in this way were remelted in high vacuum in a Bridgeman's furnace and kept at a temperature 30°C above the melting point of Ag (961°C) for two hours, after which they were cooled down at constant rate, reaching room temperature in approximately seven hours.

The homogeneity in the three alloys was checked by chemical analysis. Three bits taken from different points of the sample showed the same Mn concentration c within the accuracy of the method used.

3 — RESULTS AND CONCLUSIONS

The temperature dependence of the magnetic susceptibility for the three different concentrations of Mn is represented in Fig. 1. From these curves we obtained the functions $g(T)$; in fact Fig. 2 gives $d(\chi T)/dT = \bar{C}g(T)$, where $\bar{C} = \lim_{T \rightarrow \infty} (\chi T)$ is the Curie

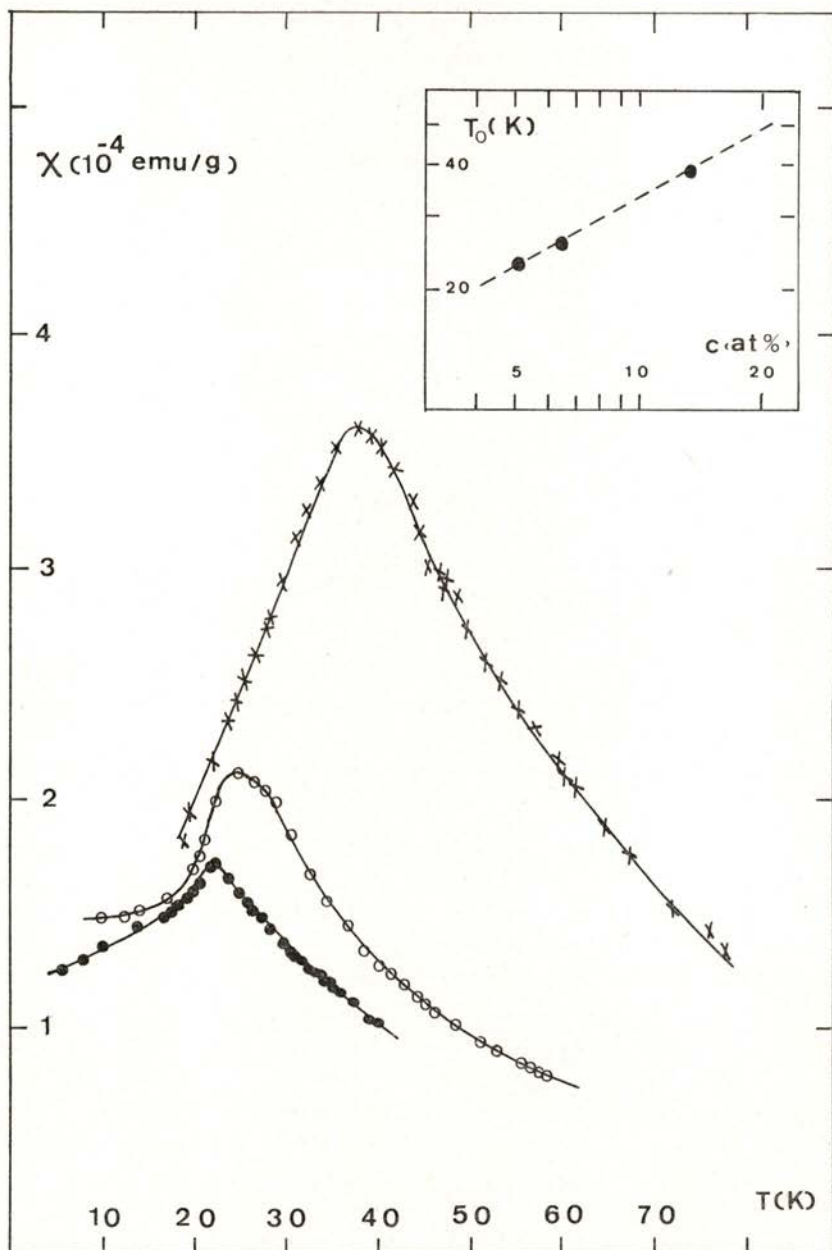


Fig. 1 — Magnetic susceptibility of three Ag Mn samples: \times — 13.00 at %, o — 6.35 at %, \bullet — 4.96 at %. The insert shows, in a log-log diagram, the concentration dependence of T_0 : 38.1 K (13.00 %), 25.0 K (6.35 %) and 22.4 K (4.96 %).

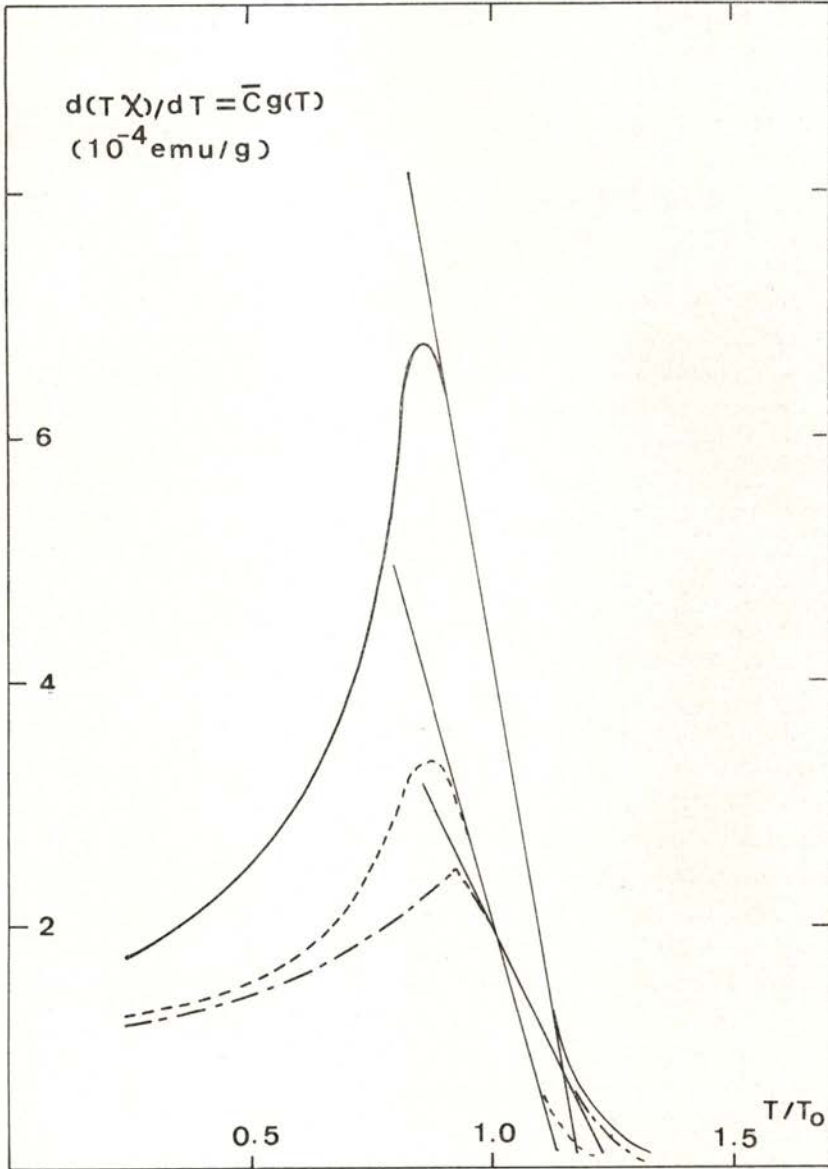


Fig. 2 — The function $\bar{C}g(T)$ as a function of T/T_0 : the straight lines represent the derivatives $\bar{C}dg(T)/dT$ at T_0 for the three samples: -6.15×10^{-5} (emu/g. K) for 13.00 %, -5.08×10^{-5} (emu/g. K) for 6.35 % and -3.26×10^{-5} (emu/g. K) for 4.96 %.

constant of the alloy, as a function of T/T_0 . All three T_0 values, calculated from (5), were consistent with the position of the susceptibility maxima shown in Fig. 1; they are, however, slightly larger than those reported by Korn [8] and Kouvel [9]. Also the second derivatives of χ at T_0 calculated from the experimental values agree, within the experimental accuracy, with those obtained from $dg(T)/dT$, supporting, therefore, the theoretical model.

Mulder *et al.* [10] have shown that samples of Cu Mn slowly cooled from the melt have wider distributions of T_B than those rapidly quenched. Results from A.C. susceptibility measurements on a quenched sample are almost independent of a superimposed D.C. magnetic field up to values of 2 kOe [10]. However, for the slowly cooled alloys the D.C. magnetic field rounds up the maximum of the susceptibility. This rounding of the maximum in the case of Ag Mn alloys is clearly seen in Fig. 1. If one were to accept Wohlfarth's assumption (C independent of T_B) the curves of Fig. 2 would give directly the distribution function $f(T_B)$. If, on the other hand, one were to accept Wohlfarth's expressions for the blocking temperature $T_B = vK/25k_B$, and 'constant' $C = vM_S^2/3k_B$, where v is the effective particle volume, and where both the effective anisotropy coefficient, K , and intrinsic magnetization of the cluster material, M_S , are assumed independent of temperature, one would have $C \propto T_B$ and $g(T) = (T/T_1) f(T)$, in which T_1 is the average blocking temperature. This does not coincide with T_0 , but, in principle, the sharper the transition the less they will differ. The distribution functions calculated in this way are shown, for the three Ag Mn samples, in Fig. 3; they are similar to those given in ref. [10]. Here the higher the concentration, the sharper becomes the distribution function $f(T)$ in the vicinity of T_0 , confirming, possibly, that the effect of the D.C. magnetic field is the less pronounced the higher the manganese concentration of the alloy.

One of us (JMMS) is grateful to the Japan Society for the Promotion of Science for a grant awarded him in the year 1979. We would like to thank Mr. M. Aoki and Mrs. F. Sakai for their invaluable assistance in the preparation and chemical analysis of the samples.

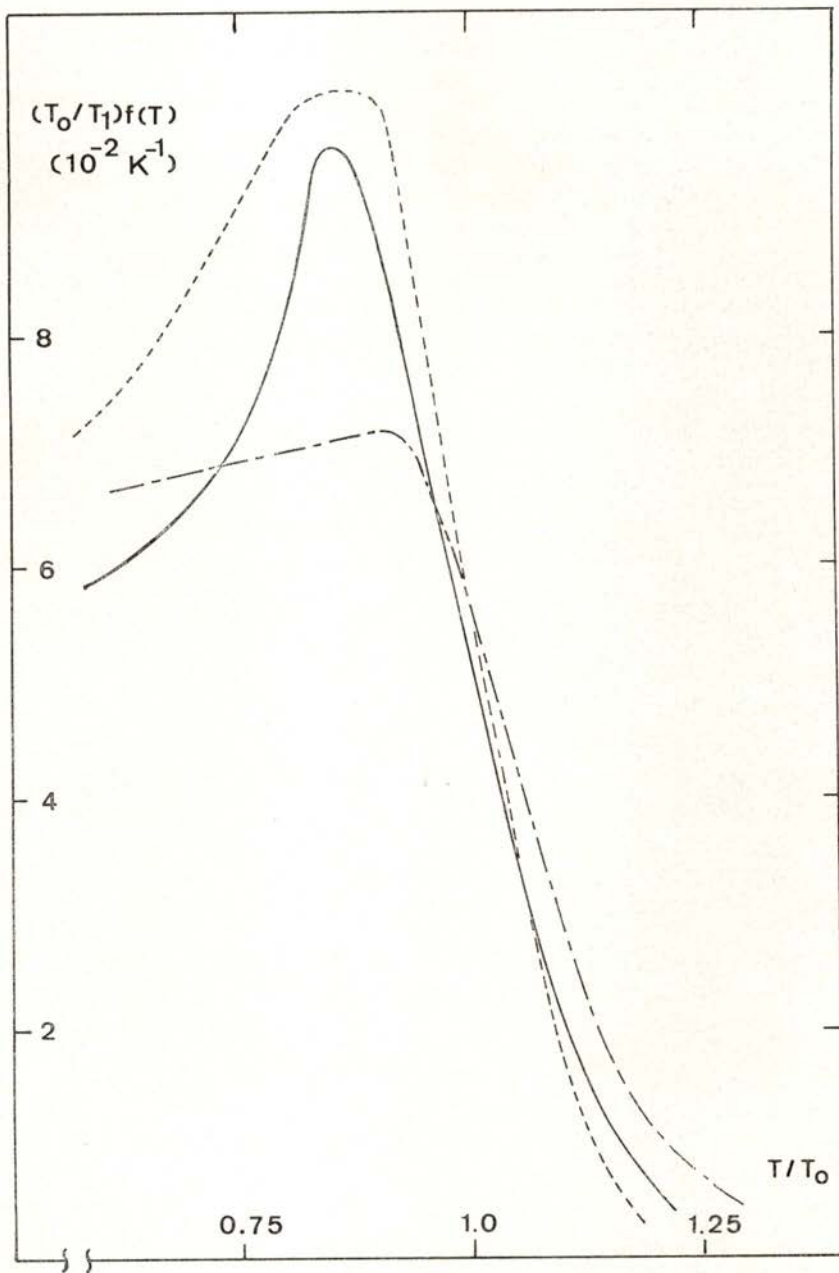


Fig. 3 — The distribution function $f(T)$ multiplied by T_0/T_1 for the three samples of Ag Mn: — (13.00 %), --- (6.35 %), - · - · (4.96 %).

REFERENCES

- [1] THOLENCE, J. L., *J. Appl. Phys.*, **50** (1979), 7310.
- [2] CANNELLA, V. and MYDOSH, J. A., *Phys. Rev.*, **B6** (1972), 4220.
- [3] HEBER, G., *Appl. Phys.*, **10** (1976), 101.
- [4] ANDERSON, P. W., *Amorphous Magnetism*, 2, (1977), 1.
- [5] WOHLFARTH, E. P., *Physics Letters*, **70A** (1979), 489.
- [6] NÉEL, L., *Ann. Géophys.*, **5** (1949), 99.
- [7] MATSUI, M., HIROAKI, N. and CHIKAZUMI, S., *Japan. J. Appl. Phys.*, **15** (1976), 299.
- [8] KORN, D., *Z. Phys.*, **214** (1968), 136.
- [9] KOUVEL, J. S., *J. Phys. Chem. Solids*, **24** (1963), 795.
- [10] MULDER, C. A. M., von DUYNVELDT, A. J. and MYDOSH, J. A., *Journal Magn. and Mag. Materials*, **15-18** (1980), 141.

AN AUTOMATIC FARADAY TYPE MAGNETOMETER WITH A WIDE RANGE SENSITIVITY

J. F. D. MONTENEGRO (*)

Physics Department, The University, Southampton SO9 5NH, U.K.

(Received 16 November 1981)

ABSTRACT—A new type of force magnetometer was designed and built. It can detect forces down to 10^{-4} dynes and the design enables measurement of weak and strong magnetic moments, with a resolution better than one part in 10^5 . This was attained by keeping the sample in a static position by means of a feedback system. The balance is controlled by a minicomputer which allows the determination of a few thousands of data points per run; it is, thus, possible to test the data by statistical methods.

1 — INTRODUCTION

Methods for measuring the magnetisation of magnetic materials can be divided in two categories [1]:

- i) force methods wherein one measures the magnetic force exerted on a sample placed in an inhomogeneous magnetic field;
- ii) induction methods wherein one measures the signal induced in a detecting coil by the changing magnetic moment of the sample.

The Faraday method is an example of the first category. Due to its high sensitivity in measuring paramagnetic and diamagnetic susceptibilities it is a convenient method when dealing with small samples. Packing errors are nonexistent, since this method measures magnetic moments directly.

The principal difficulty associated with this method is the determination of the field gradient. If, as is usually done, this is

(*) Present address: Universidade do Minho, 4700 Braga; and Centro de Física da Universidade do Porto, 4000 Porto, Portugal.

produced by specially shaped pole pieces, the gradient is a complicated function and not easily determined with high accuracy. If the field gradient is produced by coils or current strips, it is usually very small and so the sensitivity is small. Moreover, it cannot be assumed that the field gradient will be independent of the permeability of the pole tips, i.e., of the field produced by the electromagnet.

The second category is exemplified by the vibrating sample magnetometer. Although this method has a lower sensitivity than the Faraday method it has the advantage of having an output which is directly proportional to the sample magnetisation at all fields.

The classical Faraday method does not stand as a convenient absolute method [2]; the limitation arises from the variation in the force due to the profile of the magnetic field when the specimen displacement takes place [3], which makes the field and field gradient determinations not very accurate. A variety of magnetometers based on different methods have been reported [4], [5], [6].

In the type presented in this work the sample is always at the same position due to an almost instantaneous restoring force, acting on the sample by a feedback system. A further problem associated with this method is that with a horizontal field it is impossible to have a vertical force without having a horizontal one and that any horizontal stiffness needed to overcome the horizontal force, inevitably decreases the sensitivity of the system to vertical forces.

This problem was solved in our magnetometer by deliberately making the system stiff in both directions and then using an extremely sensitive method for sensing the vertical force. A change on sample position can be detected with a sensitivity of 3×10^{-8} mm. The lateral motion is prevented by flat spirals made out of phosphor bronze (0.15 mm thickness).

2 — ELECTRONIC DESIGN OF THE DISPLACEMENT TRANSDUCER

Lion [7] and Neubert [8] discussed many of the factors affecting the choice of an electromechanical transducer for

slowly varying displacements. Some more obvious features of a capacitive transducer are:

a) The forces exerted on the moving member by the measuring apparatus are electrostatic ones and these can be made small enough for most purposes.

b) The system responds to the average displacement of a large area of a moving member.

c) Since the resistance of practical conductors can be taken as zero in the present context the performance is determined almost wholly by the geometry of the transducer, and this can be made fairly simple.

The capacitance between two isolated electrodes of simple geometry can usually be written, at least approximately, in the form of an area divided by a separation.

For an isolated pair of nearly parallel plates one larger than the other, the capacitance is very sensitive to a change in the average separation of the plates, and very insensitive to any other relative motion.

Let A be the area of the smaller plate, and ϵ the permittivity of the medium between the plates. Suppose that when the separation is changed from X_0 to $(X_0 - X)$, the capacitance changes from C_0 to C_1 . Then, neglecting edge effects [9],

$$\begin{aligned} (C_1 - C_0) (1 - X/X_0) &= \epsilon A X/X_0^2 \\ &= C_0 X/X_0 \end{aligned} \quad (1)$$

A particular convenient arrangement uses three nearly equally spaced parallel plates, the outer two being a fixed distance apart. A displacement of the middle plate causes one of the two capacitances so formed, say C_1 , to increase and the other, C_2 , to decrease. If the separation of the plates are respectively $(X_0 - X)$ and $(X_0 + X)$, and C_0 is the value of C_1 and C_2 when X is zero then

$$\begin{aligned} (C_1 - C_2) (1 - X^2/X_0^2) &= 2 \epsilon A X/X_0^2 \\ &= 2C_0 X/X_0 \end{aligned} \quad (2)$$

The arrangement has thus the additional advantages of:

- i) doubling the output

- ii) reducing the nonlinearity
- iii) making the electrostatic force on the centre plate zero, when the system is exactly balanced.

Departures from linearity are predictable and stable. There is continuous and smooth change in output against displacement. The geometry of the transducer is more easily calculated than with magnetic devices because there is no penetration of the electrostatic field in the metal electrodes. Sensitivity is determined mainly by the external circuit, and with a good design a resolution of 1 part in 10^7 or better is possible. Stability is mostly a matter of mechanical design, although dielectric losses may cause some variation.

Fig. 1 shows a circuit of a differential capacitive transducer with an inductive divider connected to form an a.c. bridge circuit.

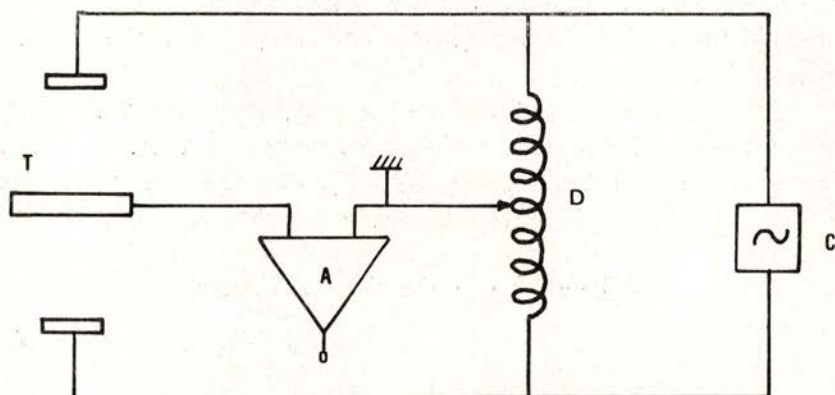


Fig. 1 — The A.C. bridge circuit.

The carrier signal C energizes both the inductive divider D and the transducer T. Since the transducer draws very little current the impedance of the leads to it is not significant. Also the inductive divider has low output impedance, and so earth admittances cause little error. The output impedance of the transducer is high and needs a suitable amplifier to retain as much of the output signal as possible. The carrier phase and amplitude is detected by a phase-sensitive detector so that the sense and amplitude of the displacement is indicated. This circuit may have

an analogue output which indicates the 'out of balance' signal between the halves of the bridge.

The differential capacitive sensor has an impedance of about 1 pF between each plate. There is a large shunt impedance due to the input cable capacities of the order of 1,000 pF. However, because the input amplifier is a 'virtual ground amplifier', (Fig. 2),

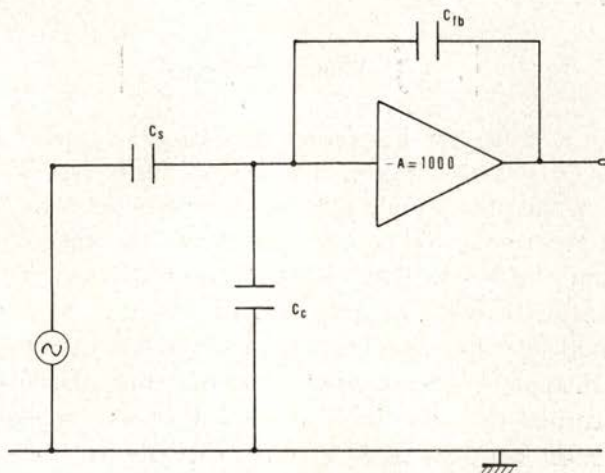


Fig. 2 — Input amplifier used as a 'virtual ground amplifier'.

then the effect of the shunt capacity can be greatly reduced. Considering the circuit of Fig. 2, the gain to signal will be C_s/C_{fb} . With the given values $C_s = 1$ pF and $C_{fb} = 10$ pF; this gives a gain of 1/10 to the signal. However if the input capacitance were to be measured it would be about 10,000 pF, as the amplifier acts as a capacitance multiplier on C_{fb} . Now if this is shunted by the 1,000 pF cable capacitance it will only give rise to a 10% fall in gain to signals via C_s .

The signal to noise ratio gets progressively worse as the input shunt capacity increases. If it is necessary to make very high resolution measurements, care must be taken to see that the cable capacity is kept to a minimum.

The accurate measurement of a.c. signals is often affected by the presence of noise. The noise may often be reduced by special screening and earthing arrangements. However these are

sometimes inappropriate and usually quite difficult to apply. In any case they do nothing to reduce random noise, the limiting factor to resolution in measurement of small signals.

The output of the phase-sensitive detector (in this work) is a d.c. signal on which a double frequency carrier signal (ripple) and wideband noise are superimposed; these spurious signals can be almost totally removed by filtering in a later stage. The d.c. output level is given by

$$\left| \left(\frac{1}{\pi} \int_0^{\pi} A \sin x \, dx \right) \cos \phi \right|$$

The term inside the brackets is the average value of a rectified sine wave over half a cycle. The $\cos \phi$ term comes from the difference in the phase angle between the detector drive waveform and the input signal. When the angle ϕ is 90° then there is no output from the p.s.d.. This means that the leakage resistance of the transducer will not give rise to any d.c. output, and an accurate null can still be obtained. This is one major advantage of the p.s.d. type of circuit. Another is that the signal component has been turned to a d.c. level, and as a direct consequence the wideband noise can now be filtered by a simple RC low pass filter.

In reality, the plates of the transducer are not isolated. If the conductors in the neighbourhood of the plates are not set to definite potentials (i.e. are left electrically floating), they can have a large effect on any capacitance measurement, and it is essential to connect them to a common terminal which will most conveniently be earthed. These conductors must therefore remain as far as possible fixed relative to the plates. The necessarily flexible leads to the plates must be arranged with care, but it is much easier to avoid stray capacitance between two leads than between one lead and earth.

It should be mentioned at this stage some of the most important mechanical disturbances likely to occur [10].

Temperature variations are a serious factor originating expansion of the components in a degree which cannot be neglected. Also temperature-time variations can be of importance even in devices made out entirely of the same material as thinner parts will respond faster than thicker ones to external temperature changes.

In these circumstances a symmetrical design and a thermostatically controlled enclosure are required. Also the instrument should be situated in a massive evacuated metal box, its conducting walls providing an adequate electrostatic insulation, important mainly at frequencies at which the mechanical components resonate, i.e. 50 Hz and above. Low frequency vibrations can also cause disturbances if they make the instrument platform tilt, since this may change the relative direction of gravity and the elastic forces in the structure.

3—DESCRIPTION AND PERFORMANCE OF THE MAGNETOMETER

The conditions of the design of the type of magnetometer presented here give rise to the following characteristics:

1. It is based on the classical Faraday method but having the advantage of a feedback system restoring the sample position (see Fig. 3).
2. Forces as small as 1×10^{-4} dynes can be detected.
3. Noise at output — 0.1 mV r.m.s.
4. Signal-to-noise ratio — better than 5.0.
5. Precision — up to 1.5×10^{-6} g $\langle \rangle$ 1×10^{-4} dynes.
6. Resolution — 1 part in 10^5 .

Fig. 3 shows schematically a sketch of the magnetometer and the associated electronic circuits. The output in the form of a single ended voltage across a standard resistor can be fed into three devices simultaneously: a X, T/Y recorder, a digital voltmeter and a minicomputer with two simultaneous outputs (punched paper tape and printed data onto a teletype).

4—CALIBRATION AND FIELD GRADIENT

Although it is possible, in principle, to measure the field gradient absolutely, it is difficult to attain an accuracy much better than about 0.1 %, so the field gradient was determined,

in this work, as a function of field using samples of known magnetisation.

It is, however, very clear that the accuracy of the final measurements can be no greater than the accuracy with which the field gradient can be determined. This, in turn, is limited by the accuracy with which the magnetisation of the sample used for calibration is known. There are two somewhat different approaches to the problem. In the first place one can use a paramagnetic sample. The magnetic moment of an ideal paramagnet is directly proportional to the field so that the field gradient is determined in terms of the field and the susceptibility.

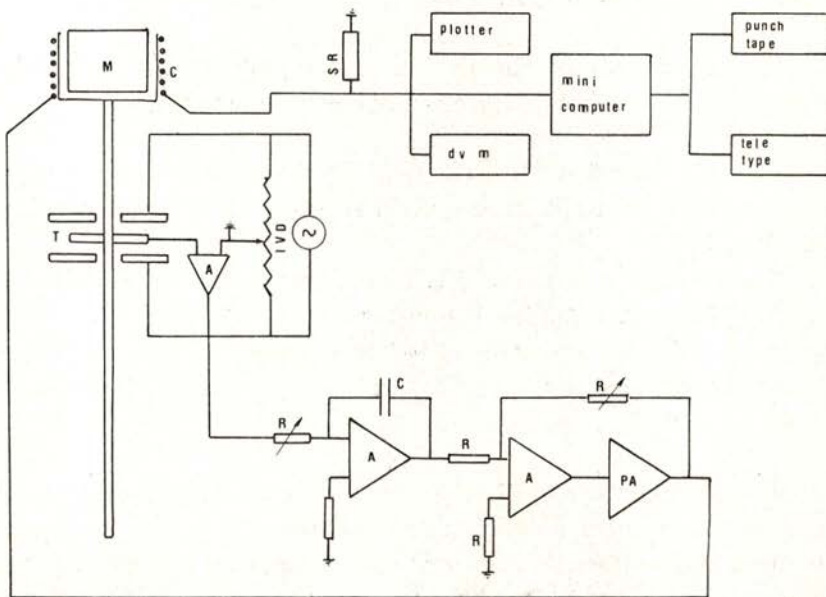


Fig. 3 — Sketch of the magnetometer and the corresponding logging system.

In practice ideal paramagnets have a rather low susceptibility, the forces to be measured would be rather small and the errors involved correspondingly high. To overcome the latter problem one can select a real material with a large paramagnetic susceptibility but in this case there is a risk that its susceptibility might be field dependent. Our solution to this problem was to

use the high susceptibility of a rare earth metal at room temperature and to establish the field-independence of its susceptibility by an independent experiment.

Alternatively one can use a ferromagnetic sample, the advantage here being that the forces to be measured are large and the field does not have to be measured. Instead, the field-dependence of its ferromagnetic moment must be known, either from a previous, independent measurement or by other means. This is essentially the method of Aldred et al. [11]. They used a sample of pure iron and noted that, according to simple spin wave theory and using values of the spin wave stiffness obtained from inelastic neutron scattering, the intrinsic magnetisation of iron at 5.3 K would be independent of field (up to 20 kOe) to within 0.001 %. They then assumed that would be true in practice and used this constant value of the magnetisation of iron at 5.3 K to determine the field gradient.

The paramagnetic samples used for the calibration were single crystals of Tb, Dy and Ho. In order to test the field independence of these samples, susceptibility measurements were performed using a constant field gradient (by means of Helmholtz coils). These measurements were made in applied fields up to 80 kOe.

In this particular experiment the magnetometer output is proportional to the magnetisation values. That is, at each value of the field the ratio output/H (applied field) is proportional to χ . Thus a study of how this ratio varies with the field will establish the degree of field independence of the susceptibility. Table 1 shows, for the Tb sample, magnetised along its easy axis at room temperature, values of output/H as a function of H. The value of the standard deviation obtained is 2×10^{-5} and thus the field independence of χ is established within 0.001 %.

Using the magnetometer described in this work three runs for each sample were performed at room temperature, along the easy axis. The resulting field gradients thus obtained were in good agreement within 0.001 %. The averaged field gradient was used in all measurements of this work.

The field gradient was also determined using a sample of annealed polycrystalline iron at 5.3 K. Because of its polycrystalline nature, the saturation magnetisation is reached asymp-

TABLE 1 — Magnetometer Output as a function of H

Applied field H (kOe)	Force \times const. (volt)	Force \times const./H (volt/kOe)
10	19.1426	1.91426
20	38.2859	1.91429
30	57.4289	1.91429
40	76.5712	1.91428
50	95.7144	1.91429
60	114.856	1.91426
70	133.998	1.91427
80	153.144	1.91430

totically, the departure from saturation being represented by the second term in the equation [11]

$$\sigma(H, 5.3) = \sigma(\infty, 5.3) - 0.07619 \alpha K_1^2 [\sigma(\infty, 5.3) \rho^2 H_i^2]^{-1} + \chi H_i \quad (3)$$

with $\sigma(\infty, 5.3) = 221.71$ emu/g, $K_1 = 5.25 \times 10^5$ erg cm⁻³ and $\rho = 7.85$ g cm⁻³, where $\sigma(\infty, T)$ is the saturation magnetisation at T(K), H_i is the internal field, $K_1(T)$ is the first anisotropy constant, ρ is the density and χ the intrinsic susceptibility. α is a numerical factor arising from interactions between the crystal grains [13]; in the field range 10 to 18 kOe it varies from 0.61 to 0.68.

Although this second term has a well-established theoretical basis it has never been put to a satisfactory test and the field-dependence of the factor α has never been verified by experiment. Fortunately the term accounts to no more than 8×10^{-3} e.m.u./g within the field range 10-18 kOe and the uncertainties in this correction are unlikely to be important. The intrinsic susceptibility term is another matter. The experimentally determined values of χ for iron range from 4.14×10^{-6} to 5.46×10^{-6} emu/g.

For the lowest of these values χH changes 3.3×10^{-2} emu/g when H goes from 10 to 18 kOe and this clearly is important.

Let us consider briefly the effect of this term. Suppose the true field gradient is G and we measure the force F on a ferromagnetic sample for which

$$\sigma = \sigma_0 + \chi H = \sigma_0 (1 + \chi H / \sigma_0). \quad (4)$$

Then

$$F = k G \sigma \quad (5)$$

Suppose we overlook or otherwise ignore the χH term, then we shall determine a spurious field gradient G' given by

$$F = k G' \sigma_0 \quad (6)$$

so that

$$G' = G (1 + \chi H / \sigma_0) \quad (7)$$

If we now use this spurious value G' to determine the magnetisation σ_1 of another material for which the magnetisation is genuinely independent of the field then we shall measure a force

$$F = k G \sigma_1 \quad (8)$$

but we shall determine a spurious magnetisation σ_1' given by

$$F = k G' \sigma_1' \quad (9)$$

Clearly

$$\sigma_1' / \sigma_1 = (1 + \chi H / \sigma_0)^{-1} \quad (10)$$

and since $\chi H \ll \sigma_0$ this may be written to very good approximation as

$$\sigma_1' = \sigma_1 (1 - \chi H / \sigma_0) \quad (11)$$

or

$$\sigma_1' = \sigma_1 - \sigma_1 \chi H / \sigma_0 \quad (12)$$

To correct for this spurious field dependence all we need to do is to add a term $\sigma_1 \chi H / \sigma_0$ to all the values of the magnetisation. However, if we are principally concerned with analysing the field-dependence of the magnetisation this simply has the effect of adding a temperature-dependent susceptibility $\sigma_1 \chi / \sigma_0$. Since

χ is not known with certainty, for iron, the term may as well be omitted from equation (3). When a definite value for χ for iron is finally obtained all the results achieved through the use of a spurious value for G can be corrected using the simple procedure outlined above. It should be mentioned that, using polycrystalline iron as a calibration sample the field gradients were determined using the equations,

$$\sigma(H, 5.3) = \sigma(\infty, 5.3) - 0.07619 K_1^2 [\sigma(\infty, 5.3) \rho^2 H_i^2]^{-1} \quad (13)$$

and

$$\sigma(H, 5.3) = \sigma(\infty, 5.3) - 0.07619 K_1^2 [\sigma(\infty, 5.3) \rho^2 H_i^2]^{-1} + \chi H_i \quad (14)$$

It was found that field gradients calculated from equation (13) agreed better with those obtained from the paramagnetic samples than those calculated from equation (14) using $\chi = 5.46 \times 10^{-6}$.

The results are shown for comparison in Table 2.

TABLE 2 — Comparison of the field gradients

A/C	B/C	Internal field H_i (kOe)
1.000002	0.99941	5.6
1.000003	0.99896	10.7
1.000005	0.99833	18.1

A — field gradient derived from equation (13)

B — field gradient derived from equation (14)

C — field gradient derived from paramagnetic samples

This result, especially the closeness of the figures in the first column is very difficult to explain. We cannot rule out the possibility that all the measurements of χ for iron are incorrect

and that the true value is much less than the accepted values. However the value of χ needed to reconcile the figures in column 1 is only $\sim 1.5 \times 10^{-8}$ and this poses great theoretical problems. The great weight of evidence is in favour of a susceptibility of about 4×10^{-6} in which case the use of equation (14) is certainly incorrect. The most likely explanation seems to be that the determination of the field gradient from paramagnetic samples involves a knowledge of the field. The minimum value in column 2 is only .99833 and this could be accounted for by an error in the characteristics (here taken to include reproducibility and accuracy of positioning) of the Hall probe used to measure the field. However it is surprising that the error acts in such a way as to cancel almost exactly the effect of the χH term in equation (14).

Three sources of systematic errors are present in a given run. The first is due to uncertainty in the force measured at zero field. This will produce systematic errors at all points of a particular isotherm. The second is due to possible temperature differences between the sample and the thermometer. The runs are not strictly isothermal and some temperature drift occurs with time. However the occurrence of a temperature drift always leads to the possibility of a temperature lag between the thermometer and the sample and consequently to a systematic error in the temperature. The third source occurs when the calibration sample is removed from the apparatus and another sample introduced. Because of slight spacial variations in the field gradient, any uncertainty in positioning a sample would produce a systematic error in the magnetisation.

The use of small pole gaps in a conventional magnet produces a reaction, the so-called image effect between the specimen and the pole-pieces. This varies directly with the permeability of the pole faces and so depends on the state of saturation of the magnet.

In the present arrangement image effects are automatically included in the determination of the field gradient. There are grounds for believing that these effects are small. Several measurements were made, under identical conditions, of the forces on different specimens of the same material. The force per unit mass was constant to within 0.2 % for a considerable range of masses [12].

5 — FINAL REMARKS

Undoubtedly the advantages of the magnetometer described above are obvious and manifold, and only the most important points will be stressed and schematized here.

1. The great accuracy and sensitivity of the instrument is due to the high resolution of the sensor (differential capacitive transducer) allied to the high precision inductive voltage divider (with a division accuracy of 1 p.p.m.).

2. The instrument allows the investigations to be performed on a practically static sample position, which evidently permits a very precise measurement of the internal field.

3. The automatization of the system through its connection to a minicomputer gives the enormous advantage of the acquisition of a great number of data points up to 1,000 in a single run, where the applied field varies up to 20 kOe during a sweep of approximately 30 seconds.

The successive readings during the scanning of the applied field are done at well controlled steps by means of a convenient electronic triggering system designed for the purpose. In the present work it was found satisfactory the use of intervals of 35 Oe between steps.

The applied field is read at static sample position by means of a Hall probe and the system trigger-minicomputer receives simultaneously at each chosen step a pair of readings, one from the probe and the other from the magnetometer.

As a result the pair of readings field-force is a well defined one for each run at any time. This is a crucial advantage of this set up which will support the high accuracy of the relative measurements.

4. The fact that each run proceeds in a very short time (~ 30 s) assures that temperature fluctuations in the sample will be minimal. Also, it makes possible to obtain a very good average over a large number of repeated runs in a reasonable period of time.

5. Finally, perhaps the most important feature is the possibility of applying in a reliable manner powerful computer fitting procedures which are only possible over a large number of data

points. It is, therefore, quite clear that the high precision combined to the great number of points obtained are the most significant features of the magnetometer.

6—SUMMARY AND CONCLUSIONS

The instrument constructed proved very successful and it has been used for several measurements [14], [15], [16]. The use of high-speed data acquisition coupled with the use of a mini-computer to process the data leads to a new level of precision of measurements of this kind which, coupled with the immense amount of data collected, enables one to investigate the excitations from the ground state of ferromagnetic materials, from the measured field dependence of the intrinsic magnetisation at various temperatures.

Moreover, these measurements can be performed, on suitable crystals, without the use of unusually high magnetic fields using an ordinary laboratory electromagnet.

We acknowledge a grant from INIC (Portugal) and we are grateful to Professor E. W. Lee who provided useful discussions and experimental facilities at the University of Southampton.

REFERENCES

- [1] ZIJLSTRA, H., *Experimental Methods in Magnetism 2, Measurements of Magnetic Quantities*. (Wiley, New York, 1967).
- [2] HILL, G. J., *J. Phys.*, **E1**, 52 (1968).
- [3] GARBER, M., HENRY, W. G. and HOEVE, H. G., *Can. J. Phys.*, **38**, 1595 (1960).
- [4] ARGYLE, B. E., CHARAP, S. H. and PUGH, E. W., *Phys. Rev.*, **132**, 2051 (1963).
- [5] FONER, S., FREEMAN, A. J., BLUM, N. A., FRANKEL, R. B., MC NIFF, E. I. and PRADDANDE, H. C., *Phys. Rev.*, **181**, 863 (1969).
- [6] MATSUI, M., NISHIO, H. and CHIKAZUMI, S., *Jap. J. Ap. Phys.*, **15**, 299, (1976).
- [7] LION, K. S., *Instrumentation in Scientific Research* (MacGraw Hill, New York, 1959).
- [8] NEUBERT, H. K. P., *Instrument Transducers* (Oxford University Press, London, 1963).

- [9] JONES, R. V. and RICHARDS, J. C. S., *J. Phys.*, **E6**, 589 (1973).
- [10] WOLFENDALE, P. C. F., *J. Phys.*, **E1**, 817 (1968).
- [11] ALDRED, A. T. and FROEHLE, P. H., *Intern. J. Magnetism*, **2**, 195 (1972).
- [12] CRANGLE, J. and GOODMAN, G. M., *Proc. Roy. Soc. London*, **A321**, 477 (1971).
- [13] LEE, E. W., *Encyclopaedic Dictionary of Physics*, Pergamon Press.
- [14] DANIELS, M., *Ph. D. Thesis*, Southampton University (1981).
- [15] KHAN, W. I., MELVILLE, D. and MONTENEGRO, J. F. D., *IEEE Trans. Mag.*, **14**, 674 (1978).
- [16] LEE, E. W. and MONTENEGRO, J. F. D., *J. of Magn. and Mag. Mat.*, **2**, 282 (1981).

MEASUREMENT OF SURFACE ACOUSTIC WAVES IN RARE EARTH METALS AT LOW TEMPERATURE

M. S. NEJAD and S. B. PALMER

Department of Applied Physics, University of Hull, Hull HU5 2DX, U.K.

ABSTRACT—The velocity and attenuation of a 5 MHz surface acoustic wave have been measured in polycrystalline Al, Gd and Tb as a function of temperature from 300-200 K. Similar measurements have also been made in the hexagonal basal plane of a single crystal of Tb. In all cases the results have been compared to calculations based on the bulk elastic moduli. In Al the agreement is good while in the two rare earth elements there are a number of discrepancies some of which can be understood in terms of the magnetic properties of these materials.

1 — INTRODUCTION

The surface properties of rare earth metals are particularly interesting for a variety of reasons. The elements are highly reactive and the surfaces can form oxides, hydrides, nitrides and carbides. While the oxides and nitrides are in higher concentrations close to the surface the hydrides are thought to be uniformly distributed throughout the materials.

Thermal cycling of the metals can produce residual stress which may be enhanced close to the surface [1]. In the magnetic phases, and particularly the spiral spin antiferromagnetic phase, it has been postulated that the magnetic structure of rare earth metals is different at the surface to that in the bulk of the material [2]. Finally the surface domain structure contains closure domains that are again different to the domain structure in the bulk of

the material. Some of these surface properties can be studied by surface acoustic wave propagation, measuring the temperature dependence of the velocity V_s and attenuation α_s of the surface acoustic wave (SAW or Rayleigh wave).

There are a range of experimental techniques for launching and receiving SAWs but many of them are not suited to low temperature environments or to the study of small samples. After carefully investigating several techniques [3] we found that the angled transducer method could be used down to at least 200 K on samples with a dimension in the propagation direction of as little as 2-3 mm. To test the reliability of the technique, measurements were first of all carried out on a polycrystalline aluminium sample and the results compared to surface wave velocities calculated from bulk single crystal elastic constants.

Since our temperature range was limited to temperatures above 200 K then in order to study the effect of magnetic order on the surface wave propagation we restricted our attention to the two heavy rare earth metals Gd and Tb. Both crystallise in the hexagonal close packed structure with five bulk single crystal elastic constants C_{ij} [4]. Gd orders ferromagnetically at a Curie temperature T_c of 293 K with magnetic moments aligned along the hexagonal c-axis. Below a spin re-orientation temperature (T_{sr}) of 240 K the moments move away from c-axis to lie along an easy cone oriented at an angle θ to the c-axis. θ initially rises rapidly to an angle of $\sim 70^\circ$ before falling to $\sim 35^\circ$ where it remains down to 4.2 K.

Tb is paramagnetic down to Néel temperature (T_N) of ~ 226 K where it orders in a spiral spin antiferromagnetic phase. This phase only exists over a small temperature range of approximately 7 K and below ~ 217 K, the Curie temperature, Tb is a basal plane ferromagnet. The available temperature range therefore allowed study of magnetic phase changes of both Gd and Tb. We report here measurements of the temperature dependence of V_s and α_s in polycrystalline samples of Gd and Tb which are compared to surface wave velocities calculated from bulk single crystal and polycrystalline elastic constants. In addition we have measured the temperature dependence of the surface wave velocity in the basal plane of a single crystal sample of Tb which can be compared directly with calculated values.

2 — CALCULATION OF SURFACE WAVE VELOCITIES

In an isotropic medium a simple expression relates the surface acoustic wave velocity to the bulk longitudinal and shear velocities (V_L and V_T respectively):

$$(2 - V_S/V_T)^2 = 4 [1 - (V_S/V_L)^2]^{1/2} [1 - (V_S/V_T)^2]^{1/2} \quad (1)$$

The longitudinal bulk wave velocity is related to the bulk modulus K and the shear modulus G by:

$$V_L = [(K + 4/3 G)/\rho]^{1/2}$$

where ρ is the sample density. The shear wave velocity is given by

$$V_T = [G/\rho]^{1/2}$$

Hill [7] pointed out that the bulk and shear moduli can be calculated from the single crystal elastic constants by taking the mean of the two approaches adopted by Voigt [8] and by Reuss [9]

$$K = 1/2 (K_V + K_R) \quad ; \quad G = 1/2 (G_V + G_R)$$

In the case of a hexagonal crystal, for example, one has for the Voigt approach:

$$K_V = 1/9 [C_{33} + 2(C_{11} + C_{12} + 2C_{13})]$$

$$G_V = 1/15 [C_{33} + 2(C_{11} - C_{12} - 2C_{13})] + 1/5 [2C_{44} + C_{66}]$$

while, following Reuss,

$$1/K_R = 2S_{11} + S_{33} + 2(S_{12} + 2S_{13})$$

$$1/G_R = 4[S_{33} - S_{12} + 2(S_{11} - S_{13})] + 3[2S_{44} + S_{66}]$$

where the C_{ij} are the five independent elastic stiffness moduli [$C_{66} = 1/2(C_{11} - C_{12})$] of the hexagonal symmetry and S_{ij} are the elastic compliance moduli defined by

$$S_{ij} = (-1)^{i+j} \Delta C_{ij} / \Delta C$$

where ΔC is the determinant of the C_{ij} and ΔC_{ij} is the minor of the element C_{ij} . Hence it is a straightforward matter to calculate the surface acoustic wave velocity in an isotropic polycrystal from the single crystal moduli.

The study of surface wave propagation in hexagonal single crystals involves numerically complex computation to obtain the surface wave velocities. It is normal to use a «surface Green's

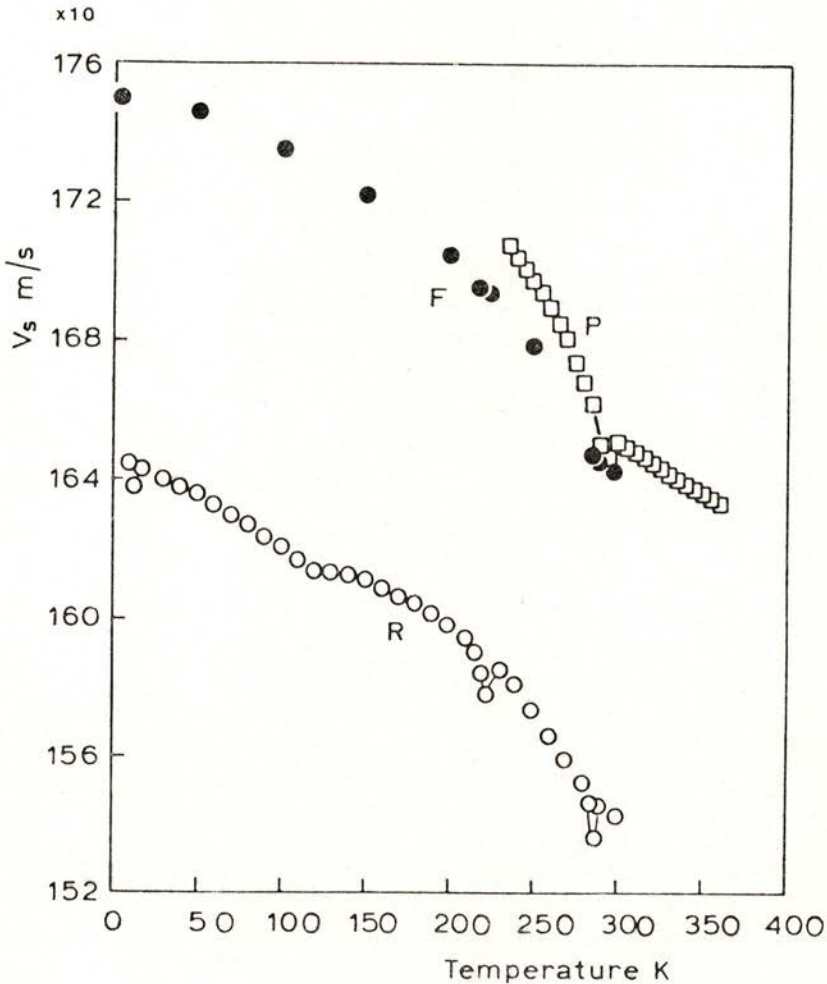


Fig. 1 — Computed Isotropic Surface Wave Velocity in Gadolinium Versus Temperature: \square Data from S. B. Palmer, [4]; \circ Data from M. Rosen, [11]; \bullet Data from E. S. Fisher, [10].

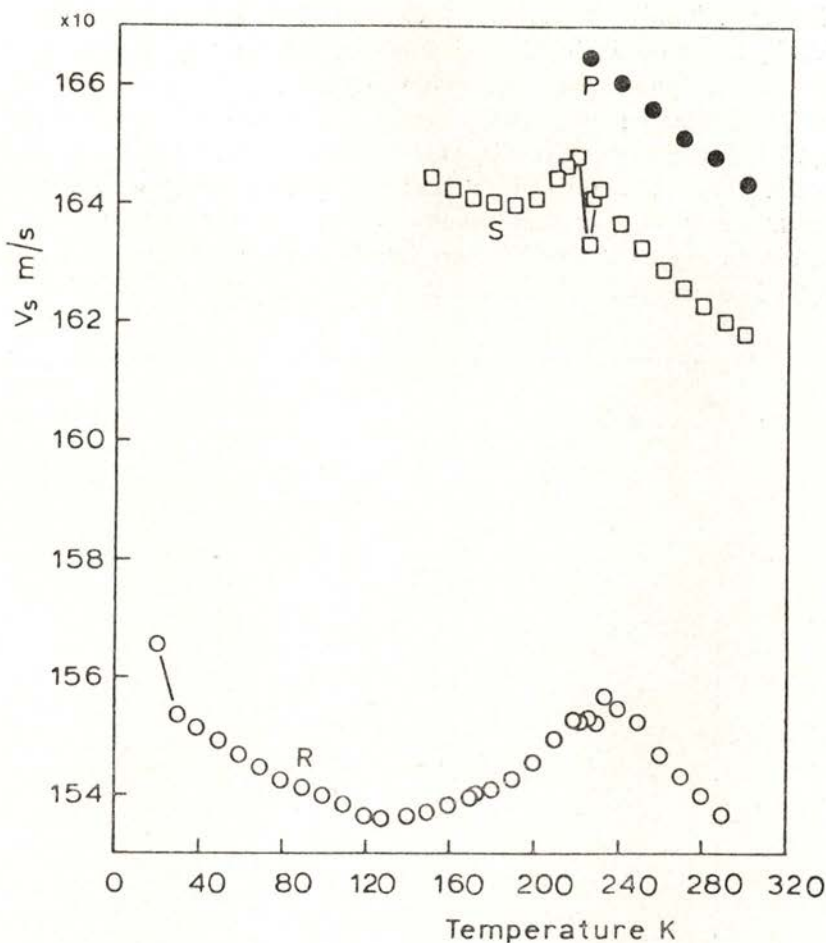


Fig. 2 — Computed Surface Wave Velocity in Polycrystal Terbium for Different Temperatures: □ Data from K. Salama, [12]; ○ Data from M. Rosen, [11]; ● Data from S. B. Palmer, [4].

function approach» where the velocity formula can be transformed to an algebraic equation similar to that of the isotropic case [10]. The most simple solution is obtained for propagation of surface waves in the basal plane of the hexagonal crystal which is transversely isotropic. The relationship between V_S and the C_{ij} can be written

$$C_{33} (V_S^2 - C_{44}/\rho) (V_S^2 - C_{11}/\rho + C_{13}^2/C_{33}\rho) = C_{44} V_S^4 (V_S^2 - C_{11}/\rho) \quad (2)$$

This is a bicubic equation in V_s and it is interesting to note that by using the isotropic limit one can derive eq. (1) from eq. (2).

Fig. 1 shows the computed isotropic surface wave velocity in Gd obtained from eq. (1) using two different sets of single crystal elastic constants [4], [11] and the polycrystalline data of Rosen [12]. It can be seen that the polycrystalline values lie below the single crystal results which are themselves in fair agreement. Gaps in the data are due to one or more of the single crystal constants being unavailable due to experimental problems.

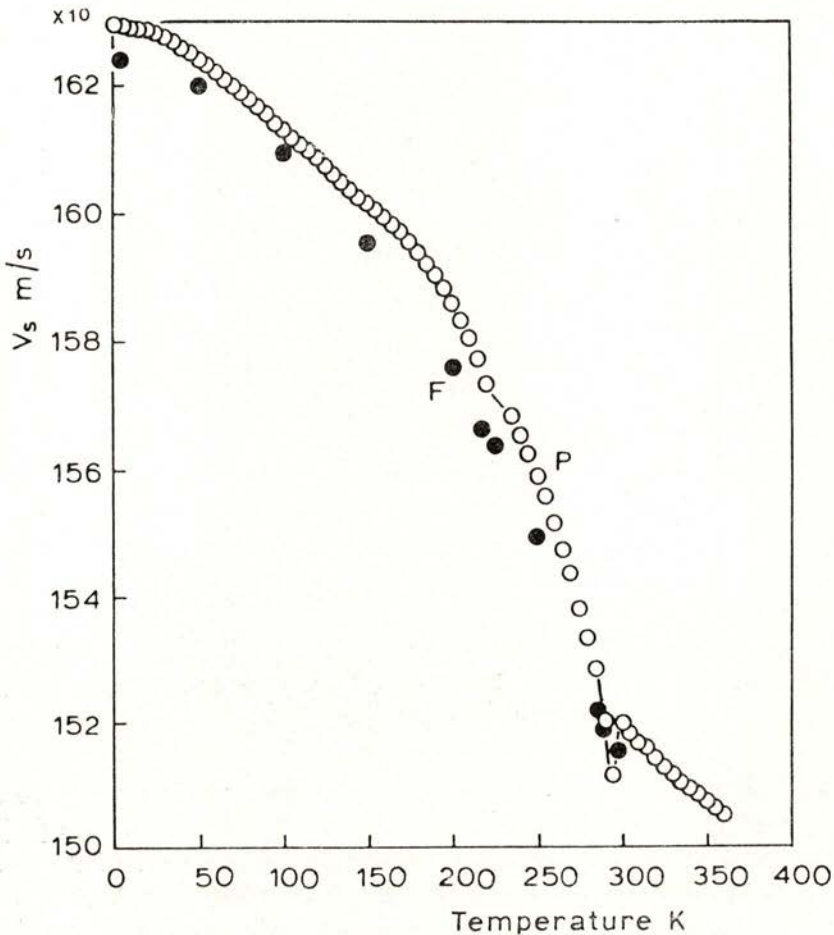


Fig. 3 — Computed Surface Wave Velocity in Basal Plane of Hexagonal Single Crystal of Gadolinium as a function of temperature:

○ Data from S. B. Palmer, [4]; ● Data from E. S. Fisher, [10].

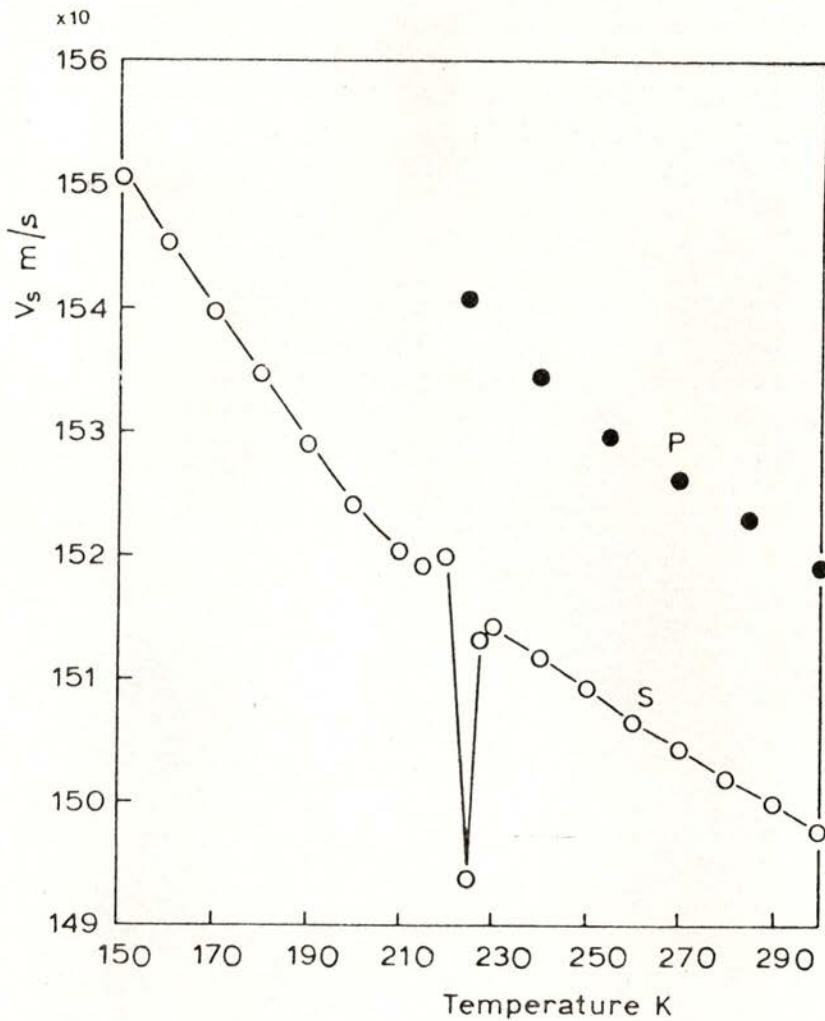


Fig. 4 — Computed Surface Wave Velocity in Basal Plane of Terbium Single Crystal as a function of temperature:
 ○ Data from K. Salama, [12]; ● Data from S. B. Palmer, [4].

Fig. 2 shows similar data for Tb where again Rosen's polycrystalline results [12] lie well below the values calculated from the single crystal elastic constants [4], [13]. In Fig. 3 we plot the computed surface wave velocity in the basal plane of the single crystal Gd computed from the available single crystal data [4], [11]. Fig. 4 shows a similar calculation for Tb. Anomalies are observed

in all four figures which can be attributed to the magnetic phase changes described earlier. In all the figures the individual points have been calculated from the tabulated data in the papers, leading to widely spaced points in some cases. Rosen does not give tabulated points and these have been estimated from the published figures.

3 — EXPERIMENTAL DETAILS

The surface acoustic waves were launched and detected using plate transducers mounted at an angle of 45° on opposite edges of the sample (Fig. 5). The transducers operated in a compressional

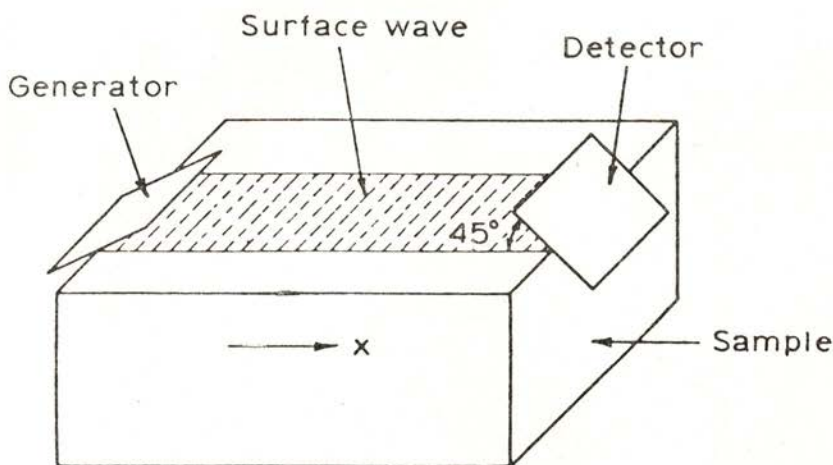


Fig. 5 — Schematic diagram of angled transducer arrangement for surface wave experiment.

mode at a resonant frequency of 5 MHz and were fabricated from PZT 5A ceramic. The transducer was bonded to the edge of the sample with Rapid Araldite which provided a long bond life over an appreciable temperature range. Masking tape was used whilst the araldite was setting to prevent spreading onto the sample surface. The two opposing edges of the sample were lapped

parallel to optical tolerances; in all cases parallelism of better than 15 seconds of arc was achieved. The sample surface that supported the surface wave was polished to a flatness of better than one tenth of the acoustic wavelength ($\lambda/10 \sim 30 \mu$). Normally flatness of better than 5μ was achieved. The polycrystalline samples of Al, Gd and Tb were prepared using standard diamond cutting and diamond lapping techniques, after which they were etched and annealed. For the rare earths a standard etch of a 50-50 solution of acetic and nitric acids was used and annealing took place at approximately 60°C for 5 hours [1]. The single crystal of Tb was spark planed to its final shape at the Centre for Materials Science, University of Birmingham. It was tetragonal with surfaces perpendicular to the a, b and c axes.

To generate the surface acoustic wave the transmit transducer was excited by a 5 MHz R.F. pulse of $0.5 \mu\text{s}$ pulse width and 25 volt peak height, from an Exact pulse generator (Model 7260). The pulse repetition frequency was ~ 20 Hz allowing the surface wave echoes to decay before the next pulse packet was launched. The transit time of the pulse was measured with the time delay facility of an oscilloscope. Due to problems of attenuation and pulse interference the transit time could only be measured from the initial launching of the surface wave to the first surface acoustic wave arrival at the detector.

Temperatures were maintained with a standard cold finger cryostat [14] in conjunction with a commercial temperature controller. Temperature measurement was achieved with two copper constantan thermocouples, one measuring the sample temperature, the other the environmental temperature. Temperature measurements were accurate to ± 1 K with point to point sensitivity of better than 0.2 K.

The major contribution to the errors in the measurement of the absolute velocity of the SAW arises from the location of the corresponding points on the initial generating pulse and the transmitted SAW signal.

One could be out by ± 1 cycle leading to an absolute error in V_s of $\pm 7\%$ in a typical sample. If the appropriate cycles are correctly identified the absolute error reduces to $\pm 0.4\%$ and arises from bond errors associated with the coupling of the trans-

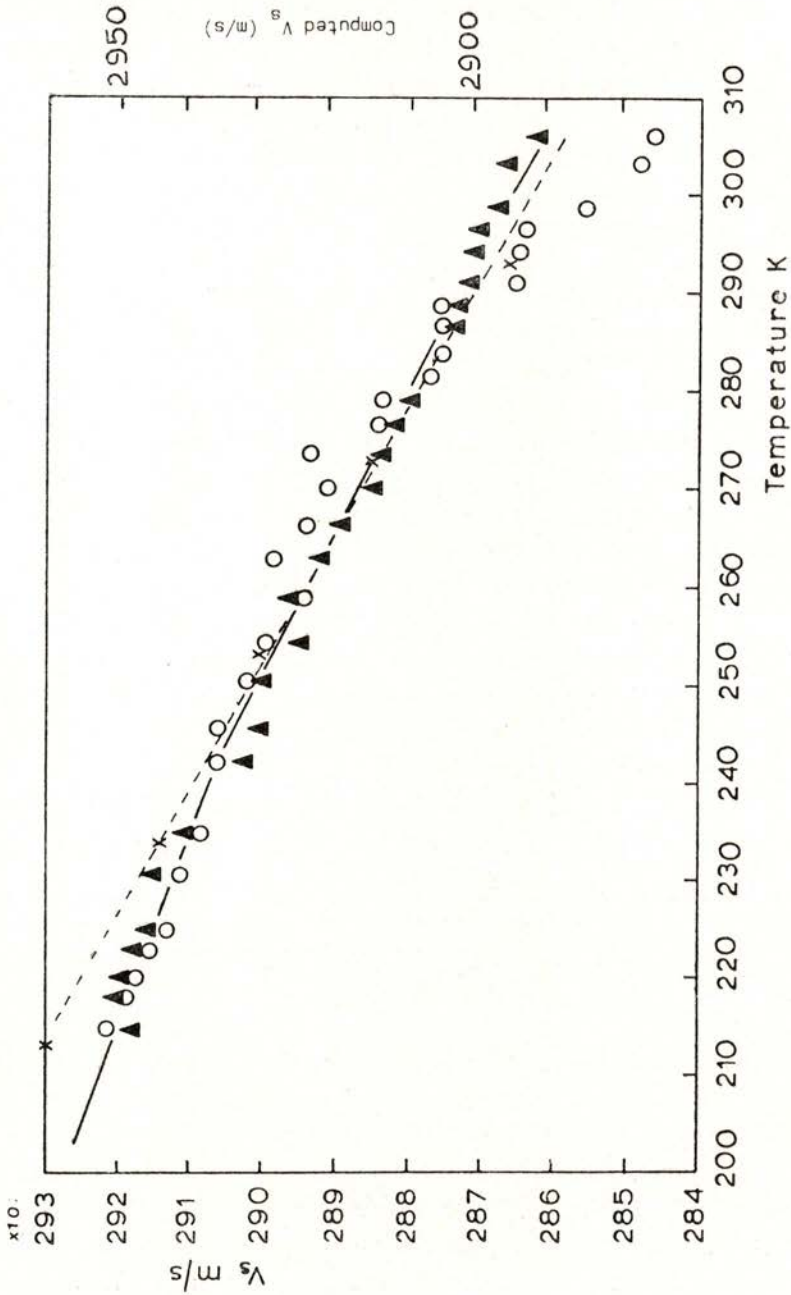


Fig. 6—Comparison between three measurements of SAW velocity in Al. as a function of temperature. Solid line: Rel. V_s liquid bond and \blacktriangle Rel. V_s solid bond. X --- Computed V_s from single crystal data of Sutton [14].

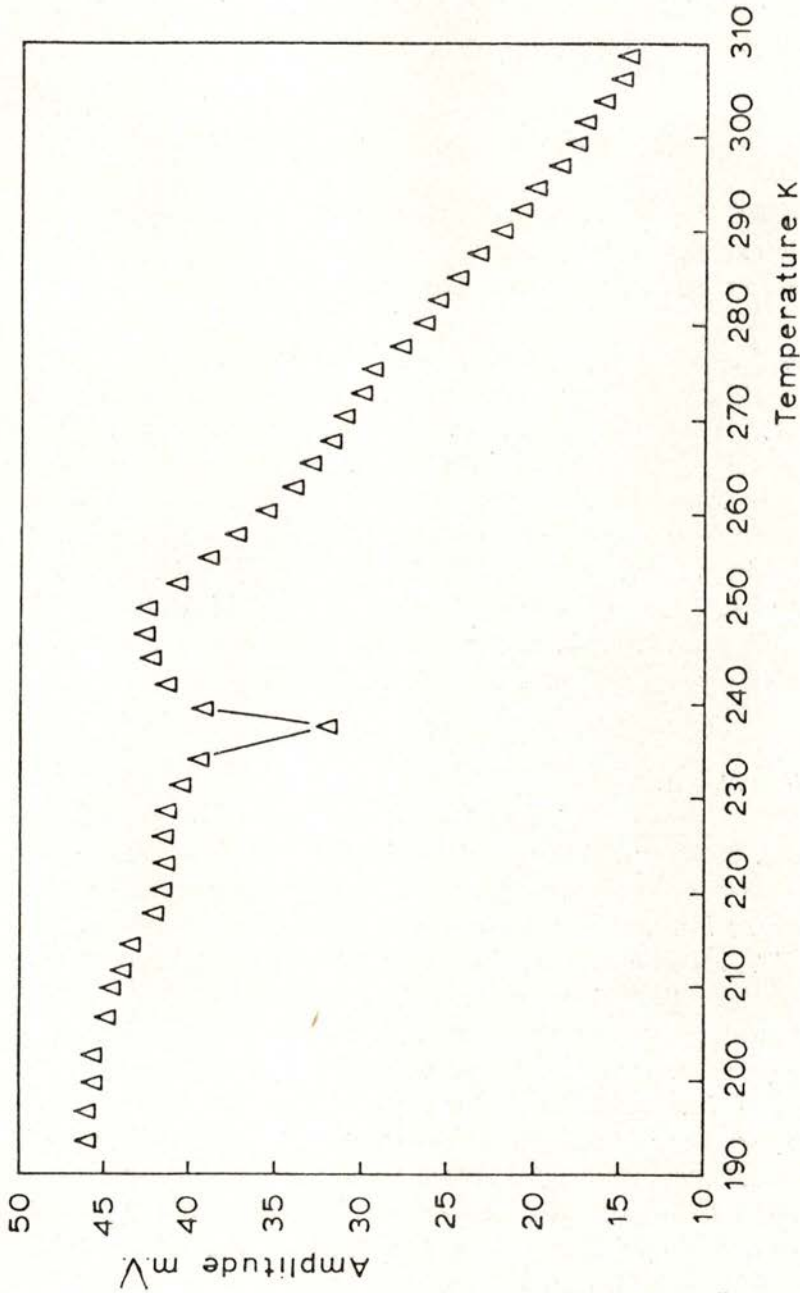


Fig. 7 — SAW Amplitudes in Al for different temperatures. Angled transducers. Lubricant oil bond.

ducer to the sample and from timing errors. This value is reduced still further when one is only interested in the point to point accuracy.

4—RESULTS AND DISCUSSION

Initial experiments were carried out using a polycrystalline aluminium sample with a range of bonding agents between the transducer and sample edge. The temperature dependence of V_s with both an oil bond and an araldite bond are shown in Fig. 6 where they are compared to values calculated, via eq. (1), from the single crystal elastic constants. The absolute values differ by $\sim 1\%$, while the temperature dependence of the experimentally determined and calculated values of V_s are in good agreement. However when one measures the signal amplitude as a function of temperature, which should be related to the surface wave attenuation α_s , it is immediately obvious (Fig. 7) that the oil bond is not suitable since the minimum in α_s at ~ 240 K is produced by the solidification of the oil bond. All reliable measurements were therefore carried out with a Rapid Araldite bond.

Gadolinium

Fig. 8 shows the temperature dependence of V_s and α_s for the surface acoustic wave in the sample of polycrystalline Gd. The insets indicate that there are only minor anomalies at both T_c and T_{st} . The measured V_s is in good agreement at room temperature with the value calculated from single crystal elastic constants, and appreciably higher than the polycrystalline calculations (Fig. 9). In contrast to Al the temperature dependence of the measured V_s is at least a factor three greater than the calculated values, which are themselves consistent. This difference is far in excess of what one might expect from experimental errors.

The measured relative attenuation obtained from the amplitude of a single pulse is compared in Fig. 10 to the polycrystalline results of Rosen [12]. In all cases the ordered phase produces an increase in the ultrasonic attenuation.

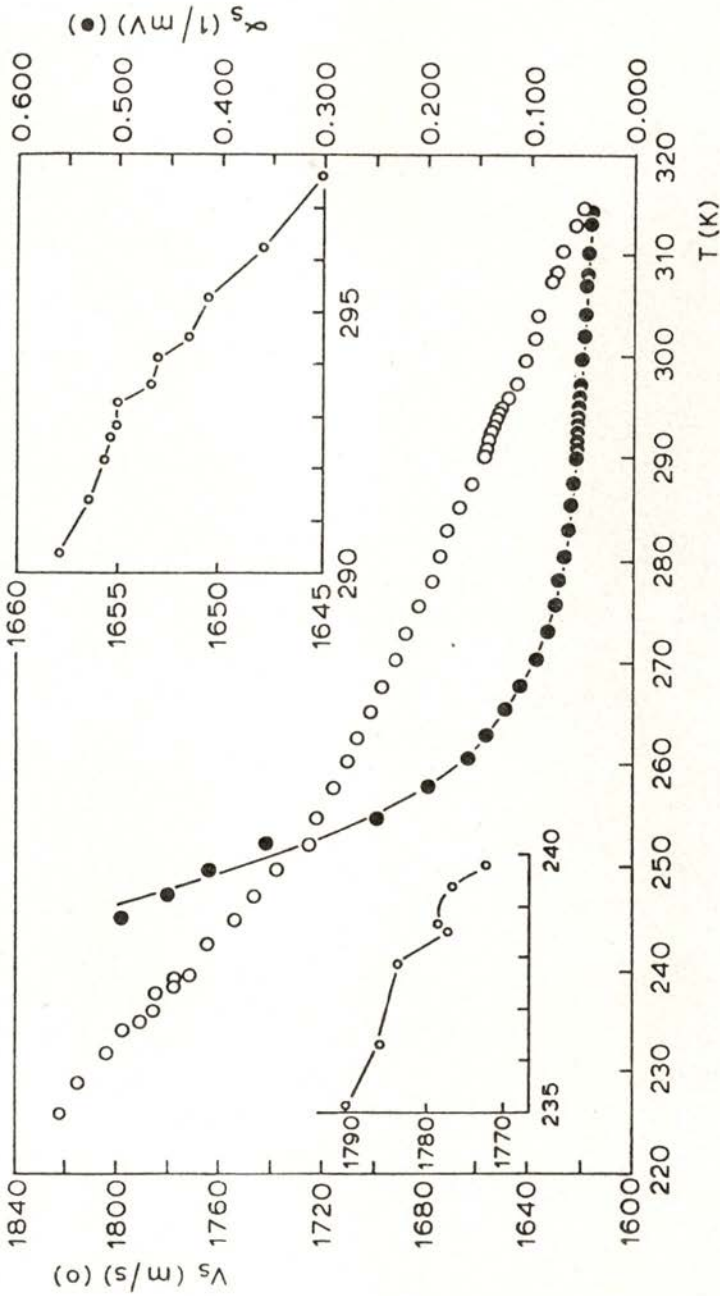


Fig. 8 — Surface acoustic wave propagation in polycrystalline gadolinium. \circ velocity; \bullet relative attenuation.

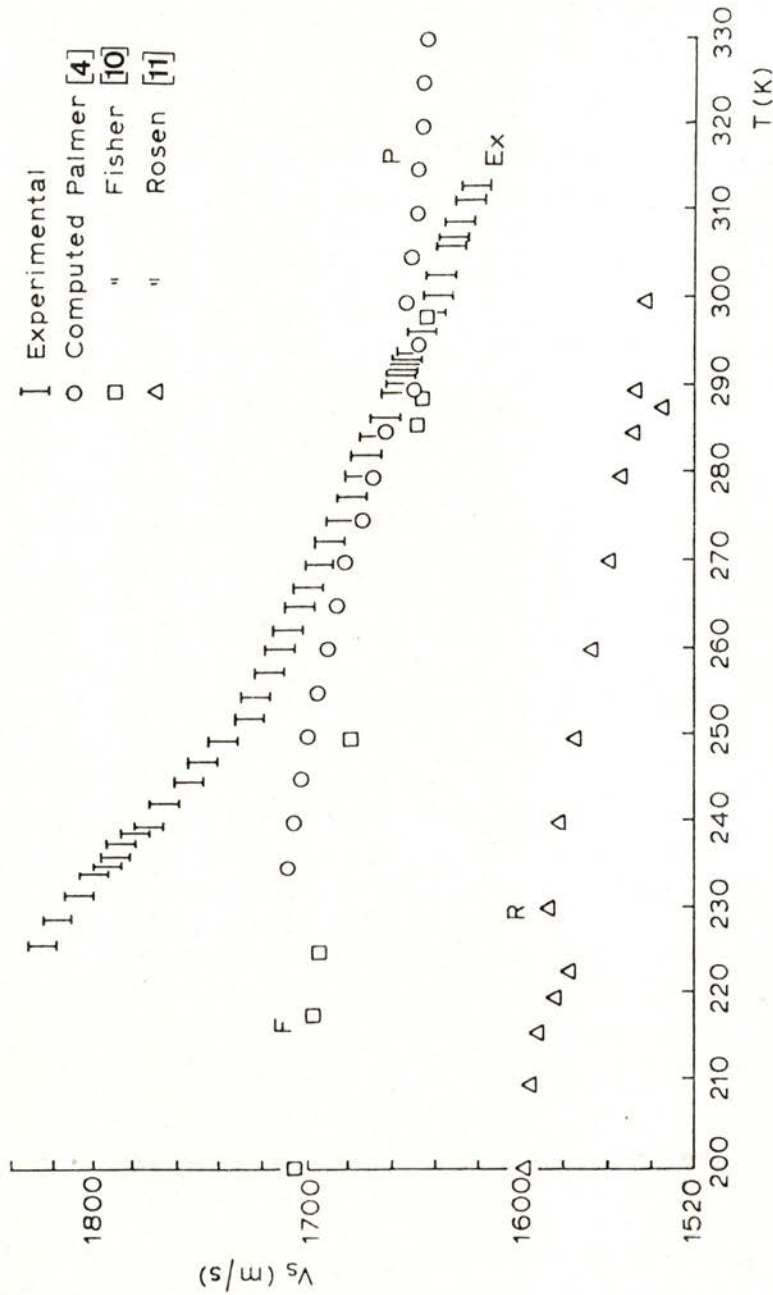


Fig. 9 — Polycrystalline gadolinium. Comparison of Experimental and Computed Values of V_s .

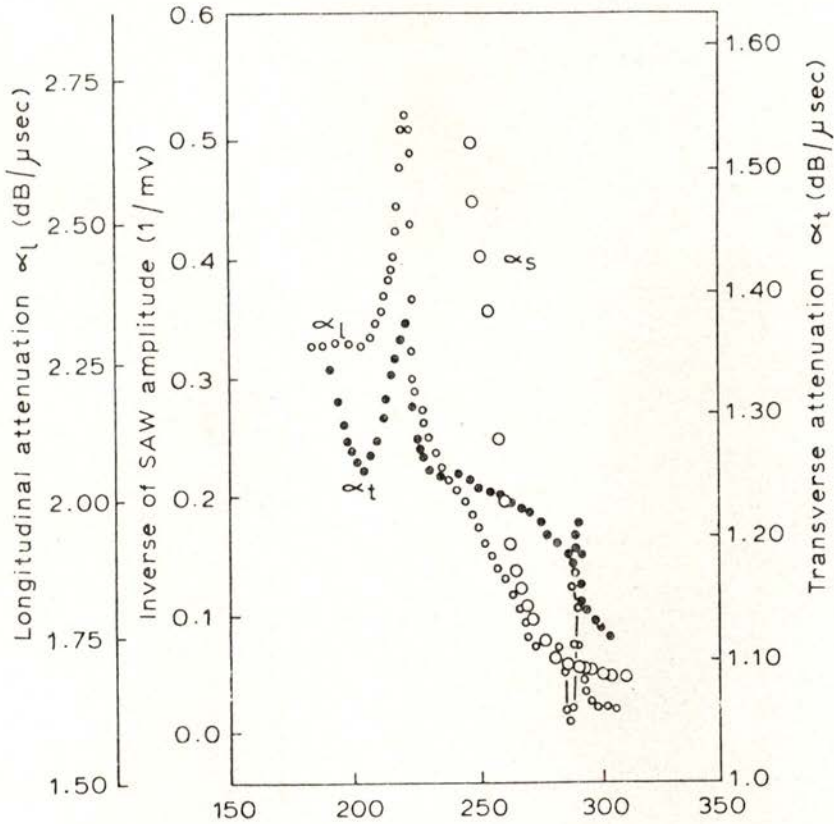


Fig. 10 — Comparison of inverse SAW amplitude (α_s) and bulk wave attenuation (α_l , α_t) from Rosen [11].

Terbium

The temperature dependence of V_s and α_s for polycrystalline Tb is shown in Fig. 11. In the paramagnetic phase V_s increases with decreasing temperature in a similar manner to Gd. In contrast, however, there is a rapid decrease in V_s in the antiferromagnetic phase which is accompanied by an increase in α_s . Both changes are somewhat modified by the onset of ferromagnetism at ~ 216 K. When compared to calculated values (Fig. 12) V_s increases much more rapidly in the paramagnetic phase and in addition decreases much more rapidly in the ordered phases. The minimum observed at T_N for the calculated surface wave velocity

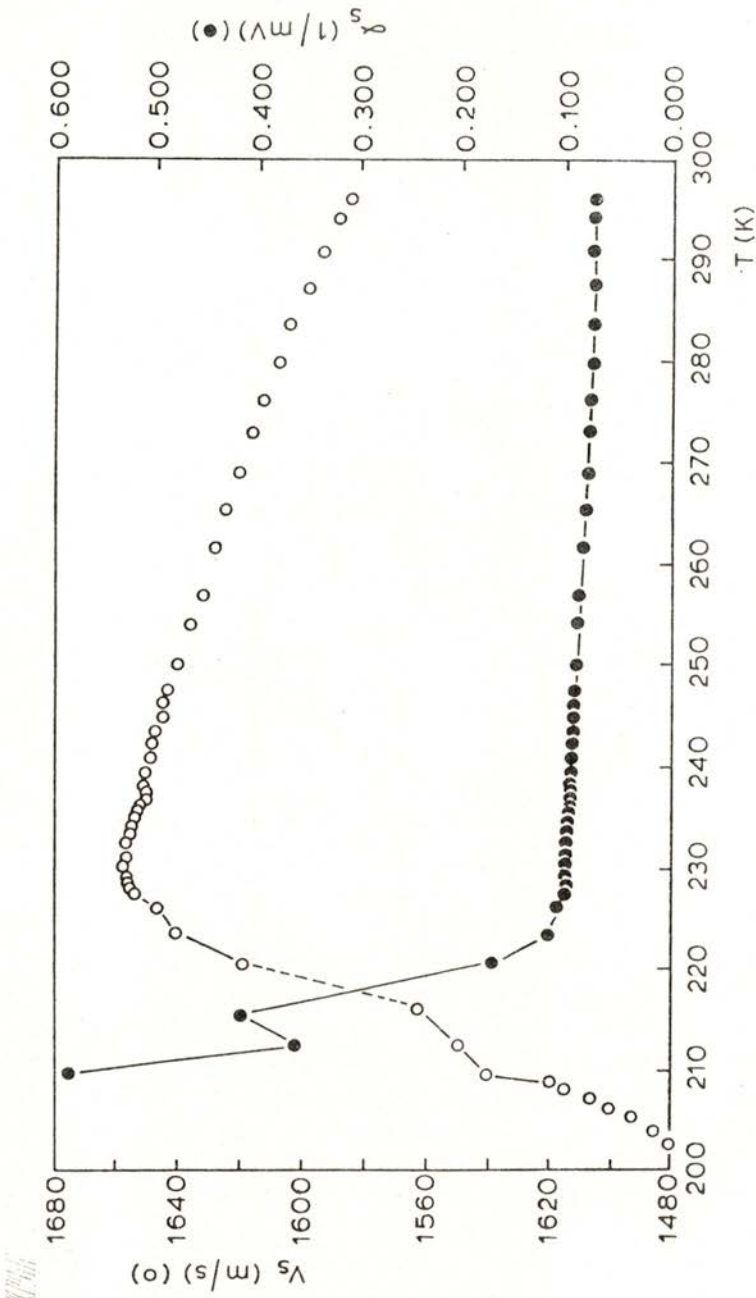


Fig. 11 — Surface acoustic wave propagation in polycrystalline terbium: ○ velocity; ● relative attenuation.

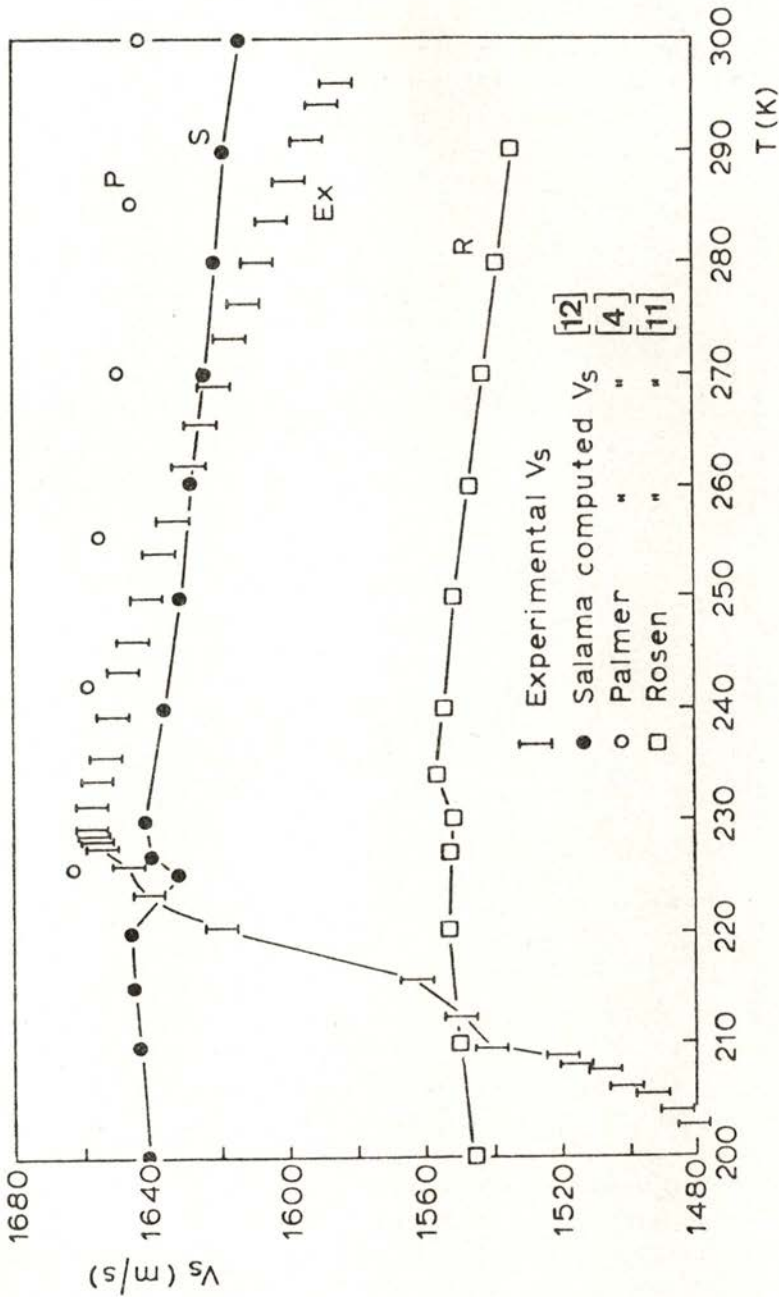


Fig. 12 — Polycrystalline terbium, comparison of experimental and computed values of V_s .

is much weaker than the measured decrease. It is difficult to make any suitable comment on the absolute values of the different curves with such a wide variation between the different sets of data although again the measured values are in better agreement with the calculations based on the single crystal elastic constants.

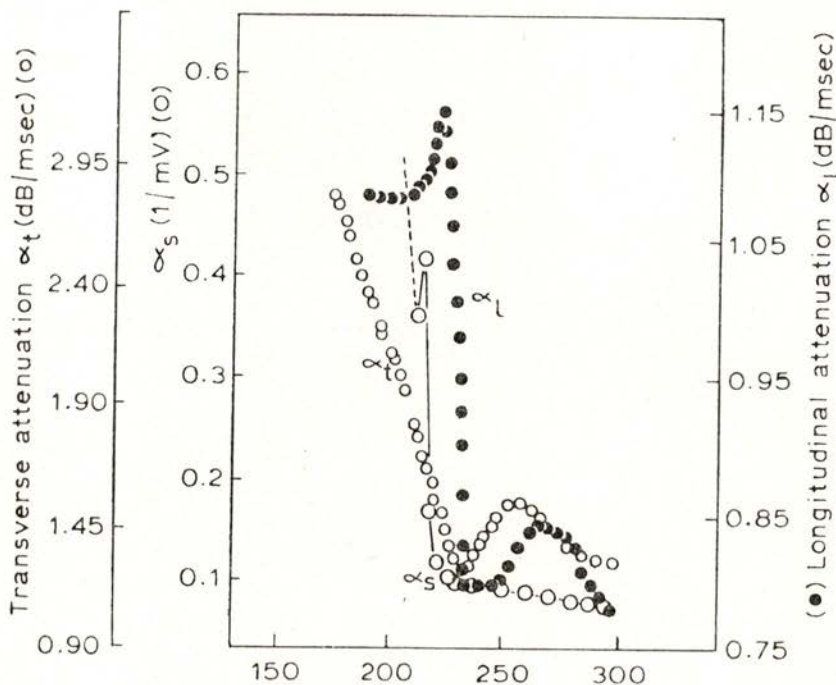


Fig. 13 — Comparison of inverse SAW amplitude (α_s) and bulk wave attenuation (α_l , α_t) from Rosen [11].

The temperature dependence of α_s (Fig. 13) shows some of the characteristics of both the longitudinal and shear wave propagation, as is to be expected for an acoustic mode that contains elements of both atomic displacements. The surface wave attenuation shows no evidence of any peaks in attenuation above T_N as is observed with the bulk waves.

The single crystal of Tb available for the propagation of a surface acoustic wave in the basal plane had a dimension of only 2.2 mm parallel to the propagation direction. This is approaching the limit of the present experimental technique and the results

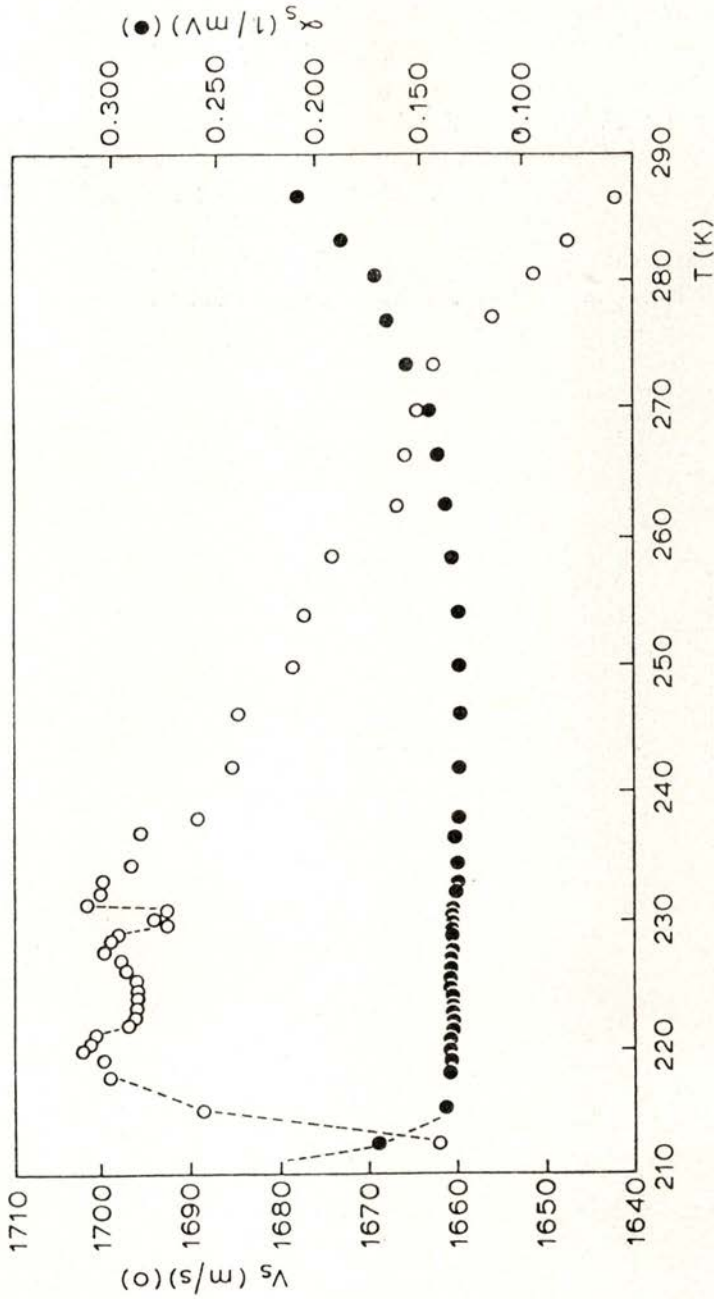


Fig. 14 — Surface acoustic wave propagation in the basal plane (parallel to 'b' direction) in single crystal terbium
 O velocity ● relative attenuation.

are therefore less reliable than the polycrystalline measurements. The temperature dependence of both V_s and α_s , propagating parallel to a 'b' direction are shown in Fig. 14. The onset of magnetic order produces marked changes in V_s in the region of T_N and a rapid decrease at T_c . In contrast the attenuation of the wave is only affected well below T_c . A comparison of V_s with calculated values from single crystal elastic constants, using eq. (2), indicates again that the temperature dependence of V_s is much higher in the paramagnetic phase than one would expect from bulk calculations (Fig. 15). The large discrepancy between the absolute values

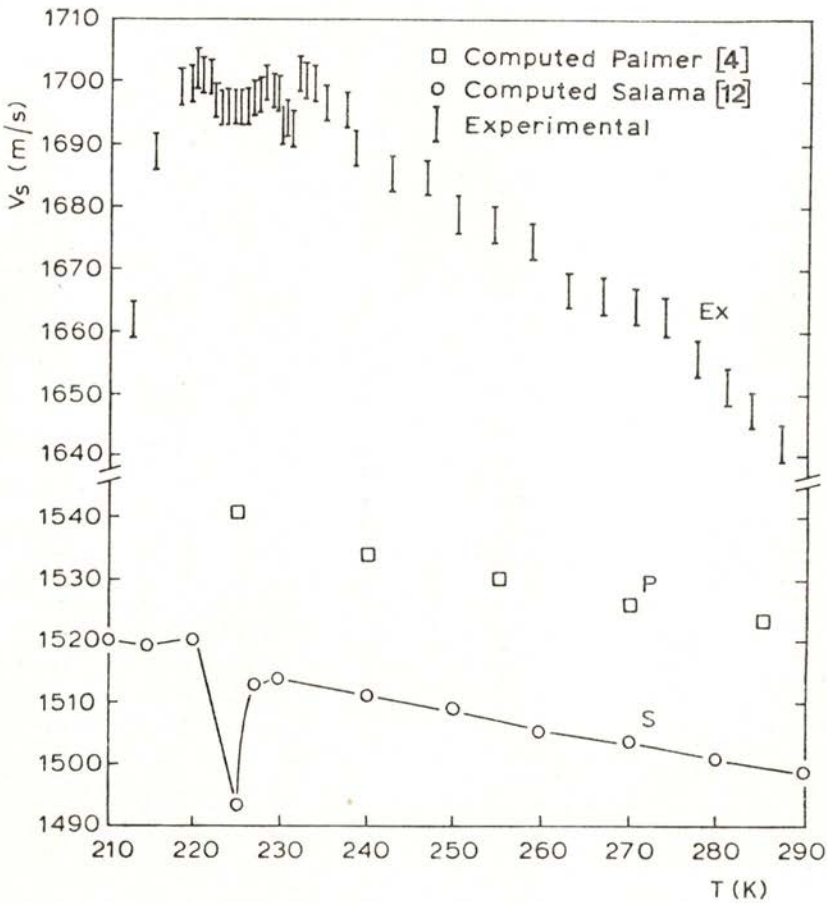


Fig. 15—Single crystal terbium: comparison of experimental and computed values of V_s for propagation in the basal plane.

of V_s is probably due to the small sample length available which will enhance the errors introduced by bond effects and timing problems.

We have demonstrated for the first time that the magnetic phase changes in the rare earth metals are reflected in the properties of surface acoustic wave propagation, although the nature of the changes observed are not always what one would predict from bulk wave behaviour. Nevertheless in the ordered regions these differences may well be due to magnetic domain properties and to magnetic stresses localised in the surface. Evidence for the presence of these surface stresses can be found in measurements of the surface wave velocity at room temperature before and after a low temperature run.

TABLE 1 — SAW velocity at room temperature before and after low temperature run (L.T.R.): Tb single crystal, propagation along b-axis, in the basal plane

Day	Procedure	S.A.W. Velocity m/s	Temperature K
Day 1	Measured velocity followed by L.T.R.	1642	286.6
Day 2	Measured velocity followed by L.T.R.	1637	284.8
Day 3	Measured velocity followed by L.T.R.	1625	285.7
Day 4	Measured velocity	1619	287.2
Day 7	Measured velocity	1642	286.8

Table I shows the effect on V_s of repeated thermal cycling down to 200 K on the Tb single crystal. It is observed that V_s decreases after a low temperature run and that repeated thermal cycling over a period of four days produced a total decrease in $V_s \sim 1.3\%$. At the end of the fourth day the sample was allowed to remain in the cryostat at room temperature and after a further

three days the SAW velocity was again measured at room temperature and was found to have recovered its original value. Some of this annealing of the residual stresses may have taken place in the araldite bond but it is more likely that the majority is produced by stress relief of the sample. No such effects have been observed in bulk ultrasonic propagation indicating that we are dealing with a surface phenomenon.

The behaviour of both Gd and Tb in the paramagnetic phase is rather more puzzling. For the cubic Al the calculated and measured values of V_s have the same temperature dependence in the paramagnetic phase. This is not the case for the hexagonal Gd and Tb where in every instance the measured temperature dependence is in excess of the calculated value. For different elements and for different crystallographic directions in a single element the ratio of experimental to computed gradients varied from 1.5 to 4 indicating again that it could not be an experimental error. There are two possible origins for these differences, either the mechanical properties of the surfaces of these rare earth metals are markedly different to the bulk or the theoretical expressions available for the calculation of V_s are in error. Further work is in progress to illuminate these possibilities.

The authors would like to thank the Centre for Materials Science, University of Birmingham, and particularly D. Fort for the provision of samples. One of us (M.S.N.) would like to acknowledge financial support from the University of Tehran.

REFERENCES

- [1] PALMER, S. B. GREENOUGH, R. D., *J. Mag. Mag. Mat.*, **1** (1976), 310.
- [2] EVENSON, W. E. and LIU, S. H., *Phys. Rev.*, **178** (1969), 783.
- [3] NEJAD, M. S., *Ph. D. Thesis*, University of Hull (1981).
- [4] PALMER, S. B., LEE, E. W. and ISLAM, M. N., *Proc. Roy Soc. Lond.*, **A338** (1974), 341.
- [5] CABLE, J. W. and WOLLAN, E. D., *Phys. Rev.*, **165** (1968), 733.
- [6] FERON, J. L., *Ph. D. Thesis*, University of Grenoble (1969).
- [7] HILL, R., *Proc. Phys. Soc. Lond.*, **65** (1952), 350.
- [8] HUNTINGTON, H. B., *Solid State Physics* (edited by Seitz, F. and Turnbull, D.) Vol. 7, Academic Press N. Y. (1958).

- [9] See for example VELASCO, V. R. and GARCIA-MOLINER, F., *Surface Science*, **83** (1979), 376.
- [10] FISHER, E. S. and DEVER, D., *Proc. 6th Rare Earth Research Conference (U.S.A.)* (1967).
- [11] ROSEN, M., *Phys. Rev.*, **174** (1968), 504.
- [12] SALAMA, K., BROTZEN, F. R. and DONOHO, P. L., *J. Appl. Phys.*, **43** (1972), 4254.
- [13] PEPPER, A. R. and SMITH, J. M., *J. Sci. Inst.*, **42** (1965), 328.
- [14] SUTTON, P. M., *Phys. Rev.*, **91** (1953), 816.



EFFECTS OF UNIAXIAL STRESS ON THE 27084 cm^{-1} AND 26942 cm^{-1} ABSORPTION LINES IN DIAMOND

MARIA HELENA NAZARÉ ⁽¹⁾ and JOÃO PAULO CASQUILHO ⁽²⁾

Departamento de Física e Centro de Física (INIC)

3800 Aveiro, Portugal

(Received 29 December 1981)

ABSTRACT—This note reports uniaxial stress measurements on the 27084 cm^{-1} and 26942 cm^{-1} zero phonon absorption lines in type I_a diamond. The centre where these transitions occur is shown to be trigonal.

1 — INTRODUCTION

The absorption line at 27084 cm^{-1} (Fig. 1) was first reported by Clark et al [1] in irradiated and annealed type I_a diamond and afterwards named H₁₃. According to Clark and Norris [2] this transition could occur at the H₃ defect.

During the present study it was observed that the H₁₃ absorption band was present both in natural and treated type I_a diamond and was not detected in type II_a diamond.

The occurrence of the band in natural specimens is enough to cast some doubt about its origin being at the H₃ defect. We know now that the H₃ defect is produced when a radiation damage defect is trapped at the A centre and has a C_{2v} point group (Davies et al [3]), although we must point out that even the H₃ centre has been detected in natural I_{aA} diamonds and thought to have been produced through a process of natural irradiation and annealing. However the H₁₃ band can not have its origin at the H₃ defect, since, as it is shown in the following sections, it occurs at a centre with trigonal symmetry, while the H₃ defect has a rhombic I symmetry. (Davies et al [3]).

(1) Author for correspondence.

(2) Now at Departamento de Física, Universidade Nova de Lisboa.

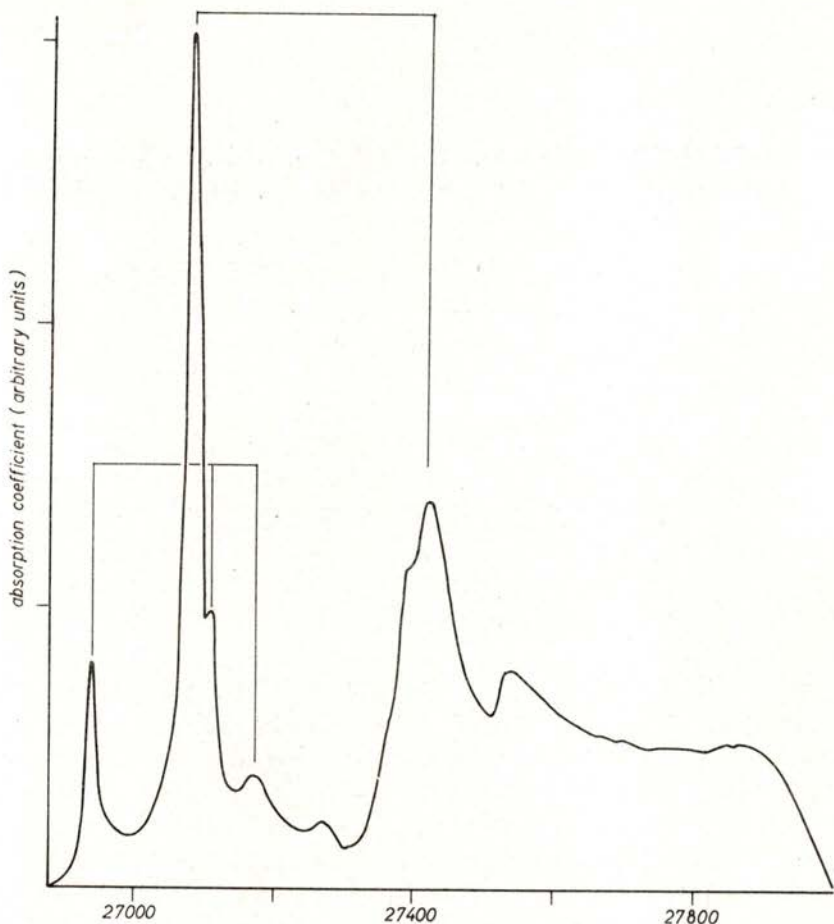


Fig. 1—The H_{13} absorption spectrum at liquid nitrogen temperature in a type I_a diamond, after electron-irradiation and annealing. Features connected by lines are the 26942 cm^{-1} zero-phonon line and one-phonon band with $\hbar\omega \sim 170\text{ cm}^{-1}$ and $\hbar\omega \sim 230\text{ cm}^{-1}$, and the 27084 cm^{-1} zero-phonon line and one-phonon band with $\hbar\omega \sim 350\text{ cm}^{-1}$.

2 — EXPERIMENTAL DETAILS

In the study of the 27084 cm^{-1} and the 26942 cm^{-1} absorption lines a set of seven samples was used. All of them were natural I_a diamond. Uniaxial stress measurements have been made at liquid nitrogen temperature. In all cases a Spex 1704

monochromator fitted with a 1200 lines mm^{-1} grating was used. Light from a 150 W Xe arc lamp was polarized by a calcite prism and detected by an RCA C31034 photomultiplier.

3 — RESULTS AND DISCUSSION

3.1 — The H_{13} absorption band

The H_{13} absorption band is shown in Fig. 1. The widths, spacings and splitting patterns under uniaxial stress suggest that the lines at 26942 cm^{-1} and 27084 cm^{-1} are zero-phonon lines. It is apparent from Fig. 1 that the zero-phonon line at 26942 cm^{-1} is replicated by its one phonon-side band of $\hbar\omega \sim 170 \text{ cm}^{-1}$ and $\hbar\omega \sim 230 \text{ cm}^{-1}$ while the zero phonon line at 27084 cm^{-1} is replicated by the one phonon side band of $\hbar\omega \sim 350 \text{ cm}^{-1}$.

During the present study we measured the integrated strength of the two zero-phonon lines at 77 K and observed that a correlation could be established in a set of seven diamonds (Fig. 2a).

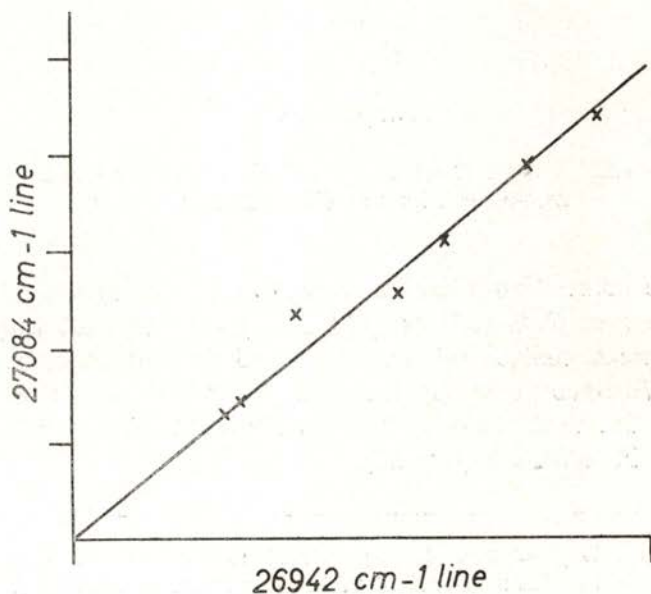


Fig. 2 a — Correlation of the intensities of the 27084 cm^{-1} and 26942 cm^{-1} zero-phonon lines in seven specimens, all of them natural I_a diamond; data taken at 77 K. Notice the different scales used for the two line intensities.

All the specimens were natural I_a diamond; two of them had been irradiated at room temperature with 2 Mev electrons and then annealed at 800°C for about 30 minutes. The H_{13} absorption band was not detected in type II_a diamond.

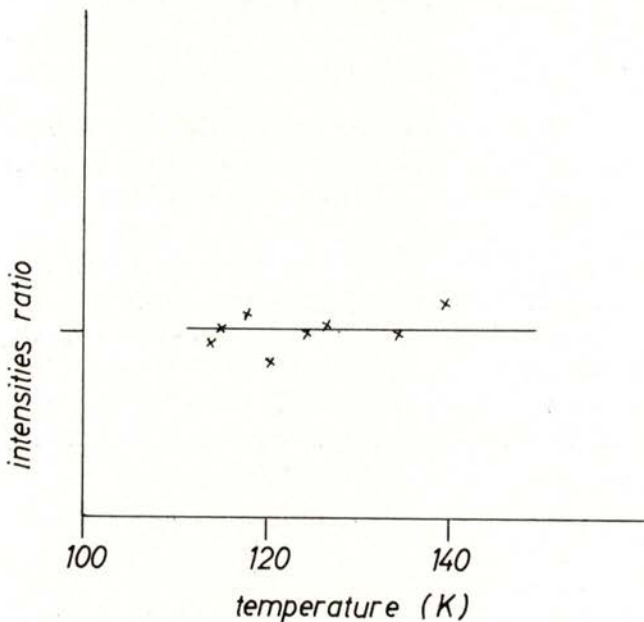


Fig. 2 b — Ratio between the intensities of the 27084 cm^{-1} and 26942 cm^{-1} zero-phonon lines at different temperatures.

The correlation together with the energy spacing between the two zero-phonon lines (142 cm^{-1}) suggest that they occur at the same centre and are originated from a common ground state. We have measured the strengths of the two zero-phonon lines at different temperatures, all above 77 K, and found their ratio to be constant (Fig. 2b).

Fig. 3 — Effects of uniaxial stress on the 26942 cm^{-1} and 27084 cm^{-1} zero-phonon lines. Spectra measured at 77 K for a stress of 1.6 GPa. The spikes show the theoretical results for an E to A_1 transition with the π spectra shown above and the σ below the horizontal line. In 3 a and 3 b (facing page) spectra shown by full and broken curves are measured with electric vector of light parallel (π) and perpendicular (σ) to the stress axis, respectively.

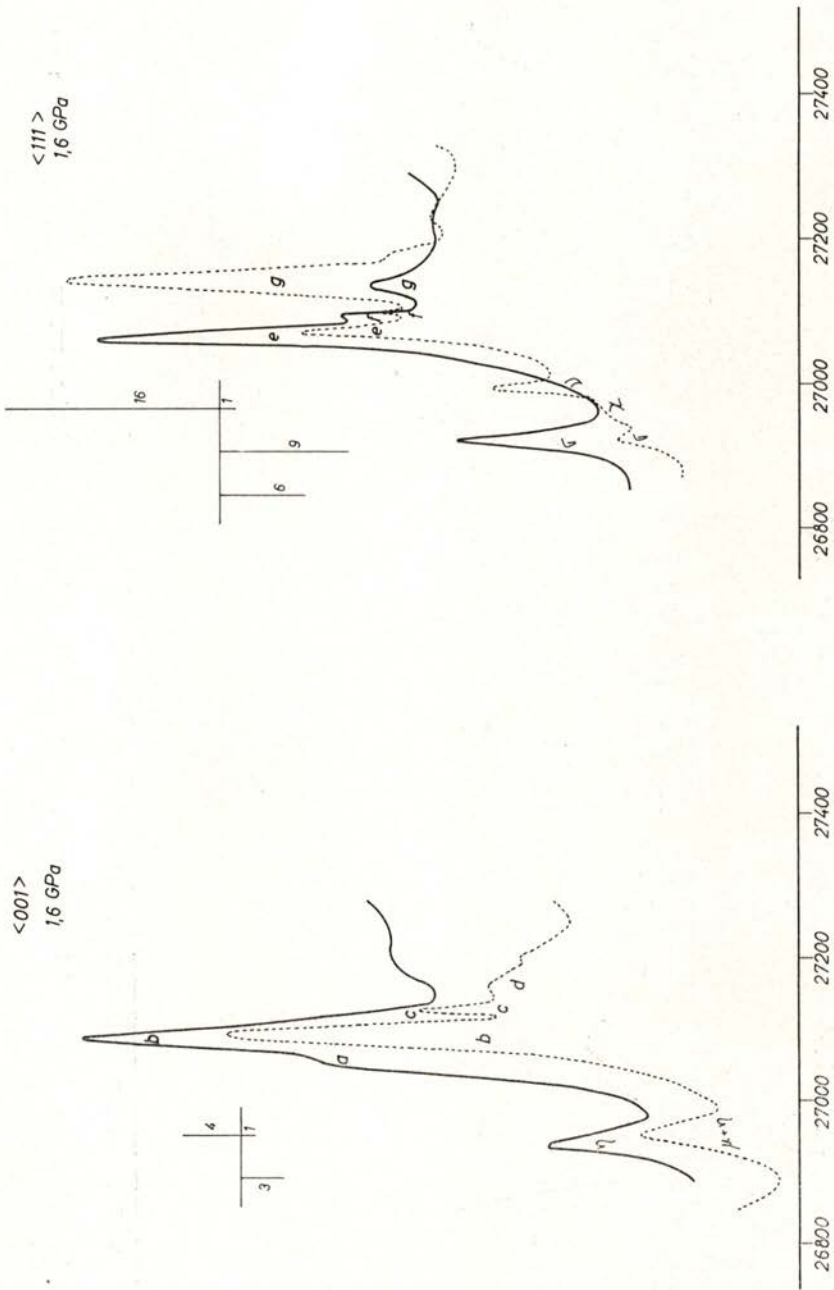


Fig. 3 a) and b) — Effects of uniaxial compression along $\langle 001 \rangle$ and $\langle 111 \rangle$ (for detailed caption see facing page).

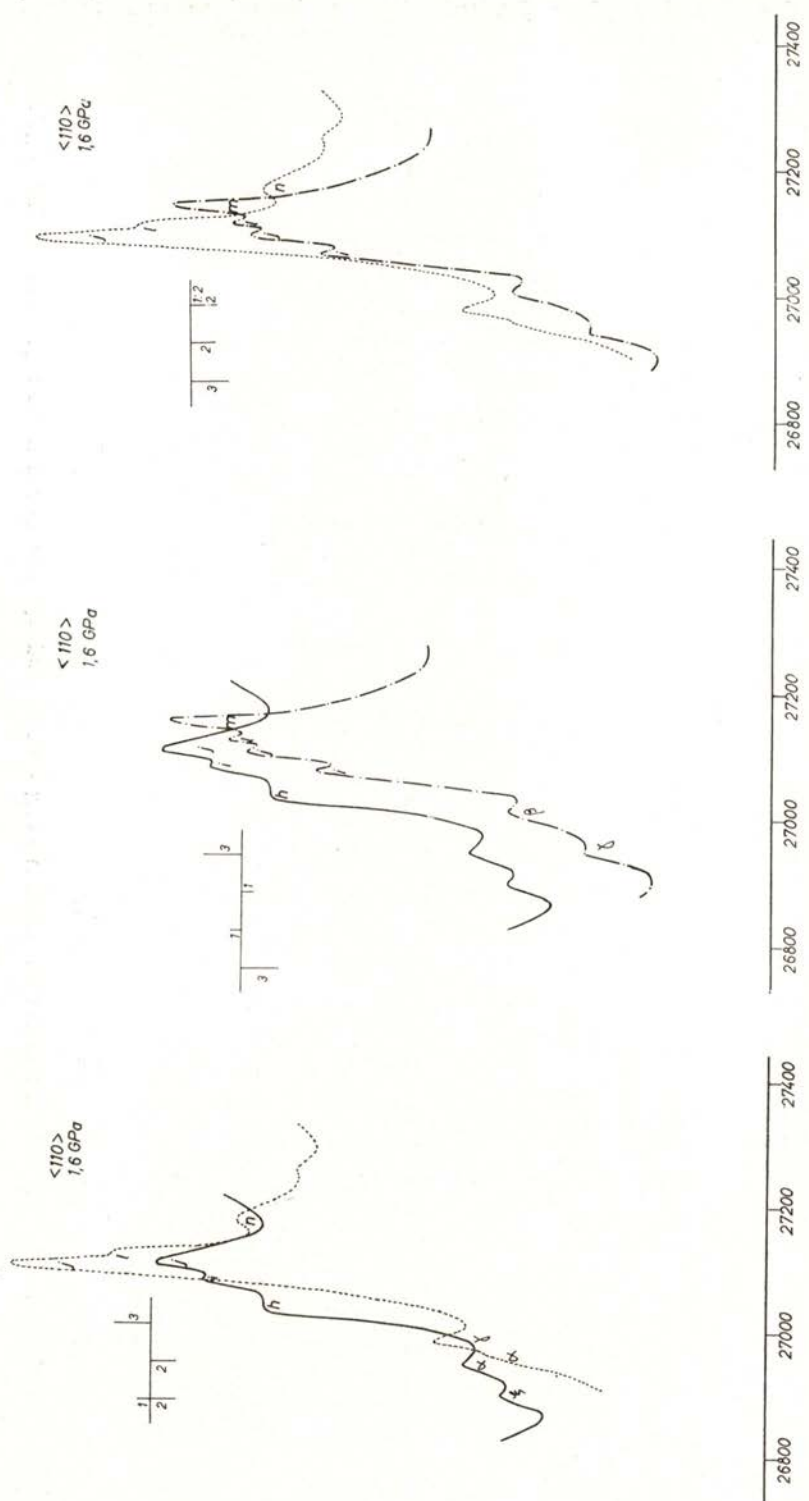


Fig. 3 c), d) and e) — Uniaxial compression along $\langle 110 \rangle$. Full curves π ; broken curves σ_{001} ; chain curves σ_{110} .

3.2 — *Uniaxial stress data*

Uniaxial stress of up to 2 GPa have been applied along $\langle 001 \rangle$, $\langle 111 \rangle$ and $\langle 110 \rangle$ crystallographic directions; absorption measurements have been taken at 77 K. Typical spectra are given in Fig. 3. The energy of the stress split components as a function of applied stress is given in Fig. 4. We consider first the line at 26942 cm^{-1} . At higher stresses the intensities of the absorption components vary with stress. The energies of several of stress split components are seen to vary non-linearly with stress (Fig. 4). The intensities of many of the stress split components of the 27084 cm^{-1} line are also stress dependent.

3.3 — *Phenomenological interpretation of the data*

At low stress the 26942 cm^{-1} line splits in the way characteristic of an electric dipole transition between an E and an A_1 (or A_2) state at a trigonal centre (Kaplyanskii [4], [5]). The intensity variations are consistent with thermalisation among the components of the E state, identifying it as the ground state. This is confirmed by the satisfactory agreement between Kaplyanskii's first order perturbation theory and the experimental results for the stress split components, there being four arbitrary parameters in the theory (Table 1; Fig. 3).

The line at 27084 cm^{-1} in spite of being about 5 times stronger than the 26942 cm^{-1} line is not so easy to analyse. Its stress splitting is inconsistent with any of the cases tabulated by Kaplyanskii [4], [5] and by Hughes and Runciman [6] and can only be understood if the transition occurs at a trigonal centre between two double degenerate levels (Davies and Nazaré [7]). Given the large number of predicted transitions and the thermalisation effects in the split ground state not all the stress split components are observed (Fig. 3, Table 2). This tentative assignment is supported by the fact that transitions at 26942 cm^{-1} and 27084 cm^{-1} correlate in strength (Fig. 2; 3.1) and that the 26942 cm^{-1} zero-phonon transition occurs at a trigonal centre.

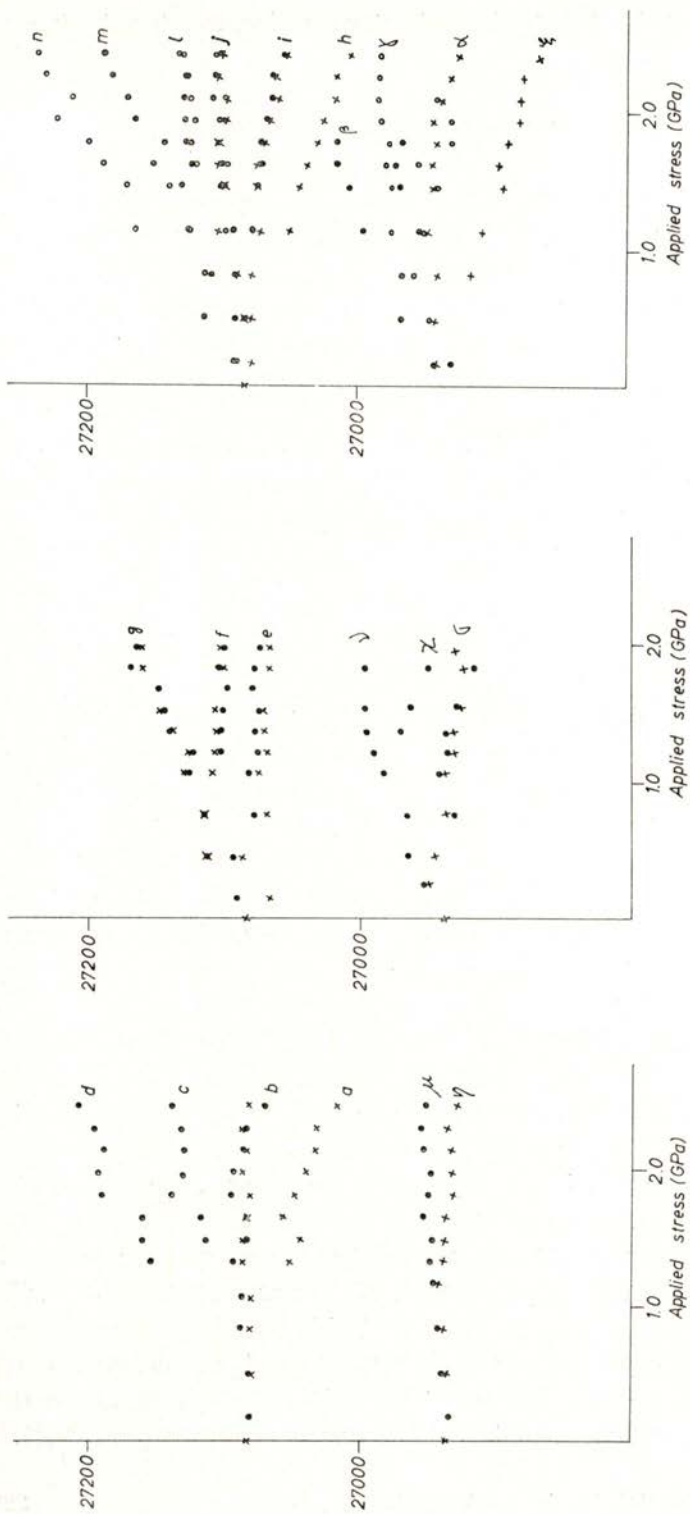


Fig. 4—Energies of the stress split components of the 26942 cm^{-1} and 27084 cm^{-1} zero-phonon lines as functions of applied stress at 77 K. a) $\langle 001 \rangle$, b) $\langle 111 \rangle$ and c) $\langle 110 \rangle$ compressions. Experimental data are shown by crosses for π polarization and by dots for σ polarization. Under $\langle 110 \rangle$ compression σ_{001} data are shown by open circles, and σ_{110} data by full circles.

TABLE 1 — Effect of uniaxial stress on the 26942 cm⁻¹ line

Stress axis	Line	Initial state	Shift rate		Best fit (°)
			Experiment	Theory (1)	
<001>	η	Θ	0	$A_1 - 2/3 B - 2\sqrt{2/3} C$	4
	μ	ϵ	8	$A_1 + 2/3 B + 2\sqrt{2/3} C$	10
	α	Θ	2	$A_1 + 1/2 A_2 - 1/3 B + 2\sqrt{2/3} C$	6
	β	ϵ	40	$A_1 + 1/2 A_2 + 1/3 B - 2\sqrt{2/3} C$	35
<110>	γ	Θ	20	$A_1 - 1/2 A_2 + B$	12
	ξ	ϵ	-30	$A_1 - 1/2 A_2 - B$	-24
	ν	$\left\{ \begin{array}{l} \Theta \\ \epsilon \end{array} \right\}$	34	$A_1 + A_2$	34
<111>	χ	ϵ	17	$A_1 - 1/3 A_2 + 8/9 B - 4\sqrt{2/9} C$	19
	σ	Θ	-10	$A_1 - 1/3 A_2 - 8/9 B + 4\sqrt{2/9} C$	-22

(1) The differences between the perturbations to the energies of the ground and excited states are shown in terms of the stress parameters, A_1 , A_2 , B and C . Kaplyanskii's notation is obtained from the one used in this table through the transformations: $A_1 \rightarrow A_1$; $A_2 \rightarrow 2 A_2$; $B \rightarrow 3 (B+C)/4$; $C \rightarrow 3 (B-C)/2\sqrt{2}$

(2) Stress parameters used (units cm⁻¹ G Pa⁻¹): $A_1 = 7.25$, $A_2 = 26.48$, $B = 17.67$, $C = -9.22$.

In view of the present data it is highly probable that the two zero-phonon absorption lines at 26942 cm⁻¹ and 27084 cm⁻¹ are electric dipole transitions occurring at the same trigonal centre from the same double degenerate ground state into an A_1 (or A_2) and E excited states respectively. In this case it is evident that under large stresses the intensities of the lines are stress dependent not only through thermalisation but also through interaction of neighbour states. That interaction is also responsible for the non-linearity of the shift rates of some of the stress split components.

TABLE 2—The effect of uniaxial stress on a E to E transition at a trigonal centre according to Davies and Nazaré [7].

Stress axis	Initial state	Final state	Shift rate (1)
$\langle 001 \rangle$	Θ	Θ	$A'_1 + 2/3 B_1 + 2\sqrt{2/3} C_1$
	Θ	ϵ	$A'_1 - 2/3 B_2 - 2\sqrt{2/3} C_2$
	ϵ	Θ	$A'_1 + 2/3 B_2 + 2\sqrt{2/3} C_2$
	ϵ	ϵ	$A'_1 - 2/3 B_1 - 2\sqrt{2/3} C_1$
$\langle 111 \rangle$	$\left\{ \begin{matrix} \Theta \\ \epsilon \end{matrix} \right\}$	$\left\{ \begin{matrix} \Theta \\ \epsilon \end{matrix} \right\}$	$A'_1 + A'_2$
	Θ	Θ	$A'_1 - 1/3 A'_2 + 4/9 B_1 - 4\sqrt{2/9} C_1$
	Θ	ϵ	$A'_1 - 1/3 A'_2 - 4/9 B_2 + 4\sqrt{2/9} C_2$
	ϵ	Θ	$A'_1 - 1/3 A'_2 + 4/9 B_2 - 4\sqrt{2/9} C_2$
$\langle 110 \rangle$	Θ	Θ	$A'_1 + 1/2 A'_2 + 1/3 B_1 - 2\sqrt{2/3} C_1$
	Θ	ϵ	$A'_1 + 1/2 A'_2 - 1/3 B_2 + 2\sqrt{2/3} C_2$
	ϵ	ϵ	$A'_1 + 1/2 A'_2 - 1/3 B_1 + 2\sqrt{2/3} C_1$
	ϵ	Θ	$A'_1 + 1/2 A'_2 + 1/3 B_2 - 2\sqrt{2/3} C_2$
	Θ	Θ	$A'_1 - 1/2 A'_2 - B_1$
	Θ	ϵ	$A'_1 - 1/2 A'_2 + B_2$
	ϵ	ϵ	$A'_1 - 1/2 A'_2 + B_1$
	ϵ	Θ	$A'_1 - 1/2 A'_2 - B_2$

(1) The differences between the perturbations to the energies of the ground and excited states are shown in terms of the stress parameters A'_1 , A'_2 , B_1 , B_2 , C_1 and C_2 . In terms of the basis set $|\Theta\rangle$, $|\epsilon\rangle$ of an E electronic state the stress parameters are defined as:

$$A'_1 = \langle \Theta^e | C_{A_1} | \Theta^e \rangle - \langle \Theta^g | C_{A_1} | \Theta^g \rangle$$

$$A'_2 = \langle \Theta^e | C'_{A_1} | \Theta^e \rangle - \langle \Theta^g | C'_{A_1} | \Theta^g \rangle$$

$$B_{1,2} = \langle \Theta^e | C_{E_\Theta} | \Theta^e \rangle \mp \langle \Theta^g | C_{E_\Theta} | \Theta^g \rangle$$

$$C_{1,2} = \langle \Theta^e | C'_{E_\Theta} | \Theta^e \rangle \mp \langle \Theta^g | C'_{E_\Theta} | \Theta^g \rangle$$

The C_{A_1} , C'_{A_1} , C_{E_Θ} and C'_{E_Θ} are electronic operators transforming as A_1 and E_Θ ; the superscripts g and e label the ground and excited state.

4—SUMMARY AND SUGGESTIONS FOR FURTHER WORK

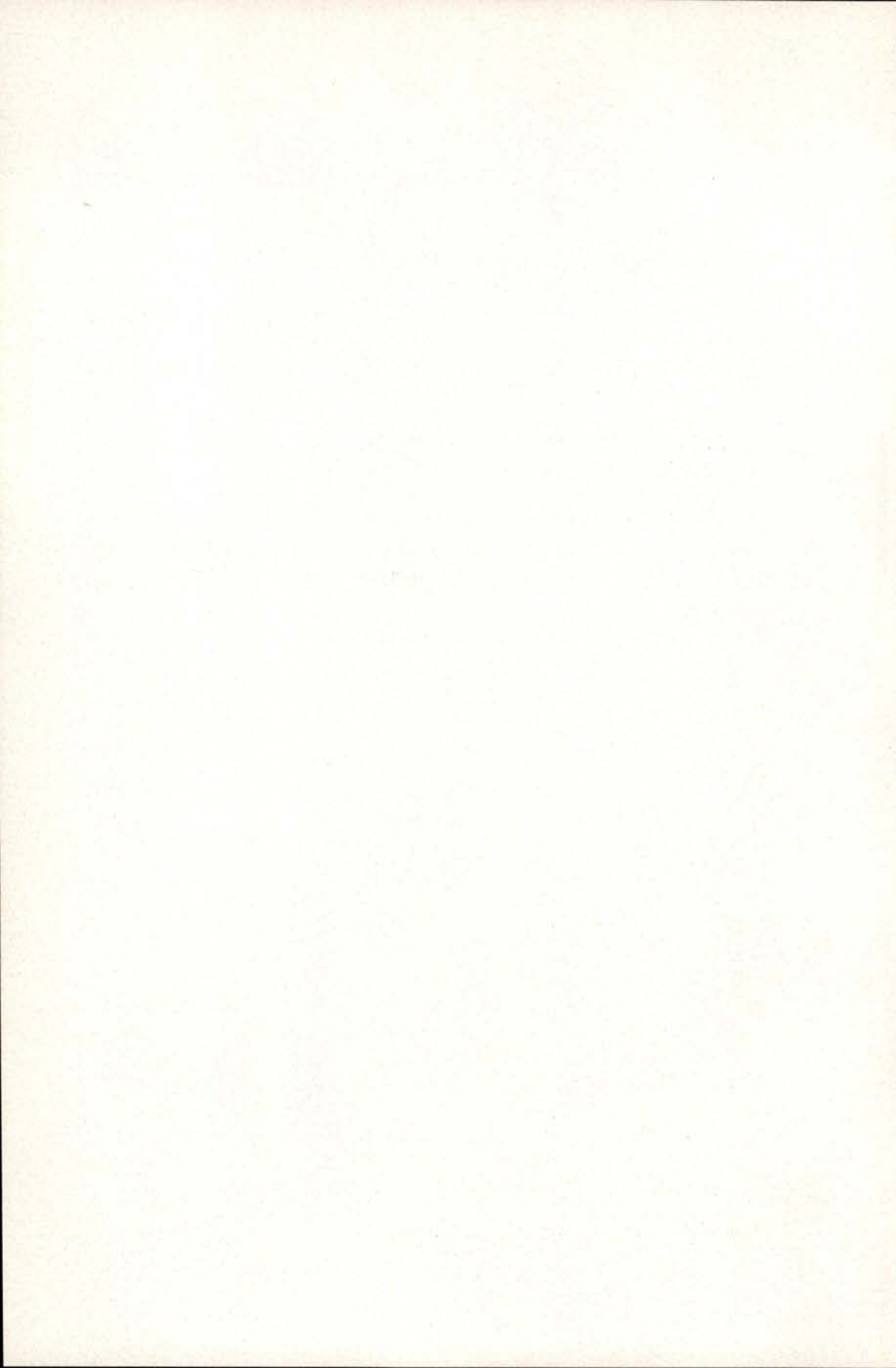
Uniaxial stress measurements have suggested that the transitions at 26942 cm^{-1} and 27084 cm^{-1} occur at a centre with trigonal symmetry, both from a common ground state. However, this is a tentative interpretation of the data, and it clearly requires further work namely on luminescence and uniaxial stress at liquid helium temperature. A detailed discussion of the vibronic system in Fig. 1 will be given later.

We wish to acknowledge Dr. M. F. Thomaz for valuable discussion. We are also grateful to José Januário for the assistance with the experiments.

Financial support is acknowledged to the Gulbenkian Foundation, the Junta Nacional de Investigação Científica e Tecnológica, DIALAP and Sociedade Portuguesa de Empreendimentos.

REFERENCES

- [1] CLARK, C. D., DITCHBURN, R. W. and DYER, H. B., *Proc. R. Soc.*, **A237** (1956), 75.
- [2] CLARK, C. D. and NORRIS, C. A., *J. Phys.*, **C3** (1970), 651.
- [3] DAVIES, G. NAZARE, M. H. and HAMER, M. F., *Proc. R. Soc.*, **A351** (1976), 245.
- [4] KAPLYANSKII, A. A., *Opt. Spectrosc.*, **16** (1964), 329.
- [5] KAPLYANSKII, A. A., *Opt. Spectrosc.*, **16** (1964), 557.
- [6] HUGHES, A. E. and RUNCIMAN, W. A., *Proc. Phys. Soc.*, **90** (1967), 827.
- [7] DAVIES, G. and NAZARE, M. H., *J. Phys.*, **C13** (1980), 4127.



THE ORIGIN OF THE «N2» ABSORPTION BAND IN NATURAL YELLOW DIAMONDS

GORDON DAVIES

Wheatstone Physics Laboratory, King's College,
The Strand, London WC2R 2LS, U.K.

(Received 31 December 1981)

ABSTRACT—The N2 band, which is partly responsible for the yellow colour of many natural diamonds is shown to correlate in strength with the well-known N3 band, and to occur at a centre with the same symmetry. Assuming the N2 and N3 bands are transitions at the same optical centre it is shown that the shape of the N2 band and the relative strengths of the N2 and N3 bands are consistent with the N2 band being a forbidden transition which is made allowed by vibronic coupling with the N3 band.

1 — INTRODUCTION

The majority of diamonds are brown or yellow in colour. These colours may be produced by a variety of crystal defects, such as the «H3» centre (a defect composed of two substitutional nitrogen atoms and a vacancy [1]), or the single substitutional nitrogen atom characteristic of «type I b diamond» [2], or the «2.6 eV» centre (whose structure is unknown [3]), or the «N3» centre. This paper is concerned solely with the N3 centre. Its presence in a diamond may be identified by its characteristic absorption spectrum (Fig. 1). There is a sharp zero-phonon line observed at 24080 cm^{-1} (2.985 eV) and a series of phonon sidebands stretching to higher energy. To lower energy lies the «N2» band. Although the N2 band has significantly smaller absorption than the N3 band, the N2 band absorbs light which is visible to the human eye, while the N3 band absorbs mainly in the near ultraviolet part of the spectrum. As a result, both the N2 and N3

bands contribute about equally to giving the diamond its perceived yellow colour. From a gemmological point of view the N2 band is therefore an important feature of a diamond, even though it is a relatively weak contributor to the absorption spectrum. This paper presents the results of the first detailed scientific study of the N2 band.

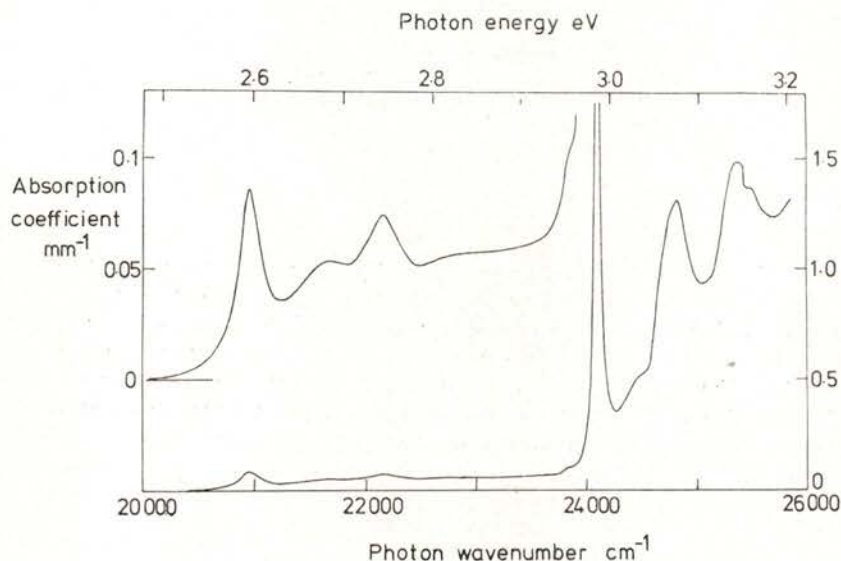


Fig. 1 — The absorption spectrum of a yellow diamond showing the N2 and N3 bands, measured at liquid nitrogen temperature. The N2 band is also shown magnified ten times.

Many studies have established that the N3 band is caused by an electric-dipole transition from a non-degenerate orbital ground state to a doubly degenerate excited state of an optical centre with C_{3v} symmetry [4], [5], [6]. An electron paramagnetic resonance signal is produced by an electron spin of a half at the N3 centre [7], [8], [9] and from this EPR spectrum it has been suggested that the N3 centre is composed of three nitrogen atoms all bonded to one common lattice site [10]. The model is consistent with the C_{3v} symmetry of the N3 centre deduced from the optical data. The presence of nitrogen is also consistent with the observations that the N3 centre may be synthesised when

nitrogen is made to migrate through a diamond during high temperature experiments [11].

When excited by near ultraviolet radiation the N3 centre emits a blue photoluminescence, with a spectrum which is approximately a mirror-image of the absorption band [12]. The radiative decay time [13] of the N3 luminescence is affected by the presence of pairs of substitutional nitrogen atoms in the diamonds. Allowing for this, the intrinsic decay time of the N3 centre is 41 ± 1 ns at low temperature ($T < 400$ K). At higher temperature the decay time becomes shorter, being less than 10 ns at $T > 700$ K. Even at low temperatures the luminescence efficiency of the N3 centre is only 0.3 (in the absence of extrinsic quenching by the pairs of nitrogen atoms). Thomaz and Davies [13] have suggested that these results arise because the electrons excited to the E level of the N3 centre are metastable and may de-excite to a non-radiative level of the N3 centre. At very low temperature it was assumed that tunnelling could occur between the E state and the nonradiative state, and at high temperature the electrons could be excited thermally over the energy barrier between the two states. The non-radiative state was postulated to be the excited state of the N2 absorption band. No resonant luminescence has been detected from this band — it is therefore non-radiative (for some as yet unspecified reason) as required by these ideas. It was suggested [13] that the N2 band is non-radiative because it is an electric-dipole forbidden transition; that is, the non-radiative nature of the N2 band is a feature intrinsic to the transition and is not the result of a fast non-radiative decay to other levels. This suggestion was based on a qualitative inspection of the N2 spectrum. In contrast to the N3 band and almost all electronic transitions seen in diamond [14], [15], the N2 band does not have a sharp zero-phonon line at its low energy side (Fig. 1). Instead only broad structure is observed, reminiscent of phonon sidebands. This structure could be caused by a transition to the N2 electronic level plus a vibration, the role of the vibration being to introduce deformations in the centre which mix together the N2 and N3 electronic states, thereby transferring absorption from the N3 band to the N2 band. This model can only work if the N2 and N3 bands occur at the same optical centre.

The first stage in investigating the N2 band is therefore to establish if it occurs at the N3 centre. In § 3 data are presented

which confirm that the two bands correlate in intensity with each other. In §§ 4, 5 uniaxial stress measurements are reported which show that the N2 band occurs at a trigonal optical centre, as does the N3 band. Assuming then that the N2 band is a forbidden transition at the N3 centre, we must investigate whether it is reasonable for the N2 band to be induced at its observed intensities by a vibronic mixing with the N3 states. The theory and calculations are presented in § 6 and shown, in § 7, to be consistent with the observed spectra.

2 — EXPERIMENTAL DETAILS

Natural diamonds were used throughout this study, and all the measurements were made with the specimens at liquid nitrogen temperature. The diamonds were chosen to be apparently homogeneously coloured to the naked eye. For the correlation data of Fig. 2, below, the N2 and N3 bands were measured through the same section of each specimen. Typical variations in band-strengths in different regions of the diamonds was $\pm 5\%$, on a scale of several micro-metres. For the uniaxial stress measurements, the diamonds were polished to cubes of about 1.5 mm edges, with either (001), (110), ($\bar{1}\bar{1}0$) faces or (111), ($\bar{1}\bar{1}0$), ($1\bar{1}\bar{2}$) faces. The spectra were analysed using a Spex 1701 monochromator fitted with a DC-operated photomultiplier.

3 — N2, N3 CORRELATION

Measurement of the strength of the N2 band is straightforward since all its features are wide (at least 200 cm^{-1} , 25 meV) and so they are negligibly broadened by the random strain fields present in all diamonds (e.g. as a result of substitutional pairs of nitrogen atoms [16]) and which vary from one specimen to another. The peak absorption coefficient at the lowest energy N2 feature is therefore an adequate measurement of the N2 band. (This feature is at 20940 cm^{-1} , 2.596 eV). To measure the N3 bandstrength it is convenient to use the zero-phonon line, integrating its absorption coefficient to allow for the variable line-

width in different diamonds. The data have been expressed in terms of the zeroth moment of the line:

$$M_0 = \int d\nu a(\nu) / \nu$$

where $a(\nu)$ is the absorption coefficient in mm^{-1} at photon wavenumber ν . In practice the zero-phonon line is often too intense for its peak absorption to be measured accurately. Then the absorption coefficient at the minimum near 25000 cm^{-1} (3.10 eV) has been used instead and converted into a zero-phonon strength by means of the calibration data of Fig. 2a. This is an adequate procedure as long as there is no background wavelength-dependent absorption in the specimens (as there is in many brown diamonds [3], for example). The non-linearity in Fig. 2a is caused by the errors in measuring very strongly absorbing zero-phonon lines.

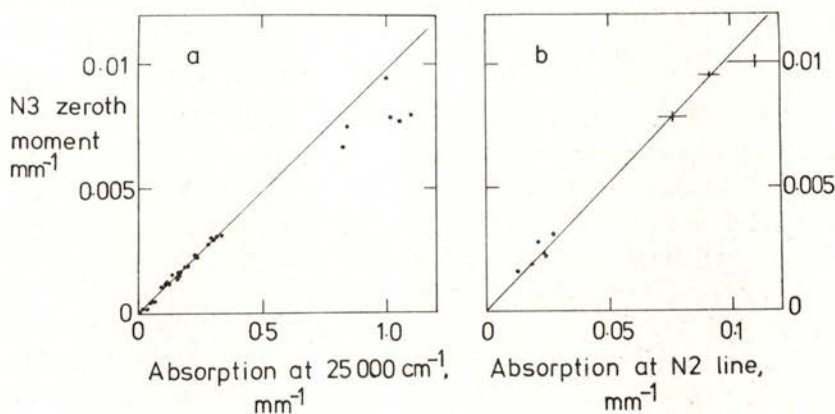


Fig. 2 — a) Correlation of the N3 absorption in the zero-phonon line and at the minimum of absorption near 25000 cm^{-1} (3.10 eV), measured at liquid nitrogen temperature. b) Correlation of the N2 and N3 absorption in nine specimens measured at liquid nitrogen temperature. The data of figure 2, are based on a re-analysis of spectra taken for reference [8].

Fig. 2b shows the results of the N2/N3 correlation for nine specimens. The correlation coefficient is 0.995. These measurements confirm a similarly high correlation observed between the N2 and N3 bands in eighteen diamonds by Clark et al [17].

From the spectra we may estimate the strength of the N2 band relative to the N3 band. Clearly from Fig. 1 the N3 band is probably superimposed on the high energy tail of the N2 band, and there is no way of separating the two bands using the absorption spectrum. (In fact, if the vibronic model outlined in § 1 is correct, there is no distinction between the N2 band and the N3 band: they are both parts of the same vibronic bandshape.) However, it is possible to measure the strength of absorption in the N2 band which lies on the low energy side of the N3 zero-phonon line, and also we can measure (as the «N3 strength») the absorption in the N2/N3 system on the high energy side of the N3 line. The two zeroth moments are related by:

$$M_{N2} / M_{N3} = \int_{20000}^{23800} d\nu a(\nu) \nu^{-1} / \int_{23800}^{29000} d\nu a(\nu) \nu^{-1} \quad (1)$$

$$= 0.046 \pm 0.004$$

4 — UNIAXIAL STRESS MEASUREMENTS

The effect of uniaxial compressions on the N3 zero-phonon line was reported by Crowther and Dean [5]. Data taken in this study (Fig. 3a) are in close agreement with that earlier work. The N2 line at 20940 cm⁻¹ (2.596 eV) responds to stresses as shown, for the first time, in Fig. 3b. These data must be interpreted remembering that the full width at half height of the N2 line is 200 cm⁻¹ (25 meV). Consequently the apparent splitting of the line under < 001 > compression (Fig. 3b) is not reliable (it does not exceed 1/20 of the linewidths). On the other hand at the highest < 111 > stresses the N2 line observed with electric

Fig. 3 (next page) — Energies of the stress-split components of (a) the N3 zero-phonon line (upper diagrams), and (b) the N2 line (lower diagrams), taken at liquid nitrogen temperature under < 001 >, < 111 > and [110] compressions. Crosses show data taken with electric vector \mathbf{v} of the light parallel to the stress \mathbf{s} , circles are for $\mathbf{v} \perp \mathbf{s}$. For the N3 data with $\mathbf{s} \parallel [110]$, closed circles are for $\mathbf{v} \parallel [1\bar{1}0]$ and open circles for $\mathbf{v} \parallel [001]$. For the N2 data with $\mathbf{s} \parallel [1\bar{1}0]$, \mathbf{v} is $\parallel [1\bar{1}1]$. The lines show the least squares fit of the Hamiltonian (equation 2) with the matrix elements listed in Table 1. N2 data labelled 'd' are predicted to be at the mean of lines c and e.

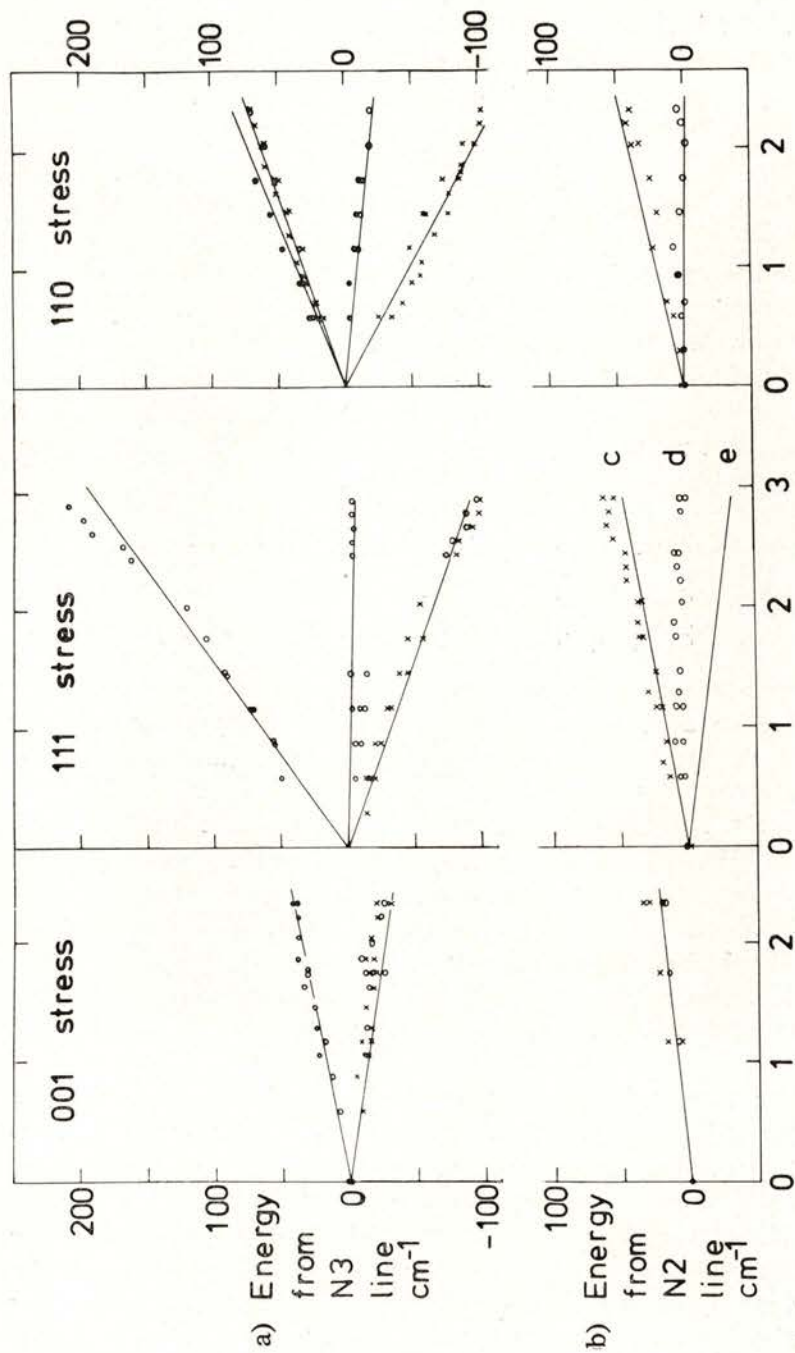


Fig. 3 — Effect of uniaxial compression (in G Pa); detailed caption in facing page.

vector \mathbf{v} of the light polarised perpendicular to the stress axis \mathbf{s} was 15 cm^{-1} wider than the N2 line observed with $\mathbf{v} \parallel \mathbf{s}$. Assuming a Lorentzian lineshape for the N2 line, this implies an unresolved splitting of about 50 cm^{-1} in the $\mathbf{v} \perp \mathbf{s}$ spectrum.

5 — ANALYSIS OF THE UNIAXIAL STRESS DATA

A trigonal optical centre like the N3 centre may have its main three-fold axis directed along any of the $\langle 111 \rangle$ axes of the diamond. One orientation has the three-fold axis along $[111]$: we will define this to be the Z axis of that centre. The X and Y axes are chosen to lie along $[\bar{1}\bar{1}2]$ and $[1\bar{1}0]$ respectively. Y is normal to a reflection plane of the C_{3v} centre. The Hamiltonian of the centre can then be written [18]:

$$\begin{aligned}
 H = H_0 + c_{A1} (s_{xx} + s_{yy} + s_{zz}) + c'_{A1} (s_{xy} + s_{yz} + s_{zx}) \\
 + c_{EX} (s_{xx} + s_{yy} - 2s_{zz}) + c_{EY} \sqrt{3} (s_{xx} - s_{yy}) \\
 + c'_{EX} (s_{yz} + s_{zx} - 2s_{xy}) + c'_{EY} \sqrt{3} (s_{yz} - s_{zx})
 \end{aligned} \quad (2)$$

Here H_0 is the Hamiltonian at zero stress. The stress tensor components s_{ij} are defined with respect to the crystal axes x, y, z of the diamond. The electronic operators c_{A1}, \dots, c'_{EY} transform under the operations of the C_{3v} point group as shown by their subscripts. The lines on Fig. 3a show the least squared deviation fit of the Hamiltonian (equation 2) to the experimental data for the N3 line, assuming it to be an electric dipole allowed transition between an orbitally non-degenerate ground state and an orbitally doubly degenerate excited state (§ 1). The matrix elements of the c_{A1}, \dots, c'_{EY} operators are listed in Table 1. These results are closely in agreement with those of Crowther and Dean [5].

The results for the N2 line are more difficult to analyse because of the large width of the line (200 cm^{-1} , 25 meV , at zero stress). However, there is no resolved splitting with stress along $\langle 001 \rangle$ in contrast to the results for $\langle 111 \rangle$ and $\langle 110 \rangle$ stresses (Fig. 3b). This suggests that the N2 optical centre also has trigonal symmetry (so that all orientations of the centre make the same angle with the $[001]$ stress axis, and so are equally perturbed.) Further, since an orbitally degenerate state at a trigo-

TABLE 1 — Matrix elements of the operators c_{A_1}, \dots, c'_{E_Y} of equation (2) derived from least squares fits to figure 3.

Matrix element	This work	Reference [5]
$\langle EX c_{A_1} EX \rangle - \langle A1 c_{A_1} A1 \rangle$	2	4
$\langle EX c'_{A_1} EX \rangle - \langle A1 c'_{A_1} A1 \rangle$	62	69
$\langle EY c_{EX} EY \rangle$	8	9
$\langle EY c'_{EX} EY \rangle$	10	12

Units are $\text{cm}^{-1} (\text{GPa})^{-1}$, typical uncertainty $\pm 4 \text{ cm}^{-1}$. $|EX\rangle$, $|EY\rangle$ are the zero-phonon levels of the E electronic states, $|A1\rangle$ the zero-phonon level of the A_1 ground electronic state.

b) N2 line, N2 excited state as an A_1 state.

$$\begin{aligned} \langle a1 | c_{A_1} | a1 \rangle - \langle A1 | c_{A_1} | A1 \rangle &= 8 \text{ cm}^{-1} (\text{GPa})^{-1} \\ \langle a1 | c'_{A_1} | a1 \rangle - \langle A1 | c'_{A_1} | A1 \rangle &= 13 \text{ cm}^{-1} (\text{GPa})^{-1} \end{aligned}$$

Here $|a1\rangle$ is the excited state of the N2 line, $|A1\rangle$ its ground state.

c) N2 line, N2 excited state as an A_2 state.

$$\begin{aligned} \langle A2 | c_{A_1} | A2 \rangle - \langle A1 | c_{A_1} | A1 \rangle &= 9.5 \text{ cm}^{-1} (\text{GPa})^{-1} \\ \langle A2 | c'_{A_1} | A2 \rangle - \langle A1 | c'_{A_1} | A1 \rangle &= -21 \text{ cm}^{-1} (\text{GPa})^{-1} \end{aligned}$$

Here $|A2\rangle$ is the excited state of the N2 line, $|A1\rangle$ its ground state.

nal centre is split by a $\langle 001 \rangle$ stress [18] we conclude that both the ground and excited states of the N2 line are non-degenerate, or that if they are degenerate, the degeneracy is difficult to lift through applied stresses.

At a trigonal centre a transition between non-degenerate states is allowed when the electric vector of the light is parallel to the trigonal axis [19] (i. e. the Z axis as defined above). For this case, the least squares fit of the Hamiltonian (equation 2) to the data in Fig. 3b yields a close fit with the matrix elements listed in Table 1b. However, if the N2 line is an allowed transition we have to explain the lack of luminescence from it, and (more difficult) the extreme width of the line.

As an alternative we consider the N2 line to be a forbidden transition between non-degenerate states at the N3 centre, as implied by the stress data of Fig. 3b and the correlation of Fig. 2b. In this model the N2 transition is allowed through vibronic mixing with the N3 level (§ 1). Since the N3 transition is an allowed electric dipole transition between non-degenerate and doubly-degenerate states it occurs when the electric-vector of the light is polarised perpendicular to the trigonal axis of the centre (i. e. in the XY plane as defined above). The N2 transition is then expected to split under stress as expected for a « σ » oscillator at a trigonal centre, in Kaplyanskii's notation [19]. Under $\langle 111 \rangle$ stress two stress-split components are predicted [19] when the electric vector \mathbf{v} of the light beam is perpendicular to the stress axis \mathbf{s} . In the experiment only one component is resolved (Fig. 3b) although from the linewidths it is likely that there are two unresolved components (§ 4). Assuming that the observed line is at the mean position of the two predicted stress-split components, the least squares fit of the Hamiltonian (equation 2) to the data yields the fit shown in Fig. 3b with the parameters of Table 1c. Inspection of this fit shows that two lines expected with $\mathbf{v} \perp \mathbf{s}$ for $\mathbf{s} \parallel \langle 111 \rangle$ would indeed not be resolved.

The uniaxial stress data are thus consistent with the N2 line occurring at a trigonal centre, between non-degenerate orbital electronic states but with an electric dipole in the XY plane perpendicular to the trigonal axis of the centre. This assignment is in agreement with the model of § 1 in which the N2 band is vibronically induced from the N3 band. (An XY dipole transition between non-degenerate electronic states does not violate group theory selection rules because the N2 excited state is interpreted as a *vibronic* state which transforms as the E irreducible representation: see § 6 below.)

6 — A VIBRONIC MODEL

The data presented in § 4 and § 5 are consistent with the model that the N2 transition is an electric-dipole forbidden transition and is observed through vibronic mixing with the N3 transition. In this section we will investigate a simple model which

describes the interaction, to see if the order of magnitude of the parameters used in the model are plausible.

For definiteness we assume that the ground state of the N3 line transforms as A_1 in the C_{3v} point group, and that the N2 level is an A_2 state: the transition from A_1 to A_2 is electric dipole forbidden in C_{3v} symmetry [20]. The doubly degenerate N3 excited state must transform as E. Next we specify the relevant phonons at the optical centre. The dominant phonons observed in the N3 vibronic bands are the totally symmetric phonons [21]. However these are incapable of making the A_2 and E electronic states interact. For the vibronic mixing we must consider E modes of vibration at the centre. These E modes can produce a Jahn-Teller effect in the E states, and Thomaz and Davies [13] suggested that the radiative decay time measurements on the N3 band gave evidence for a weak Jahn-Teller relaxation. We will therefore consider the interaction of the A_2 and E electronic states brought about by one E mode of vibration which can also produce a Jahn-Teller effect in the E electronic state. By considering only one E mode, and by ignoring all the A_1 modes, we can minimise the number of parameters required by theory, although at the expense of realism.

If we switch off the interaction between the A_2 and E states, and also switch off the Jahn-Teller effect in the E states, we can write the vibronic states as Born-Oppenheimer products of electronic states (denoted by ϕ) and harmonic vibrational states (denoted by χ):

$$\begin{aligned}
 \psi_{A_1pq}(\mathbf{r}, Q_X, Q_Y) &= \phi_{A_1}(\mathbf{r}) \chi_p(Q_X) \chi_q(Q_Y) \\
 \psi_{A_2pq}(\mathbf{r}, Q_X, Q_Y) &= \phi_{A_2}(\mathbf{r}) \chi_p(Q_X) \chi_q(Q_Y) \\
 \psi_{EXpq}(\mathbf{r}, Q_X, Q_Y) &= \phi_X(\mathbf{r}) \chi_p(Q_X) \chi_q(Q_Y) \\
 \psi_{EYpq}(\mathbf{r}, Q_X, Q_Y) &= \phi_Y(\mathbf{r}) \chi_p(Q_X) \chi_q(Q_Y)
 \end{aligned}
 \tag{3}$$

Here, Q_X and Q_Y represent the vibrational coordinates in the E mode, and \mathbf{r} represents the electronic coordinates. The integers p, q are the mode occupation numbers. The adiabatic potentials in the A_1, A_2 and E states are

$$V = W_i + \frac{1}{2} m \omega^2 (Q_X^2 + Q_Y^2) \tag{4}$$

where W_i is the energy of the relevant electronic state, $\hbar\omega$ is the quantum of the E vibrational mode and m is its reduced mass. We now introduce the additional terms:

$$V' = d_X Q_X + d_Y Q_Y \quad (5)$$

into equation 4. The electronic operators d have matrix elements between the A_2 and E electronic states of

$$-\int dr \phi_X^* d_X \phi_X = \int dr \phi_Y^* d_X \phi_Y = \int dr \phi_X^* d_Y \phi_Y = \int dr \phi_Y^* d_Y \phi_X = k \quad (6a)$$

and

$$\int dr \phi_X^* d_Y \phi_{A_2} = -\int dr \phi_Y^* d_X \phi_{A_2} = \int dr \phi_{A_2}^* d_Y \phi_X = -\int dr \phi_{A_2}^* d_X \phi_Y = c \quad (6b)$$

with all other terms zero. These operators, which describe the perturbations produced by atomic movements Q_X, Q_Y , are related through the elastic constants, to the operators c_{EX}, \dots, c'_{EY} which describe perturbations produced by stresses. The important difference between the vibronic mixing and the stress perturbation is that the vibronic term depends linearly on the vibrational coordinates Q_X, Q_Y while the stress perturbation is independent of the vibrational coordinate. Matrix elements of the stress perturbation taken between the uncoupled states of equation (3) are only non-zero for states of the same vibrational quantum numbers. Matrix elements of V' , the vibrational coupling, exist only between the uncoupled states of equation (3) which differ by one in one of the vibrational occupation numbers: For example the term $d_X Q_X$ has non-zero matrix elements between the uncoupled states of equation (3) of:

$$\int dr dQ_X dQ_Y \psi_{EX,pq}^* d_X Q_X \psi_{EX,p+1,q} = -k [(p+1)\hbar/(2m\omega)]^{1/2} \quad (7)$$

$$\int dr dQ_X dQ_Y \psi_{A_2,pq}^* d_X Q_X \psi_{EY,p+1,q} = -c [(p+1)\hbar/(2m\omega)]^{1/2}$$

The Jahn-Teller relaxation energy S_{Exc} , measured in units of $\hbar\omega$, of the E electronic state due solely to the effect of V' on the EX and EY electronic states is:

$$S_{\text{Exc}} = k^2/2m\hbar\omega^3 \quad (8)$$

Similarly we define a parameter S_{AE} to describe the interaction of the A_2 and the E electronic states as:

$$S_{\text{AE}} = c^2/2m\hbar\omega^3 \quad (9)$$

The problem has now been reduced to determining the eigenvectors and eigenvalues of the secular matrix given by expressions like equations (6) to (9) in terms of the uncoupled basis states of equation (3). The calculations have been carried out using the parameters contained in reference [13]: i.e. with $S_{\text{Exc}} = 0.69$ and with the energy difference ($W_{\text{E}} - W_{\text{A}_2}$) of the electronic states at $Q_{\text{X}} = Q_{\text{Y}} = 0$ (equation 4) being $W_{\text{E}} - W_{\text{A}_2} = 4.625 \hbar\omega$. The energy origin was defined at $W_{\text{E}} = 0$. Results are given in Figs. 4 to 6

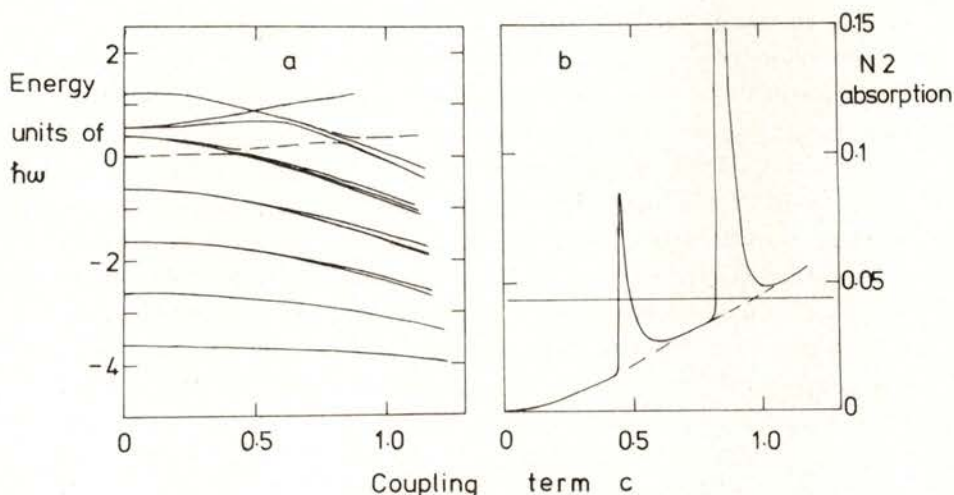


Fig. 4— a) Lowest energy vibronic levels for the model of § 6. Parameters used are: $k = 1.17$, $m = 1$, $\hbar\omega = 1$, $W_{\text{E}} = 0$, $W_{\text{A}_2} = -4.625$. Broken line shows N3 «zero-phonon» state. b) Intensity of all the transitions with energies less than the N3 zero-phonon line, using the parameters as in (a). The N3 zero-phonon line was formally defined as the lowest energy transition with over 0.2 of the total absorption. The horizontal line shows the value derived from equation (1).

as functions of the coupling c . Fig. 4a shows the energy levels for the lowest vibronic states. With increasing S_{AE} the N2 levels move to lower energy. Qualitatively this movement may be thought of as arising from the repulsion of the 'N2' levels as the interaction between them is increased. More quantitatively we can get some insight into the behaviour of this system by looking at the adiabatic potential surfaces given by equation (4) modified by equation (5). These potential surfaces are the solutions for V of the determinantal equation:

$$\begin{vmatrix} W_E + U - kQ_X - V & kQ_Y & cQ_Y \\ kQ_Y & W_E + U + kQ_X - V & -cQ_X \\ cQ_Y & -cQ_X & W_{A_2} + U - V \end{vmatrix} = 0 \quad (10)$$

where U denotes $\frac{1}{2} m\omega^2 (Q_X^2 + Q_Y^2)$. Cross-sections through the surfaces and computed energy levels are shown in Fig. 5.

The repulsion of the 'N2' and 'N3' levels as S_{AE} increases causes successive vibronic levels of the 'N2' set to cross the 'N3' zero-phonon level (Fig. 4a). At these crossing points there is a particularly large effect on the calculated shape of the absorption spectrum (Fig. 6). The spectra have been calculated from the eigenvectors of the vibronic secular equation. Light polarised along the X axis of the optical centre (as defined in § 5) can induce transitions only from the state $\psi_{A_{100}}$ to ψ_{EX00} when the vibronic interaction V' is switched off. At 0 K and $V' = 0$ this would be the only transition allowed, in this model. With $V' \neq 0$ the vibronic eigenstates are linear combinations of the uncoupled states $\psi_{A_{2pq}} \dots \psi_{E_{Ypq}}$. Transitions with X polarised light can then occur from $\psi_{A_{100}}$ to any vibronic state which contains an admixture of ψ_{EX00} . The relative intensity of the transition is simply the square of the coefficient of the ψ_{EX00} term in the linear combination.

From experiment we know the strength of the N2 band relative to the N3 band (equation 1). Similarly we may calculate the total absorption strength predicted to lie at energies below the N3 zero-phonon line in spectra like Fig. 6. The result, Fig. 4b, shows a series of peaks at the resonance conditions when the

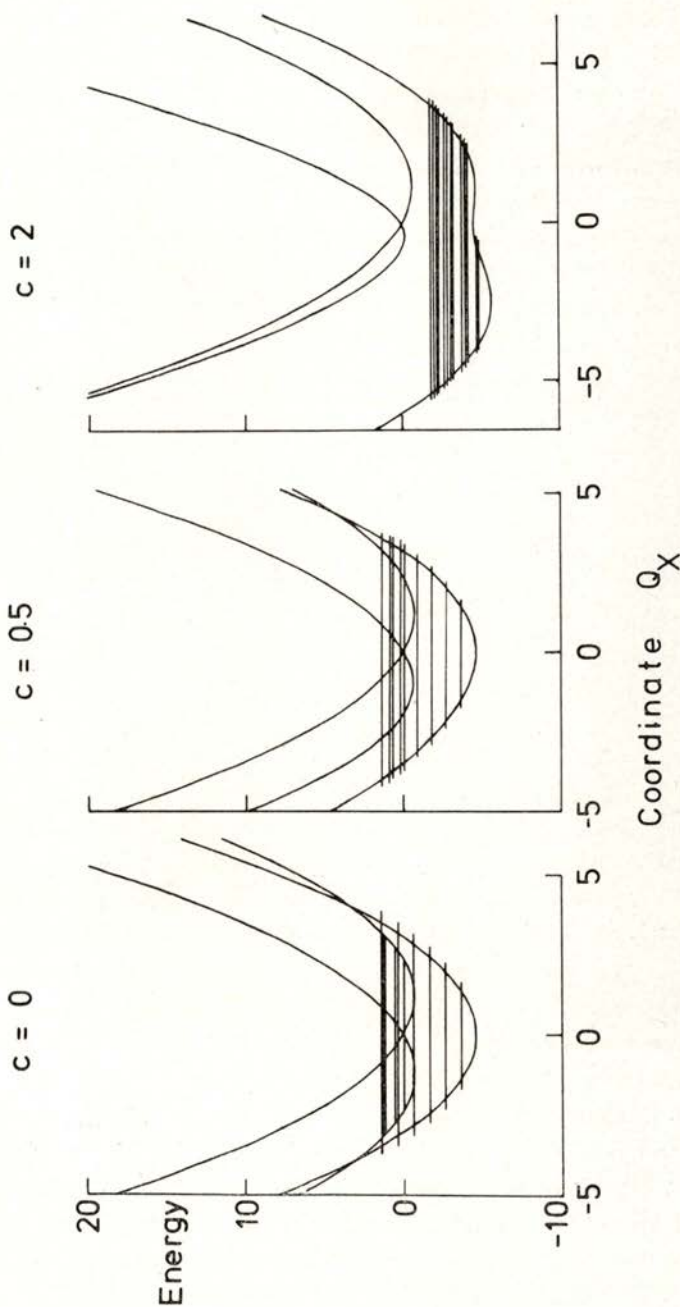


Fig. 5—Cross-sections through the adiabatic potentials (equation 10) along the Q_x axis with $Q_y = 0$. Parameters are $m = 1$, $\hbar\omega = 1$, $W_{A_2} = -4.625$, $k = 1.17$. At left the N3 state undergoes a Jahn-Teller distortion without interacting with the N2 level ($c = 0$). The centre shows weak interaction ($c = 0.5$) and at right strong interaction ($c = 2.0$). The vibronic energy levels are shown by horizontal lines. The lowest energy level is the non-degenerate N2 zero-phonon level with weak coupling, and is a near degenerate triplet with strong coupling as three minima are formed in the adiabatic potential.

'N2' vibronic levels coincide with the 'N3' zero-phonon level. In reality there is not a single E vibrational mode which interacts with the electronic states, and the vibronic coupling is spread out over a range of vibrational frequencies. Consequently these resonances will not occur to the extent shown on Fig. 4b: these large peaks are an artifact of this single mode model. However it would be reasonable to expect to see some small resonance effects near to the N3 zero-phonon line, and possibly the structure near 23800 cm^{-1} (2.950 eV) is caused by this mechanism.

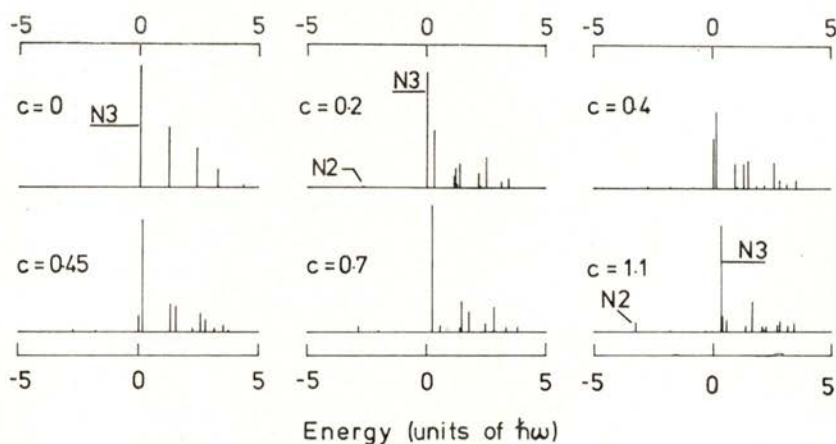


Fig. 6 — Calculated spectra with $m = 1$, $\hbar\omega = 1$, $W_E = 0$, $W_{A2} = -4.625$ and $k = 1.17$, for different values of c . Each of these lines is the «zero-phonon» line for a suitable progression of totally symmetric phonon sidebands.

Ignoring the resonance peaks on Fig. 4b, the required relative strengths of the N2 and N3 bands are obtained when $S_{AE} = 0.4$. The calculated bandshape is then as shown in Fig. 6. For comparison with experiment we have to imagine each of the spikes in Fig. 6 as acting as the 'zero-phonon' line for the progressions of totally symmetric phonons [21] which have been ignored in this model. There is, however, consistency with the measured spectrum of Fig. 1 in that the N2 band is predicted to have its strongest feature at the low energy side (the 'N2 line').

7 — SELF-CONSISTENCY CHECKS ON THE
VIBRONIC MODEL

The model proposed for the origin of the N2 bands has the following properties in agreement with experiment:

i) It requires the N2 and N3 transitions to occur at the same optical centre, and hence the N2 and N3 bandstrengths must correlate linearly with each other, as observed in Fig. 2b, and the symmetry of the N2 optical centre has to be the same as the symmetry of the N3 centre, since they are identical, and this has been demonstrated in § 5.

ii) The N2 electronic transition is a forbidden electric-dipole transition. Therefore, after excitation into the N3 level, any de-excitation process which takes the centre into the N2 vibronic levels will lead to a strong quenching of the luminescence because the zero-phonon transition from the N2 zero-phonon state to the ψ_{A100} state remains forbidden even after allowing for the vibronic interaction. It is predicted from the model that weak luminescence transitions will occur near 18550 cm^{-1} , 2.3 eV, as the N2 zero-phonon level decays to the one phonon states ψ_{A110} and ψ_{A101} . These transitions are predicted to have less than 10^{-2} of the N3 luminescence transition probability and a width of 200 cm^{-1} (25 meV), since, like the N2 absorption line, they are transitions which create one of the E modes of vibration. Not surprisingly, these transitions are not convincingly observed in the low temperature luminescence spectrum.

To these general results we can add:

iii) The calculated N2 absorption bandshape has the N2 line (i.e. the lowest energy feature) as the strongest line (Fig. 6), and this is as observed (Fig. 1).

iv) The strength of the interaction required to produce the observed N2 bandstrength is $S_{AE} = 0.4$. The definition of S_{AE} was chosen in equation (9) to be analogous to a Huang-Rhys factor. At deep levels in diamond Huang-Rhys factors are typically of the order of unity, and in particular S values close to 0.5 are observed in the pseudo-Jahn-Teller distortions occurring at the H3

and H4 optical centres in diamond [15]. The vibronic coupling derived for the N2 and N3 levels is therefore typical for diamond.

v) The mixing of the uncoupled states of equation (3) leads to the observed N3 zero-phonon level containing some admixture from ϕ_{A2} . This admixture lowers the probability of luminescence transitions from the N3 zero-phonon level to the ϕ_{A1} electronic state. From the calculations of § 6, and again smoothing out the resonance effects at the values of S_{AE} which give level crossing, the N3 luminescence decay time is predicted to be 10% longer than the radiative lifetime of the pure ϕ_{EX} or ϕ_{EY} to ϕ_{A1} transition. This provides a small contribution to making the radiative decay time of the N3 luminescence decay time ($\tau = 150$ ns after allowing for the non-radiative decay to the N2 levels [13]) so much larger than the values reported for other electric dipole transitions in diamond (typically ~ 20 ns [22]).

A positive test of the vibronic model would come from applying a static deformation to the diamond so as to induce absorption transitions between the ϕ_{A1} electronic ground state and the N2 zero-phonon level. To a good approximation the N2 zero-phonon level is composed solely of the ψ_{A200} state of equation (3). The N2 one-phonon states (which are observed as the N2 line) are admixtures of the ψ_{A201} state with ψ_{EX00} , and the ψ_{A210} state with ψ_{EY00} (see equation 7). It is the ϕ_{EX} and ϕ_{EY} components which make the N2 line observable. With an applied static stress which transforms, say, as EX, the ψ_{A200} (N2 zero-phonon) state interacts with the ψ_{EY00} component of the ψ_{A210} , ψ_{EY00} (N2 one-phonon) state, transferring intensity to the N2 zero-phonon line. Additional mixing occurs directly between the N2 and N3 zero-phonon lines. The experiment consists of applying measured stresses to the diamond while the known parameter S_{AE} in the vibronic model refers to atomic movements Q_X , Q_Y (equations 5, 6, 9) at the N2/N3 optical centre. To estimate the size of the induced N2 zero-phonon line we must therefore convert the known parameter S_{AE} to a stress matrix element by means of a suitable elastic constant which will differ from the known elastic constants of diamond because of the presence of the optical centre. To do this we make the assumption that the elastic constants near the optical centre are the same for all the vibronic levels of the N2/N3 excited states. Now, the relaxation energies S_{AE} , S_{Exe} are

proportional to the squares of the matrix elements c and k (equations 6, 8, 9). Since, from Table 1,

$$\langle EY | c_{EX} | EY \rangle \approx \langle EY | c'_{EX} | EY \rangle$$

for the N3 states we estimate the interaction of the A2 and E electronic states by:

$$\int dr \phi_{A2}^* c_{EX} \phi_{EY} \sim \int dr \phi_{A2}^* c'_{EX} \phi_{EY} \sim (S_{AE}/S_{Exc})^{1/2} \int dr \phi_{EY}^* c_{EX} \phi_{EY}$$

The integral on the right is obtained from Table 1 for

$$\int dr \phi_{EY}^* c_{EX} \phi_{EY} = \langle EY | c_{EX} | EY \rangle \cdot K(E)^{-1}$$

where $K(E)$ is the Ham reduction factor [23] with a value $K(E)=0.6$ at $S_{Exc}=0.69$. Hence $\int dr \phi_{EY}^* c_{EX} \phi_{EY} \sim 11 \text{ cm}^{-1} (\text{GPa})^{-1}$. This value may be scaled into the vibronic secular matrix (§ 6) since we have already assumed that $\hbar\omega = 1186 \text{ cm}^{-1}$. Thus $\int dr \phi_{EY}^* c_{EX} \phi_{EY} \sim 0.01 \hbar\omega (\text{GPa})^{-1}$. From the eigenstates of the vibronic secular matrix including a $\langle 001 \rangle$ stress of 3 GPa the strength of the induced N2 zero-phonon line is predicted to be $\sim 10^{-4}$ of the total N2 and N3 absorption. Experiments to observe this line with $\langle 001 \rangle$ stresses of up to 2.5 GPa applied at liquid nitrogen temperature have not shown detectable absorption, but an N2 zero-phonon line would only have been detected if its strength exceeded approximately 2×10^{-3} of the total absorption. No change in the N3 radiative decay time has been observed under $\langle 001 \rangle$ stresses by M. F. Thomaz (private communication); and again the effect predicted by the theoretical model is very small.

Finally, the vibronic model discussed here has ignored the effects of totally symmetric modes. For the N3 zero-phonon line the largest stress response is given by the $\langle EX | c'_{A1} | EX \rangle$ term (Table 1) which describes the perturbations produced by totally symmetric, volume-conserving compressions along the trigonal axis of each centre (i.e. stresses $2s_{ZZ}-s_{XX}-s_{YY}$ in the coordinates defined at the beginning of § 5). This coupling is presumably

responsible for the N3 band being predominantly coupled to totally symmetric modes [21]. The totally symmetric perturbations of the N2 line are about three times smaller (Table 1c) implying a Huang-Rhys factor for the N2 totally symmetric coupling some 9 times smaller than for the N3 line. This is qualitatively as observed (Fig. 1): there are no pronounced phonon sidebands of the N2 line as there are for the N3 line.

The difference in the totally symmetric coupling for the N2 and N3 lines has an effect on the vibronic theory. The interaction of the ϕ_{A_2} and ϕ_{EX}, ϕ_{EY} states is quenched by their relative displacements in the totally symmetric modes, analogous to a Ham reduction. However, the effect is not very large. Each vibronic matrix element (equation 7) is reduced by a factor determined by the overlap of the totally symmetric vibrational states. This factor will be less than about three for the vibronic states of interest and will not affect the general results given here.

8 — SUMMARY

Experimental data presented in this paper confirm that the strengths of the N2 and N3 absorption bands correlate with each other (Fig. 2). Uniaxial stress data on the N2 line have been shown to be consistent with it occurring at a trigonal centre (§ 5) as does the N3 line. The different magnitudes of the stress responses of the N2 and N3 lines are consistent with the different strengths of their phonon sidebands (§ 7). The suggestion [13] that the N2 line is a forbidden transition made allowed by vibronic interaction with the N3 level has been shown to be quantitatively reasonable (§ 6). Positive confirmation of this model has not been achieved. The theory predicts that the N2 zero-phonon line will be induced by stress, but will be too weak to observe, and experiments have not detected it. However the model does provide a natural explanation for the large width of the N2 line, and for the lack of luminescence observed from the N2 line (§ 7).

REFERENCES

- [1] G. DAVIES, *J. Phys.*, **C9**, L537 (1976).
- [2] H. B. DYER, F. A. RAAL, L. DU PREEZ and J. H. N. LOUBSER, *Phil. Mag.*, **11**, 763 (1965).

- [3] A. T. COLLINS and K. MOHAMMED, *J. Phys.*, **C14**, in press.
- [4] C. D. CLARK and C. A. NORRIS, *J. Phys.*, **C3**, 651 (1970).
- [5] P. A. CROWTHER and P. J. DEAN, *J. Phys. Chem. Solids*, **28**, 1115 (1967).
- [6] A. A. KAPLYANSKII, V. I. KOLYSHKIN and V. N. MEDVEDEV, *Sov. Phys. Solid State*, **12**, 1193 (1970).
- [7] B. HENDERSON, *Industrial Diamond Review*, March 1980, pp. 92-97.
- [8] G. DAVIES, C. M. WELBOURN and J. H. N. LOUBSER, *Diamond Research*, 1978, pp. 23-30.
- [9] G. DAVIES and I. SUMMERSGILL, *Diamond Research*, 1973, pp. 2-5.
- [10] M. YA SHCHERBAKOVA and E. V. SOBOLEV, *Dokl. Akad. Nauk. SSSR*, **204**, 851 (1972); J. H. N. LOUBSER and A. C. J. WRIGHT, *Diamond Research*, 1973, pp. 16-20; M. YA SHCHERBAKOVA and V. A. NADOLINNYI, *Zhurnal Struct. Khimii*, **19**, 305 (1978).
- [11] R. M. CHRENKO, R. E. TUFT and R. M. STRONG, *Nature*, **270**, 141 (1977); B. P. ALLEN and T. EVANS, *Proc. R. Soc.*, **A375**, 93 (1981).
- [12] P. G. N. NAYAR, *Proc. Ind. Acad. Sci.*, **A14**, 1 (1941).
- [13] M. F. THOMAZ and G. DAVIES, *Proc. R. Soc.*, **A362**, 405 (1978).
- [14] J. WALKER, *Rep. Prog. Phys.*, **42**, 1605 (1979).
- [15] G. DAVIES, *Rep. Prog. Phys.*, **44**, 787 (1981).
- [16] G. DAVIES, *J. Phys.*, **C3**, 2474 (1970).
- [17] C. D. CLARK, R. W. DITCHBURN and H. B. DYER, *Proc. R. Soc.*, **A234**, 363 (1956).
- [18] A. E. HUGHES and W. A. RUNCIMAN, *Proc. Phys. Soc.*, **80**, 827 (1967).
- [19] A. A. KAPLYANSKII, *Opt. Spectrosc.*, **16**, 329 (1964).
- [20] M. TINKHAM, *Group Theory and Quantum Mechanics* (New York: McGraw-Hill) (1964).
- [21] G. DAVIES, *J. Phys.*, **C7**, 3797 (1974).
- [22] M. D. CROSSFIELD, G. DAVIES, A. T. COLLINS and E. C. LIGHTOWLERS, *J. Phys.*, **C7**, 1909 (1974); M. D. CROSSFIELD, PhD. thesis, University of London (1981).
- [23] F. S. HAM, in *Electron paramagnetic resonance*, edited by D. Geshwind (New York: Plenum Press) (1972), pp. 1-119.



CONTENTS
FASCÍCULO 1-2

NUCLEAR PHYSICS

Time-Dependent Generator Coordinate Method and the N-N Interaction

L. P. BRITO and C. A. SOUSA 1

Fundamental Properties of Liquid Argon, Krypton and Xenon as Radiation Detector Media.

T. DOKE 9

CONDENSED MATTER PHYSICS

The Estimated Intensity Variance as a Mean of Expected and Sample Variances.

W. GONSCHOREK 49

The Thermal and Magnetic Properties of Some Rare Earth-Pd₃ Phases of the AuCu₃ Structure

J. M. MACHADO DA SILVA, W. E. GARDNER, I. R. HARRIS . . . 61

GENERAL AND MATHEMATICAL PHYSICS

An Epitome of Configurational Data on Connected Clusters

J. A. M. S. DUARTE 99

CONTENTS
FASCICULO 3-4

NUCLEAR PHYSICS

- The Asymptotic Approximation in Heavy Ion Transfer Reactions
A. M. GONÇALVES and F. D. SANTOS 139
- Absolute Cross Sections for the $^{64}\text{Zn}(^{12}\text{C}, X)$ and $^{58}\text{Ni}(^{12}\text{C}, X)$ Reactions
H. KAWAKAMI, A. P. DE LIMA, J. H. HAMILTON, A. V. RAMAYYA,
R. M. RONNINGEN, M. D. BARKER, G. D. GALAMBOS,
A. C. RESTER, H. K. CARTER, R. L. MLEKODAJ and
E. H. SPEJEWSKI 163

CONDENSED MATTER PHYSICS

- Temperature Dependence of the Magnetic Susceptibility of Some Ag Mn
Alloys
J. M. MACHADO DA SILVA, H. ABE, H. MIYAJIMA and
J. M. ARAÚJO 181
- An Automatic Faraday-Type Magnetometer with a Wide Range Sen-
sitivity
J. F. D. MONTENEGRO 189
- Measurement of Surface Acoustic Waves in Rare Earth Metals at Low
Temperature
M. S. NEJAD and S. B. PALMER 205
- Effects of Uniaxial Stress on the 27084 cm^{-1} and 26942 cm^{-1} Absor-
ption Lines in Diamond
M. H. NAZARÉ and J. P. CASQUILHO 229
- The Origin of the "N2" Absorption Band in Natural Yellow Diamonds
GORDON DAVIES 241

AUTHOR INDEX

- ABE, H. — See J. M. MACHADO DA SILVA
- ARAÚJO, J. M. — See J. M. MACHADO DA SILVA
- BARKER, M. D. — See H. KAWAKAMI
- BRITO, P. L., SOUSA, C. A. — Time-Dependent Generator Coordinate Method and the N-N Interaction 1
- CARTER, H. K. — See H. KAWAKAMI
- CASQUILHO, J. P. — See M. H. NAZARÉ
- DAVIES, G. — The Origin of the "N₂" Absorption Band in Natural Yellow Diamonds 241
- DOKE, T. — Fundamental Properties of Liquid Argon, Krypton and Xenon as Radiation Detector Media 9
- DUARTE, J. A. M. S. — An Epitome of Configurational Data on Connected Clusters 99
- GALAMBOS, G. D. — See H. KAWAKAMI
- GARDNER, W. E. — See J. M. MACHADO DA SILVA
- GONÇALVES, A. M., SANTOS, F. D. — The Asymptotic Approximation in Heavy Ion Transfer Reactions 139
- GONSCHOREK, W. — The Estimated Intensity Variance as a Mean of Expected and Sample Variances 49
- HAMILTON, J. H. — See H. KAWAKAMI
- HARRIS, I. R. — See J. M. MACHADO DA SILVA
- KAWAKAMI, H., LIMA, A. P. DE, HAMILTON, J. H., RAMAYYA, A. V., RONNINGEN, R. M., BARKER, M. D., GALAMBOS, G. D., RESTER, A. C., CARTER, H. K., MLEKODAJ, R. L., SPEJEWSKI, E. H. — Absolute Cross Sections for the ⁶⁴Zn(¹²C, X) and ⁵⁸Ni(¹²C, X) Reactions 163

LIMA, A. P. DE — See H. KAWAKAMI	
MIYAJIMA, H. — See J. M. MACHADO DA SILVA	
MLEKODAJ, R. L. — See H. KAWAKAMI	
MONTENEGRO, J. F. D. — An Automatic Faraday-Type Magnetometer with a Wide Range Sensitivity	189
NAZARÉ, M. H., CASQUILHO, J. P. — Effects of Uniaxial Stress on the 27084 cm^{-1} and 26942 cm^{-1} Absorption Lines in Diamond . . .	229
NEJAD, M. S., PALMER, S. B. — Measurement of Surface Acoustic Waves in Rare Earth Metals at Low Temperature	205
PALMER, S. B. — See M. S. NEJAD	
RAMAYYA, A. V. — See H. KAWAKAMI	
RESTER, A. C. — See H. KAWAKAMI	
RONNINGEN, R. M. — See H. KAWAKAMI	
SANTOS, F. D. — See A. M. GONÇALVES	
SILVA, J. M. MACHADO DA, GARDNER, W. E., HARRIS, I. R. — The Thermal and Magnetic Properties of Some Rare Earth-Pd ₃ Phases of the AuCu ₃ Structure	61
SILVA, J. M. MACHADO DA, ABE, H., MIYAJIMA, H., ARAÚJO, J. M. — Temperature Dependence of the Magnetic Susceptibility of Some Ag Mn Alloys	181
SOUSA, C. A. — See L. P. BRITO	
SPEJEWSKI, E. H. — See H. KAWAKAMI	

Composto e impresso
na
IMPRESA PORTUGUESA
Rua Formosa, 108 a 116
4000 Porto



SOCIEDADE PORTUGUESA DE FÍSICA
AV. REPÚBLICA 37-4.º, 1000 LISBOA, PORTUGAL

PORTUGALIAE PHYSICA publishes articles or research notes with original results in theoretical, experimental or applied physics; invited review articles may also be included.

Manuscripts, with an abstract, may be written in English or French; they should be typewritten with two spaces and in duplicate. Figures or photographs must be presented in separate sheets and be suitable for reproduction with eventual reduction in size; captions should make the figures intelligible without reference to the text. Authors are requested to comply with the accepted codes concerning references.

There is no page charge. Author(s) will get 50 free reprints (without covers); these are to be shared among all the authors of the article. Authors interested in more reprints should say so when sending their manuscripts; quotations shall be sent with the proofs.

Subscription rates for volume 12:

1,200 Escudos (US\$20) — individuals
3,000 Escudos (US\$50) — libraries

PORTUGALIAE PHYSICA may also be sent on an exchange basis; we welcome all suggestions to such effect.

All mail to be addressed to

PORTUGALIAE PHYSICA

C/O LABORATÓRIO DE FÍSICA, FACULDADE DE CIÊNCIAS
PRAÇA GOMES TEIXEIRA
4000 PORTO PORTUGAL

PORTUGALIAE PHYSICA

VOL. 12 · NUMB 3/4 · 1981

CONTENTS

NUCLEAR PHYSICS

- The Asymptotic Approximation in Heavy Ion Transfer Reactions
A. M. GONÇALVES and F. D. SANTOS 139
- Absolute Cross Sections for the $^{64}\text{Zn}(^{12}\text{C}, X)$ and $^{58}\text{Ni}(^{12}\text{C}, X)$ Reactions
H. KAWAKAMI, A. P. DE LIMA, J. H. HAMILTON, A. V. RAMAYYA,
R. M. RONNINGEN, M. D. BARKER, G. D. GALAMBOS,
A. C. RESTER, H. K. CARTER, R. L. MLEKODAJ and
E. H. SPEJEWSKI 163

CONDENSED MATTER PHYSICS

- Temperature Dependence of the Magnetic Susceptibility of Some Ag Mn Alloys
J. M. MACHADO DA SILVA, H. ABE, H. MIYAJIMA and
J. M. ARAÚJO 181
- An Automatic Faraday-Type Magnetometer with a Wide Range Sensitivity
J. F. D. MONTENEGRO 189
- Measurement of Surface Acoustic Waves in Rare Earth Metals at Low Temperature
M. S. NEJAD and S. B. PALMER 205
- Effects of Uniaxial Stress on the 27084 cm^{-1} and 26942 cm^{-1} Absorption Lines in Diamond
M. H. NAZARÉ and J. P. CASQUILHO 229
- The Origin of the "N2" Absorption Band in Natural Yellow Diamonds
GORDON DAVIES 241
- CONTENTS AND AUTHOR INDEX (VOL. 12) 263

